Electronic Thesis and Dissertation Repository

10-4-2017 3:00 PM

Dynamic Studies of Guest Molecules in Metal-Organic Frameworks and Zeolites via Solid-State Nuclear Magnetic Resonance

Bowei Wu, *The University of Western Ontario*

Supervisor: Yining Huang, *The University of Western Ontario*

A thesis submitted in partial fulfillment of the requirements for the Master of Science degree in Chemistry
© Bowei Wu 2017

Follow this and additional works at: https://ir.lib.uwo.ca/etd

Part of the Inorganic Chemistry Commons, Materials Chemistry Commons, and the Physical Chemistry Commons

Recommended Citation

Abstract

Metal-organic frameworks (MOFs) are synthetic compounds with crystalline microporous structures, consisting of metal centres joined by organic linkers. Zeolites are a class of crystalline porous materials featuring negatively charged aluminosilicate frameworks and charge-balancing cations. In this work, solid-state nuclear magnetic resonance (SSNMR) is used to probe guest molecule locations and dynamics in MOFs and zeolites, yielding detailed information of guest motion within these porous materials. Chapter 2 describes SSNMR dynamic studies of $^{13}CO_2$, ^{13}CO and C_2D_4 adsorption behaviour in the α - zinc formate MOF, $[Zn_3(HCOO)_6]$, which were performed at variable temperatures (VTs) using the ^{13}C DEPTH-Echo, ^2H quadrupolar echo, and ^1H - ^{13}C cross polarization pulse (CP) sequences. The simulated experimental spectra indicate these adsorbed guest molecules undergo the same type of specific, well-defined motions within the α - zinc formate MOF. Chapter 3 details studies on ion-exchanged FAU and LTA zeolites that were used as porous adsorbents to adsorb $^{13}CO_2$ guests. The results suggest that the adsorption behaviour and dynamics of CO_2 in zeolites are greatly influenced by (i) the specific charge balancing cations, (ii) the particular Si/Al ratios, and (iii) the type of zeolite framework. VT ^{13}C DEPTH-echo and ^1H-^{13}C cross polarization SSNMR experiments have revealed that some CO_2 guests are almost immobilized upon the extra-framework cations, while other CO_2 guests form carbonate-like species while strongly interacting with cations.

Keywords

Co-Authorship Statement

Paul D. Boyle (Department of Chemistry, Western University, London, Ontario, Canada) is credited for performing the single crystal structure determination and refinement of the CO_2-loaded α - zinc formate MOF described in Chapter 2.

Victor V. Terskikh (Department of Chemistry, University of Ottawa, Ottawa, Ontario, Canada) is credited for ^{67}Zn spectral acquisition and CASTEP computational calculations of the NMR parameters in α - zinc formate samples at an ultra-high magnetic field of 21.1 T in Chapter 2.

Acknowledgments

Recalling the moment when I first landed in London and started my journey on graduate life in Western University, I'm still grateful to my supervisor, Dr. Yining Huang, who gave me this precious chance to explore the fascinating world of chemistry. During the two years, Dr. Huang has offered me so much help, not only in my research study, but also supported me in my tough times. Meanwhile, the friendly and knowledgeable environment here in the Chemistry Department has helped me conquer many obstacles standing in my path.

First of all, my deepest and sincerest gratitude should be given to Professor Yining Huang, who gave me the opportunity and led me into the "Solid-State NMR forest" to explore the unknown territories. Without his kind and continuous support, I don't think I could progress so far on my research and finish my graduate studies. Secondly, I would like to give many of my thanks to Dr. Bryan E.G Lucier, the post-doctoral fellow in our group. He taught me useful techniques and tips about how to run our SSNMR spectroscopy efficiently, and always saved my experiments when I met troublesome problems. Meanwhile, Bryan had offered me countless brilliant suggestions in editing my papers and written works. I would also like to give a special thanks to the NMR facility manager in the Chemistry Department, Dr. Mathew Willians, for his knowledgeable support with SSNMR experiments and his hard work helping me set up my experiments and processing my results. He is always patient and prepared for any questions and problems. When I have met some hardware or software issues with the SSNMR spectrometers, he was always able to quickly solve them, and my experimental results would be of lower quality without his help. I also give thanks to many other faculty and staff that has helped me. Dr. Victor V. Terskikh from the Department of Chemistry at the University of Ottawa is thanked for running samples at the 21.1 T high field SSNMR spectroscopy facility. Dr. Paul Boyle, working in the chemistry X-ray facility, helped me with single-crystal XRD structural determination and my studies in his graduate course. Dr. Roberta L. Flemming from Earth Sciences also gave me a great deal of help in my studies in her graduate course and a post-course project. Dr. Audrey Bouvier from Earth Sciences helped me with ICM-MS experiments to analyze elemental components in my zeolite samples. I also want to give my thanks to Yves Rambour from the glassblowing shop,

Table of Contents

List of Tables

List of Figures

be observed, which are attributed to carbonate spices, adsorbed CO_2, and mobile CO_2 guests.

Figure 3-14. Simulated ^{13}C spectral lineshapes of (a) Resonance I, carbonate species, (b) Resonance II, mobile CO_2 guests, and (c) Resonance III, adsorbed CO_2 guests in zeolite LSX from 433 K to 123 K. The lineshapes corresponding to the carbonate species in (a) do not change much with temperature, and reach their maximum span around 293 K; the width of the mobile CO_2 guest powder patterns in (b) generally gets broader at lower temperatures; the span of adsorbed CO_2 guests in (c) becomes broader at very high and very low temperatures.

Figure 3-15. VT static ^{13}C SSNMR spectra of CO_2 guests in (a) NaY, (b) HY and (c) NH_4Y. The sharp and featureless resonances suggest that no obvious interactions are taking place between CO_2 guests and the charge balancing cations that serve as adsorption sites.

Figure 3-16. Static ^1H - ^{13}C CP SSNMR spectra of CO_2 loaded HY and NH_4Y zeolites at 293 K. The rather noisy lineshape for H-Y reveals that only a small amount of CO_2 guest interacts directly with the zeolite protons in (a), while the more intense signal for the NH_4-Y zeolite suggests some CO_2-H interactions are present in (b).

Figure 3-17. The cation distribution of Na^+, H^+, and NH_4^+ in Faujasite type Y zeolites. The possible CO_2 guest locations and behaviour have also been shown. The loading level of CO_2 guests in this work is about 1.76, 1.42 and 1.30 guest per α – super cage, respectively, and CO_2 guests in these figures represent all possible CO_2 locations. The Na^+ cations in Na-Y can only be found in their preferred Site I and Site II positions due to the low Si/Al ratio of zeolite type Y in (a). The protons in (b)H-Y exist in the form of bridging H-O hydroxyl groups where two H1 are at opposite positions of a hexagonal prism, sticking into the α - cage, and H2 and H3 are pointing into the plane of 6-member ring structure of sodalite cage in (b). The ammonium cations prefer the positions at Site I' and II in zeolite Y framework, as shown in (c). Mobile CO_2 guest is not shown.

Figure 3-18. Static VT ^{13}C SSNMR spectra of CO_2 loaded within the (a) Li, (b) Na, (c) K and (d) Ca-exchanged type A zeolites. Each of the four exchanged cations have a distinct

List of Abbreviations

ALPO	aluminophosphate
BDC	1,4-benzendicarboxylate
CP	cross polarization
CSA	chemical shift anisotropy
DABCO	1,4-diazabicyclo[2.2.2]octane
DMF	N,N-dimethylformamide
DI	dipolar interaction
EFG	electric field gradient
EXPRESS	Exchange Program for Relaxing Spin System
FAU	faujasite
FID	free induction decay
FT	Fourier transformation
FTIR	Fourier transformation infra-red
ICP-MS	inductively coupled plasma – mass spectrometry
IR	infra-red
LTA	Linde type A
LSX	low-silica X
MAS	magic angle spinning
MOF	metal-organic framework
NMR	nuclear magnetic resonance
PAS	principal axis system
ppm	parts per million
PSA	pressure swing adsorption
pXRD	powder X-ray diffraction
QI	quadrupolar interaction
REDOR	rotational-echo double-resonance
SAPO	silicoaluminophosphate
SCXRD	single-crystal X-ray diffraction
SEDOR	spin-echo double-resonance
SSNMR	solid-state nuclear magnetic resonance
TMS	tetramethylsilane

T-sites	tetrahedra sites
VT	variable temperature
XRD	X-ray diffraction
ZSM	Zeolite Socony Mobil

List of Appendices

Chapter 1

1 Introduction

1.1 Metal-Organic Frameworks (MOFs)

1.1.1 MOF background

Metal-organic frameworks (MOFs) are a class of cutting-edge synthetic compounds with a crystalline porous structure consisting of metal centres connected by organic linkers. The bonding between metal cations and organic linkers leads to an infinite and highly organized three-dimensional porous structure. The pores in MOFs are typically 1 nm or less in diameter, which classifies MOFs as microporous materials (*i.e.*, pore size < 2 nm) according to IUPAC recommendations.[1] The porous channels and various functional groups that are present within MOFs assist in guest molecule adsorption. Due to the microporous nature of MOFs, they are considered excellent adsorbents and should be well-suited for the uptake of guest gas molecules such as CO_2, CO, and C_2H_4.

(a)   (b)   (c)
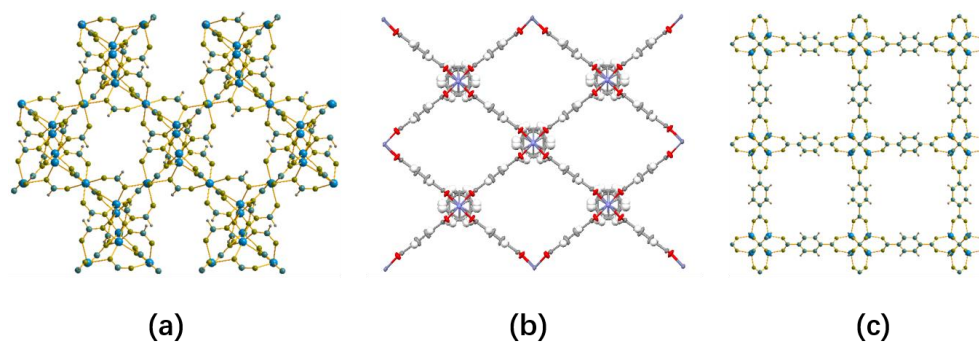
Figure 1-1. The framework structures of (a) α – zinc formate,[2] (b) $Zn_2(BDC)_2DABCO$[3] and (c) MOF-5[4].

The first MOF synthesis was performed by Hoskins and Robson in 1989, in which they created a material consisting of infinite polymeric frameworks of 3D-linked molecular rods based on Cu^+, Zn^{2+}, or Cd^{2+} cations and bridging ligands.[5] In 1995, Yaghi coined the phrase "metal organic framework" to refer to such materials.[6] In 1999, Li and co-workers synthesized and refined the structure of MOF-5, opening the door to a new

field of inorganic chemistry.[4] Since then, hundreds of MOFs have been synthesized and reported, featuring a wide array of structures and many interesting properties. Many of these MOFs exhibit desirable properties such as high gas storage capacities, gas separation abilities, and high catalytic activities.[7]

The diversity of MOFs originates from the numerous metal elements with various charges and coordination numbers that can be combined with many different types of organic linkers to make these materials. Multiple functional groups can be introduced onto each type of organic linker, further expanding the range of MOFs accessible to material scientists. Because MOFs are 3D frameworks, the same combination of metal centre and linker can result in more than one particular MOF phase or topology depending on the synthetic route employed, which again broadens the range and diversity of MOF systems that can be created. With the proper choice of metal centre, organic linkers, and synthetic route, crystalline MOFs can be designed to address specific purposes or applications. For example, there are several MOFs have been successfully commercialized to serve in specific fields such as Basolite® C300 ($Cu_3(C_9H_3O_6)_2$, known as Cu-BTC MOF or HKUST-1)[8] and Z377 ($Zn_4(C_{27}H_{15}O_6)O$, known as MOF-177)[9] produced by BASF Corporation.

Several synthesis methods have been reported to produce highly crystalline MOFs, such as solvothermal,[10] ionic liquid,[11] microwave-assisted,[12] electrochemical,[13] mechanochemical,[14] and sonochemical synthesis.[15] Solvothermal synthesis is considered a reliable first choice for MOF synthesis, however, this route is also associated with the troublesome problem of waste solvents that are usually toxic organic molecules. As an alternative solution, a new method called mechanochemical synthesis has been developed,[16] which employs ball milling of solid reagents to trigger chemical reactions through mechanical and thermal energy. For instance, two MOFs known as HKUST-1($Cu_3(BTC)_2$, BTC = 1,3,5-benzenetricarboxylate) and MOF-14 ($Cu_3(BTB)_2$, BTB = 4,4',4'' -benzenetribenzoate) have been successfully synthesized and characterized using mechanochemical synthesis,[16] and exhibit excellent properties.

1.1.2 Applications of MOFs

Metal-organic frameworks, as a class of solid microporous materials, are well-suited for applications in selective gas adsorption and separation,[7a] reaction catalysis,[7b] luminescence[17] and many other fields,[18] as outlined below.

MOFs have been a topic of intense research in the past decade due to their applications in selective gas adsorption and separation. The crystalline, microporous nature of MOFs and their relatively narrow pore sizes allows MOFs to separate noble gases, isotopes, halogens, O_2/N_2, CO/CO_2, nitric oxides, halo hydrocarbons, aromatic organics, organic isomers and many other gases with similar physical and/or chemical properties.[7a] MOFs can separate gas mixtures that cannot be separated by other solid adsorbents such as zeolites, activated carbon, and silica gel.

Catalytic properties are always considered an important and valuable function in solid materials. The diversity of the organic linkers and metal clusters that can be incorporated within MOFs can be combined to address specific applications, such as organic catalysis.[7b] However, MOF applications as catalysts have been limited by the challenge of combining catalytic function with a relatively high thermal stability, and devising specific syntheses for catalytic MOFs has also been quite challenging and time-consuming. Recently, a functionalized Ir–Zr-MOF has shown promising catalytic activity for the hydrogenation of aromatics, and this MOF is thermally stable up to 350°C in air.[19] Introducing the capability to selectively catalyze preferred molecules within MOFs can be achieved by tuning the pore sizes during the synthesis process. Ravon and co-workers have reported that in their works, MOF-5 with tunable pore sizes can be applied as an acid catalyst with shape selectivity.[20] In the coming years, it is believed that MOFs will become a viable alternative to classic solid catalysts such as zeolites.

The luminescent properties of MOFs are of great interest, and the mechanisms of luminescence in MOFs have been well-studied, particularly the complicated interactions involved with charge transfers between the linkers and metal centres of MOFs, as well as those localized on the ligands and metals, respectively.[17] In some cases, the guest molecules present in MOF structures may also contribute to the emission effects, which

means that MOFs could potentially serve as luminescent sensors of guest molecules, with many practical applications.[21]

1.1.3 MOFs and gas adsorption

MOFs can be specifically designed and synthesized as functional adsorbents, with many industrial applications explored and developed in recent years.[22] In contrast to the rigid structure of zeolites, some MOFs have flexible frameworks that can adjust their pore dimensions and pore shapes to accommodate a diverse set of guest molecules.[23] Another advantage is that MOFs can be designed and modified to meet specific demands in both gas separation and adsorption at the same time.[7a] Six structural features and mechanisms have been reported for guest adsorption in MOFs:[24] open-metal sites; hydrogen-bond donor and acceptors; acid-base interactions; electrostatic interactions; π-complexation interactions and breathing effects. The diversity in possible adsorption mechanisms and adsorption sites means that MOFs can act as gas adsorbents to separate and store target gases from a mixture, with practical applications in the purification of natural gas, O_2/N_2 separation, and greenhouse gas separation and storage.[25] Research on greenhouse gas capture, especially CO_2, has been a popular topic in recent years.[26] MOFs can also be designed for the adsorption of many other gases, such as CH_4, C_2H_4, C_2H_2 and CO, and so on.[7a]

CO_2 gas is mainly produced by the combustion of fossil fuels and is now believed to be one of the main causes of global warming.[27] Several strategies, such as the use of aqueous alkanolamine absorbents, have been studied and developed to capture CO_2 from flue gases produced by industrial sources.[28] The mechanism of CO_2 capture by alkanolamines involves the formation of C-N chemical bonds with CO_2 gas, turning it into a carbonate or bicarbonate species. But several obvious drawbacks of this strategy, such as amine adsorbent decomposition[29] and corrosive aqueous solutions[30], have significantly limited its effective usage. There are also disadvantages with other porous solid adsorbents such as zeolites, which have high sensitivity of water absorption,[31] dramatically decreasing its CO_2 gas adsorption capability despite the high surface area and microporous nature of zeolites. MOFs are a good potential CO_2 adsorbent due to their

porous structure and relatively good thermal stability in mild conditions.[32] MOFs can be considered as a hybrid compound that includes the chemisorption capabilities associated with alkanolamines and the porous structure and high BET surface areas associated with zeolites: CO_2 adsorption in MOFs is due to both the functional groups and the porous structure present within MOF structures. Liang et al. reported that the Cu-BTC MOF adsorbs 12.7 mol/kg CO_2 at 15 bar,[33] while Furukawa et al. detailed how MOF-200 can adsorb 53.34 mol/kg CO_2 at 50 bar,[34] which are excellent CO_2 uptake capacities.

CO gas is produced as a problematic toxic waste gas from industrial factories and combustion engines, and is a by-product from incomplete combustion. The binding of CO with hemoglobin in blood is much stronger than haemoglobin-O_2 binding, leading to a severe problem where the blood is unable to transport oxygen; this may result in death.[35] It is necessary to develop solid adsorbents which can easily and efficiently separate and adsorb trace amounts of CO from gas mixtures and from the air. Currently, studies on CO adsorption mainly focus on adsorption in MOFs with open metal sites,[36] and there are relatively fewer studies on CO adsorption than there are for CO_2 adsorption. There have been some studies on CO adsorption focused on adsorption capabilities and capacities,[37] but relatively few have been devoted to the motion of adsorbed CO,[38] which is considered a key piece of data for improving CO adsorption in MOFs.

C_2H_4, or ethylene, is a simple organic gas involved in many organic reactions, and is the starting point in the synthesis of compounds such as polymers, epoxyethane, various diols and ethanol.[39] The large-scale production method of ethylene is steam cracking of naphtha, olefins or other petroleum compounds.[40] The ethylene product exists in the resulting gas mixture along with many other organic gases, such as methane, propane and ethane.[41] Currently, factories and manufacturers primarily use condensation and distillation processes to extract ethylene from gas mixtures, but this process consumes a relatively large amount of energy. A solid ethylene adsorbent to separate ethylene from gas mixtures under mild conditions would be very useful. MOFs are now the most promising solid adsorbents for this task. Studies have indicated that there are MOFs, such as MIL-101–Cr–SO_3Ag, and M_2(dobdc) (M = Mg, Mn, Fe, Co, Ni, Zn; dobdc = 2,5-dioxido-1,4-benzenedicarboxylate), which can selectively adsorb ethylene over other gases,[42] which qualifies these materials as potential candidates for ethylene adsorbents.[43]

However, there are relatively few studies on the molecular dynamics of adsorbed ethylene in MOFs, or the mechanisms of ethylene adsorption in MOFs.[43-44]

There are many ways to characterize guest adsorption in MOFs. Studies on adsorbed gases within MOFs via IR[45] or Raman[46] spectroscopy were used to examine the vibrational and stretching motion status; pressure swing adsorption can be employed to determine the guest separation capabilities from flue gas sources;[47] powder or single-crystal X-ray diffraction (pXRD, SCXRD) can accurately suggest guest locations and distributions in the MOF framework;[48] and BET experiments can be used to measure MOF surface areas that are one of the main determinants of guest molecule uptake capabilities.[49] However, none of these characterization techniques can intimately probe the local environment about the guest gas atoms or the atoms within the MOF. There is a need for a non-destructive method that can probe guest adsorption and MOF structure at the molecular level.

1.1.4 SSNMR of MOFs

Nuclear magnetic resonance (NMR) acts as a sensitive probe of the local environment surrounding the nucleus of interest, and has been widely used to investigate local structure in various types of materials including MOFs.[50] Solution NMR is popular for examining highly soluble compounds, however, many compounds are either insoluble or decompose in solution. Solid state NMR (SSNMR) experiments are a good option for characterizing such systems, however, SSNMR is relatively more complicated and involves longer experimental times, and also demands the choice of the correct pulse sequence and experimental conditions. SSNMR spectra are distinct from solution NMR spectra and feature broad powder patterns, which make spectral interpretation and simulations much more challenging. In solution NMR, the spectral signals are usually sharp resonances, since rapid molecular tumbling removes the effects of many directionally-dependent NMR interactions. However, in SSNMR spectra, signals are observed as broad powder patterns, which are generated by the directionally-dependent resonance frequencies of all possible molecular orientations in the solid phase. In this manner, SSNMR powder patterns can provide more useful information on atomic and

molecular levels than the spectra obtained from solution NMR, since SSNMR probes the local environment in three dimensions rather than providing an isotropic, motionally averaged picture.[51]

Studies on MOFs via SSNMR spectroscopy mainly focus on structural determination,[50b] investigation of properties such as catalysts[52] and host-guest interactions,[50b] as well as guest dynamics,[53] which strongly support the design and development of new MOF species. By probing the metal centres and organic linkers using SSNMR, the coordination numbers and local chemical environments of metal centres as well as linker orientations and interactions can be examined. For instance, in the CPO-27-Mg MOF,[54] the coordinated water molecules can be removed from metal centres after activation process. The removal of H_2O and formation of the resulting open metal sites are observable in ^{25}Mg metal SSNMR spectra.[54] When guest molecules are introduced and adsorbed onto open-metal sites in MOFs, the metal spectra vary accordingly.[55] Information such as the rotation of some organic linkers can also be detected by SSNMR, such as of the 1,4-benzendicarboxylate (BDC) linker, which contains flipping benzene rings. By conducting ^2H SSNMR experiments in $M_2(BDC)_2DABCO$ (M = Zn, Cu, Co and Ni) MOF, the flipping rates of benzene rings from BDC linkers could be calculated in various situations.[56] Once guest molecules are adsorbed into MOF structures, they may preferentially attach to certain adsorption sites according to the properties of the guest molecules. For instance, CO and CO_2 guests prefer to adsorb onto MOF protons from hydrogen-bond donor groups, such as H-O and H-C groups, while C_2H_4 and C_2H_2 prefer binding to hydrogen-bond acceptors, such as O, Cl, and F atoms.[57] As for open metal sites, exposed metal centres usually carry positive charges and readily coordinate guests with available electron pairs or localized negative polarization.[24] Metal centres that have been fully saturated by coordination to organic linkers are no longer exposed within the MOF cavities, and cannot directly interact with guests. For example, our group has reported that adsorbed CO_2 in α – magnesium formate interacts chiefly with the protons from H-C formate groups that point towards the 1-dimensional channel interior, and CO_2 does not interact with the Mg metal because it has already been saturated by formate linkers.[58] Adsorbed CO_2 guests are continually in fast motion upon, and between, adsorption sites.[53, 58, 59] Thus, variable-temperature (VT) SSNMR experiments targeting adsorbed guests are

8

useful for revealing the specific molecular motions of adsorbed guests. By acquiring VT SSNMR experiments, the apparent or observed NMR parameters of the target guest molecular can be extracted by analyzing experimental spectra via simulation packages, as well as the specific motional patterns of adsorbed guests within MOFs structures. Additionally, by tabulating the observed NMR parameters at different experimental temperatures and comparing them to the known static parameters of the stationary guest molecules, guest motional patterns can be simulated and the guest molecular dynamics adsorbed in the MOF can be obtained, which are very helpful for understanding the adsorption mechanisms and guest-host interactions present.

1.2   Zeolites

1.2.1 Zeolite background
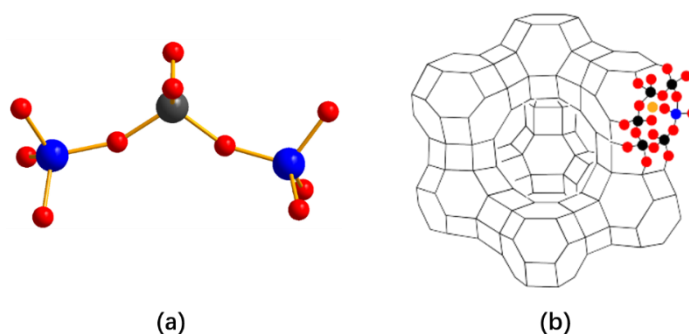
Figure 1-2. The structure of zeolites. (a) A visual representation of silicon (black ball) and aluminum (blue ball) tetrahedral sites with oxygen bridging atoms (red balls); and (b) the framework structure of FAU type zeolites (recreated from ref. 60a).

Zeolites are a class of microporous aluminosilicate materials that were originally discovered in nature and can now be manufactured in mass amounts. Most zeolites are thermally stable and their structures do not collapse, even after being exposed to high temperatures (*e.g.*, 600 °C) for dehydration or calcination.[60b] The first discovery of a zeolite was in 1756, when the Swedish mineralogist Axel Fredrick Cronstedt observed that a large amount of steam was generated upon heating a type of unknown mineral.[61] This material family was named "zeolite", which stems from classical Greek, where ζεω (zeo) means "to boil" and λίθος (lithos) means "stone."[62] The mineral that released the

steam was later named stilbite.[61] Zeolites have been known and studied for more than 250 years. The porous structures of zeolites suggest that they can adsorb and trap small molecules, which can also allow catalysis reactions to take place between the zeolite and guest molecules within the zeolite cavities. This makes zeolites useful for applications as adsorbents and reaction bases in manufacturing and production, especially in the refining and catalysis industries.[63]

Natural aluminosilicate zeolites usually have three-dimensional structures consisting mainly of $Si(IV)O_4$ tetrahedral building blocks. Some of these $Si(IV)O_4$ tetrahedra are substituted by $Al(III)O_4$ tetrahedra at a specific ratio, known as the Si/Al ratio. The presence of $Al(III)O_4$ tetrahedra, which have a net negative charge, in turn makes the entire framework of zeolites negatively charged. To balance those charges, various cations are introduced in the large structural cages, tunnels or cavities within the zeolite. The existence of these extra-framework cations and the porous structure of zeolites makes these practical materials for sieving and selecting guest molecules with certain dimensions and properties, allowing preferred molecules to go deeper into and/or fully penetrate through the pores. Inside the porous structures of zeolites, a wide array of diverse catalytic reactions take place, which are believed to occur due to the existence of various cations. The cations may also contribute to properties such as gas adsorption and separation, depending on the specific pore structures, cation types, and cation locations. When zeolites are immersed in aqueous solution, the loosely bound cations within the zeolite pores are hydrated and can be exchanged with other cations present in the aqueous solution. Some synthetic zeolites with certain pore structures or cations are designed to carry out particular functions, such as organic catalysis reactions in the petrol industry,[64] as well as the ion exchange-based removal of radioactive and heavy-metal ions from contaminated and polluted water.[65] Specific ion-exchanged zeolites have well-defined roles in industry and can be produced in large-scale amounts.

1.2.2 Applications of Zeolites

Zeolites are mainly used in three industrial areas: catalysis, gas adsorption and separation, and ion exchange.[66] Many other applications for zeolites also have been explored and developed, such as detoxification,[67] insect pest control,[68] protein

adsorption,[69] and animal feed additives.[70] High thermal stability is another advantage of zeolites, allowing them to be recycled for future use by using thermal treatment for desorption. Zeolites have become widely used due to their low prices, ability to be produced in large quantities and environmentally-friendly properties.

The catalytic applications of zeolites are mainly involved in three key reactions within the petrol industry: cracking, isomerization and hydrocarbon synthesis.[71] Diverse catalytic reactions can take place inside the porous structures of zeolites, especially those with specifically designed pore structures and cation types for carrying out reactions. For example, zeolite ZSM-5 has a remarkable shape-selectivity for durene formation in methanol-to-gasoline conversion, and aromatic and aliphatic compound isomerization.[72] In the early history of zeolites,[73] zeolite Y was first used as an isomerization catalyst by Union Carbide in 1964[74] and zeolite X was firstly used as a cracking catalyst in 1962.[75] The important applications of zeolites in the petroleum industry are due to the zeolite Brønsted acidities, which are strongly dependent on the structures and chemical compositions of zeolites, such as the Si/Al ratios of both the proton-form and ammonium-form of zeolites.[76]

Zeolites behave differently in gas adsorption and separation, depending on their specific pore structures.[77] The most commonly used applications of zeolites in gas adsorption and separation include the removal of H_2O, CO, CO_2, ozone, sulfur compounds, nitrogen oxide and sulfur oxides from gas mixtures, as well as the purification of many other gases.[66] In nuclear related industries, zeolite Na-A and Na-X have been employed along with Ca-exchanged forms for applications such as xenon purification from radioactive krypton.[66]

The ion-exchange capability of zeolites has led to applications in the removal of radioactive and heavy-metal ions from contaminated and polluted water.[78] For example, zeolite Na-A is used in water softening due to its selective ion exchange for Ca^{2+}. Natural zeolites, such as clinoptilolite, have the ability to remove radioactive Cs^+, Sr^{2+} and Co^{2+}

from contaminated water.[79] Some zeolites are also well-suited for removing urea and NH^{4+} from solutions, which has applications in artificial kidneys.[80]

1.2.3 Zeolites for gas adsorption and their characterization

Zeolites are one of the most widely used, economical, and mass-produced gas adsorbents;[81] the annual global production of zeolites is about 4 million tons.[82] Although zeolites are relatively more stable than MOFs at high temperatures, the zeolite guest uptake capacity is relatively lower than that of MOFs. For example, zeolite 13X exhibits the highest CO_2 adsorption capacity among zeolites at 6.9 mol/kg at 15 bar, but this value is just 54% of the Cu-BTC MOF, which was able to adsorb 12.7 mol/kg of CO_2 under the same condition.[33]

Studies on zeolites have shown that cations located in zeolite ring structures are accessible to adsorbed guest molecules and can act as adsorption sites.[83] The strength of interactions between cations and guest molecules vary based on the Si/Al ratios, cation types, guest molecule types, pore sizes and hydration status.[84] Any steric blocking of adsorption sites by molecules such as H_2O can limit the guest adsorption capabilities in zeolites. The strong affinity between water molecules and extra framework cations means that zeolites are easily saturated by moisture when exposed to air. The use of an activation process involving high heat to desorb guest molecules is necessary to fully dehydrate zeolites before performing experiments on guest-free zeolites, via IR,[85] SSNMR,[86] XRD[87] or neutron diffraction.[88]

In recent years, the removal and storage of CO_2 has drawn attention due to global warming, which is strongly linked to CO_2 emissions from fossil fuel combustion. The stable and robust structure of zeolites makes these good prospects for CO_2 adsorbents. Since the development of synthetic zeolites, a great deal of research has been conducted on zeolite CO_2 adsorption. X-ray diffraction powder patterns[89] along with TEM microscope[90] and electron-density maps[87a] of zeolites provide accurate positions of zeolite framework atoms, extra-framework cations and adsorbed guest molecules. BET surface area experiments[91] along with guest adsorption/desorption experiments have been conducted to obtain a quantitative measure of CO_2 uptake capabilities and relevant parameters in various zeolites.[92] IR,[93] Raman[94] and FTIR[95] experiments permit

investigation of vibrational motions and the adsorption status of CO_2 guests within zeolite frameworks. Simulations of CO_2 guest behaviour in zeolites can predict possible host-guest interactions with zeolites, and can indicate the proper characterization methods necessary to validate the simulation results.[96] Solid-state NMR (SSNMR) experiments can precisely determine the local environment about the SiO_4 and AlO_4 tetrahedron sites (T-sites) within zeolites and can probe their nearby chemical environments within the zeolite structure.[97]

1.2.4 SSNMR for the study of zeolites

SSNMR studies of zeolites mainly focus on structural determination, examinations of zeolite framework crystallization mechanisms, the distribution of extra-framework cations and their dynamics, in-situ studies of organic catalysis processes, host-guest interactions, and guest motional dynamics.

The most valuable application of SSNMR spectroscopy for zeolite studies is structural determination.[98] Zeolite frameworks consist of crystalline 3-dimensional networks of SiO_4 and AlO_4 T-sites in aluminosilicate zeolites, of AlO_4 and PO_4 T-sites in aluminophosphate (ALPO) zeolites, and of SiO_4, AlO_4 and PO_4 T-sites in silicoaluminophosphate (SAPO) zeolites.[99] These T-sites can be characterized using ^{27}Al, ^{29}Si, and ^{31}P NMR experiments, including the use of magic angle spinning (MAS),[100] rotational-echo double-resonance (REDOR)[101] and cross polarization (CP)[102] experiments to collect structural information. ^{17}O SSNMR can also be used to study the bridging oxygen atoms and hydroxyl groups that join two T-sites[103]. SSNMR studies have also been applied to analyze the crystallization mechanism of zeolites, by manually stopping the zeolite growth process at chosen time points and studying the "frozen" intermediates.[104] The composition of the mixture obtained at specific points in time can be analyzed by SSNMR to understand intermediate structures, and those can then be compared with the structure at other time points in order to understand the entire zeolite crystal growth process and deduce the corresponding crystallization mechanisms. Using SSNMR experiments, the intermediates and final products produced by zeolite synthetic

methods such as hydrothermal reactions,[104] mechanical grinding[105] and ball milling[106] have been examined.

SSNMR can also be used to analyze extra-framework cation and guest molecule dynamics, as well as the interactions between guests and zeolite frameworks. SSNMR studies on exchanged cation behaviour and guest-cation interactions in zeolites should shed light on the mechanisms behind zeolite applications in catalysis and gas adsorption/separation.[107] In-situ SSNMR studies of zeolite catalysis have been reported, in which the researchers introduced CO_2, H_2O or other reagent molecules into zeolite frameworks to catalyze the synthesis of organic products, such as formic acid.[108] Complicated organic catalysis reactions, such as alkylation, carboxylation, and organic rearrangement and cracking reactions via zeolite catalysts have also been reported, which have many industrial applications. The entire catalytic process was monitored in real-time by SSNMR spectroscopy, and the intermediate status and mechanism of the reaction was described in detail.[109] SSNMR has also been used to study host-guest interactions and guest dynamics within zeolites. The porous structures of zeolites provide 3-dimensional cavities and channels to act as convenient locations to adsorb or interact with guest molecules. Liu and co-workers were able to introduce noble gases, such as xenon, along with organic molecules into zeolite cavities to study host-guest interactions.[110] Zeolites have also proven capable of selective CO_2 adsorption from gas mixtures including N_2, CO_2, CH_4 or other gases due to their highly selective gas separation and purification properties.[111] However, SSNMR studies of adsorbed CO_2 dynamics in zeolites are quite rare.[112]

The high sensitivity of SSNMR spectroscopy to the local chemical environment of target nuclei makes this characterization method extremely useful for understanding and analyzing host-guest interactions in zeolites. Recent advances in SSNMR hardware, pulse sequences, and increased magnetic fields have also made this a powerful characterization method for precisely probing guest adsorption and dynamics at the molecular level.

1.3   Physical background of SSNMR

1.3.1 NMR interactions

Nuclei have intrinsic spin angular momentum, which gives rise to nuclear spin (I). Some nuclei are NMR-inactive with a spin of 0, while NMR-active nuclei have non-zero spins. The guideline to predict nuclear spin is illustrated in Table 1.

Table 1-1. The guideline to predict nuclear spin, I

Number of protons	Number of neutrons	Spin (I)	Example
Even	Even	0	^{12}C
Odd	Odd	Integer (i.e. 1)	^{2}H
Odd	Even	Half-integer (i.e. 3/2)	^{7}Li
Even	Odd	Half-integer (i.e. 1/2)	^{13}C

The nuclear spin (I) gives rise to a nuclear spin magnetic moment (μ):[113]

$$\mu = \gamma \hbar I \qquad\qquad (1)$$

Where γ is the gyromagnetic ratio of the nucleus, and $\hbar$ is the reduced Planck's constant ($h/2\pi$). The nuclear spin may interact with external magnetic fields (*i.e.*, the NMR magnet), and also with other internal nuclear spins. There are five nuclear spin interactions:[51] the Zeeman, chemical shift (CS), dipolar, J-coupling, and quadrupolar interactions. This study involves four of those interactions: the Zeeman interaction, chemical shift interaction, dipolar coupling interaction and quadrupolar interaction, which are described below. The relative magnitudes of all five interactions are listed in Table below.

Table 1-2. Nuclear interactions and magnitudes

Nuclear interaction	Magnitude (Hz)
Zeeman	$10^6 - 10^9$
Dipolar	$0 - 10^5$
Chemical shift	$0 - 10^5$
Quadrupolar	$0 - 10^9$
J-(spin-spin) coupling	$0 - 10^4$

Zeeman is the strongest interaction among these five nuclear interactions (Table 1-2), and all other interactions can be considered as perturbations of the Zeeman interaction.[113] The four nuclear interactions involved in this study contribute to the identification and characterization of host-guest interactions. A brief introduction and background of these four nuclear interactions are included in this section.

1.3.1.1   Zeeman interaction

The Zeeman interaction describes the interaction between an NMR-active nucleus spin (I) and an external magnetic field (B_0). It is the strongest interaction in NMR, and the most important. When an external magnetic field is present, the degenerate ground energy magnetic state of the nucleus splits into $2I+1$ energy levels, according to the possible nuclear spin states. Each energy level differs by a magnetic quantum number m_I ($m_I = I, I-1 \ldots -I+1, -I$). Figure 1-3 displays the effect of the Zeeman interaction on the spin energy levels of a spin-1/2 nucleus such as ^{13}C. After being placed in B_0, the degenerate energy levels of a spin-1/2 nucleus split into two distinct energy levels corresponding to the two possible nuclear spin states, spin +1/2 and spin -1/2. The spin energy level -1/2 refers to nuclear spins aligned opposing B_0, and this spin state thus has a relatively higher energy. The +1/2 spin energy level corresponds to nuclear spins which are oriented parallel to the direction of B_0, and have a relatively lower energy. It is important to note that the spin alignment is not static; spins "precess" about the parallel or antiparallel orientations with respect to the magnetic field.

$$m_I$$

$$-1/2$$

$$\Delta E = h\nu = \left(\tfrac{h}{2\pi}\right)\gamma B_0$$

$$E$$

$$+1/2$$

Without B_0 With B_0
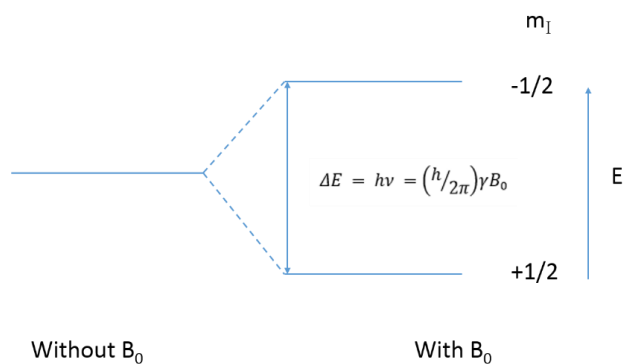
Figure 1-3. The splitting of degenerate spin energy levels of a spin 1/2 nucleus.[113]

The energy difference between two nuclear spin states in an external field B_0 can be calculated according to the following equation:[113]

$$\Delta E = h\nu = \frac{h}{2\pi}\gamma B_0 \qquad (2)$$

Where ν_0 is the nucleus-dependent Larmor frequency, γ is the gyromagnetic ratio and B_0 is the applied external magnetic field. For an isolated nucleus, the application of radiofrequency[114] radiation at the "Larmor" resonant frequency ν_0 can trigger single-quantum nuclear spin state transitions from a low spin energy level (+1/2) to a high spin energy level (-1/2) in the presence of B_0.[113] The Larmor frequency can be calculated from equation (3):[115]

$$\nu_0 = \frac{\gamma}{2\pi} B_0 \qquad (3)$$

Applying a higher magnetic field creates a larger energy difference between the energy levels, resulting in a more detectable transition and a stronger NMR signal.

1.3.1.2 Chemical shift interaction

In compounds and molecules, the application of an external magnetic field B_0 causes the induced motion of electrons and their negative charges, which generates a local

magnetic field. These local magnetic fields slightly shield or deshield nuclei from B_0, resulting in a very small shift in the nuclear Larmor resonant frequency. This interaction is known as the anisotropic (directionally dependent) chemical shift (CS) interaction. The degree that the CS interaction modifies the Larmor frequency depends on the local magnetic environment and resulting local magnetic fields about the nucleus of interest, resulting in small or large distributions of chemical shift values.[115] Chemical shielding and chemical shift are related: chemical shielding refers to the absolute change in nuclear shielding, but chemical shift describes the difference between the observed resonant frequency and that of a standardized reference with a known resonant frequency or chemical shift value. Chemical shifts are used far more often than chemical shielding, since this parameter does not vary with B_0 and is experimentally measured. The relationship between chemical shielding (σ), chemical shift (δ) and resonance frequency (v) is expressed below:[113]

$$\sigma_{sam} = \left(\frac{v_{ref} - v_{sam}}{v_{ref}} \right) \times 10^6 \tag{4}$$

$$\delta_{sam} = \left(\frac{v_{sam} - v_{ref}}{v_{ref}} \right) \times 10^6 = \left(\frac{\sigma_{ref} - \sigma_{sam}}{\sigma_{ref}} \right) \approx \sigma_{ref} - \sigma_{sam} \tag{5}$$

Where the subscript "sam" refers to "sample" and "ref" stands for "reference".
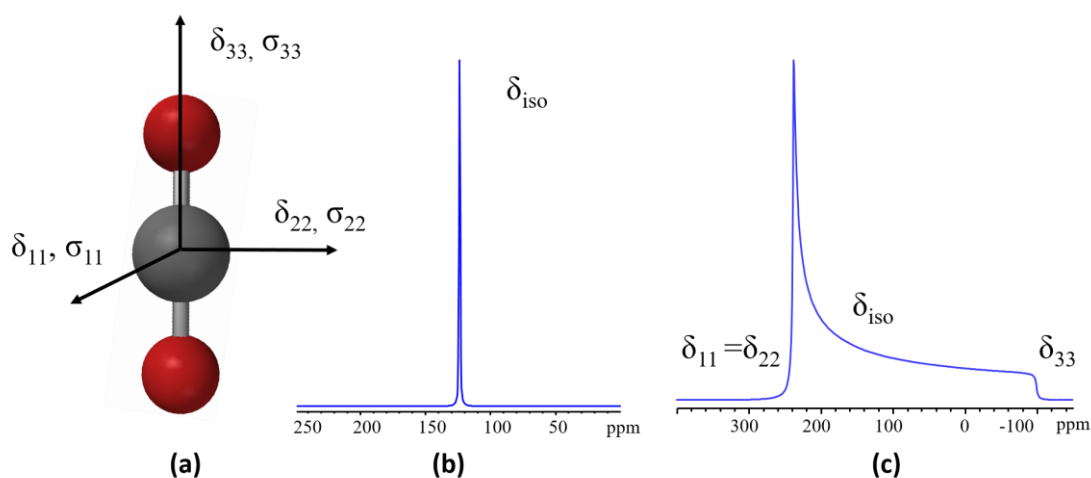
Figure 1-4. (a) A visual representation of the ^{13}C chemical shielding and chemical shift tensors in CO_2; (b) a simulated ^{13}C NMR spectrum of fast isotropically tumbling CO_2 (δ_{iso} = 125 ppm); (c) a simulated ^{13}C solid-state NMR spectra of rigid CO_2 molecule (δ_{iso} = 125 ppm).[116]

The anisotropic chemical shift interaction can be characterized by a tensor defined by three principle components (δ_{11}, δ_{22} and δ_{33}), which are oriented along three orthogonal directions in the molecular frame about the nucleus (Figure 1-4a). For those small molecules tumbling rapidly (Figure 1-4 b), the fast tumbling motion results a sharp resonance, which represents an averaged isotropic (directionally independent) value of the anisotropic CS interaction. In the solid state, molecules are orientated randomly in all possible orientations with respect to the external magnetic field, giving rise to a broadened anisotropic CS powder pattern (Figure 1-4c).

In this report, CSA is described using the Herzfeld-Berger (HB) convention, along with the chemical shift tensor components δ_{11}, δ_{22} and δ_{33}. The HB convention uses three key NMR parameters to describe the CS interaction, as expressed below:[117]

$$\delta_{\text{iso}} = (\delta_{11}+\delta_{22}+\delta_{33})/3 \qquad (6)$$

$$\Omega = \delta_{11}-\delta_{33} \qquad (7)$$

$$\kappa = 3(\delta_{22}-\delta_{\text{iso}})/\Omega \qquad (8)$$
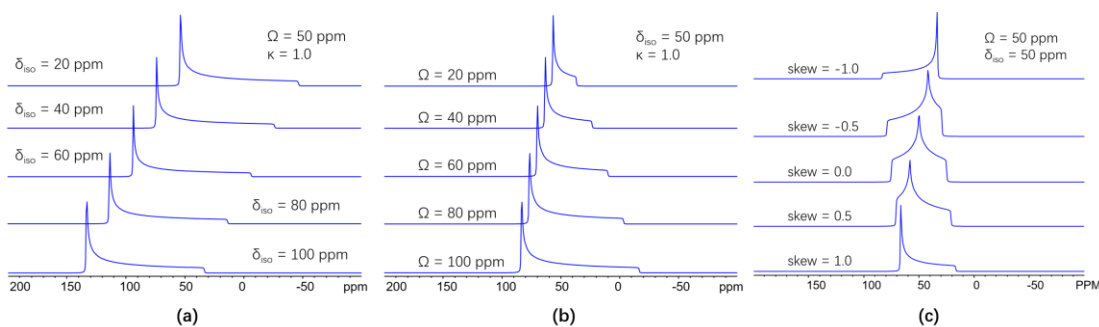
Figure 1-5. The influence of (a) isotropic chemical shift, (δ_{iso}); (b) span, (Ω) and (c) skew, (κ) on simulated ^{13}C spectral lineshapes.

δ_{iso} is the averaged isotropic chemical shift, where positive and negative values are associated with relatively deshielded and shielded nuclei, respectively, versus the reference compound (Figure 1-5a); Ω is the span of the spectrum, and this parameter describes the spectral breadth (Figure 1-5b); and κ is the skew of the powder pattern, which ranges from -1 to 1, and determines the relative position of the central powder

pattern "horn" (Figure 1-5c). When the skew is equal to -1 or 1, the CS tensor is axially symmetric, and gives rise to a characteristic powder pattern. In other situations when the skew is near zero, the CS tensor is axially asymmetric, giving rise to a different sort of characteristic powder pattern. Generally, axially symmetric CS powder patterns can be observed when local environment about the nucleus is of C_3 or higher rotational symmetry, giving rise to skew values of 1 or -1. For axially asymmetric CS tensors and spectra ($-1 < \kappa < 1$), there is a C_2 or less rotational symmetry in the local structure.

1.3.1.3   Dipolar interaction

The dipolar interaction (DI) is the magnetic through-space interaction that occurs between two nuclei. These two spins are usually distinct nuclei which are denoted as spin I and spin S. Each spin has a unique magnetic moment and generates a local magnetic field, which can loosely be considered as a small bar magnet. When the two spins are close to each other, each spin's local magnetic field perturbs the other *via* the dipolar interaction. The dipolar coupling constant (D) is used to measure the magnitude or strength of the dipolar interaction, as described in Equation 9. The magnitude of the dipolar interaction can be calculated from equations 9 and 10 below, where the r_{IS} is the inter-spin distance, α is the angle between the inter-spin vector and the orientation of external magnet, μ_0 is the permeability of vacuum, γ_I and γ_S are the magnetogyric ratios of the two spins, ν_L is the nuclear Larmor frequency in a specific applied magnetic field, and ν is the observed Larmor frequency after considering the effects of the dipolar interaction. The dipolar interaction strongly depends on the inter-spin distance and gyromagnetic ratio of the two nuclei participating in the interaction.

$$\text{D} = \frac{\mu_0}{4\pi} \frac{\gamma_I \gamma_S}{r_{IS}^3} \frac{\text{h}}{2\pi} \tag{9}$$

$$\nu = \nu_L \pm \frac{1}{2}\text{D}\,(1\text{-}3\cos^2\alpha) \tag{10}$$

The principle of the dipolar interaction is shown in Figure 1-6a. Meanwhile, the typical NMR spectrum of dipolar interactions between heteronuclear is shown in Figure 1-6b, which is called the Pake doublet,[118] featuring two horns and two feet. The Pake

doublet consists of two mirrored individual powder patterns generated from the dipolar perturbations of the Zeeman interaction. The two horns of the Pake doublet are generated

(a)   (b)
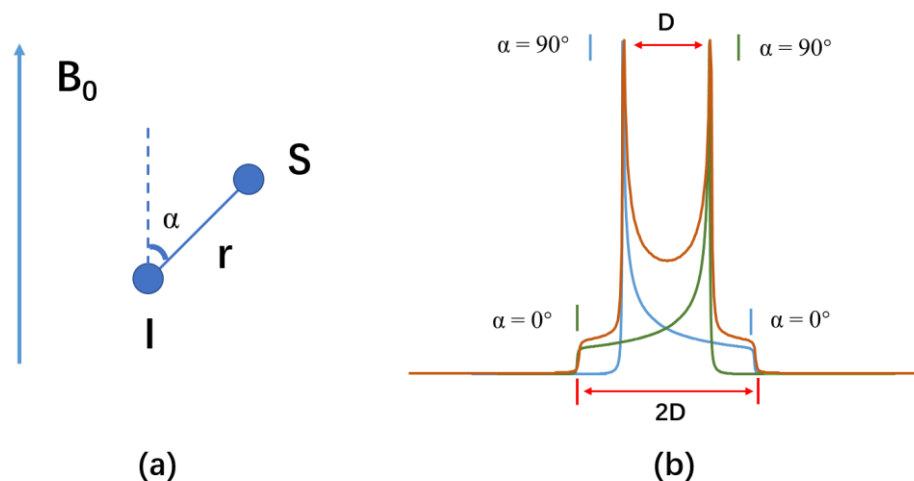
Figure 1-6. The magnetic dipolar interaction. Part (a) shows a schematic illustration the principles behind the dipolar interaction, where the two blue dots represent two heterogeneous nuclei I and S, r is the internuclear distance and α is the angle between S-I vector to the external magnetic field B_0. The figure in (b) shows a simulated static dipolar coupling spectrum generated from two heterogeneous nuclei I and S. The blue and green lines represent the dipole perturbation of nuclei S either in the parallel or anti parallel direction to the nuclei I respect to magnetic field. The red line is the integrated Pake doublet that results from the dipolar interaction. The two horns of the Pake doublet are generated by the perpendicular S-I vector with respect to B_0, and the two feet are contributed by the parallel S-I vector with respect to B_0. The gap in frequency between the spectral horns is equals to D in Equation 9, while the width between the two spectral feet is equals to 2D

by the perpendicular S-I vector orientations with respect to B_0, and the two feet are contributed by the parallel S-I vector with respect to B_0 (Figure 1-6b). The gap in frequency between the spectral horns is equal to D in Equation 9, while the width between the two spectral feet is equal to 2D; these facts can be used to calculate the

dipolar constant D in a practical sense from SSNMR spectra. Dipolar interactions typically affect static spectra and make spectra more complicated to interpret. Like many other anisotropic NMR interactions, the dipolar interaction contains a term of $1\text{-}3\cos^2\alpha$ (Equation 10), where α is the sample orientation with respect to the magnetic field. Magic angle spinning (MAS) experiments involving spinning the sample at an angle of $54.74°$ causes the $1\text{-}3\cos^2\alpha$ term to equal 0, eliminating the spectral effects of the dipolar interaction.

1.3.1.4   Quadrupolar interaction

Nuclei with a spin greater than 1/2 have an electric quadrupole moment, which results from an uneven spherical charge distribution between the protons and neutrons within the nucleus. Nuclei with a spin >1/2 have a nuclear quadrupole moment (Q), which can couple with the local electric field gradients (EFG) around the nucleus in a process known as the anisotropic quadrupolar interaction (QI). The EFGs results from features such as surrounding ligands, chemical bonds, and point charges. The EFG can be modeled by a second-rank tensor which can be described by three orthogonal vectors V_{11}, V_{22} and V_{33} in a principal axis system (PAS), with these components ordered $|V_{33}| > |V_{22}| > |V_{11}|$. When describing the quadrupolar interaction, two parameters can be used: the quadrupolar coupling constant C_Q and the asymmetry parameter η_Q, as shown below.[119]

$$C_Q = \frac{eQV_{33}}{h} \qquad\qquad (11)$$

$$\eta_Q = \frac{V_{11} - V_{22}}{V_{33}} \qquad\qquad (12)$$

The magnitude of C_Q describes the strength of the quadrupolar interaction and breadth of the experimental spectrum, which is dependent on the degree of local spherical symmetry about the nucleus. A greater C_Q value gives a wider powder pattern breadth and corresponds to a less spherically symmetric local electronic environment about the quadrupolar nucleus. η_Q is the asymmetry parameter of the EFG tensor and describes its axial symmetry. The values of η_Q range from 0 to 1. If $\eta_Q = 0$, the the EFG tensor is

axially symmetric. As the η_Q value approaches 1, the EFG tensor becomes more and more axially asymmetric.

(a) ^{13}C - Spin 1/2 Nucleus   (b) ^{2}H - spin 1   Quadrupolar Nucleus
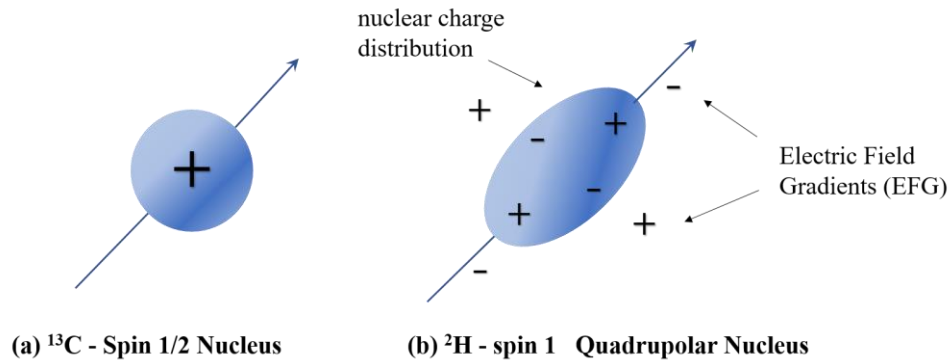
Figure 1-7. The simulated shape of the nuclear charge distribution within (a) half-integer and (b) quadrupolar nuclei, along with (c) a hypothetical depiction of the EFG about a nucleus.[120]

(a) Axially symmetric EFG tensors   (b) Axially asymmetric EFG tensors
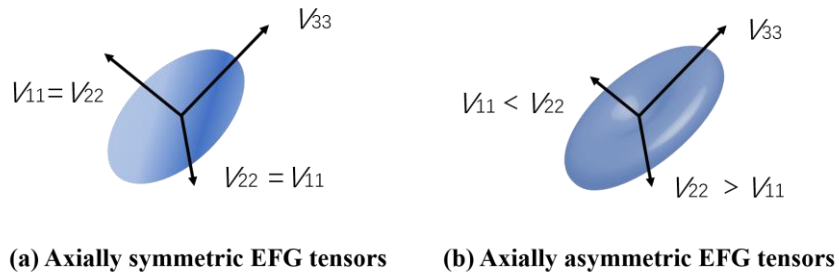
Figure 1-8. The imaginary (a) ellipsoidal, axially symmetric and (b) plate-like, axially asymmetric EFG tensor models affected by C_Q value.
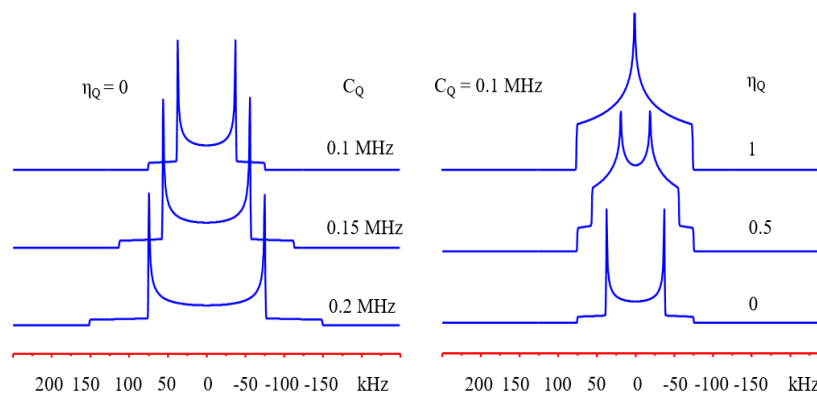
Figure 1-9. A simulated ^{2}H quadrupolar-dominated NMR lineshape at 9.4T using different C_Q and η_Q values.
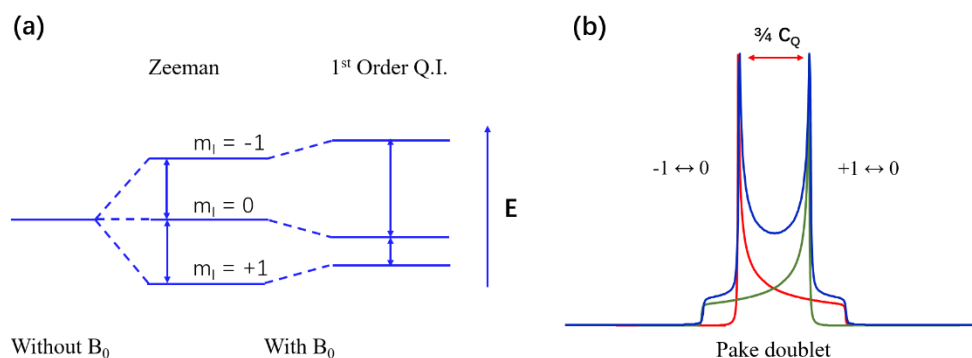
Figure 1-10. (a) Qualitative illustration of the energy level splitting of an integer quadrupolar nucleus, e.g. ^{2}H, and (b) shows a simulated static spectrum generated from quadrupolar nuclei. The red and green lines represent two spin transitions: $-1 \leftrightarrow 0$ and $+1 \leftrightarrow 0$. The blue line is the integrated Pake doublet resulting from the quadrupolar interaction.

Figure 1-9 shows the influences of C_Q and η_Q on the ^{2}H SSNMR spectrum, which is always a symmetric pattern known as a Pake doublet. In this case, the Pake doublet arises from the quadrupolar interaction rather than the dipolar interaction. In Figure 1-10, the energy splitting of the spin states of an integer quadrupolar nucleus are shown, along with a simulated spectrum. For first-order quadrupolar nuclei such as ^{2}H, C_Q can be calculated from the frequency difference between the two horns of the Pake doublet, which should equal 3/4 of C_Q. As C_Q decreases, the width of the powder pattern narrows, and there is a

relatively shorter distance between the two spectral horns. In contrast, when C_Q is held constant and η_Q increases from 0 to 1, the width of the powder pattern remains the same while the two horns gradually converge.

1.4   Experimental background of SSNMR

1.4.1 Instrumental mechanism of SSNMR experiments

Solid-state NMR involves the use of numerous pulse sequences to probe different nuclei in diverse chemical environments. In Figure 1-11, a classical 90° pulse sequence is demonstrated in a Cartesian coordination system as a vector model to illustrate the mechanisms underlying SSNMR spectroscopy.
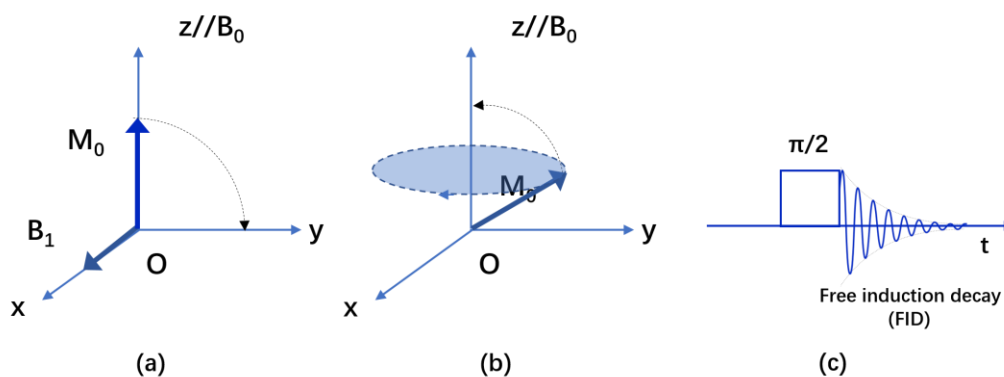
Figure 1-11. Illustration of the one-pulse NMR experiment in the vector model is shown in (a) and (b), with the time-domain signal shown in (c).

In a typical SSNMR spectrometer, the external magnetic field B_0 is considered to be along the z axis of the coordinate system. In a SSNMR experiment, the sample is placed at the coordinate origin in Figure 1-11a, and the magnetic moments of nuclei in the sample align and produce a net local magnetization along the z axis, which is denoted as M_0. The excitation and detection coil is situated in the xy plane. In order to tip the magnetic field vector M_0 into the xy plane, a second magnetic field B_1 is generated along x axis using an rf pulse through the coil (Figure 1-11a). In this situation, after B_1 is turned off (Figure 1-11b), the M_0 vector will gradually precess from the xy plane back to the +z

direction to achieve thermal equilibrium in the presence of B_0. The precessing and reorienting magnetic field generated by the movement of the net nuclear magnetization back to +z produces an oscillating magnetic signal, which then produces an electrically induced current in the coil known as the free induction decay (FID), in the time domain (Figure 1-11c). A Fourier transformation is then performed on the FID to convert the time domain to the frequency domain, in units of ppm or Hz.

1.4.2 NMR pulse sequences

1.4.2.1   One-pulse

The one-pulse sequence is the simplest and most fundamental sequence applied in NMR experiments: the target nucleus is excited by a square 90° pulse at its Larmor frequency, and then the pulse is turned off and the receiver starts acquiring the FID (Figure 1-12a). At a given power level, the appropriate pulse length causing spins to flip 90° from the +z direction into the xy plane is in the μs regime and is called the "90° pulse width", or pw90°.

1.4.2.2   90°-90° Echo

The 90°-90° echo is also called the solids-echo, or quadrupolar-echo pulse sequence, which is often used for the acquisition of powder patterns broadened by the QI. In quadrupolar nuclei, the refocusing of the spins into echoes becomes challenging as there are multiple energy levels which are associated with different energy gaps, different nutation rates, and thus different selective NMR pulse lengths. Consequently, treating the quadrupolar nuclei with a typical 90°-180° Hahn-echo sequence results in incomplete refocusing and distorted spectra. However, if a π/2 pulse is used in place of the π pulse (Figure 1-12b), the pulse sequence is known as a solids (quadrupolar) echo, and the corresponding FID from the central transition (spin transition from +1/2 to -1/2)[113] will yield undistorted, clear SSNMR spectra in most instances.

1.4.2.3   DEPTH-Echo

The Hahn-Echo pulse sequence allows for refocusing of spin magnetization to obtain undistorted broad powder patterns.[121] The sequence consists of one π/2 pulse to tip the

magnetization along the y-axis followed by a π pulse (Figure 1-12d) to refocus the magnetization, where τ represents a short (i.e., microseconds) delay between pulses.
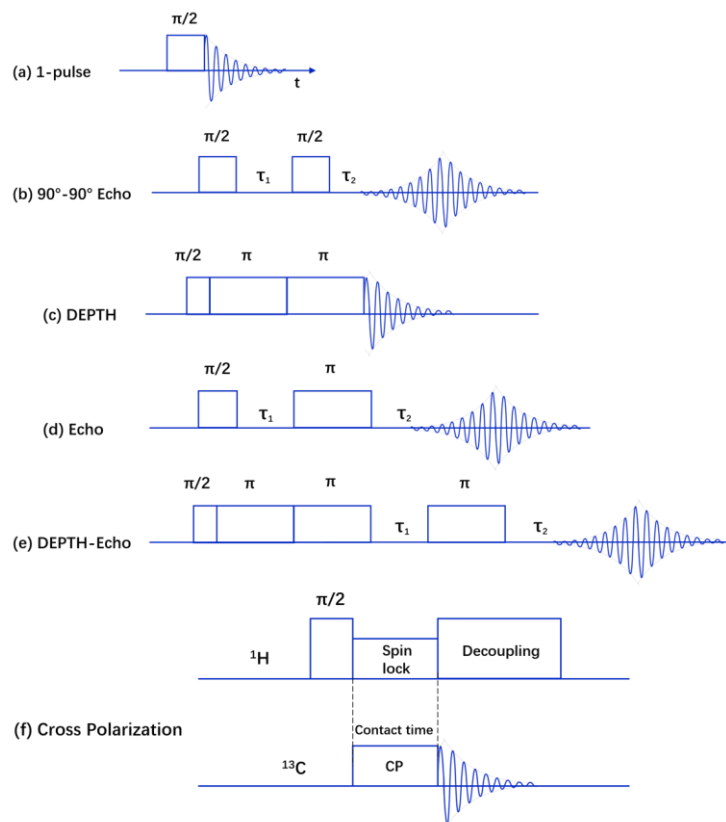
Figure 1-12. The pulse sequences involved in this study are: (a) one-pulse sequence, (b) 90° - 90° echo sequence (c) DEPTH sequence;[119] (d) Hahn-Echo sequence; (e) DEPTH-Echo sequence;[59b] and (f) the cross polarization sequence[122].

In this study, a combined DEPTH – Echo[59b] pulse sequence was investigated to acquire broad CO_2 powder patterns without background signals or distortions. The pulse sequence scheme of DEPTH-Echo is illustrated in Figure 1-12e. The pulse sequence starts with the regular DEPTH pulse sequence[119], which is often used to eliminate background signals from NMR spectra.[119] It begins with one $\pi/2$ (90°) pulse to generate B_1. The $\pi/2$ pulse is followed by two consecutive π pulses to eliminate background signals (Figure1-11c). Then, a third π pulse is applied after some delay to refocus the signal over

the course of some time denoted as τ_2. This process is known as an "echo", after which the FID is collected.

1.4.2.4   Cross Polarization

^{1}H-^{13}C CP SSNMR experiments transfer spin polarization from abundant and NMR-favourable ^{1}H nuclei to less favourable ^{13}C nuclei, in order to achieve faster signal acquisition and higher signal-to-noise ratios in spectra (Figure 1-12f) by exploiting the magnetic dipolar coupling interaction between the more abundant (^{1}H) and less abundant (^{13}C) nuclei and satisfying the Hartmann-Hahn condition, shown in Equation 13.

$$\gamma_D B_D = \gamma_A B_A \qquad (13)$$

where γ_D and γ_A are the gyromagnetic ratios of dilute spin D and abundant spin A, and B_D and B_A are the radio frequency fields that are applied on the two separate rf channels for the two nuclei. In the ^{1}H-^{13}C CP experiments used in this work, the pulse sequence begins with the application of a 90° pulse on the ^{1}H channel, which is the abundant nuclei A, followed by a spin-lock pulse B_A to keep the magnetization on the ^{1}H channel from dephasing. Then, another pulse B_D is applied on the ^{13}C (diluted nuclei) channel as the spin-lock initiates to transfer spin polarization from ^{1}H to ^{13}C nuclei. The magnetization of ^{13}C is built up due to the dipolar coupling interactions between ^{13}C and ^{1}H nuclei. The period of time chosen to transfer spin polarization from ^{1}H to ^{13}C is known as the mixing time or contact time. After the contact time, the spin lock pulse and mixing pulses on both channels are turned off to collect the CP-enhanced FID of ^{13}C nuclei. The contact time duration of ^{1}H-^{13}C CP experiments determines which ^{13}C nuclei can be observed with respect to their ^{1}H proximity, acting as a convenient spectral filter and source of local structural information. Shorter contact times favour ^{13}C nuclei which are spatially close to ^{1}H or directly bound to it. Longer contact times favour ^{13}C nuclei which are more distant from ^{1}H. For example, the use of different contact times from ^{1}H nuclei to ^{13}C of guest CO_2 within MOFs and zeolites can help establish the spatial proximity between the framework adsorption sites and the guest molecules.[58, 59b]

1.4.3 Processing and simulation software

Four types of software were used to process raw SSNMR data, simulate the apparent NMR parameters, simulate dynamic motions of adsorbed small molecules and predict quadrupolar parameters form existing framework structures: NUTS, WSolids, EXPRESS and CASTEP, respectively.

NUTS[123] is a piece of software used for basic NMR spectrum processing. It is used to process raw data acquired at the NMR facility. Several commands are used for processing and optimizing NMR powder patterns to enhance signal/noise ratio and lineshape quality. WSolids[124] is used to analytically simulate processed SSNMR powder patterns in order to acquire the apparent chemical shift, quadrupolar and other nuclear interaction parameters. Multiple powder patterns can be simulated at the same time, and the intensity ratios between different resonances can also be obtained simultaneously.

EXPRESS[125] (EXchange Program for RElaxing Spin Systems) is software mainly used for simulating the effects of dynamics on specific nuclei, in order to obtain molecular the associated molecular motion types, rates, and motional angles. For EXPRESS motional simulations, the experimental SSNMR spectrum was simulated using specific motional information along with the known SSNMR parameters of the rigid guest molecules: rigid CO_2 ($\Omega = 335$ ppm, $\kappa = 1$),[116] rigid CO ($\Omega = 353$ ppm, $\kappa = 1$)[116] and rigid C_2D_4 ($C_Q = 230$ kHz, $\eta_Q = 0$).[126].

CASTEP[127] (CAmbridge Serial Total Energy Package) is a plane-wave density functional theory (DFT) calculation package that employs first-principles quantum mechanical description of electrons and nuclei to predict and calculate nuclei NMR interaction parameters for crystalline solids and many other materials in specific chemical environments based on known and computationally-optimized crystal structures.

1.5   Outline of thesis

Using SSNMR, the structure and properties of zeolites and MOFs can be investigated, particularly as they relate to guest adsorption and guest dynamics. Variable temperature (VT) SSNMR experiments are the most direct method to investigate guest molecule dynamics in these types of porous systems. Analyzing the gas adsorption behaviour and understanding the host-guest interactions in solid adsorbents such as MOFs and zeolites is quite useful for establishing structure-property relationships that are critical for constructing cutting-edge materials and realizing many desired applications. Simulations of experimental spectra can extract NMR parameters and help understand the origins of the chemical shift parameters, dipolar coupling constant, and quadrupolar coupling constant. In addition, VT SSNMR experiments can yield molecular motion patterns and trends.

The first chapter in this thesis gives a general introduction to both the MOF and zeolite frameworks, including their structures and current applications. The exploration of gas adsorption behaviour in these materials via SSNMR and other characterization methods is also discussed. Then, the physical background of several NMR nuclei interactions is discussed in order to explain the origins of NMR parameters and SSNMR powder patterns. After this, a brief introduction to modern SSNMR spectroscopy and the various pulse sequences used in this thesis are detailed. The simulation and computational software packages are also briefly explained, which are employed to extract and analyze basic NMR parameters from experimental spectra and gain valuable information on motion patterns, guest dynamics and local chemical environments.

The second chapter of this thesis describes SSNMR studies on CO_2, CO and C_2D_4 dynamics when adsorbed in the α-zinc formate MOF and the associated host-guest interactions. VT ^{13}C SSNMR was used to probe CO_2 and CO motional dynamics at temperatures ranging from 433 K to 123 K, and ^2H VT SSNMR was used to investigate C_2D_4 motional dynamics from 363 K to 123 K. ^1H-^{13}C cross polarization experiments were also performed to locate the guest adsorption sites within the α-zinc formate MOF. SSNMR simulations yield the types of guest motion present in this MOF, along with the respective angles and rates. ^{67}Zn high field SSNMR experiments were carried out to

detect the chemical environment and bonding status of Zn metal centres, and any changes in these local environments during processes such as CO_2 guest adsorption.

In the third chapter, VT SSNMR studies on FAU and LTA type, commercial, synthesized and ion-exchanged zeolites were performed to investigate the various behaviour of adsorbed CO_2 guests in the zeolite frameworks in the presence of different cations. VT ^{13}C SSNMR experiments yield information on the dynamic behaviour of adsorbed CO_2 guests in the FAU type zeolite X, with alkali (Li^+, Na^+, K^+) and alkali earth (Mg^{2+}, Ca^{2+}) exchanged metal cations, as well as Na^+, H^+ and NH_4^+ cations in zeolite Y and both Na^+ and K^+ cations in low-silicate zeolite X (LSX). ^1H-^{13}C cross polarization experiments were conducted to study CO_2 guest adsorption in zeolite Y, containing H^+ and NH_4^+ cations. Additionally, VT ^{13}C SSNMR experiments on LTA type zeolites carrying Li^+, Na^+, K^+ and Ca^{2+} exchanged cations suggest that distinct behaviour of adsorbed CO_2 guest takes place as compared to the FAU type zeolites.

The last chapter of this work shows summary and future work. For the second Chapter, more attempts can be carried on trapping guests within the non-porous β – zinc formate MOF and bulk compound zinc formate dihydrate, taking advantage of the transformation of these two compounds from porous α – zinc formate MOF. For the third Chapter, the investigations on dynamic CO_2 adsorption behaviour can be further extended to other valuable zeolites via SSNMR spectroscopy for modifications.

1.6 Bibliography

1.   Rouquerol, J.; Avnir, D.; Fairbridge, C.; Everett, D.; Haynes, J.; Pernicone, N.; Ramsay, J.; Sing, K.; Unger, K., Recommendations for the characterization of porous solids (Technical Report). *Pure Appl. Chem.* **1994,** *66* (8), 1739-1758.

2.   Wang, Z.; Zhang, Y.; Kurmoo, M.; Liu, T.; Vilminot, S.; Zhao, B.; Gao, S., [$Zn_3(HCOO)_6$]: A porous diamond framework conformable to guest inclusion. *Aust. J. Chem.* **2006,** *59* (9), 617-628.

3.   Kim, H.; Samsonenko, D. G.; Das, S.; Kim, G. H.; Lee, H. S.; Dybtsev, D. N.; Berdonosova, E. A.; Kim, K., Methane sorption and structural characterization of the sorption sites in $Zn_2(bdc)_2(dabco)$ by single crystal X-ray crystallography. *Chem. Asian J.* **2009,** *4* (6), 886-891.

4.   Li, H.; Eddaoudi, M.; O'Keeffe, M.; Yaghi, O. M., Design and synthesis of an exceptionally stable and highly porous metal-organic framework. *Nature* **1999,** *402* (6759), 276-279.

5.   Hoskins, B. F.; Robson, R., Infinite polymeric frameworks consisting of three dimensionally linked rod-like segments. *J. Am. Chem. Soc.* **1989,** *111* (15), 5962-5964.

6.   Yaghi, O.; Li, H., Hydrothermal synthesis of a metal-organic framework containing large rectangular channels. *J. Am. Chem. Soc.* **1995,** *117* (41), 10401-10402.

7.   (a) Li, J.-R.; Kuppler, R. J.; Zhou, H.-C., Selective gas adsorption and separation in metal–organic frameworks. *Chem. So. Rev.* **2009,** *38* (5), 1477-1504; (b) Lee, J.; Farha, O. K.; Roberts, J.; Scheidt, K. A.; Nguyen, S. T.; Hupp, J. T., Metal–organic framework materials as catalysts. *Chem.l Soc. Rev.* **2009,** *38* (5), 1450-1459.

8.   (a) Godino-Ojer, M.; López-Peinado, A.; Maldonado-Hódar, F.; Pérez-Mayoral, E., Highly efficient and selective catalytic synthesis of quinolines involving transition-metal-doped carbon aerogels. *ChemCatChem* **2017,** *9* (8), 1422-1428; (b) Delgado, J. A.; Águeda, V. I.; Uguina, M. A.; Brea, P.; Grande, C. A., Comparison and evaluation of agglomerated mofs in biohydrogen purification by means of pressure swing adsorption (psa). *Chem. Eng. J.* **2017**.

9.   Szczęśniak, B.; Osuchowski, Ł.; Choma, J.; Jaroniec, M., Highly porous carbons obtained by activation of polypyrrole/reduced graphene oxide as effective adsorbents for CO_2, H_2 and C_6H_6. *J. Porous Mater.* **2017**, 1-7.

10.   Park, H.; Krigsfeld, G.; Parise, J. B., Solvothermal synthesis and structural characterization of new Zn−triazole− sulfoisophthalate frameworks. *Cryst. Growth Des.* **2007,** *7* (4), 736-740.

11.   Sang, X.; Zhang, J.; Xiang, J.; Cui, J.; Zheng, L.; Zhang, J.; Wu, Z.; Li, Z.; Mo, G.; Xu, Y., Ionic liquid accelerates the crystallization of Zr-based metal–organic frameworks. *Nat. Commun.* **2017,** *8*.

12.   Hillman, F.; Zimmerman, J. M.; Paek, S.-M.; Hamid, M. R.; Lim, W. T.; Jeong, H.-K., Rapid microwave-assisted synthesis of hybrid zeolitic–imidazolate frameworks with mixed metals and mixed linkers. *J. Mater. Chem. A* **2017,** *5* (13), 6090-6099.

13.   Zhang, F.; Zhang, T.; Zou, X.; Liang, X.; Zhu, G.; Qu, F., Electrochemical synthesis of metal organic framework films with proton conductive property. *Solid State Ion.* **2017,** *301*, 125-132.

14.   Yuan, W.; O'Connor, J.; James, S. L., Mechanochemical synthesis of homo-and hetero-rare-earth (III) metal–organic frameworks by ball milling. *CrystEngComm.* **2010,** *12* (11), 3515-3517.

15.   Kim, S.-H.; Yang, S.-T.; Kim, J.; Ahn, W.-S., Sonochemical synthesis of $Cu_3(BTC)_2$ in a deep eutectic mixture of choline chloride/dimethylurea. *Bull. Korean Chem. Soc.* **2011,** *32* (8), 2783-2786.

16.   Klimakow, M.; Klobes, P.; Thünemann, A. F.; Rademann, K.; Emmerling, F., Mechanochemical synthesis of metal− organic frameworks: a fast and facile approach toward quantitative yields and high specific surface areas. *Chem. Mater.* **2010,** *22* (18), 5216-5221.

17.   Allendorf, M.; Bauer, C.; Bhakta, R.; Houk, R., Luminescent metal–organic frameworks. *Chem. Soc. Rev.* **2009,** *38* (5), 1330-1352.

18.   Furukawa, H.; Cordova, K. E.; O'Keeffe, M.; Yaghi, O. M., The chemistry and applications of metal-organic frameworks. *Science* **2013,** *341* (6149), 1230444.

19.   Rasero-Almansa, A. M.; Corma, A.; Iglesias, M.; Sánchez, F., Post-functionalized iridium–Zr-MOF as a promising recyclable catalyst for the hydrogenation of aromatics. *Green Chem.* **2014,** *16* (7), 3522-3527.

20.   Ravon, U.; Domine, M. E.; Gaudillère, C.; Desmartin-Chomel, A.; Farrusseng, D., MOF-5 as acid catalyst with shape selectivity properties. *Stud. Surf. Sci. Catal.* **2008,** *174*, 467-470.

21.   Cui, Y.; Yue, Y.; Qian, G.; Chen, B., Luminescent functional metal–organic frameworks. *Chem. Rev.* **2011,** *112* (2), 1126-1162.

22.   Czaja, A. U.; Trukhan, N.; Müller, U., Industrial applications of metal–organic frameworks. *Chem. Soc. Rev.* **2009,** *38* (5), 1284-1293.

23.   Lin, Z.-J.; Lü, J.; Hong, M.; Cao, R., Metal–organic frameworks based on flexible ligands (FL-MOFs): structures and applications. *Chem. Soc. Rev.* **2014,** *43* (16), 5867-5895.

24.   Khan, N. A.; Hasan, Z.; Jhung, S. H., Adsorptive removal of hazardous materials using metal-organic frameworks (MOFs): a review. *J. Hazard. Mater.* **2013,** *244*, 444-456.

25.   Keskin, S.; van Heest, T. M.; Sholl, D. S., Can Metal–Organic Framework Materials Play a Useful Role in Large-Scale Carbon Dioxide Separations? *ChemSusChem* **2010,** *3* (8), 879-891.

26.   Férey, G.; Serre, C.; Devic, T.; Maurin, G.; Jobic, H.; Llewellyn, P. L.; De Weireld, G.; Vimont, A.; Daturi, M.; Chang, J.-S., Why hybrid porous solids capture greenhouse gases? *Chem. Soc. Rev.* **2011,** *40* (2), 550-562.

27. Cox, P. M.; Betts, R. A.; Jones, C. D.; Spall, S. A.; Totterdell, I. J., Acceleration of global warming due to carbon-cycle feedbacks in a coupled climate model. *Nature* **2000,** *408* (6809), 184.

28. Sumida, K.; Rogow, D. L.; Mason, J. A.; McDonald, T. M.; Bloch, E. D.; Herm, Z. R.; Bae, T.-H.; Long, J. R., Carbon dioxide capture in metal–organic frameworks. *Chem. Rev.* **2011,** *112* (2), 724-781.

29. Talzi, V.; Ignashin, S., NMR study of decomposition of monoethanolamine under conditions of industrial gas treatment. *Russ. J. Appl. Chem.* **2002,** *75* (1), 80-85.

30. Veawab, A.; Tontiwachwuthikul, P.; Chakma, A., Corrosion behavior of carbon steel in the CO_2 absorption process using aqueous amine solutions. *Ind. Eng. Chem. Res.* **1999,** *38* (10), 3917-3924.

31. Williams, D. B. G.; Lawton, M., Drying of organic solvents: quantitative evaluation of the efficiency of several desiccants. *J. Org. Chem.* **2010,** *75* (24), 8351-8354.

32. (a) Park, K. S.; Ni, Z.; Côté, A. P.; Choi, J. Y.; Huang, R.; Uribe-Romo, F. J.; Chae, H. K.; O'Keeffe, M.; Yaghi, O. M., Exceptional chemical and thermal stability of zeolitic imidazolate frameworks. *Proceedings of the National Academy of Sciences* **2006,** *103* (27), 10186-10191; (b) Cavka, J. H.; Jakobsen, S.; Olsbye, U.; Guillou, N.; Lamberti, C.; Bordiga, S.; Lillerud, K. P., A new zirconium inorganic building brick forming metal organic frameworks with exceptional stability. *J. Am. Chem. Soc.* **2008,** *130* (42), 13850-13851.

33. Liang, Z.; Marshall, M.; Chaffee, A. L., CO_2 adsorption-based separation by metal organic framework (Cu-BTC) versus zeolite (13X). *Energy Fuels* **2009,** *23* (5), 2785-2789.

34. Furukawa, H.; Ko, N.; Go, Y. B.; Aratani, N.; Choi, S. B.; Choi, E.; Yazaydin, A. Ö.; Snurr, R. Q.; O'Keeffe, M.; Kim, J., Ultrahigh porosity in metal-organic frameworks. *Science* **2010,** *329* (5990), 424-428.

35. Coburn, R. F., Mechanisms of carbon monoxide toxicity. *Prev. Med.* **1979,** *8* (3), 310-322.

36. Valenzano, L.; Civalleri, B.; Sillar, K.; Sauer, J., Heats of adsorption of CO and CO_2 in metal–organic frameworks: quantum mechanical study of CPO-27-M (M= Mg, Ni, Zn). *J. Phys. Chem. C* **2011,** *115* (44), 21777-21784.

37. Saha, D.; Deng, S., Adsorption equilibria and kinetics of carbon monoxide on zeolite 5A, 13X, MOF-5, and MOF-177. *J. Chem. Eng. Data* **2009,** *54* (8), 2245-2250.

38. (a) Lucier, B. E.; Chan, H.; Zhang, Y.; Huang, Y., Multiple modes of motion: Realizing the dynamics of CO adsorbed in M-MOF-74 (M= Mg, Zn) by using solid-state NMR spectroscopy. *Euro. J. Inorg. Chem.* **2016,** *2016* (13-14), 2017-2024; (b) Gul-E-Noor, F.; Mendt, M.; Michel, D.; Pöppl, A.; Krautscheid, H.; Haase, J. r.; Bertmer, M., Adsorption of small molecules on $Cu_3(btc)_2$ and $Cu_{3-x}Zn_x(btc)_2$ metal–organic frameworks (MOF) as studied by solid-state NMR. *J. Phys. Chem. C* **2013,** *117* (15), 7703-7712.

34

39. The Essential Chemical Industry – online. Ethene (Ethylene). http://www.essentialchemicalindustry.org/chemicals/ethene.html (Accessed August 4, 2017).

40. Kurt, P., Ethylene production process. US Patent 2,960,518, Sept. 23, 1958.

41. Lowrance, E. G., Ethylene production process. US Patent 3,530,199, Jun 22, 1967.

42. (a) Zhang, Y.; Li, B.; Krishna, R.; Wu, Z.; Ma, D.; Shi, Z.; Pham, T.; Forrest, K.; Space, B.; Ma, S., Highly selective adsorption of ethylene over ethane in a MOF featuring the combination of open metal site and π-complexation. *Chem. Commun.* **2015,** *51* (13), 2714-2717; (b) Geier, S. J.; Mason, J. A.; Bloch, E. D.; Queen, W. L.; Hudson, M. R.; Brown, C. M.; Long, J. R., Selective adsorption of ethylene over ethane and propylene over propane in the metal–organic frameworks M_2 (dobdc)(M= Mg, Mn, Fe, Co, Ni, Zn). *Chem. Sci.* **2013,** *4* (5), 2054-2061.

43. Li, B.; Zhang, Y.; Krishna, R.; Yao, K.; Han, Y.; Wu, Z.; Ma, D.; Shi, Z.; Pham, T.; Space, B., Introduction of π-complexation into porous aromatic framework for highly selective adsorption of ethylene over ethane. *J. Am. Chem. Soc.* **2014,** *136* (24), 8654-8660.

44. Gücüyener, C.; van den Bergh, J.; Gascon, J.; Kapteijn, F., Ethane/ethene separation turned on its head: selective ethane adsorption on the metal− organic framework ZIF-7 through a gate-opening mechanism. *J. Am. Chem. Soc.* **2010,** *132* (50), 17704-17706.

45. Leclerc, H.; Vimont, A.; Lavalley, J.-C.; Daturi, M.; Wiersum, A. D.; Llwellyn, P. L.; Horcajada, P.; Férey, G.; Serre, C., Infrared study of the influence of reducible iron (iii) metal sites on the adsorption of CO, CO_2, propane, propene and propyne in the mesoporous metal–organic framework MIL-100. *Phys. Chem. Chem. Phys.* **2011,** *13* (24), 11748-11756.

46. Saha, D.; Deng, S., Ammonia adsorption and its effects on framework stability of MOF-5 and MOF-177. *J. Colloid Interface Sci.* **2010,** *348* (2), 615-620.

47. Devic, T.; Salles, F.; Bourrelly, S.; Moulin, B.; Maurin, G.; Horcajada, P.; Serre, C.; Vimont, A.; Lavalley, J.-C.; Leclerc, H., Effect of the organic functionalization of flexible MOFs on the adsorption of CO_2. *J. Mater. Chem.* **2012,** *22* (20), 10266-10273.

48. Xue, D.-X.; Cairns, A. J.; Belmabkhout, Y.; Wojtas, L.; Liu, Y.; Alkordi, M. H.; Eddaoudi, M., Tunable rare-earth fcu-MOFs: a platform for systematic enhancement of CO_2 adsorption energetics and uptake. *J. Am. Chem. Soc.* **2013,** *135* (20), 7660-7667.

49. Walton, K. S.; Snurr, R. Q., Applicability of the BET method for determining surface areas of microporous metal−organic frameworks. *J. Am. Chem. Soc.* **2007,** *129* (27), 8552-8556.

50. (a) Sutrisno, A.; Huang, Y., Solid-state NMR: A powerful tool for characterization of metal–organic frameworks. *Solid State Nucl. Magn. Reson.* **2013,** *49*, 1-11; (b) Hoffmann, H. C.; Debowski, M.; Müller, P.; Paasch, S.; Senkovska, I.; Kaskel, S.; Brunner, E., Solid-state NMR spectroscopy of metal–organic framework compounds (MOFs). *Materials* **2012,** *5* (12), 2537-2572; (c) Mali, G., Looking into metal-organic

frameworks with solid-state NMR spectroscopy in *Metal-Organic Frameworks*, InTech: 2016; (d) Marchetti, A.; Chen, J.; Pang, Z.; Li, S.; Ling, D.; Deng, F.; Kong, X., Understanding surface and interfacial chemistry in functional nanomaterials via solid-state NMR. *Adv. Mater.* **2017**.

51.   Duer, M. J., *Solid state NMR spectroscopy: principles and applications*. John Wiley & Sons: 2008.

52.   Lapina, O. B., Modern ssNMR for heterogeneous catalysis. *Catal. Today* **2017,** *285*, 179-193.

53.   Wang, W. D.; Lucier, B. E.; Terskikh, V. V.; Wang, W.; Huang, Y., Wobbling and hopping: studying dynamics of CO_2 adsorbed in metal–organic frameworks via ^{17}O solid-state NMR. *J. Phys. Chem. Lett.* **2014,** *5* (19), 3360-3365.

54.   Xu, J.; Terskikh, V. V.; Huang, Y., ^{25}Mg solid-state NMR: A sensitive probe of adsorbing guest molecules on a metal center in metal–organic framework CPO-27-Mg. *J. Phys. Chem. Lett.* **2012,** *4* (1), 7-11.

55.   Lieder, C.; Opelt, S.; Dyballa, M.; Henning, H.; Klemm, E.; Hunger, M., Adsorbate effect on $AlO_4(OH)_2$ centers in the metal−organic framework MIL-53 investigated by solid-state NMR spectroscopy. *J. Phys. Chem. C* **2010,** *114* (39), 16596-16602.

56.   Khudozhitkov, A. E.; Kolokolov, D. I.; Stepanov, A. G.; Bolotov, V. A.; Dybtsev, D. N., Metal-cation-independent dynamics of phenylene ring in microporous MOFs: a ^2H solid-state NMR study. *J. Phys. Chem. C* **2015,** *119* (50), 28038-28045.

57.   Getman, R. B.; Bae, Y.-S.; Wilmer, C. E.; Snurr, R. Q., Review and analysis of molecular simulations of methane, hydrogen, and acetylene storage in metal–organic frameworks. *Chem. Rev.* **2011,** *112* (2), 703-723.

58.   Lu, Y.; Lucier, B. E.; Zhang, Y.; Ren, P.; Zheng, A.; Huang, Y., Sizable dynamics in small pores: CO_2 location and motion in the α-Mg formate metal–organic framework. *Phys. Chem. Chem. Phys.* **2017,** *19* (8), 6130-6141.

59.   (a) Chen, S.; Lucier, B. E.; Boyle, P. D.; Huang, Y., Understanding the fascinating origins of CO_2 adsorption and dynamics in MOFs. *Chem. Mater.* **2016,** *28* (16), 5829-5846; (b) Zhang, Y.; Lucier, B. E.; Huang, Y., Deducing CO_2 motion, adsorption locations and binding strengths in a flexible metal–organic framework without open metal sites. *Phys. Chem. Chem. Phys.* **2016,** *18* (12), 8327-8341.

60.   (a) Chris P. Schaller, Ph.D., College of Saint Benedict / Saint John's University https://employees.csbsju.edu/cschaller/PrinciplesChem/network/NWalumina.htm (Accessed August 4, 2017) (b) Roelofsen, D. P. Molecular sieve zeolites properties and applications in organic synthesis. TU Delft, Delft University of Technology, 1972.

61.   Colella, C.; Gualtieri, A. F., Cronstedt's zeolite. *Microporous and Mesoporous Mater.* **2007,** *105* (3), 213-221.

62.   Flanigen, E. M.; Jansen, J.; van Bekkum, H., *Introduction to zeolite science and practice*. Elsevier: c; Vol. 58.

63.   (a) Degnan Jr, T. F., Applications of zeolites in petroleum refining. *Top. Catal.* **2000,** *13* (4), 349-356; (b) Park, D. H.; Kim, S. S.; Wang, H.; Pinnavaia, T. J.; Papapetrou, M. C.; Lappas, A. A.; Triantafyllidis, K. S., Selective petroleum refining over a zeolite catalyst with small intracrystal mesopores. *Angew. Chem.* **2009,** *121* (41), 7781-7784.

64.   Venuto, P. B., Organic catalysis over zeolites: a perspective on reaction paths within micropores. *Microporous Mater.* **1994,** *2* (5), 297-411.

65.   Erdem, E.; Karapinar, N.; Donat, R., The removal of heavy metal cations by natural zeolites. *J. Colloid Interface Sci.* **2004,** *280* (2), 309-314.

66.   Auerbach, S. M.; Carrado, K. A.; Dutta, P. K., *Handbook of zeolite science and technology*. CRC press: 2003.

67.   Miazzo, R.; Rosa, C.; De Queiroz Carvalho, E.; Magnoli, C.; Chiacchiera, S.; Palacio, G.; Saenz, M.; Kikot, A.; Basaldella, E.; Dalcero, A., Efficacy of synthetic zeolite to reduce the toxicity of aflatoxin in broiler chicks. *Poult. Sci.* **2000,** *79* (1), 1-6.

68.   Bhattacharyya, A.; Bhaumik, A.; Rani, P. U.; Mandal, S.; Epidi, T. T., Nano-particles-A recent approach to insect pest control. *Afr. J. Biotechnol.* **2010,** *9* (24), 3489-3493.

69.   Klint, D.; Eriksson, H., Conditions for the adsorption of proteins on ultrastable zeolite Y and its use in protein purification. *Protein Expr. Purif.* **1997,** *10* (2), 247-255.

70.   Papaioannou, D.; Katsoulos, P.; Panousis, N.; Karatzias, H., The role of natural and synthetic zeolites as feed additives on the prevention and/or the treatment of certain farm animal diseases: a review. *Microporous and Mesoporous Mater.* **2005,** *84* (1), 161-170.

71.   Rahimi, N.; Karimzadeh, R., Catalytic cracking of hydrocarbons over modified ZSM-5 zeolites to produce light olefins: A review. *Appl. Catal. A* **2011,** *398* (1), 1-17.

72.   (a) Derouane, E. G., Shape selectivity in catalysis by zeolites: the nest effect. *J. Catal.* **1986,** *100* (2), 541-544; (b) Derouane, E. G.; Gabelica, Z., A novel effect of shape selectivity: molecular traffic control in zeolite ZSM-5. *J. Catal.* **1980,** *65* (2), 486-489.

73.   Van Bekkum, H.; Flanigen, E.; Jacobs, P.; Jansen, J., Zeolites and molecular sieves: An historical perspective. *Introduction to Zeolite Science and Practice* **2001**, 11-35.

74.   Breck, D. W., Crystalline zeolite Y. US Patent 3,130,007, May 12, 1961.

75.   Dyer, A., An introduction to zeolite molecular sieves. 1988.

76.   Alvarez, F.; Henriques, C.; Lemos, F.; Lopes, J.; Ribeiro, M., Structure-activity relationship in zeolites. *J. Mol. Catal. A: Chem.* **1995,** *96* (3), 245-270.

77.   Banerjee, R.; Furukawa, H.; Britt, D.; Knobler, C.; O'Keeffe, M.; Yaghi, O. M., Control of pore size and functionality in isoreticular zeolitic imidazolate frameworks and their carbon dioxide selective capture properties. *J. Am. Chem. Soc.* **2009,** *131* (11), 3875-3877.

78.	Kesraoui-Ouki, S.; Cheeseman, C. R.; Perry, R., Natural zeolite utilisation in pollution control: A review of applications to metals' effluents. *J. Chem. Technol. Biotechnol.* **1994,** *59* (2), 121-126.

79.	Smičiklas, I.; Dimović, S.; Plećaš, I., Removal of Cs^{1+}, Sr^{2+} and Co^{2+} from aqueous solutions by adsorption on natural clinoptilolite. *Appl. Clay Sci.* **2007,** *35* (1), 139-144.

80.	Wernert, V.; Schäf, O.; Ghobarkar, H.; Denoyel, R., Adsorption properties of zeolites for artificial kidney applications. *Microporous Mesoporous Mater.* **2005,** *83* (1), 101-113.

81.	Yang, R. T., *Gas separation by adsorption processes*. Butterworth-Heinemann: 2013.

82.	Li, K.; Valla, J.; Garcia-Martinez, J., Realizing the commercial potential of hierarchical zeolites: new opportunities in catalytic cracking. *ChemCatChem* **2014,** *6* (1), 46-66.

83.	Hudson, M. R.; Queen, W. L.; Mason, J. A.; Fickel, D. W.; Lobo, R. F.; Brown, C. M., Unconventional, Highly Selective CO_2 Adsorption in Zeolite SSZ-13. *J. Am. Chem. Soc.* **2012,** *134* (4), 1970-1973.

84.	(a) Shailaja, J.; Lakshminarasimhan, P.; Pradhan, A. R.; Sunoj, R.; Jockusch, S.; Karthikeyan, S.; Uppili, S.; Chandrasekhar, J.; Turro, N. J.; Ramamurthy, V., Alkali ion-controlled excited-state ordering of acetophenones included in zeolites: Emission, solid-state NMR, and computational studies. *J. Phys. Chem. A* **2003,** *107* (18), 3187-3198; (b) Shepelev, Y. F.; Butikova, I.; Smolin, Y. I., Crystal structures of the partially K-, Rb-, and Cs-exchanged forms of NaX zeolite in both the hydrated and the dehydrated (400° C) states. *Zeolites* **1991,** *11* (3), 287-292.

85.	Flanigen, E. M.; Khatami, H.; Szymanski, H. A., Infrared structural studies of zeolite frameworks. ACS Publications: 1971.

86.	Hunger, M.; Horvath, T., Multi-nuclear solid-state NMR study of the local structure of SiOHAl groups and their interaction with probe-molecules in dehydrated faujasite, mordenite and aeolite ZSM-5. *Ber. Bunsenges. Physik. Chem.* **1995,** *99* (11), 1316-1320.

87.	(a) Pluth, J. J.; Smith, J. V., Accurate redetermination of crystal structure of dehydrated zeolite A. absence of near zero coordination of sodium. refinement of silicon, aluminum-ordered superstructure. *J. Am. Chem. Soc.* **1980,** *102* (14), 4704-4708; (b) Perez, C. A.; de Resende, N. S.; Salim, V. M.; Schmal, M., Water interaction in faujasite probed by in situ X-ray powder diffraction. *J. Phys. Chem. C* **2017,** *121* (5), 2755-2761.

88.	Plevert, J.; Di Renzo, F.; Fajula, F.; Chiari, G., Structure of dehydrated zeolite Li−LSX by neutron diffraction: evidence for a low-temperature orthorhombic faujasite. *J. Phys. Chem. B* **1997,** *101* (49), 10340-10346.

89.	Castaneda, R.; Corma, A.; Fornés, V.; Rey, F.; Rius, J., Synthesis of a new zeolite structure ITQ-24, with intersecting 10-and 12-membered ring pores. *J. Am. Chem. Soc.* **2003,** *125* (26), 7820-7821.

90.   Gramm, F.; Baerlocher, C.; McCusker, L. B.; Warrender, S. J.; Wright, P. A.; Han, B.; Hong, S. B.; Liu, Z.; Ohsuna, T.; Terasaki, O., Complex zeolite structure solved by combining powder diffraction and electron microscopy. *Nature* **2006,** *444* (7115), 79.

91.   Bae, Y.-S.; Yazaydın, A. O. z. r.; Snurr, R. Q., Evaluation of the BET method for determining surface areas of MOFs and zeolites that contain ultra-micropores. *Langmuir* **2010,** *26* (8), 5475-5483.

92.   (a) Ackley, M. W.; Rege, S. U.; Saxena, H., Application of natural zeolites in the purification and separation of gases. *Microporous Mesoporous Mater.* **2003,** *61* (b), 25-42; (2) Siriwardane, R. V.; Shen, M.-S.; Fisher, E. P.; Losch, J., Adsorption of CO_2 on zeolites at moderate temperatures. *Energy Fuels* **2005,** *19* (3), 1153-1159.

93.   Yamazaki, T.; Katoh, M.; Ozawa, S.; Ogino, Y., Adsorption of CO_2 over univalent cation-exchanged ZSM-5 zeolites. *Mol. Phys.* **1993,** *80* (2), 313-324.

94.   Angell, C. L., Raman spectroscopic investigation of zeolites and adsorbed molecules. *J. Phys. Chem.* **1973,** *77* (2), 222-227.

95.   Stevens Jr, R. W.; Siriwardane, R. V.; Logan, J., In situ Fourier transform infrared (FTIR) investigation of CO_2 adsorption onto zeolite materials. *Energy Fuels* **2008,** *22* (5), 3070-3079.

96.   (a) Zukal, A.; Arean, C.; Delgado, M.; Nachtigall, P.; Pulido, A.; Mayerová, J.; Čejka, J., Combined volumetric, infrared spectroscopic and theoretical investigation of CO_2 adsorption on Na-A zeolite. *Microporous Mesoporous Mater.* **2011,** *146* (b), 97-105; (2) Maurin, G.; Llewellyn, P.; Bell, R., Adsorption mechanism of carbon dioxide in faujasites: grand canonical Monte Carlo simulations and microcalorimetry measurements. *J. Phys. Chem. B* **2005,** *109* (33), 16084-16091; (c) Plant, D.; Maurin, G.; Jobic, H.; Llewellyn, P., Molecular dynamics simulation of the cation motion upon adsorption of CO_2 in faujasite zeolite systems. *J. Phys. Chem. B* **2006,** *110* (29), 14372-14378.

97.   (a) Hu, J. Z.; Wan, C.; Vjunov, A.; Wang, M.; Zhao, Z.; Hu, M. Y.; Camaioni, D. M.; Lercher, J. A., 27Al MAS NMR Studies of HBEA Zeolite at Low to High Magnetic Fields. *J. Phys. Chem. C* **2017**; (b) Dawson, D. M.; Moran, R. F.; Ashbrook, S. E., An NMR Crystallographic Investigation of the Relationships Between the Crystal Structure and 29Si Isotropic Chemical Shift in Silica Zeolites. *J. Phys. Chem. C* **2017**.

98.   (a) Fyfe, C.; Feng, Y.; Grondey, H.; Kokotailo, G.; Gies, H., One-and two-dimensional high-resolution solid-state NMR studies of zeolite lattice structures. *Chem. Rev.* **1991,** *91* (7), 1525-1543; (b) Klinowski, J., Solid-state NMR studies of molecular sieve catalysts. *Chem. Rev.* **1991,** *91* (7), 1459-1479.

99.   Davis, M. E., Zeolites and molecular sieves: not just ordinary catalysts. *Ind. Eng. Chem. Res.* **1991,** *30* (8), 1675-1683.

100.   Klinowski, J.; Ramdas, S.; Thomas, J. M.; Fyfe, C. A.; Hartman, J. S., A re-examination of Si, Al ordering in zeolites NaX and NaY. *J. Chem. Soc., Faraday Transactions 2: Mol. Chem. Phys.* **1982,** *78* (7), 1025-1050.

101.   Gullion, T.; Schaefer, J., Rotational-echo double-resonance NMR. *J. Magn. Reson.* **2011,** *213* (2), 413-417.

102.　Fyfe, C. A.; Brouwer, D. H.; Lewis, A. R.; Villaescusa, L. A.; Morris, R. E., Combined solid state NMR and X-ray diffraction investigation of the local structure of the five-coordinate silicon in fluoride-containing as-synthesized STF zeolite. *J. Am. Chem. Soc.* **2002,** *124* (26), 7770-7778.

103.　(a) Freude, D.; Loeser, T.; Michel, D.; Pingel, U.; Prochnow, D., ^{17}O NMR studies of low silicate zeolites. *Solid State Nucl. Magn. Reson.* **2001,** *20* (1), 46-60; (b) Peng, L.; Liu, Y.; Kim, N.; Readman, J. E.; Grey, C. P., Detection of Brønsted acid sites in zeolite HY with high-field ^{17}O-MAS-NMR techniques. *Nature Mater.* **2005,** *4* (3), 216.

104.　(a) Yan, Z.; Chen, B.; Huang, Y., A solid-state NMR study of the formation of molecular sieve SAPO-34. *Solid State Nucl. Magn. Reson.* **2009,** *35* (2), 49-60; (b) Huang, Y.; Richer, R.; Kirby, C. W., Characterization of the gel phases of AlPO4-11 molecular sieve synthesis by solid-state NMR. *J. Phys. Chem. B* **2003,** *107* (6), 1326-1337.

105.　Xie, B.; Song, J.; Ren, L.; Ji, Y.; Li, J.; Xiao, F.-S., Organotemplate-free and fast route for synthesizing beta zeolite. *Chem. Mater.* **2008,** *20* (14), 4533-4535.

106.　Kosanović, C.; Bronić, J.; Subotić, B.; Smit, I.; Stubičar, M.; Tonejc, A.; Yamamoto, T., Mechanochemistry of zeolites: Part 1. Amorphization of zeolites A and X and synthetic mordenite by ball milling. *Zeolites* **1993,** *13* (4), 261-268.

107.　Feuerstein, M.; Lobo, R., Characterization of Li cations in zeolite LiX by solid-state NMR spectroscopy and neutron diffraction. *Chem. Mater.* **1998,** *10* (8), 2197-2204.

108.　Wang, X.; Xu, J.; Qi, G.; Wang, C.; Wang, W.; Gao, P.; Wang, Q.; Liu, X.; Feng, N.; Deng, F., Carbonylation of ethane with carbon monoxide over Zn-modified ZSM-5 zeolites studied by in situ solid-state NMR spectroscopy. *J. Catal.* **2017,** *345*, 228-235.

109.　(a) Wang, X.; Qi, G.; Xu, J.; Li, B.; Wang, C.; Deng, F., NMR-spectroscopic evidence of intermediate-dependent pathways for acetic acid formation from methane and carbon monoxide over a ZnZSM-5 zeolite catalyst. *Angew. Chem. Int. Ed.* **2012,** *51* (16), 3850-3853; (b) Moore, J. K.; Sakwa-Novak, M. A.; Chaikittisilp, W.; Mehta, A. K.; Conradi, M. S.; Jones, C. W.; Hayes, S. E., Characterization of a mixture of CO_2 adsorption products in hyperbranched aminosilica adsorbents by ^{13}C solid-state NMR. *Environ. Sci. Technol.* **2015,** *49* (22), 13684-13691.

110.　(a) De Menorval, L.-C.; Raftery, D.; Liu, S.-B.; Takegoshi, K.; Ryoo, R.; Pines, A., Investigations of adsorbed organic molecules in Na-Y zeolite by xenon-129 NMR. *J. Phys. Chem.* **1990,** *94* (1), 27-31; (b) Ryoo, R.; Liu, S.-B.; De Menorval, L.-C.; Takegoshi, K.; Chmelka, B.; Trecoske, M.; Pines, A., Distribution of hexamethylbenzene in a zeolite studied by xenon-129 and multiple-quantum NMR. *J. Phys. Chem.* **1987,** *91* (27), 6575-6577.

111.　(a) Rastelli, H.; Chao, C. C.; Garg, D. R., Selective adsorption of CO_2 on zeolites. Google Patents: 1988; (b) Cavenati, S.; Grande, C. A.; Rodrigues, A. E., Adsorption equilibrium of methane, carbon dioxide, and nitrogen on zeolite 13X at high pressures. *J. Chem. Eng. Data* **2004,** *49* (4), 1095-1101.

112.   Omi, H.; Ueda, T.; Miyakubo, K.; Eguchi, T., Dynamics of CO_2 Molecules Confined in the Micropores of Solids as Studied by ^{13}C NMR. *Appl. Surf. Sci.* **2005,** *252* (3), 660-667.

113.   MacKenzie, K. J.; Smith, M. E., *Multinuclear solid-state nuclear magnetic resonance of inorganic materials*. Elsevier: 2002; Vol. 6.

114.   Geen, H.; Freeman, R., Band-selective radiofrequency pulses. *J. Magn. Reson. (1969)* **1991,** *93* (1), 93-141.

115.   Levitt, M. H., *Spin dynamics: basics of nuclear magnetic resonance*. John Wiley & Sons: 2001.

116.   Beeler, A. J.; Orendt, A. M.; Grant, D. M.; Cutts, P. W.; Michl, J.; Zilm, K. W.; Downing, J. W.; Facelli, J. C.; Schindler, M. S.; Kutzelnigg, W., Low-temperature carbon-13 magnetic resonance in solids. 3. Linear and pseudolinear molecules. *J. Am. Chem. Soc.* **1984,** *106* (25), 7672-7676.

117.   Macomber, R. S., *A complete introduction to modern NMR spectroscopy*. Wiley New York: 1998.

118.   Pake, G. E., Nuclear resonance absorption in hydrated crystals: fine structure of the proton line. *J. Chem. Phys.* **1948,** *16* (4), 327-336.

119.   Cory, D.; Ritchey, W., Suppression of signals from the probe in Bloch decay spectra. *J. Magn. Reson. (1969)* **1988,** *80* (1), 128-132.

120.   Patching, S., NMR-Active Nuclei for Biological and Biomedical Applications. *J. Diagn. Imaging Ther.* **2016,** *3* (1), 7-48.

121.   Hahn, E. L., Spin echoes. *Phys. Rev.* **1950,** *80* (4), 580.

122.   Hartmann, S.; Hahn, E., Nuclear double resonance in the rotating frame. *Phys. Rev.* **1962,** *128* (5), 2042.

123.   Acorn NMR Inc. http://www.acornnmr.com/nuts.htm (Accessed August 15, 2015).

124.   Eichele, K., WSolids NMR Simulation Package, Verson 1.20. 21; 2013.

125.   Vold, R. L.; Hoatson, G. L., Effects of jump dynamics on solid state nuclear magnetic resonance line shapes and spin relaxation times. *J. Magn. Reson.* **2009,** *198* (1), 57-72.

126.   Fulmer, G. R.; Miller, A. J.; Sherden, N. H.; Gottlieb, H. E.; Nudelman, A.; Stoltz, B. M.; Bercaw, J. E.; Goldberg, K. I., NMR chemical shifts of trace impurities: common laboratory solvents, organics, and gases in deuterated solvents relevant to the organometallic chemist. *Organometallics* **2010,** *29* (9), 2176-2179.

127.   Clark, S. J.; Segall, M. D.; Pickard, C. J.; Hasnip, P. J.; Probert, M. I.; Refson, K.; Payne, M. C., First principles methods using CASTEP. *Z. Kristallogr. Cryst. Mater.* **2005,** *220* (5/6), 567-570.

Chapter 2

2   Tracing induced structural changes, guest adsorption behaviours and locations in the α - zinc formate MOF

Metal-organic frameworks (MOFs) are synthetic compounds with crystalline microporous structures, consisting of metal centres joined by organic linkers. The porous crystalline structure of MOFs permits the adsorption of a variety of guest gases, with the uptake of gases such as CO_2, CO, and C_2D_4 of particular interest due to the importance of these guests in processes such as global warming, combustion, and gas separation. α - Zinc formate [α -$Zn_3(HCOO)_6$] is one MOF that can be synthesized at room temperature relatively easily with cheap and environmentally-friendly reagents. With narrow pores and 1-dimensional channels, this α - zinc formate MOF is suitable for the study of guest molecule adsorption and dynamic behaviour. Using ^{13}C, ^2H, ^{67}Zn and ^1H-^{13}C cross-polarization (CP) solid-state NMR (SSNMR) techniques, along with single crystal XRD (SCXRD) experiments for structure determination and refinement, the adsorbed guest molecule behaviour of CO_2, CO and C_2H_4 molecules have been unraveled within α - zinc formate. When adsorbed in the α - zinc formate MOF, all three guest molecules (CO_2, CO, and C_2D_4) undergo two combined motions: a localized three-fold C_3 wobbling on the adsorption sites and a non-localized, two-fold C_2 hopping between adjacent adsorption sites located along the one-dimensional zig-zag shaped channels. One interesting finding is that the motion of CO_2 molecules becomes restricted at high temperatures due to a structural phase change. CP experiments reveal that nuclei located at the adsorption site participate in significant dipolar coupling interactions with guest CO_2 molecules. Single crystal XRD is a powerful technique for structure determination and refinement, which can be combined with information obtained from SSNMR spectra to pinpoint accurate guest molecule adsorption locations. CO_2 and CO molecules form weak hydrogen bonding interactions with the hydrogen atom of the formate linker, while C_2D_4 molecules interact with the oxygen atom of the formate linker exposed to the channel interior.

2.1   Introduction

2.1.1 General introduction

Crystalline MOFs are a class of synthetic compounds composed of metal ion centres and organic linkers. The porous crystalline structure of MOFs often permits the adsorption of a variety of guest gases. MOFs have many industrial applications, such as gas adsorption and separation,[1] and catalysis.[2] The dynamic behaviour of CO_2 and many other polar molecules may differ when adsorbed in various MOFs with diverse local structures and dimensions. Studying the adsorption behaviour of guest molecules within MOFs provides information on the specific guest adsorption mechanisms, dynamics and locations, which is helpful for understanding the connection between guest molecule dynamics and adsorption capacity, as well as assisting in the design of more effective MOFs.

The porous structures and functional groups within MOFs make these promising solid adsorbents for gas storage and separation. In industrial manufacturing processes, the usage of some carbon-rich fuels with an insufficient oxygen supply may result in incomplete combustion, producing mixed flue gases including unreacted fuel, the incomplete combustion product CO and the complete combustion product CO_2. A robust solid adsorbent and purifier is necessary to capture the greenhouse gas CO_2 from the exhaust mixture, as well as the toxic gas CO. A good example of potential MOF applications in this context is ethylene. Currently, manufacturers use a repeated condensation and distillation procedure to separate ethylene products from the gas mixture. However, this is the most energy-consuming step of the entire procedure for the production of ethylene.[3] In this instance, effective and highly-selective solid adsorbents under mild conditions, such as MOFs, are necessary to selectively separate ethylene products from the mixture gas.[4] In this study, the behaviour of CO_2, CO and C_2D_4 were investigated in the promising adsorbent MOF α - zinc formate, which is environmentally friendly. Studies on the behaviour of these three guests within this promising MOF may assist in the design of more cost-efficient and environmentally friendly MOFs.

2.1.2 The α - zinc formate MOF

Zinc formate has two phases, known as the α and β phases.[5] The β phase does not have a porous structure, which means that it is not suitable to be used as a MOF adsorbent for dynamic studies of adsorbed guests. The porous α - zinc formate [α -$Zn_3(HCOO)_6$] can be synthesized at room temperature using inexpensive starting reagents[6] and has good thermal stability, staying stable at temperatures up to 413 K.[5] This porosity and thermal stability makes it possible to study CO_2, CO and C_2D_4 guest molecule adsorption behaviour through a range of temperatures. The porous α phase resides in a *P* 2_1/n monoclinic crystal structure with all Zn centres in octahedral environments, connected to six oxygen atoms belonging to formate linkers, as shown in Figure 2-1.[6] The zinc atoms form apex-sharing, Zn-centred tetrahedral nodes ($ZnZn_4$) that are linked by HCOO groups, which act as the edges of $ZnZn_4$ tetrahedra. Each HCOO formate linker has one oxygen atom bound to the central Zn^{2+} ion and the other oxygen atom bound to a neighbouring apical Zn^{2+} ion in the $ZnZn_4$ tetrahedron**.** By sharing the apical Zn^{2+} from $ZnZn_4$ units (Figure 2-1c), these tetrahedral building blocks construct a diamondoid framework (Figure 2-1a), featuring one-dimensional, zig-zag channels (Figure 2-1d). The cross-sectional free space of the channel measures about 4 × 5 Å.[6] Inside the α - zinc formate MOF channels, the exposed oxygen atoms of the formate linkers are believed to be theadsorption sites for H-bond donor molecules, such as C_2H_2 and C_2H_4. The hydrogen atoms of formate linkers that stick out into the channel interior have been proven to be the adsorption sites for H-bond acceptor guests such as CO_2 and CO.[6]

The host-guest interactions in α - zinc formate have been studied using several different guest molecules. It can be observed from some SCXRD studies that the unit cell parameters vary when benzene, DMF, or other molecules are introduced within the MOF.[6] ^{13}C SSNMR is a powerful tool for understanding the dynamic behaviour of small molecules such as CO_2[7] and CO[8] within MOFs, and ^{2}H SSNMR is typically used to study the motion of guest molecules containing hydrogen in deuterium forms, such as D_2[9] and C_2D_4[10]. To investigate the α - zinc formate framework itself, [67]Zn SSNMR experiments can be used to directly probe the local environment of zinc atoms in as-made, empty and guest-loaded samples. Herein, variable-temperature (VT) ^{13}C and ^{2}H SSNMR

experiments are conducted along with SCXRD structural refinement to investigate CO_2, CO and C_2D_4 adsorption behaviour and locations in α - zinc formate. The ^{67}Zn and ^{1}H-^{13}C CP SSNMR experiments focus on the interactions between framework and the guest molecules, providing valuable information on guest adsorption mechanisms within the α - zinc formate MOF.
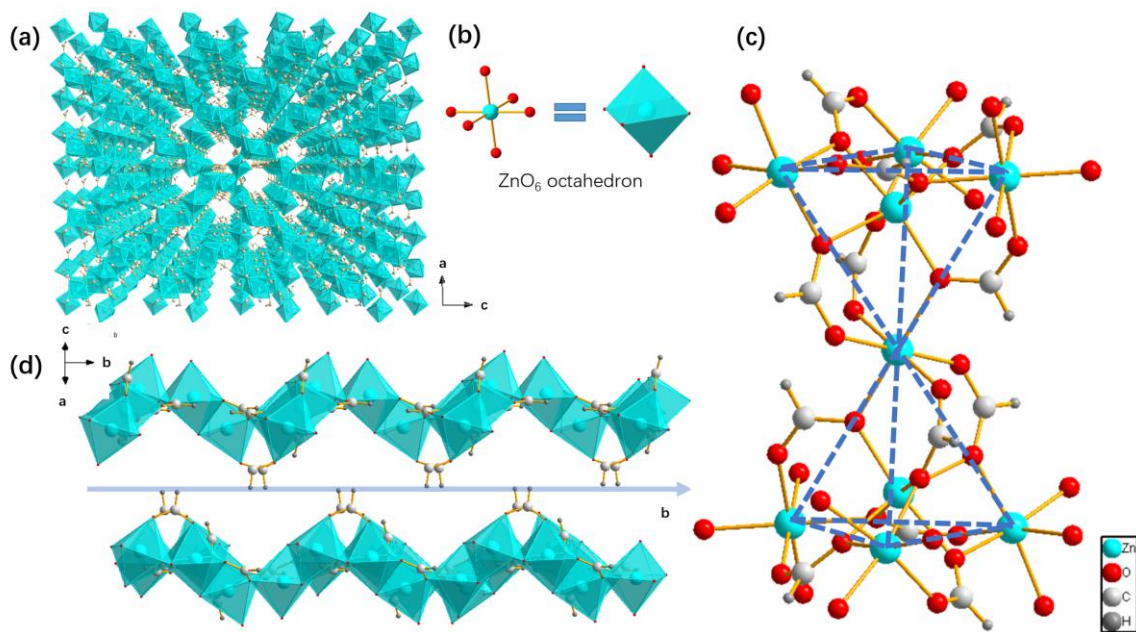
Figure 2-13 The extended crystal framework of α -Zn-formate is shown in (a), looking down to the crystallographic b axis. In (b), the local crystal structure shows the chemical environment of Zn atoms in α – $Zn_3(HCOO)_6$, where the Zn ions sit in an octahedron bound by six oxygen atoms. In (c), two $ZnZn_4$ tetrahedron nodes connect to each other by sharing an apical Zn atom, constructing (d) the one-dimensional void channel, featuring zig-zag shaped channels along the crystallographic b axis in the α – $Zn_3(HCOO)_6$ MOF.

2.2   Experimental section

2.2.1 Synthesis

The α - zinc formate MOF was synthesized at room temperature using an optimized version of the reported solution reaction:[6] a methanol solution (25 mL, Fisher Chemical, 99.8%) containing formic acid (1.6 mL, Alfa Aesar, 97%) and trimethylamine (4.2 mL, EMD Millipore Corporation, 99.5%) was gently added dropwise into a methanol solution (25 mL) of $Zn(NO_3)_2 \cdot 6H_2O$ (3.0 g, BDH Laboratory Supplies, 98%) in a 50 mL glass jar. The glass jar with the combined solutions was then covered by parafilm and some small holes were poked in the film to allow evaporation of methanol. After sitting at room temperature for three days, colorless, transparent crystals were visible and then were collected. Then these crystals were washed with methanol in a vacuum filter five times to remove unreacted chemicals. The product was then air-dried at room temperature to obtain "as-made" α - zinc formate.

2.2.2 Activation process

To load guest molecules into α - zinc formate, it was necessary to remove all residual H_2O and methanol molecules in the channels of as-made α - zinc formate. A Schlenk line was involved in the activation and gas adsorption procedure. First, ca. 0.15 g of the as-made α - zinc formate product was ground into a fine powder and then it was placed at the bottom of an L-shaped glass tube 5 mm or 7 mm in diameter. Then a small patch of glass wool was used to secure the packed MOF sample in the bottom of the tube. The L-shaped glass tube was then attached to the Schlenk line, connected to a vacuum pump, and a pressure gauge to ensure the pressure was ≤ 1 mbar under vacuum conditions. The α - zinc formate sample was then heated up to 353 K for 18 h under vacuum to remove residual solvent molecules. The sample was then cooled down to room temperature and termed "activated" or empty α - zinc formate.

2.2.3 Gas adsorption

NMR active, ^{13}C isotopically labeled and enriched $^{13}CO_2$ (Sigma-Aldrich, 99% [13]C) and ^{13}CO (Sigma-Aldrich, 99% [13]C), denoted as CO_2 and CO in this work, were used in this study as guest molecules due to the low abundance (0.96%) of ^{13}C in nature. For C_2H_4 molecules, ^{2}H labeled C_2D_4 molecules are preferred rather than $^{13}C_2H_4$ due to the strong dipolar interaction between the two carbon atoms and four hydrogen atoms in C_2H_4, which greatly complicates and distorts the spectral appearance in most cases. Thus, NMR active, ^{2}H enriched C_2D_4 (Sigma-Aldrich, 99% [2]H) was used for ^{2}H SSNMR studies.

The gas adsorption process was performed after the activation process. Isotopically labeled guest molecules were transferred from gas cylinders and stored in separate round bottom flasks. The flasks were then attached to the Schlenk line and a known amount of gas was released to the Schlenk line, occupying a volume of 82.7 mL in total. The gas loading level in the MOF was expressed by a molar ratio of guest molecules to Zn. The loading level of 0.1 guest molecule per Zn atom (0.1 GM / Zn) was used for most experiments, while a lower loading level of 0.075 CO per Zn atom (0.075 CO / Zn) was used for the high-temperature (HT) VT experiments. The bottom of the L-shaped glass tube was kept in liquid nitrogen to condense guest molecules from the Schlenk line and trap the guests within the MOF samples. A flame-sealing procedure was then performed to separate the L-shaped glass tube with guest molecule loaded MOF sample from the Schlenk line. The resulting flame-sealed glass tube with the guest-loaded MOF sample was then used for all SSNMR experiments.

2.2.4 Powder X-ray diffraction (pXRD)

Powder X-ray diffraction was conducted to identify the MOF and confirm its purity and crystallinity. The pXRD experiments were run using a Rigaku diffractometer operating with Co K_α radiation (λ = 1.7902 Å) as the radiation source; samples were

manually ground into powders and then scanned through 2θ values ranging from 5 to 45 °
with an increment of 0.02° at a scanning rate of 10° /min. The experimental pXRD
powder patterns are shown in Figure S2-1 in the appendix, and indicate a good match
between the various synthesized α - zinc formate samples versus simulated powder
patterns based on reported crystallographic data. It should be noted that once ethanol is
introduced to as made α - zinc formate crystals, the α – phase transforms into the bulk
compound zinc formate dihydrate, shown in Figure S2-2.

2.2.5 Single-crystal X-ray diffraction (SCXRD)

To prepare the CO_2 loaded α - zinc formate MOF sample for SCXRD tests, the same
activation and gas adsorption procedure involving L-shaped glass tubes outlined above
was followed, but the α - zinc formate sample was kept in single crystal form without
grinding. In addition, during guest loading, the L-shaped glass tube containing the
activated sample was saturated by CO_2 and kept in liquid nitrogen until no more CO_2 was
adsorbed according to the pressure gauge. Then the L-shape glass tube was sealed with
flame and separated from the vacuum line.

SCXRD analysis at low temperature (120 K) was performed on CO_2 loaded α - zinc
formate. The sample (#n17100) was mounted on a Mitegen polyimide micromount with a
small amount of Paratone-N oil. All X-ray measurements were made on a Bruker-Nonius
KappaCCD Apex2 diffractometer at a temperature of 120 K. The unit cell dimensions
were determined from a symmetry constrained fit of 9044 reflections with 6.12° < 2θ <
135.18° . The data collection strategy was using several w and j scans which collected
data up to 135.17° (2θ). The frame integration was performed using SAINT.[11] The
resulting raw data was scaled and absorption corrected using a multi-scan averaging of
symmetry equivalent data using SADABS.[12]

The structure was solved by beginning with the atomic coordinates of an
isomorphous structure.[6] All non-hydrogen framework atoms were entered in the initial
solution. The atomic positions corresponding to the CO_2 molecule were obtained from a

difference Fourier map. The hydrogen atoms were introduced at idealized positions and were allowed to refine isotopically. A void space calculation was performed using PLATON[13] and indicated there were 125.6 Å of void space in the unit cell corresponding to 7.8% of the unit cell volume. The structural model was fit to the data using full matrix least-squares based on F^2. The calculated structure factors included corrections for anomalous dispersion from the usual tabulation. The structure was refined using the SHELXL-2014 program from the SHELX suite of crystallographic software.[14] Graphic plots were produced using the NRCVAX program suite.[15]

2.2.6 Direct-excitation ^{13}C and ^2H SSNMR characterization at 9.4 T

SSNMR experiments were conducted by using a Varian Infinity Plus spectrometer, equipped with a 9.4 T Oxford Instruments superconducting magnet and a double channel (HX) 5 mm Varian/Chemagnetics static probe. The experimental temperature was adjusted between 123 K and 433 K using a Varian VT temperature control unit and the experimental temperature readings were calibrated by the ^{207}Pb chemical shift of solid $Pb(NO_3)_2$.[16] Direct-excitation ^{13}C SSNMR experiments were conducted using the DEPTH-echo[7] pulse sequence. The chemical shift of all ^{13}C spectra were referenced to tetramethylsilane (TMS) while the methylene carbon of ethanol at 56.83 ppm was used as a secondary reference.[17]

In the SSNMR experiments on CO_2 loaded MOF samples, an optimized 90° pulse length of 2.95 μs was used, along with a calibrated recycle delay of 3 s for acquisitions ranging between 173 K and 353 K, and recycle delays of 5 s when the temperature was ≤ 153 K and ≥ 373 K. Each ^{13}C SSNMR spectrum was assembled from 1018 or 1739 scans, except for the spectrum acquired at 293 K, which was assembled from 46656 scans. In experiments on CO loaded MOF samples, an optimized 90° pulse length of 3.30 μs was used, along with a calibrated recycle delay of 5 s for acquisitions ranging between 173 K and 353 K, and recycle delays of 7 s when the temperature was ≤ 153 K and ≥ 373 K.

Each ^{13}C SSNMR spectrum was assembled from 1005 or 1134 scans, except for the spectrum acquired at 293 K, which was assembled from 4644 scans. The spectrum of the activated empty α - zinc formate sample was assembled from 48362 scans with a calibrated pulse delay of 3 s.

Direct-excitation ^{2}H SSNMR experiments were conducted using the 90° -90° echo pulse sequence with proton decoupling. In the tests of C_2D_4 loaded MOF sample, an optimized 90° pulse length of 2.95 μs was used, along with a calibrated recycle delay of 2 s for acquisitions at temperatures ranging between 123 K and 363 K. Each ^{2}H SSNMR spectrum was assembled from 1207 or 3028 scans, except for the spectrum acquired at 293 K, which was assembled from 19014 scans. A sample of D_2O (l) was used as a secondary chemical shift reference at $\delta_{iso} = 4.8$ ppm with respect to $(CD_3)_4Si$.[17]

2.2.7 ^{1}H-^{13}C Cross-Polarization (CP) SSNMR experiments at 9.4 T

To examine the adsorption status, adsorption locations, and possible hydrogen bonding interactions between guest molecules and adsorption sites, ^{1}H-^{13}C CP SSNMR experiments were performed at 293K and 173 K. Static, proton decoupled ^{1}H-^{13}C CP SSNMR experiments were conducted on both activated empty as well as CO and CO_2 loaded MOF samples. CP experiments were performed using variable contact times of 0.5, 1, 3, 5, 8, and 10 ms. All CP experiments used a recycle delay of 1 s and spectra were assembled from 3610 or 5560 scans. The chemical shifts in all ^{13}C spectra were referenced to tetramethylsilane (TMS), with the methylene carbon of ethanol at 56.83 ppm used as a secondary reference.[17]

2.2.8 ^{67}Zn spectra SSNMR experiments at 21.1 T

Experiments at a magnetic field of 21.1 T were carried out using a Bruker Avance II NMR spectrometer located at the National Ultrahigh-Field NMR Facility for Solids in Ottawa, ON, Canada. A home-built 7 mm single-channel static probe was used to acquire all ^{67}Zn spectra (ν_0 (^{67}Zn) =56.29 MHz). Five α - zinc formate MOF samples including the as-made and activated empty MOF, along with CO, CO_2 and C_2D_4 loaded MOF

samples were investigated. A 1.0 M $Zn(NO_3)_2$ aqueous solution at δ_{iso} = 0.0 ppm was used as a standard ^{67}Zn reference, and also for pulse calibrations.[18] All spectra were acquired using a modified 90° –90° echo pulse sequence of the form ($\pi/2 - \tau_1$ - $\pi/2$ - τ_2 –acq) with a full spectral width of 500 kHz, along with inter-pulse delays of $\tau_1 = \tau_2 = 67$ μs. A pulse delay of 0.25 s was used to obtain ^{67}Zn SSNMR spectra at 21.1 T, with a typical number of scans being 32768, requiring just about 2.5 hours of total acquisition time.

2.2.9 Chemical shift (CS) tensor convention

The ^{13}C NMR powder patterns in this study are broadened and dominated by the chemical shift (CS) interaction. The CS interaction can be modeled by a second-rank tensor defined by the three orthogonal components δ_{11}, δ_{22} and δ_{33}, which are ordered such that $\delta_{11} \geq \delta_{22} \geq \delta_{33}$. There are three NMR parameters that are used to describe SSNMR powder pattern lineshapes and the CS tensor: the isotropic chemical shift (δ_{iso}, $\delta_{iso} = (\delta_{11} + \delta_{22} + \delta_{33})/3$), the span ($\Omega$, $\Omega = \delta_{33} - \delta_{11}$), and the skew ($\kappa$, $\kappa = 3(\delta_{22} - \delta_{iso})/\Omega$).

2.2.10 Electric field gradient (EFG) tensor convention

The ^2H and ^{67}Zn powder patterns in this study are broadened and dominated by the quadrupolar interaction. The quadrupolar interaction can couple with the local electric field gradients (EFGs) in a process known as the anisotropic quadrupolar interaction (QI). The EFG tensors can be described by three orthogonal vectors in a principal axis system (PAS), in the order of $|V_{33}| > |V_{22}| > |V_{11}|$. When evaluating the quadrupolar interaction, two parameters are used: the quadrupolar coupling constant C_Q, and the asymmetry parameter η_Q, which can be described in this way: $C_Q = eQV_{33}/h$ and $\eta_Q = (V_{11} - V_{22})/V_{33}$.

2.2.11 Simulation and reference standards for dynamics

The WSolids software package[19] was used to analytically simulate the experimental spectra and extract the observed, or apparent, ^{13}C and ^2H NMR parameters. The EXPRESS software package[20] was used to simulate guest dynamics based on the

observed SSNMR spectra and CS parameters, given that the known parameters for static, stationary CO_2 are δ_{iso} = 125 ppm, Ω = 335 ppm, and κ = 1,[21] stationary CO are δ_{iso} = 185 ppm, Ω = 353 ppm, and κ = 1,[21] and stationary C_2D_4 are C_Q = 230 kHz, η_Q = 0.[17] The CASTEP simulation package[22] was used to predict and extract ^{67}Zn parameters from the known and computationally-optimized crystal structures.

The localized rotation of CO_2, CO and C_2D_4 guest molecules is modeled by a three-fold rotational "wobbling" motion, along with a non-localized two-site jumping or "hopping",[23] where the three-fold "wobbling" means a continuous and localized motion upon the single adsorption site in a cone defined by the motional angle (Figure 2-2), while the twofold hopping means a discrete jumping between two separate adsorption sites. The rate of all motions was considered as "fast" (i.e. $\geq 10^7$ Hz).
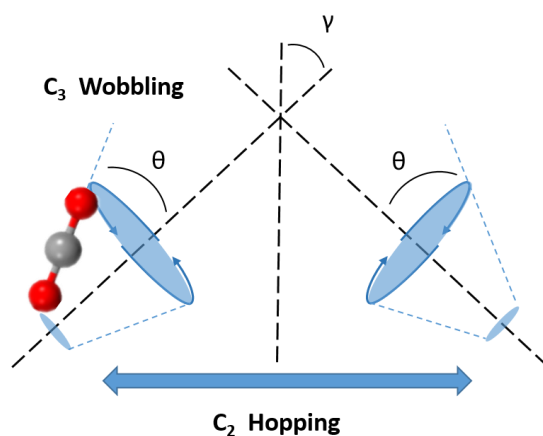
Figure 2-2. The well-defined, localized C_3 wobbling motion of a CO_2 guest through the angle θ, and inter-site C_2 hopping motion between two C_3 sites through the angle γ.

2.3   Results and discussion

2.3.1 VT ^{13}C SSNMR experiments of CO_2 loaded α - zinc formate

Within the temperature range from 433 K to 123 K (Figure 2-3a), the ^{13}C spectral lineshapes of CO_2 loaded α–zinc formate indicate that the interaction between CO_2 and the α–zinc formate MOF framework are significantly influenced by experimental temperatures. The strong and sharp resonance observed at 125 ppm from 433 K to 313 K corresponds to free mobile CO_2 at 125 ppm, which rapidly tumbles through space, averaging out the lineshape broadening associated with chemical shift anisotropy (CSA) and generating a narrow isotropic resonance. This observation is in good agreement with our previous results[24] concerning gaseous CO_2 chemical shifts, and is close to the reported δ_{iso} at 132 ppm.[21] There is also another broader powder pattern present. This asymmetric and broad powder pattern is generated by CSA, which indicates that the corresponding CO_2 molecules are not free, but are undergoing specific motions within α–zinc formate. The temperature-dependent lineshape of the broad resonance indicates that the mobility of adsorbed CO_2 within α - zinc formate changes significantly within this temperature range, and the motional angles become smaller at lower and higher temperatures (Figure 2-3). Thus, the CO_2 molecules in this MOF sample are in one of two states: freely tumbling, or adsorbed with restricted motions. The presence of one single broadened powder pattern indicates that the adsorbed CO_2 molecules with restricted motions reside in identical chemical environments and are associated with a single unique adsorption site.

The experimental ^{13}C SSNMR spectra were simulated and analyzed to obtain ^{13}C parameters for dynamic studies of adsorption behaviour; Figures 2-3(b) and 2-4 detail the experimental results along with simulations. The observed δ_{iso}, span (Ω), and skew (κ) from ^{13}C SSNMR spectra are listed in Table 2-1. The simulation results are in good agreement with experimental lineshapes, confirming that the broadened powder pattern belongs to adsorbed CO_2 within α - zinc formate.
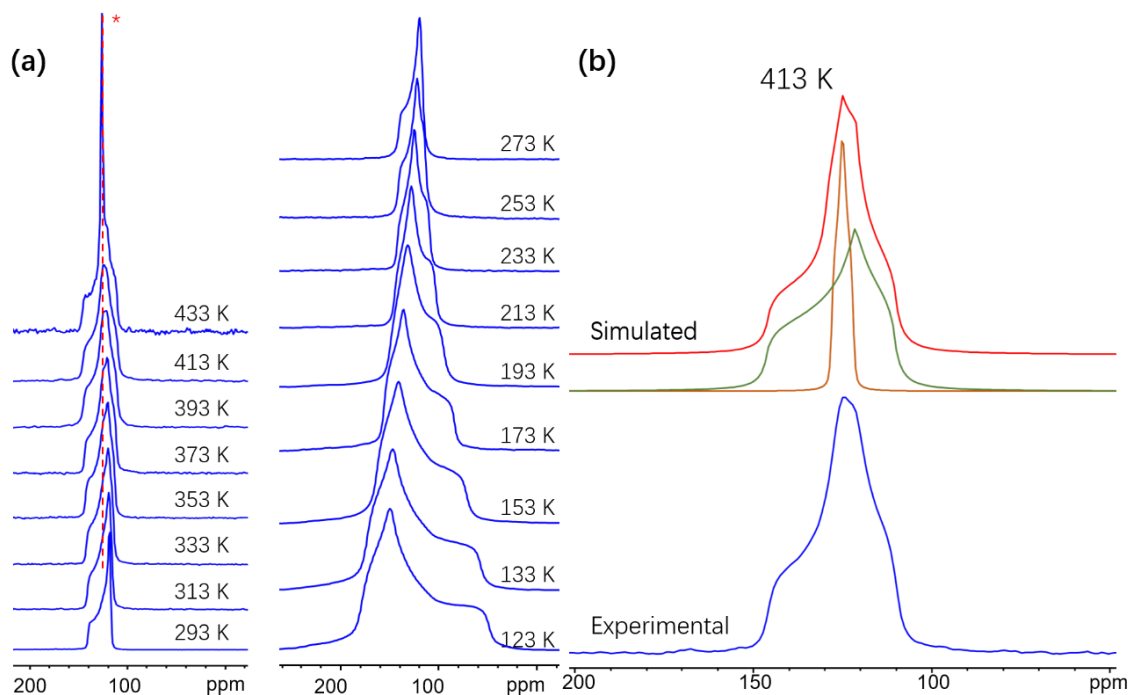
Figure 2-3. In (a), the experimental ^{13}C spectra of CO_2 adsorbed in α – zinc formate within the temperature range from 123 K to 433 K are shown. Noted that the spectra acquired in HT and LT experiments show broader spans with increasing and decreasing temperatures, respectively. The red dashed line with (*) denotes the narrow and sharp resonance contributed by free, isotropically tumbling CO_2, which is observed from 313 K to 433 K. The resonance representing free CO_2 guests gains intensity at 433 K, suggesting the CO_2 guests have escaped or desorbed from framework at this temperature. A detailed analysis of the powder pattern lineshape in (b) suggests the spectrum acquired at 413 K consists of an adsorbed CO_2 powder pattern (green) along with a sharp resonance contributed by free CO_2 (orange).

Comparing the observed span of the ^{13}C spectra of adsorbed CO_2 within α - zinc formate across the VT range to that of rigid CO_2 (Ω = 335 ppm) at 20 K, it is apparent that the guest CO_2 molecules adsorbed in α - zinc formate are undergoing certain motions so that the span is partially averaged by the motion within the experimental temperature range. The powder pattern exhibits its narrowest span of 23.5(1) ppm at 293 K (Figure 2-4). The broadest ^{13}C spectral width was observed in the LT experiments, at the lowest
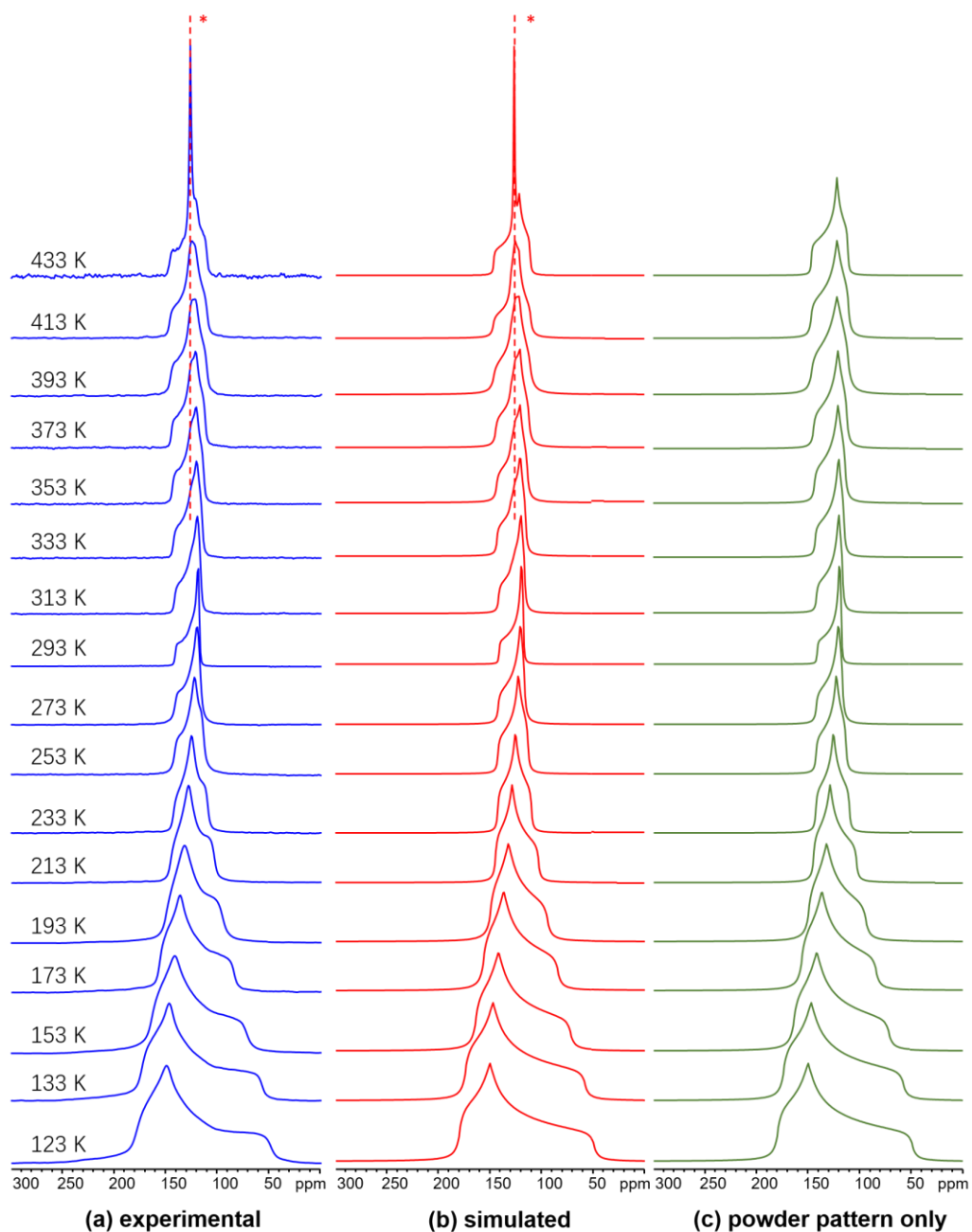
Figure 2-4. The spectra in (a) and (b) show the experimental and analytically simulated ^{13}C SSNMR spectra of adsorbed CO_2 in α – zinc formate respectively, from 123 K to 433 K. The resonance originating from free CO_2 is only present at temperatures of 313 K and above. The simulations in (c) show the powder pattern contributed solely by adsorbed CO_2 in α – zinc formate.

Table 2-1 The observed ^{13}C parameters of adsorbed CO_2 guests in α – zinc formate.

Temperature (K)	δ_{iso} (ppm)	Span (Ω, ppm)	Skew (κ)
433 K	126.0(2)	35.3(2)	-0.40(3)
413 K	126.0(2)	36.2(2)	-0.39(2)
393 K	126.0(2)	35.2(1)	-0.39(1)
373 K	125.5(1)	32.2(2)	-0.46(1)
353 K	125.7(1)	29.7(1)	-0.53(1)
333 K	125.7(1)	27.8(1)	-0.62(1)
313 K	125.7(1)	25.2(1)	-0.70(1)
293 K	125.7(1)	23.5(1)	-0.84(2)
273 K	126.0(1)	25.3(1)	-0.70(2)
253 K	125.6(1)	29.0(1)	-0.36(2)
233 K	125.5(1)	32.5(1)	-0.05(1)
213 K	125.0(1)	41.5(1)	0.23(2)
193 K	125.0(1)	55.0(1)	0.38(1)
173 K	125.5(1)	72.0(1)	0.46(2)
153 K	125.5(1)	92.0(1)	0.52(1)
133 K	126.0(1)	116.0(1)	0.54(1)
123 K	126.0(1)	130.5(2)	0.55(1)

experimental temperature of 123 K, corresponding to Ω = 130.5(1) ppm. In LT experiments from 293 K to 123 K, the simulated ^{13}C CSA parameters indicate that CO_2 within α–zinc formate is more rigid and immobile with decreasing temperatures, as shown by the greater span (Ω) value. One small spectral "shoulder" is observed at the high-frequency end of the powder pattern between 293 K and 253 K. When the experimental temperature is gradually reduced, the small shoulder moves to the low-frequency end of the power pattern around 233 K to the higher-frequency limit of the powder pattern, at 123 K. This change in powder pattern lineshape corresponds to a large change in skew (κ) values, which measures the asymmetry of the CS tensor and influences the powder pattern lineshape. Furthermore, the larger span observed from ^{13}C spectra in LT experiments also suggests that the mobility of CO_2 guests is gradually reduced with decreasing temperature. The reduced mobility and molecular motions of CO_2 at LT experiments below 293 K down to 123 K results from a loss of thermal guest energy and a correspondingly stronger interaction with the adsorption sites, as observed in several other studies from our research group.[7, 23, 24] However, the second-broadest width of the VT powder patterns (Ω = 36.2(1) ppm) appears in the HT experiments at the temperature of 413 K. At higher temperatures, much of the adsorbed CO_2 guests have been released from the framework, forming a highly intense sharp resonance at 433 K. The powder pattern spans in elevated temperature experiments increase to greater values, rather than shrinking, from 313 K to 433 K. This phenomenon suggests the adsorbed CO_2 guest mobility is reduced and the movements may be restricted in HT experiments, implying that the adsorbed CO_2 guest molecules have stronger interactions with the α - zinc formate framework despite the increase in available guest thermal energy which typically competes against the adsorptive interaction. The increasing span observed in HT experiments between 293 K to 433 K suggests reduced mobility of adsorbed CO_2 guests, which is quite unexpected and may be due to structural changes in the framework; there could be a narrowing in pore size of the α - zinc formate structure or some other major structural change at high temperatures.

2.3.2 Detailed information regarding adsorbed CO_2 guest dynamic motions in α - zinc formate

The ^{13}C spectra of adsorbed CO_2 in α - zinc formate are shown in Figure 2-4, accompanied by corresponding simulated spectra and powder patterns. The powder patterns could only be simulated when a combination of two motions was applied: a C_3 three-fold rotation with an angle θ to describe the localized rotational wobbling motion of CO_2, along with a C_2 two-fold jumping of CO_2 through an angle γ to describe the non-localized hopping motion. Using only the individual C_3 or C_2 motions does not fit the experimental lineshapes, which suggests that both motions must be combined in the simulation. Based on simulation results, the C_3 three-fold wobbling motional angles ascend from 38.9(2)° at 123 K to 50.3(2)° at 293 K. However, the C_3 wobbling motion angle decreases from 50.3(2)° to 48.5(1)° as temperatures increase from 313 K to 433 K. This phenomenon may be due to some structural changes in α – zinc formate above 293 K, hinting at less free space for adsorbed CO_2. In comparison, the C_2 hopping angle rises from 19.3(1)° at 123 K all the way up to 48.9(1)° at 433 K.

The increase in observed span values from 293 K to 433 K suggests that the CO_2 molecules are less mobile at higher temperatures, but the mobility should logically increase at higher temperatures. This interesting phenomenon implies that the CO_2 molecular motion is restricted or limited within α - zinc formate at high temperatures. This could be explained by the relative narrow pore size (4×5 Å) of the zig-zag one-dimensional channels in α - zinc formate. This narrow pore may shrink at high temperatures, and the narrowed pore size would then restrict the thermal mobility of CO_2 guests, which have a kinetic diameter of 3.3 Å[25] which is just smaller than the pore size. On the other hand, the reduced mobility might also be triggered by some strengthening of the interaction between CO_2 and the α - zinc formate framework at higher temperatures, but this seems extremely unlikely.
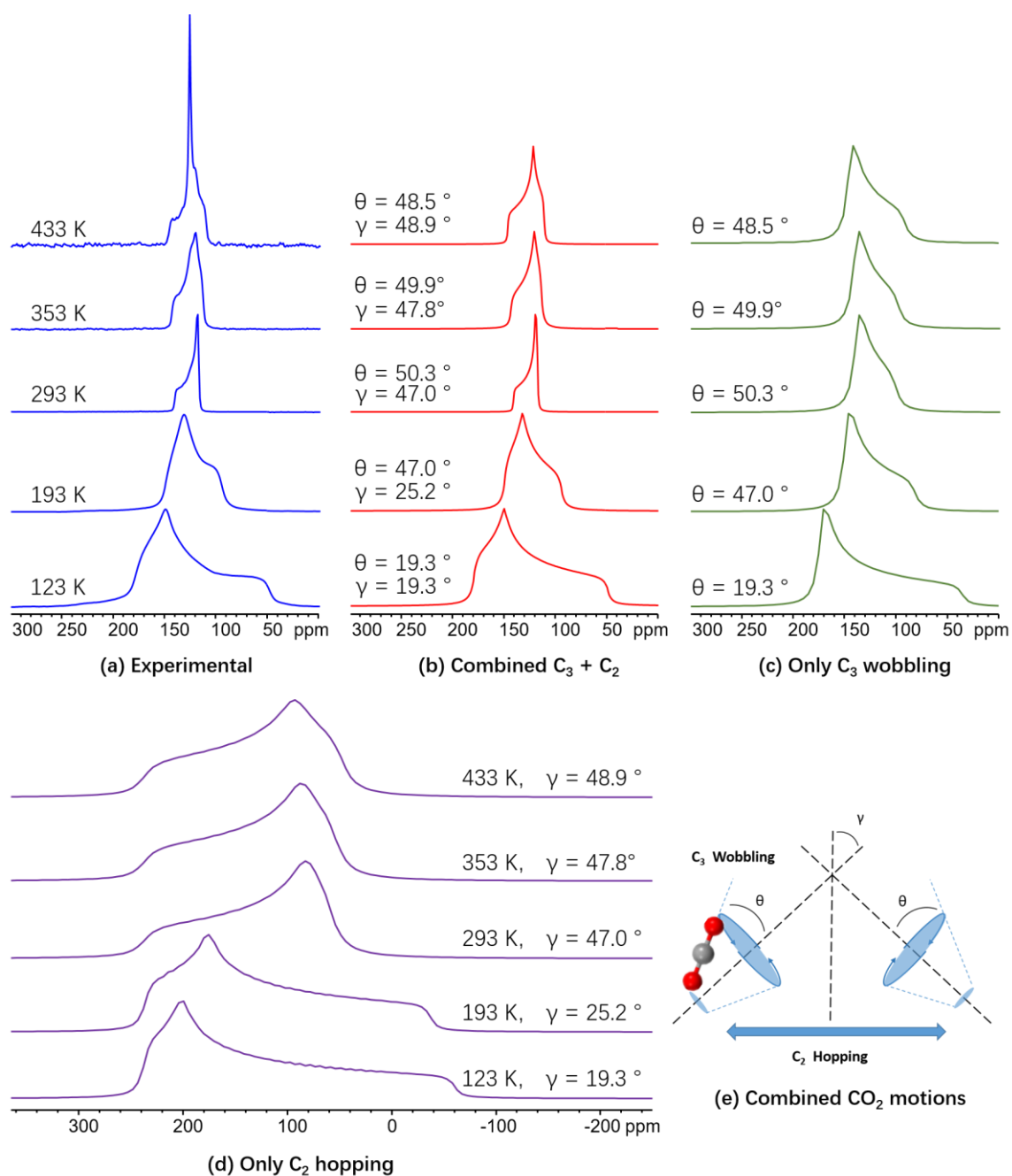
Figure 2-5. The figure shows (a) experimental ^{13}C spectra of CO_2 loaded α - Zn formate; (b) EXPRESS[20] motional simulations using the combined C_3 wobbling through the angle θ, and C_2 hopping motions through the angle γ , (c) simulations using only a C_3 localized wobbling motion and (d) simulations using only C_2 non-localized hopping of CO_2, and (e) an illustration of the combined CO_2 motional model.

This phenomenon of restricted adsorbed guest motion in SSNMR experiments of MOFs has only been observed from CO_2 guest loaded MOF samples in α – zinc formate within this study, and previously reported studies on the structurally similar α – magnesium formate,[24] and can be explained by a structural change induced by CO_2 molecules at elevated temperatures. The pore size of the formate MOF family may be reduced at high temperatures, and the narrowed porous structure limits the dynamic motion of guest CO_2 molecules. In contrast with the CO_2 guest behaviours observed in α – magnesium formate in which the ^{13}C span broadened at and above 333 K, the span of ^{13}C spectra in α – zinc formate increases above 293 K. The lower onset temperature of this span change could be due to the fact that the pore size in α – zinc formate is smaller than that of α – magnesium formate. Within the same temperature range in CO and C_2D_4 loaded α - zinc formate samples, no similar change in NMR parameters was observed, which means the structural change must be associated with the interactions between CO_2 molecules and the framework. Other potential members of the metal - formate MOF family beyond Mg and Zn may share this interesting CO_2-linked structural property in common.[24]

After testing CO_2 loaded α – zinc formate MOF samples using ^{13}C SSNMR spectroscopy at the highest temperature of 433K for about 2 hours, the sample was then cooled down to room temperature and yielded an identical ^{13}C SSNMR lineshape versus the one obtained before the HT experiments (shown in Figure 2-6). However, the resonance belonging to free CO_2 is of greater intensity than before the HT experiments, indicating that some CO_2 guests have been released or desorbed from the framework. This may be evidence of some structural change or damage. Viertelhaus has reported that after being heated up to 443 K, α – zinc formate transfers to the β phase at 1 atm.[5] PXRD tests on post-heating α – zinc formate samples with CO_2 guest loading (Figure S2-1) suggests that the α –phase framework structure has partially changed into the β – phase after the HT SSNMR experiments at 433 K, and the new phase of this framework forces

guest molecules to undergo under different dynamic motions. In this case, the pXRD powder pattern suggests that an intermediate phase in between α and β phases, or a mixture of the two phases exists, which preserves some pore structures and retains CO_2 guests in its intact and collapsed channels. This certainly influences CO_2 mobility and helps explain the unusual CO_2 motional trends observed within this MOF.
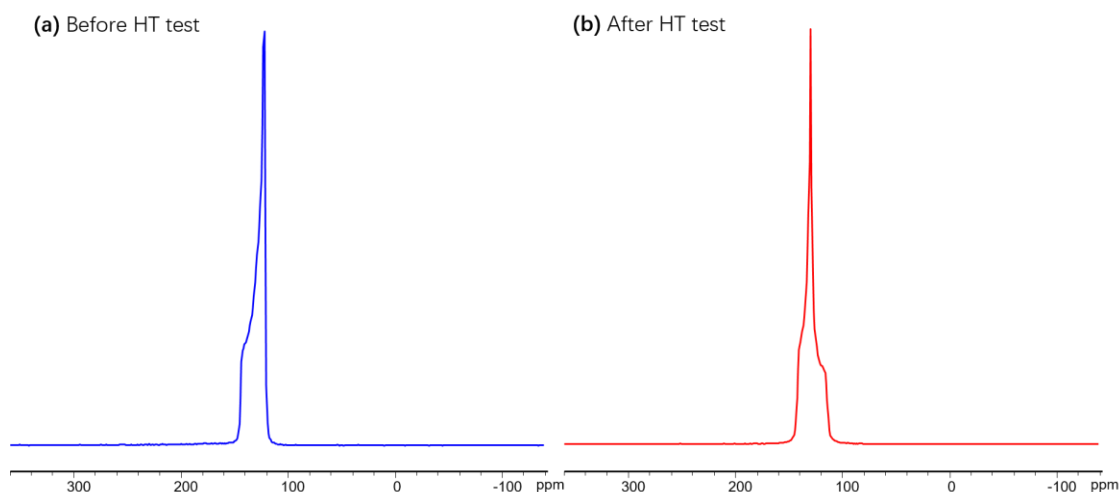
Figure 2-6. The differences in ^{13}C spectral lineshapes of adsorbed CO_2 (a) before and (b) after the HT SSNMR experiments. The remarkable change in lineshapes suggest that adsorbed CO_2 in α – zinc formate is undergoing different dynamic motions after HT experiments due to a partial phase change of the MOF structure. The portion of free CO_2 in (b) is greater than that in (a) before HT experiments.

2.3.3 ^1H-^{13}C CP experiments of adsorbed CO_2 guests in α - zinc formate

^1H-^{13}C CP NMR experiments are sensitive to distance-dependent ^1H-^{13}C dipolar interactions and the dynamic mobility of the ^1H and ^{13}C nuclei. As a result, not all ^{13}C nuclei will be detected in a CP experiment. Only those ^{13}C nuclei that are involved in strong ^1H-^{13}C dipolar coupling interactions and close to ^1H nuclei will yield observable signals in ^1H-^{13}C CP spectra.

^{1}H-^{13}C CP NMR experiments employ abundant and NMR favorable ^{1}H nuclei to transfer magnetization to unfavorable ^{13}C nuclei in order to achieve faster acquisition and higher signal-to-noise ratios by using the dipolar coupling interaction and satisfying the Hartmann-Hahn condition.[26] A spin lock pulse is first applied on the ^{1}H channel during a period of time known as the mixing time or contact time. Meanwhile another mixing pulse is applied on the ^{13}C channel at the same time so that spin magnetization is transferred from ^{1}H to ^{13}C nuclei. After the contact time, the spin lock pulse is turned off and the free induction decay (FID) of ^{13}C nuclei is collected. The contact time duration of ^{1}H-^{13}C CP experiments determines which ^{13}C nuclei are observable, acting as a convenient filter which selects ^{13}C atom species that have certain internuclear distance to ^{1}H atoms. Shorter contact times favour ^{13}C nuclei which are very close or directly bound to ^{1}H atoms of the formate linkers within the MOF framework. These resonances are normally due to the linker ^{13}C nuclei and not guests, especially when no isotopically-labelled ^{13}CO$_2$ is present, resulting in a background lineshape. In contrast, longer contact times extend the spatial range in which ^{13}C nuclei proximate to ^{1}H may be detected. For instance, detection of the framework-based ^{13}C resonances from formate linkers are favored when short contact times (e.g. 0.5 ms) are used during ^{1}H-^{13}C CP experiments, while ^{13}C nuclei of more distant CO$_2$ guests can be observed when using a longer contact time of 10 ms. Thus, in this study, ^{1}H-^{13}C CP experiments were performed at 293 K and 173 K respectively, using various contact times ranging from 0.5 to 10 ms. By comparing the differences in experimental CP powder patterns, the adsorption locations of CO$_2$ guest molecules within α-zinc formate can be investigated.

In Figure 2-7, the ^{13}C spectral lineshapes of the formate organic linkers in α - zinc formate are represented by red lines at the bottom of the figure. The spectra were acquired from activated empty α - zinc formate MOF samples at 293 K and 173 K respectively, using a short contact time of 0.5 ms. The CSA powder pattern originates from the formate carbon atoms in the framework, featuring an intense powder pattern centred at 180 ppm

62
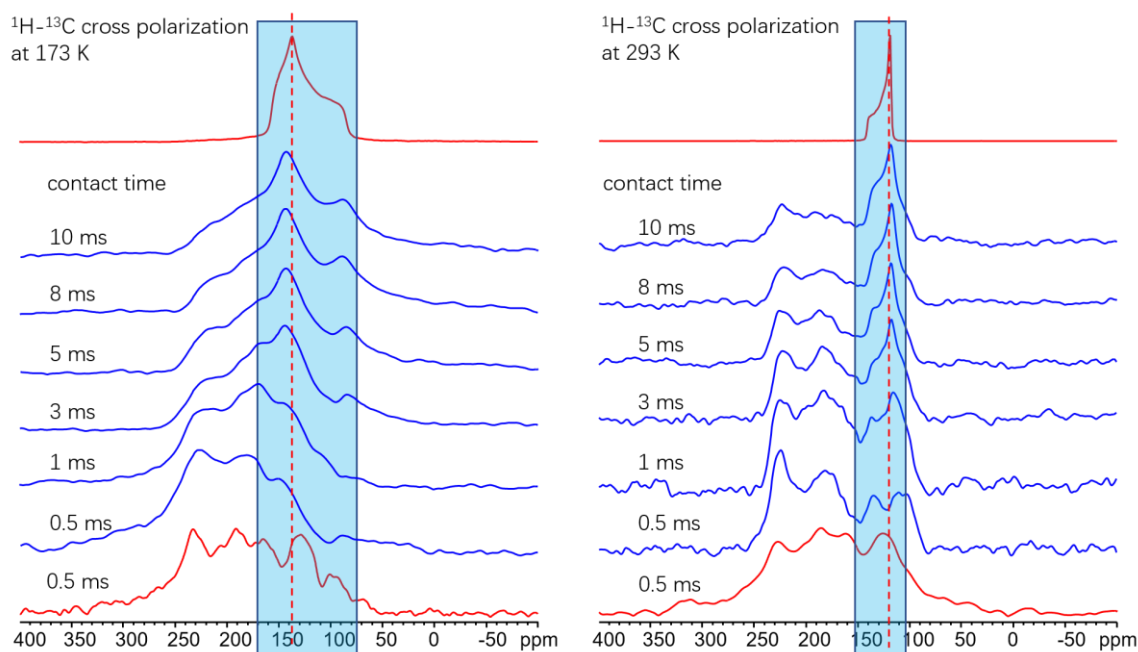
Figure 2-7. The figure shows experimental static ^1H – ^{13}C cross polarization SSNMR spectra of CO_2 loaded MOF samples at 173 K and 293 K. The spectra acquired using different contact times from 0.5 ms to 10 ms on guest loaded MOF samples are stacked in blue. The red line trace at top of each stack of spectra is the direct-excitation ^{13}C SSNMR spectrum obtained at the indicated temperature. The vertical red dashed line in each stack of spectra represents the chemical shift position of the adsorbed $^{13}CO_2$ "spectral horn" obtained from direct-excitation ^{13}C SSNMR spectra, shown at top in red.

with several overlapping broad resonances located from 130 to 230 ppm, as shown at the bottom.

For the CO_2 loaded α - zinc formate MOF sample, the ^1H – ^{13}C CP spectra acquired at 293 K and 173 K with the shortest contact time of 0.5 ms exhibit similar lineshapes as those of the empty MOF sample. No obvious resonances contributed by CO_2 guests were detected at this contact time due to the relatively long distance between the carbon atoms from CO_2 guests and the H atoms from formate linkers, along with reduced dipolar coupling interactions from the dynamic motion of CO_2 guests. When the contact times are

extended from 0.5 ms to 10 ms, one additional ^{13}C feature at about 120 ppm and 160 ppm is apparent in CP spectra acquired at 293 K and 173 K, respectively. The resonance gradually gains intensity with extended contact times, and assumes asymmetric lineshapes similar to that of observed direct-excitation ^{13}C SSNMR spectra of CO_2 loaded α - zinc formate sample (Figure 2-7, top). At high contact times, the lineshapes of the additional resonance at 293 K and 173 K become very similar to the lineshapes originating from CO_2 guests, suggesting that the most efficient CP contact time to CO_2 guests is 10 ms, and the H atoms from the framework-based formate linkers and the C atoms from CO_2 molecules are indeed somewhat proximate and involved in dipolar coupling interactions. Similar to a previous study on CO_2-loaded α - magnesium formate,[24] a longer optimal contact time in CP experiments equates to a relatively long distance between adsorbed CO_2 guests and ^{1}H in the formate linker, indicating that the dipolar coupling interactions are present but relatively weak. The dipolar coupling may be weakened by the dynamic motions of guest molecules. These ^{1}H – ^{13}C CP spectra prove that the adsorbed CO_2 molecules in α-zinc formate are interacting with the H atoms of framework-based formate linkers, which likely act as the CO_2 adsorption sites throughout all experimental temperatures.

2.3.4 CO_2 loaded α - zinc formate single crystal structure determination and refinement

For a better understanding of the location of adsorbed CO_2 molecules in α - zinc formate, SCXRD experiments at 120 K were performed. The CO_2 guest molecules were found to align along the zig-zag, one-dimensional channel parallel to crystallographic b axis, as shown in Figure 2-8a. From a view perpendicular to the *b* axis, the CO_2 guests reside close to the interior of the channel (Figure 2-8b). Each CO_2 guest in the channel interior is crystallographically equivalent, in agreement with the single ^{13}C powder pattern observed in SSNMR experiments. CO_2 can migrate to nearby adjacent adsorption sites through the C_2 hopping motion. The distance between two carbon atoms from two
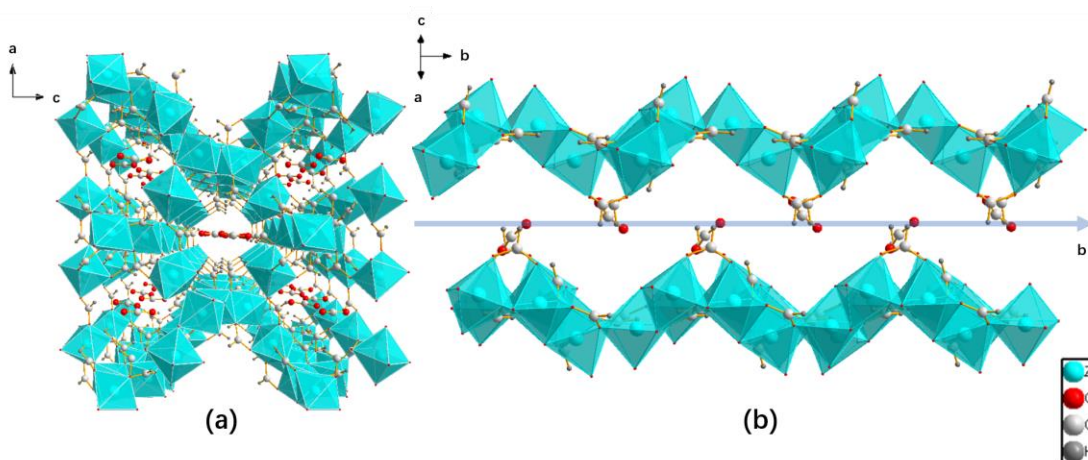
Figure 2-8 Figures show the CO_2 saturated α – zinc formate MOF crystal structure acquired at 120 K from single crystal XRD. Figure 2-8(a) is looking down along crystallographic b axis, while in (b), the view is perpendicular to the b axis. CO_2 guests are aligned along the channel as shown in (a), and are adsorbed very close to the channel inner surface as shown in (b).

adjacent CO_2 molecules is measured as 5.12 Å, which is close enough to permit the hopping motion.[7-8, 23-24, 27]

Figure 2-9 shows the local structure of CO_2 saturated α - zinc formate at 120 K. At this temperature, only one unique CO_2 guest molecule (O1X-C1X-O2X) is present in the 1-dimensional channel, and one of the oxygen atoms (O2X) in Figure 2-9b is close to the three hydrogen atoms from formate linkers that point directly into the channel, with a closest distance of 2.91 Å. This distance is close to the 3.2 Å indicated in α - magnesium formate based on molecular dynamics computational calculations.[24] Meanwhile, in a typical C-H⋯O hydrogen bond, the H⋯O distance ranges from 2.28 to 2.59 Å.[28] The CO_2 molecule is either forming weak hydrogen bonding interactions with the closest hydrogen atom H6 from the formate linker, or is engaging in some weak electrostatic interactions with H6.[28] The adsorbed CO_2 molecule is also undergoing weak hydrogen-bonding or electrostatic interactions with two other hydrogen atoms, H1 and H5. The CO_2 molecule

is not oriented parallel to the 1-dimensional channel, but is slightly bent down toward the inner side of the channel (Figure 2-9b).

The HT single crystal X-ray diffraction experiments at 353 K could not be performed because of the failure of the Paratone-N coating of single crystals. The coating was visibly cracked on the crystal surface, leading to the escape of CO_2 guests, despite many trials being attempted. Thus, HT single crystal XRD experiments could not be carried out and are a target for future studies.
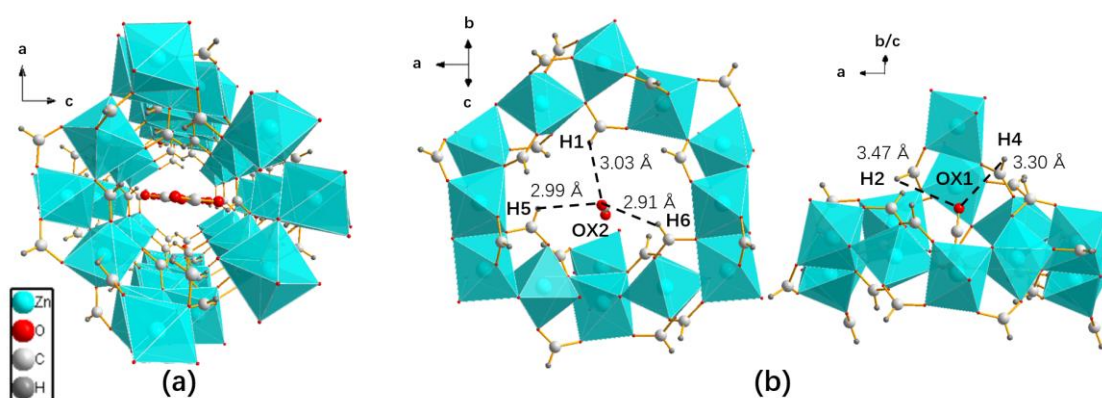
Figure 2-9 The local crystal structure of the CO_2 saturated α – zinc formate MOF is shown. In (a), the relative narrow pore size forces CO_2 guests to align along the one-dimensional zig-zag channel; (b) shows the distances of five nearest hydrogen atoms H6, H5, H1, H4 and H2 that may engage in H-bonds or electrostatic interactions with the CO_2 guest, making the distance from channel to OX2 slightly further than to OX1.

The single crystallographically unique CO_2 adsorption in α - zinc formate observed from LT SCXRD refinement is in good agreement with the results obtained from static direct-excitation ^{13}C and ^1H-^{13}C CP SSNMR spectra, which indicate that only one adsorption site for adsorbed CO_2 guests is present. The crystallographic position of CO_2 obtained from SCXRD suggests that the adsorption (and wobbling) site for CO_2 molecules is on one of the hydrogen atoms from formate linkers which sticks toward the interior of the zig-zag channel, while the C_2 hopping motion represents the migration of CO_2 molecules between two adjacent framework protons and between two equivalent CO_2 adsorption sites along the one-dimensional zig-zag channel.

2.3.5 VT ^{13}C NMR experiments of CO loaded α - zinc formate

In the temperature range from 433 K to 123 K, the ^{13}C spectra of CO loaded α–zinc formate indicates a significant adsorption interaction between CO and the α - zinc formate MOF framework. The broadening of ^{13}C powder patterns as temperature decreases from 433 K to 123 K indicates that the dynamic motions of adsorbed CO are being reduced with temperature (Figure 2-10). Due to the relatively poorer adsorption capability of CO within the α - zinc formate MOF, the loading level used in LT tests (293 K and below) was 0.1 CO / Zn to obtain accurate lineshapes, while a lower loading level of 0.075 CO / Zn was used to minimize the intensity of free CO in the HT tests (above 293 K).

The strong and sharp 185 ppm resonance observed in Figure 2-10a from 433 K to 193 K corresponds to free CO undergoing isotropic rapid tumbling. This observation is in good agreement with our previous results of free CO chemical shifts[8] and is close to the reported ^{13}C δ_{iso} at 182 ppm for CO.[21] A broad powder pattern with a defined lineshape due to CSA is also observed, indicating that some CO is adsorbed in the framework and undergoes restricted motion. The presence of one broadened powder pattern suggests that all of the adsorbed CO molecules sit in an identical chemical environment; there is one crystallographically unique CO adsorption site.

Experimental ^{13}C SSNMR spectra were simulated and analyzed to obtain ^{13}C NMR parameters for dynamic analysis. Figure 2-10b shows that the ^{13}C SSNMR spectrum of the CO loaded α - zinc formate MOF at 293 K consists of one sharp resonance and one broad powder pattern, and the detailed (a) experimental, and (b, c) simulated ^{13}C SSNMR powder patterns are shown in Figure 2-11, respectively. The observed NMR parameters of δ_{iso}, span (Ω), and skew (κ) obtained from simulations of ^{13}C SSNMR spectra are shown in Table 2-2**.**
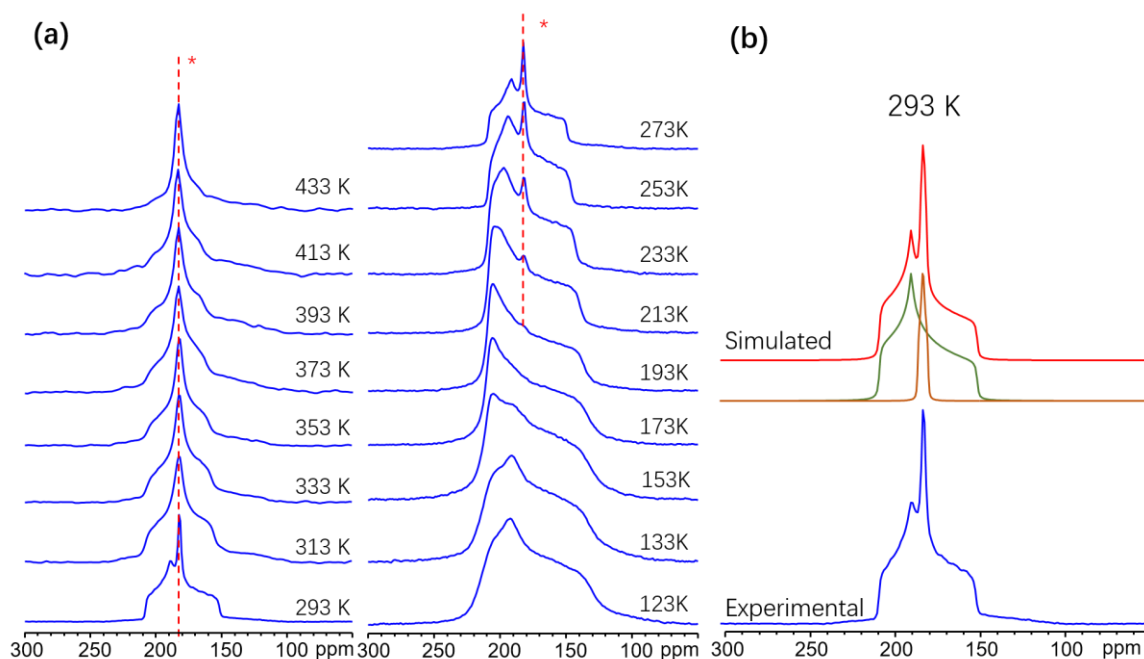
Figure 2-10. In (a), the experimental ^{13}C SSNMR spectra of adsorbed CO in α – zinc formate within the temperature range from 123 K to 433 K are shown. The red dashed line with (*) denotes the resonance contributed by mobile isotropically tumbling CO . The resonance representing free CO guests starts appearing at and above 193 K, suggesting the CO guests are partially desorbed from framework at these temperatures. An analysis of the powder pattern lineshape in (b) suggests the spectra consist of a broad adsorbed CO powder pattern along with a sharp resonance contributed by free CO.

Based on experimental and simulated results, the powder pattern exhibits its broadest width at the lowest experimental temperature of 123 K (Ω = 87.7 ppm). Compared to the span value of rigid CO obtained from prior SSNMR experiments (Ω = 353 ppm) at 20 K,[21] guest CO molecules adsorbed in α - zinc formate must be undergoing certain dynamic motions to reduce the span and modify the shape of the observed ^{13}C powder patterns. The observed span as the temperature decreases from 433 K to 123 K (Table 2-2) is temperature-dependent, which suggests that the adsorbed CO molecules undergo restricted motions and interact with the α - zinc formate framework. The simulated ^{13}C CS parameters indicate that adsorbed CO within α–zinc formate is less dynamic at lower temperatures, as shown by the greater span value. The reduced mobility of CO at low

temperatures may result from stronger interactions with the adsorption sites due to a drop in thermal energy. Additionally, the resonance representing free CO can only be observed at 193 K and above. The less intense powder pattern contributed by adsorbed CO also indicates the poor adsorption capability of CO at high temperatures, due to the escape of CO guests from the framework.

It is worth noting that an additional resonance (shown in Figure 2-11b) was employed for the simulations of the ^{13}C SSNMR experimental spectra of CO guests at and above 313 K. This resonance is believed to be the background ^{13}C resonance from formate linkers and is not due to adsorbed CO or free CO. A room-temperature ^{13}C SSNMR experiment was conducted on an activated empty α - zinc formate sample (Figure 2-12). The results reveal that the ^{13}C atoms from formate linkers may contribute a broad resonance centred at 100 ppm as a background signal when the intensity of the ^{13}CO powder patterns are relatively weak.
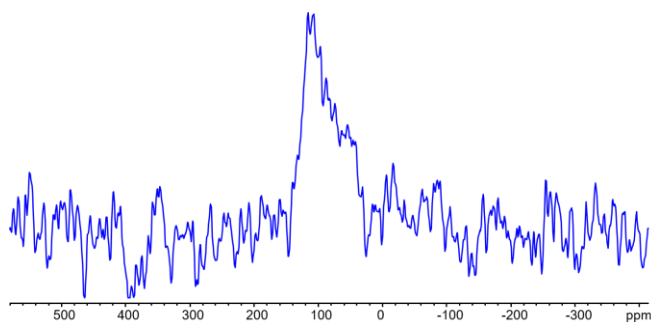
Figure 2-11. The ^{13}C SSNMR background resonance acquired from the activated empty α - zinc formate sample. A weak but broad resonance centred at 100 ppm is observed, originating from the ^{13}C atoms of the framework formate linkers.
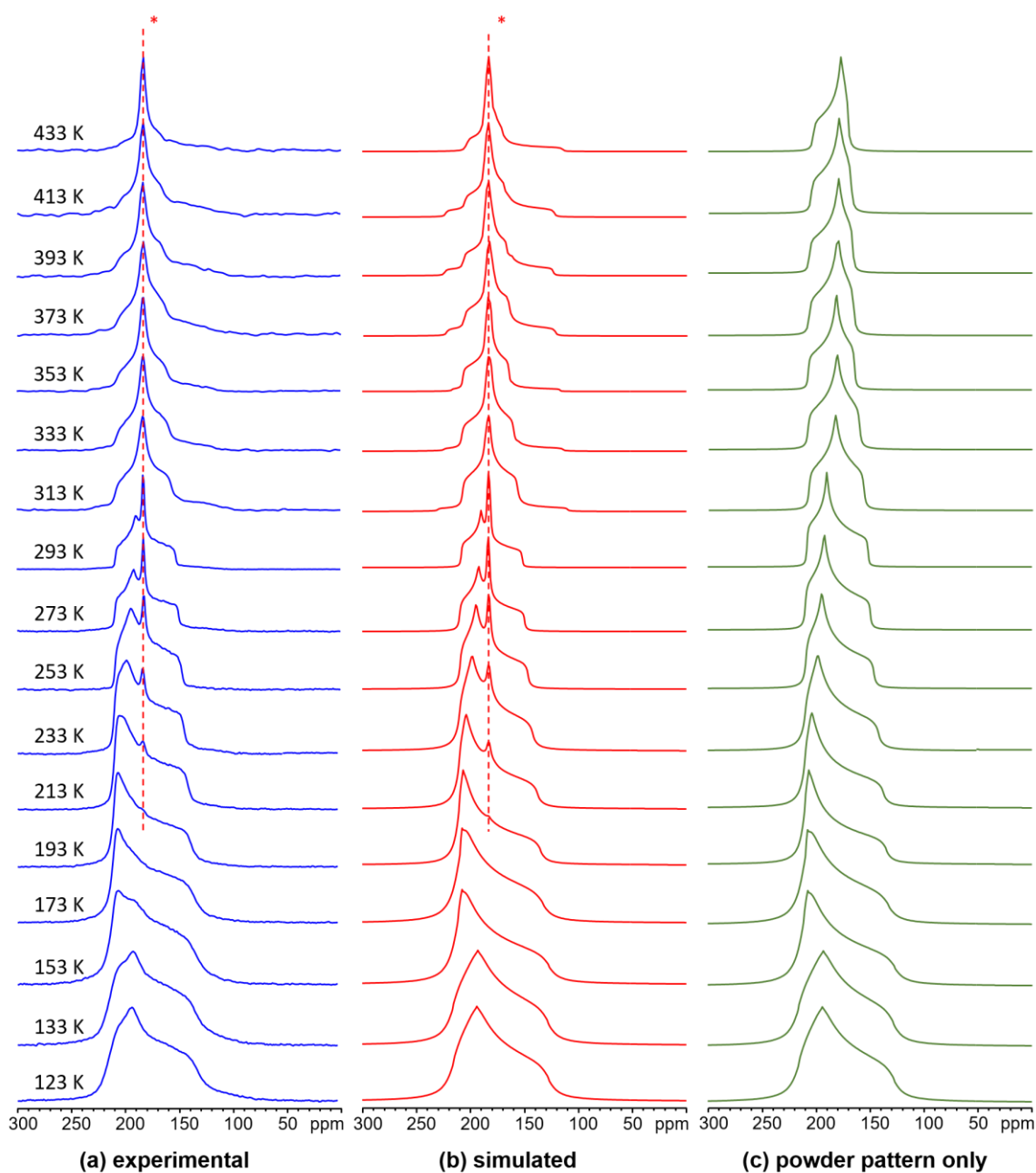
Figure 2-12. The spectra in (a) and (b) are the experimental and analytically simulated ^{13}C SSNMR spectra of adsorbed CO in α – zinc formate respectively, from 123 K to 433 K. The sharp resonance generated by free CO is present in the temperature range from 193 K and above. The spectra in (c) are the simulated powder patterns of adsorbed CO in α – zinc formate without accounting for the free CO resonance.

Table 2-2 The observed ^{13}C NMR parameters of adsorbed CO guests in α – zinc formate.

Temperature (K)	δ_{iso} (ppm)	Span (Ω, ppm)	Skew (κ)
433 K	183.0(1)	32.0(3)	-0.60(1)
413 K	184.0(1)	37.0(2)	-0.40(1)
393 K	184.0(1)	40.0(2)	-0.35(1)
373 K	184.0(1)	42.0(1)	-0.30(1)
353 K	184.0(1)	43.0(1)	-0.21(1)
333 K	183.0(1)	48.0(1)	-0.13(1)
313 K	182.0(1)	51.0.(1)	0.03(1)
293 K	183.5(1)	56.2(1)	0.35(2)
273 K	184.0(1)	60.0(1)	0.42(1)
253 K	183.5(1)	62.7(1)	0.53(1)
233 K	183.5(1)	67.6(1)	0.66(1)
213 K	184.0(1)	72.3(1)	0.83(1)
193 K	184.0(1)	75.1(1)	0.91(1)
173 K	183.1(1)	76.3(1)	0.96(1)
153 K	182.0.(1)	83.5(1)	0.93(1)
133 K	179.0(2)	87.7(1)	0.48(2)
123 K	179.0(2)	87.7(1)	0.51(2)

2.3.6 Detailed information regarding adsorbed CO guest dynamic motions in α - zinc formate

The ^{13}C spectra reveal that adsorbed CO guests are undergoing well-defined motions similar to those of adsorbed CO_2, consisting of combined C_3 localized wobbling and C_2 non-localized hopping motions. As shown in Figure 2-13, both the C_3 and C_2 motions must be employed for an accurate simulation, rather than just the individual C_3 or C_2 motions. The C_3 wobbling angle decreases from 49.7(2)° at 433 K to 43.1(1)° at 123 K, indicating that stronger H-bonding or electrostatic interactions exist between adsorbed CO guests and framework-based H atoms from formate linkers at low temperatures.

However the C_2 hopping angle exhibits an opposite trend, increasing from $51.0(2)°$ to $64.5(1)°$ within the same temperature range.
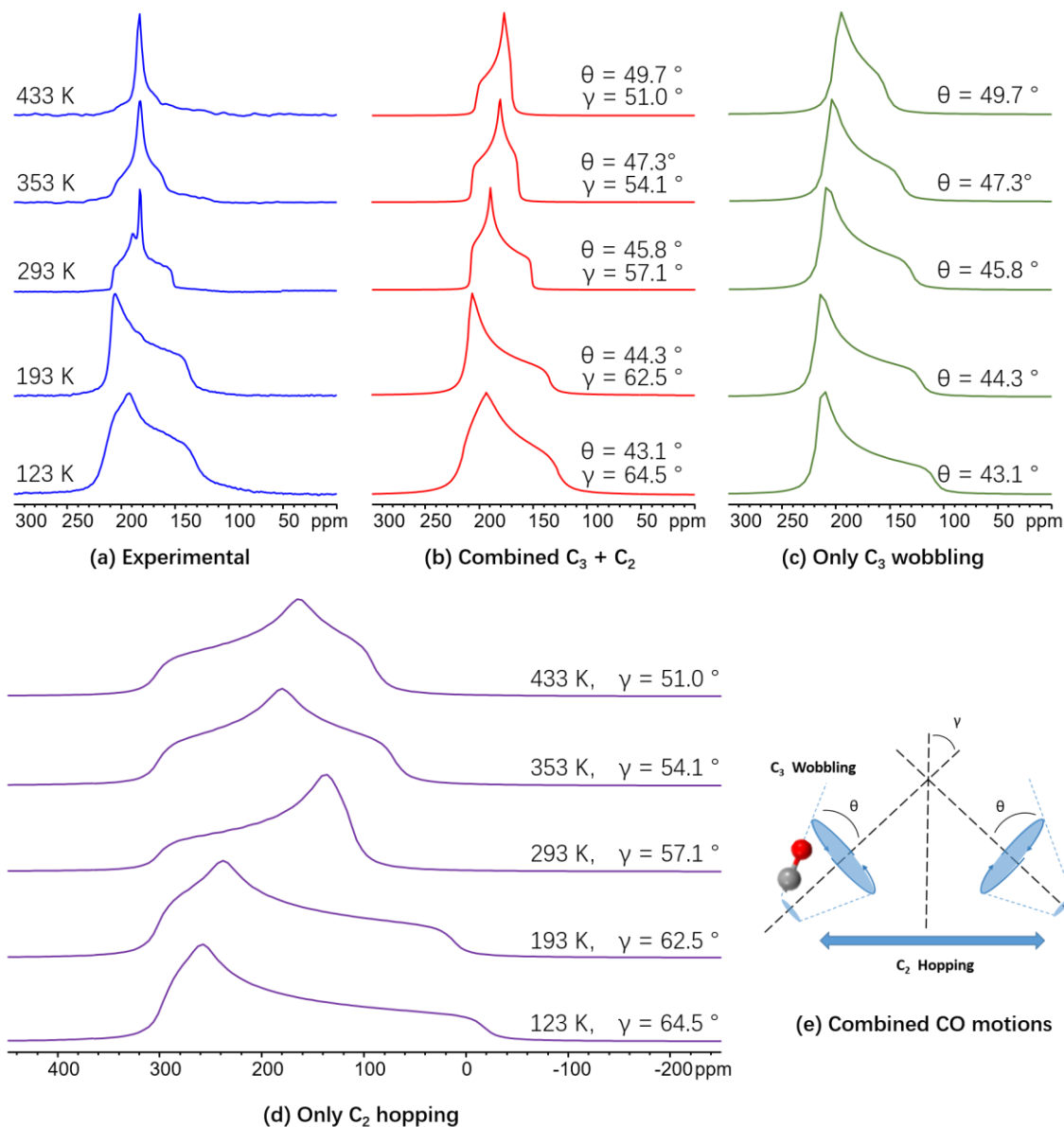
Figure 14. This figure shows (a) the experimental ^{13}C SSNMR spectra of CO loaded α - Zn formate; (b) EXPRESS[20] motional simulations of CO using the combined C_3 and C_2 motions through the angles θ and γ respectively, (c) only C_3 localized wobbling motion and (d) only C_2 non-localized hopping of CO, and (e) an illustration of the combined CO motions.
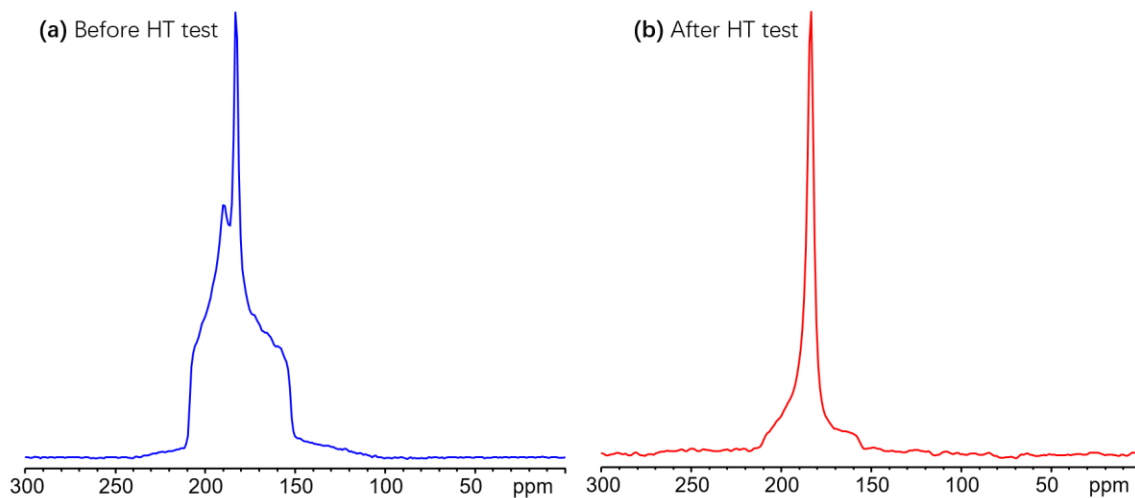
Figure 15. This figure illustrates the differences in ^{13}C spectral lineshapes of adsorbed CO in Zn-formate before (a) and after (b) the HT SSNMR experiments. Adsorbed CO yields a similar broad lineshape before and after the HT experiments with some narrowing of the span after HT experiments, while there is a large intensity increase for free mobile CO after HT testing

    After keeping the CO-loaded α - zinc formate MOF sample at the highest temperature of 433K for about 2 hours, the sample was then gradually cooled down to room temperature and yielded different NMR lineshapes compared to prior to HT experiments (shown in Figure 2-14). The main difference between these two powder patterns is that the free CO resonance increases in intensity, indicating that CO guests have somehow escaped from the α - zinc formate framework. The observed span of the broader powder pattern also narrows after the sample was heated at 433 K. For a better investigation of this phenomenon, pXRD experiments (Figure S2-1) were performed and suggested that the framework has partially transformed into the β - phase of Zn-formate after the HT experiments at 433 K. The non-porous β - phase of zinc formate framework has slightly different dimensions and forces CO guest molecules to undergo distinct dynamic motions.
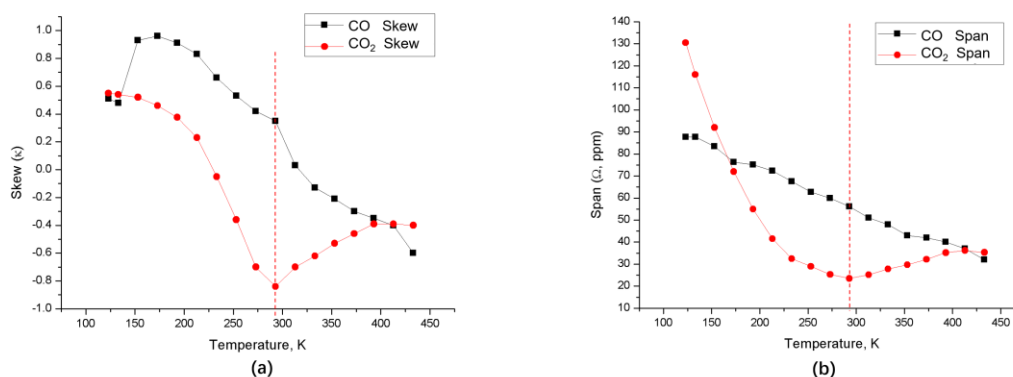
Figure 165. The figures compare the temperature-dependent trends in skew (a) and span (b) of adsorbed CO_2 and CO in Zn-formate. Adsorbed CO_2 has a valley-shape trend in both skew and span, reaching its minimum value at 293 K, while adsorbed CO demonstrates a generally linear trend in skew and span, with only a couple outliers. The different NMR parameter trends suggest the structural change in Zn-formate may only be induced by adsorbed CO_2 around 293 K, while adsorbed CO does not influence the Zn-formate structure at any temperature.

When examining the trend of span values obtained from CO_2 and CO experimental spectra from 123 K to 433 K (Figure 2-15), it can be seen that CO_2 guests show a valley-like shape in span trend while the span of CO spectra is generally linear. The span of adsorbed CO_2 guests reaches its lowest value at 293 K. At higher temperatures, some structural change or phase transition of the α - zinc formate framework has occurred, and after this, as temperatures rise, the span is broadened. For adsorbed CO guests, the ^{13}C span is consistently decreasing as temperatures rise from 123 K to 433 K, suggesting that increased molecular mobility and greater wobbling motional angles exist at HT.

2.3.7 ¹H-¹³C CP SSNMR experiments of adsorbed CO guests in α - zinc formate

^{1}H - ^{13}C CP SSNMR spectra of CO-loaded Zn-formate are shown in Figure 2-16. The background ^{13}C lineshapes, stacked at the bottom and represented by red lines, were acquired from an activated empty α - zinc formate MOF sample at 293 K and 173 K respectively, with the strongest signal evident at a short contact time of 0.5 ms. The background ^{13}C CSA powder pattern arises from the formate carbon atoms in the framework, and consists of an intense powder pattern centred at ca. 160 ppm with several overlapping broad resonances located from ca. 130 ppm to 220 ppm.
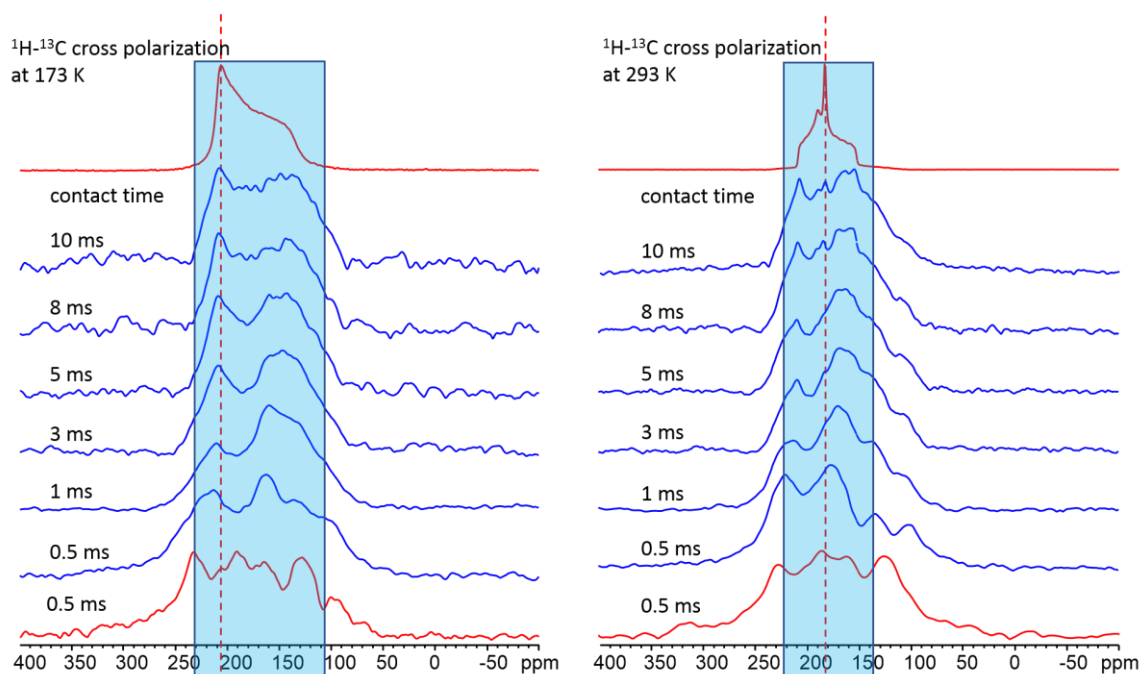
Figure 2-16. The figure shows experimental static ^{1}H – ^{13}C cross polarization SSNMR spectra of the CO loaded MOF sample at 173 K and 293 K. The spectra acquired of guest-loaded MOFs using different contact times from 0.5 ms to 10 ms are stacked in blue, while the red spectra at the bottom are the background signals of the empty MOF. The red line trace at the top of each stack of spectra represents the direct-excitation ^{13}C SSNMR spectra of CO in the MOF obtained at the indicated temperature, for the purposes of comparison with the ^{1}H-^{13}C CP SSNMR spectra.

For the CO loaded α - zinc formate MOF sample, the ^{1}H – ^{13}C CP spectra acquired at 293 K and 173 K at the shortest contact time of 0.5 ms exhibit different lineshapes from those of the empty MOF sample (Figure 2-16, blue traces). No obvious resonances contributed by CO guests were detected at this short contact time due to the relative long distance between the carbon atoms from CO guests and the H atoms from formate linkers, along with the poor CO adsorption capability of the α - zinc formate MOF and the dynamic motion of CO guests which reduce the effective ^{1}H-^{13}C dipolar coupling interactions. As contact times are extended in CP experiments, additional ^{13}C resonances located at 180 ppm of 293 K spectra, and at 210 ppm of 173 K spectra slowly gain intensity, but only form asymmetric powder patterns of poor signal/noise ratios versus the background signal. The ^{13}C resonances contributed by CO guests in CP spectra are relatively weak compared to the framework-based ^{13}C spectral lineshapes, yielding low-intensity resonances versus the framework background signal. Eventually, the lineshapes of the additional resonance at 293 K and 173 K becomes similar to the lineshapes of the CO guest resonances originating from direct-excitation ^{13}C SSNMR experiments (Figure 2-16, top red traces). This indicates that ^{1}H-^{13}C CP experiments are most efficient at a contact time of 10 ms. The increased contact time in CP experiments boosts the CP efficiency across longer distance between ^{13}C and ^{1}H nuclei involved in the dipolar coupling, indicating that the coupled ^{13}C nuclei in CO guests are relatively far from framework-based ^{1}H atoms in distance. The lower CP spectral intensity compared to that of CO_2 guests suggests the CO guests are positioned further from framework ^{1}H atoms and/or are much more mobile than CO_2 guests.

Despite the poor signal/noise ratios of the experimental spectra mentioned above, these ^{1}H – ^{13}C CP spectra of CO loaded α - zinc formate with various contact times still prove that the adsorbed CO molecules in α-zinc formate interact with the H atoms from formate linkers, thus, the H atoms likely act as the CO adsorption sites.

2.3.8 VT ^{2}H SSNMR experiments of C_2D_4 loaded α - zinc formate
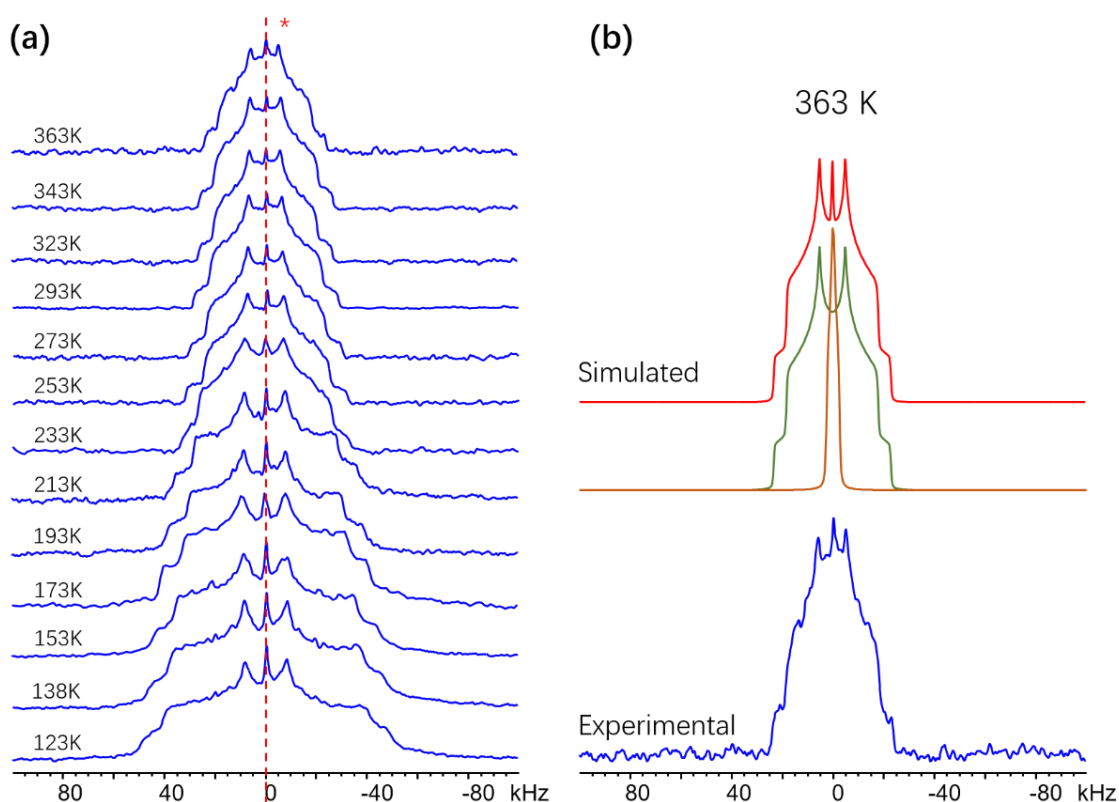
Figure 17 In (a), the experimental ^{2}H spectra of C_2D_4 adsorbed in α – zinc formate within the temperature range from 123 K to 433 K are illustrated. The red dashed line with (*) denotes the resonance contributed by free C_2D_4 from fast isotropic tumbling, which can be observed within the whole temperature range. An analysis of the lineshape in (b) confirms that the experimental spectra consists of an adsorbed C_2D_4 powder pattern with a sharp resonance contributed by free C_2D_4.

Within the temperatures range from 363 K to 123 K, the ^{2}H SSNMR spectra of adsorbed C_2D_4 within α–zinc formate feature QI-dominated powder patterns. The C_2D_4 molecules are also likely associated with certain dynamic motions. The broadening and temperature-dependent powder patterns within the experimental temperature range, from the highest temperature of 363 K to the lowest of 123 K, indicates that C_2D_4 becomes less mobile as temperature decreases, as shown in Figure 2-17. An additional sharp ^{2}H resonance at 0 kHz that is associated with gaseous mobile C_2D_4 was observed at all

temperatures. Due to an exceptionally poor signal/noise ratio of static ^{2}H experiments at HT, the experiments at higher temperature above 363 K was not conducted.

In Figure 2-17a, the sharp resonance at 0 kHz is due to the highly mobile C_2D_4, and its rapid tumbling motion averages the QI broadening and generates a narrowed resonance. Meanwhile, the broad powder pattern resembling a symmetric Pake doublet[29] lineshape arises from C_2H_4, and suggests that the adsorbed C_2H_4 guest is not free, but undergoing specific dynamic motions. Thus, there are two types of C_2D_4 molecules in this MOF sample: ones undergoing rapid isotropic tumbling, and others that are adsorbed and undergoing well-defined motions. The single broadened powder pattern indicates that there is only one crystallographically unique type of adsorbed C_2D_4 molecules.
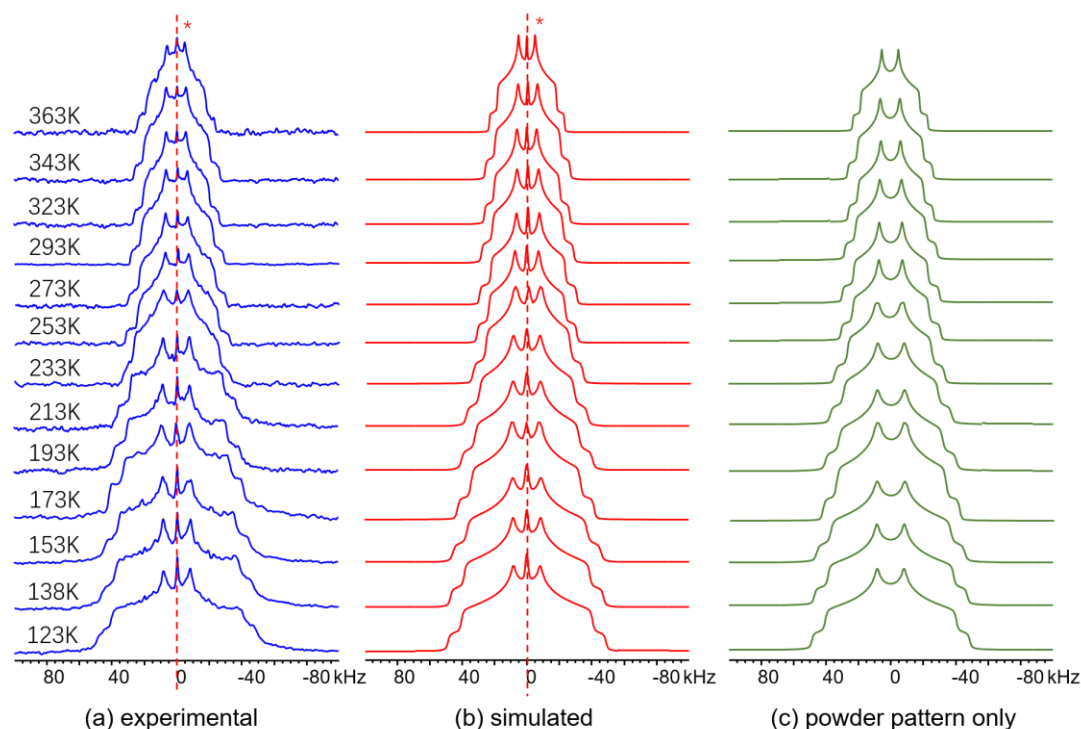
Figure 2-18. The figure shows the (a) experimental, and (b) analytically simulated ^{2}H SSNMR spectra of adsorbed C_2D_4 in α – zinc formate from 123 K to 363 K. The resonance originating from free C_2D_4 can be observed across the whole temperature range. The simulated spectra in (c) show the ^{2}H powder pattern contributed only by adsorbed C_2D_4 in α – zinc formate.

Table 2-3 The observed ^{2}H parameters of adsorbed C_2D_4 guests in α – zinc formate.

Temperature (K)	C_Q (kHz)	η_Q
363 K	31(1)	0.56(1)
343 K	32(1)	0.55(1)
323 K	35(1)	0.54(1)
293 K	38(1)	0.53(1)
273 K	40(1)	0.53(1)
253 K	41(1)	0.53(1)
233 K	45(1)	0.54(1)
213 K	50(1)	0.56(1)
193 K	54(1)	0.58(1)
173 K	56(1)	0.60(1)
153 K	61(1)	0.62(1)
138 K	63(2)	0.64(1)
123 K	65(2)	0.66(1)

Experimental ^{2}H SSNMR spectra were simulated and analyzed to obtain the ^{2}H QI parameters for dynamic studies of C_2D_4 adsorption behaviour in α - Zn-formate. Figure 2-17b shows the detailed simulation components of the powder pattern at 363 K, which is the highest experimental temperature. In Figure 2-18, spectral simulations are shown that indicate C_2D_4 guests are only adsorbed at one unique site. The observed C_Q and the η_Q parameters extracted from ^{2}H SSNMR experimental spectra are shown in Table 2-3. The reference C_Q and η_Q values were obtained from rigid C_2D_4 SSNMR experimental parameters (C_Q = 230 kHz, η_Q = 0),[30] and the simulated apparent powder patterns are in good agreement with experimental lineshapes.

Based on experimental and simulated results (Figure 2-18), the powder pattern exhibits its broadest width at the lowest experimental temperature of 123 K, corresponding to the ^{2}H NMR parameters of C_Q = 65 kHz and η_Q = 0.66. Compared to the

distinct NMR parameters for immobile C_2D_4 at 20 K (C_Q = 230 kHz, η_Q = 0),[30] the guest C_2D_4 molecules adsorbed in α - zinc formate must be undergoing certain motions to alter the observed NMR parameters, reduce C_Q values, and narrow the observed powder pattern width. The observed ^{2}H QI parameters indicate that adsorbed C_2D_4 guests within α–zinc formate are less mobile at lower temperatures, as shown by the greater C_Q values. The reduced mobility and molecular motion of C_2D_4 at low temperatures may result from stronger adsorptive interactions with the α–zinc formate MOF. However, the sharp resonance corresponding to free C_2D_4 still exists at the lowest experimental temperature at 123 K, suggesting the interaction between the α–zinc formate framework and C_2D_4 remains relatively weak.

2.3.9 Detailed information regarding adsorbed C_2D_4 guest dynamic motions in α - zinc formate

Within the whole temperature range of VT experiments, the observed C_Q and η_Q values exhibit different trends (Figure 2-20). C_Q values decrease steadily as the experimental temperature rises, from 65 kHz at 123 K to 31 kHz at the highest experimental temperature of 363 K. The observed η_Q value demonstrates a valley-shaped trend with temperature as shown in Figure 2-20: it decreases from 0.66 at 123 K to 0.53 at 253 K, followed by increases from 0.53 at 293 K to the maximum η_Q value of 0.56 at 363 K.

In the ^{2}H SSNMR spectra of adsorbed C_2D_4, the lineshape arises from the QI and resembles the shape of a symmetric Pake doublet. The simulation results for ^{2}H SSNMR spectra suggest that the Pake doublet lineshape is motionally averaged to some extent, due to combined wobbling and hopping motions. As shown in Figure 2-19, ^{2}H SSNMR spectral simulations using only individual C_3 wobbling or C_2 hopping motions cannot fit the experimental lineshapes, however, combining both motions in the simulation results in a good fit to experimental spectra. The C_3 wobbling angle of C_2D_4 increases gradually

from 36.5(1)° at 123 K to 47.0(1)° at 363 K, while the C_2 hopping angle undergoes an opposite trend, descending from 31.0° to 27.5° within the same temperature range.
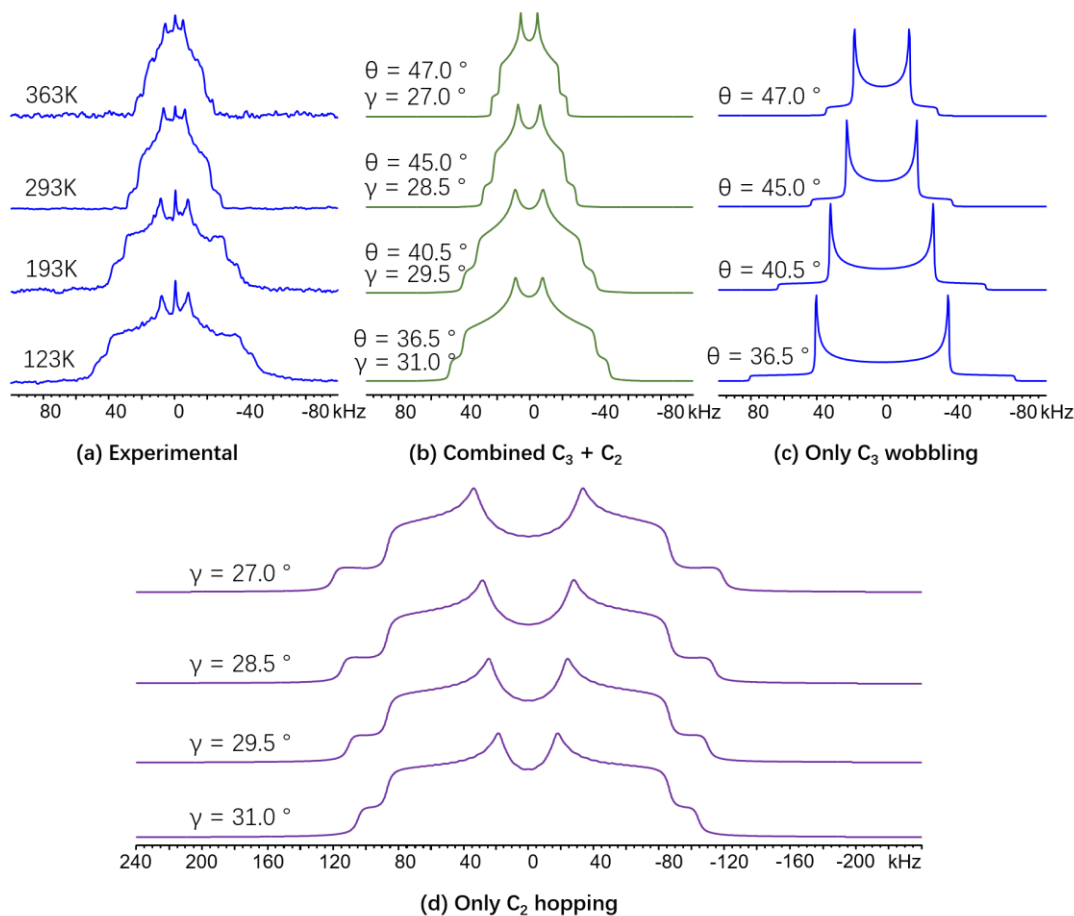
Figure 2-19. The figure shows (a) experimental static ^2H SSNMR spectra of C_2D_4 loaded α - Zn formate; and (b) EXPRESS[20] simulations of C_2D_4 motions using the combined C_3 wobbling and C_2 hopping motion, along with simulations incorporating (c) only C_3 localized wobbling motion and (d) only C_2 non-localized hopping of C_2D_4.

(a) Observed QI parameters   (b) Simulated C_2D_4 motion patterns
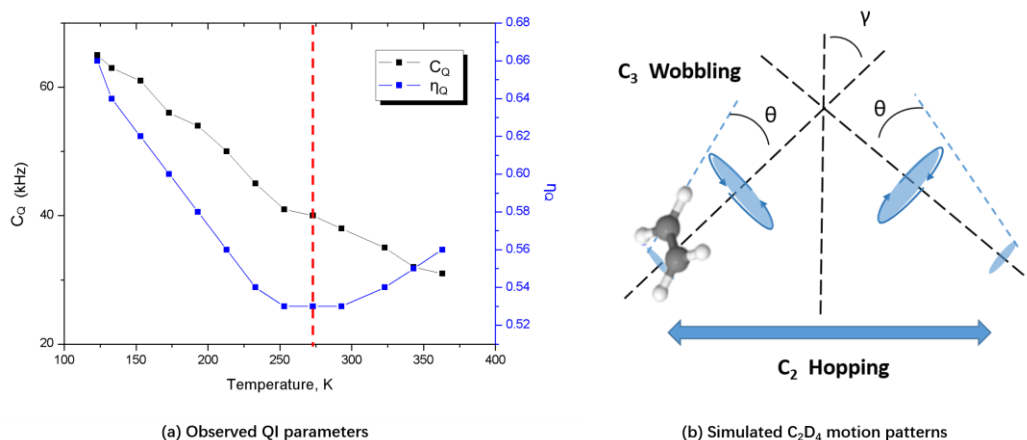
Figure 18-20. The chart in (a) demonstrates the observed quadrupolar parameters of C_2D_4 adsorbed in α – zinc formate along with the experimental temperature range, from 123 K to 363 K. Detailed values are listed in Table 3. The C_Q value decreases with increasing experimental temperatures with several small fluctuations. In contrast, η_Q decreases from 123 K to 233 K, remains constant from 253 K to 293 K, and then slightly rises at higher experimental temperatures. Note at 293 K, a red dash line is marked at the bottom of the "valley" trend in the η_Q value, and there may be some structural change in the Zn-formate MOF structure at this point. The figure in (b) is an illustration of combined C_2D_4 motions, including localized rotational C_3 wobbling (θ) and non-localized, two-site C_2 hopping (γ) between two C_3 sites

Table 2-4 EXPRESS[20] simulated motional angles of adsorbed CO_2, CO and C_2D_4 guests within the α – zinc formate MOF.

Temperature (K)	CO_2		CO		C_2D_4	
	C_2 (γ) /°	C_3 (θ) /°	C_2 (γ) /°	C_3 (θ) /°	C_2 (γ) /°	C_3 (θ) /°
433 K	48.9(1)	48.5(1)	51.0(2)	49.7(2)		
413 K	48.7(1)	48.8(1)	51.9(2)	49.1(2)		
393 K	48.4(1)	49.1(2)	52.6(2)	48.4(2)		
383 K						
373 K	48.1(1)	49.5(1)	53.3(2)	47.9(2)		
363 K					27.0(2)	47.0(1)
353 K	47.8(1)	49.9(1)	54.1(1)	47.3(2)		
343 K					27.5(1)	47.0(1)
333 K	47.6(2)	50.2(2)	54.9(2)	46.8(2)		
323 K					27.5(2)	46.0(2)
313 K	47.4(2)	50.6(2)	55.8(3)	46.2(2)		
293 K	47.0(1)	50.3(2)	57.1(1)	45.8(2)	28.5(1)	45.0(2)
273 K	46.6(2)	50.0(2)	57.9(1)	45.7(1)	28.5(1)	45.0(1)
253 K	44.5(1)	50.0(1)	58.6(2)	45.5(2)	29.0(1)	44.5(1)
233 K	35.5(1)	49.7(1)	60.5(2)	45.3(2)	29.5(2)	42.5(1)
213 K	31.5(2)	49.6(1)	61.9(1)	44.9(1)	29.5(1)	41.5(2)
193 K	25.2(1)	47.0(1)	62.5(1)	44.3(2)	29.5(1)	40.5(1)
173 K	21.1(2)	46.1(1)	63.6(1)	44.5(1)	30.0(1)	39.5(1)
153 K	20.6(1)	43.3(2)	64.3(1)	43.8(3)	30.5(1)	38.0(1)
133 K	19.5(1)	40.1(2)	64.5(1)	43.2(1)	31.0(1)	37.0(1)
123 K	19.3(1)	38.9(2)	64.5(1)	43.1(1)	31.0(1)	36.5(1)

2.3.10 ^{67}Zn High Field SSNMR experiments at 21.1 T

To investigate the influence of guest adsorption on the zinc centres in Zn-formate, static ^{67}Zn experiments were performed using high field SSNMR spectroscopy of 21.1 T in Ottawa, Ontario, Canada. The ^{67}Zn isotope is quadrupolar and the ^{67}Zn SSNMR spectrum is sensitive to the local chemical and geometric environment about Zn. In α - zinc formate, the ^{67}Zn signals of all four chemically unique zinc atoms can be detected using 21.1 T static SSNMR experiments. Five samples of as-made, activated empty, CO_2 loaded, CO loaded, and C_2D_4 loaded α - zinc formate MOF were examined at room temperature using 21.1 T high field static 67Zn SSNMR. The resulting ^{67}Zn SSNMR spectra are shown in Figure 2-21.
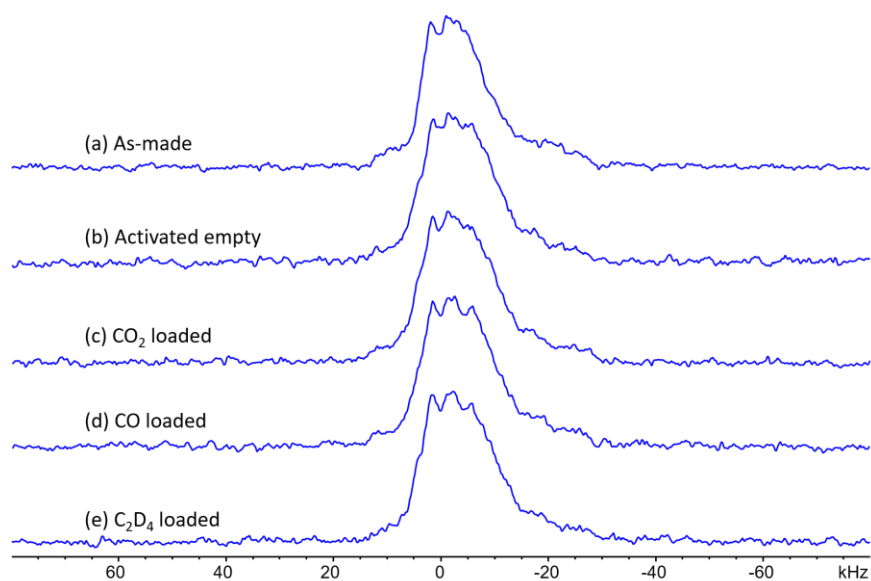
Figure 2-21. The figure compares the 21.1 T static ^{67}Zn SSNMR spectra of α – zinc formate MOF samples with different guests, as indicated in black text by the (a), (b), (c), (d) and (e) labels. No obvious differences can be observed between all five of (a) as-made, containing methanol and water solvents, (b) activated empty, (c) CO_2 loaded, (d) CO loaded and (e) C_2D_4 loaded α – zinc formate MOF samples, indicating that the adsorbed guests are not directly interacting with Zn atoms in α – zinc formate MOF.

The observed [67]Zn SSNMR experimental powder patterns are in good agreement with the simulated spectra based on [67]Zn NMR parameters calculated by the CASTEP package[22] (Figure 2-22): there are four broad overlapping [67]Zn resonances observed in experimental spectra, and the four crystallographically unique zinc atoms produce similar C_Q and η_Q quadrupolar interaction values from CASTEP calculations (Table 2-5), suggesting that all four Zn centres are located in very similar chemical environments within the α - zinc formate MOF.[6] Meanwhile, no significant differences were observed between the [67]Zn SSNMR spectra of the as-made, activated empty, CO_2, CO, and C_2D_4 loaded α - zinc formate samples. All five spectra show similar lineshapes, which reveals that the guest molecules are not directly interacting with zinc metal centres or modifying their local environments in any significant way. This may be explained by the coordination environment of zinc atoms, which are sitting in ZnO_6 octahedra, and the Zn coordination environment is fully occupied by six oxygen atoms from formate linkers. Thus, the [67]Zn spectra proves that no zinc atom is exposed to the channel and none of the Zn centres can directly interact with guests. The only adsorption site available in this MOF must be the exposed H or O atoms from formate linkers that are pointing towards the channel interior.
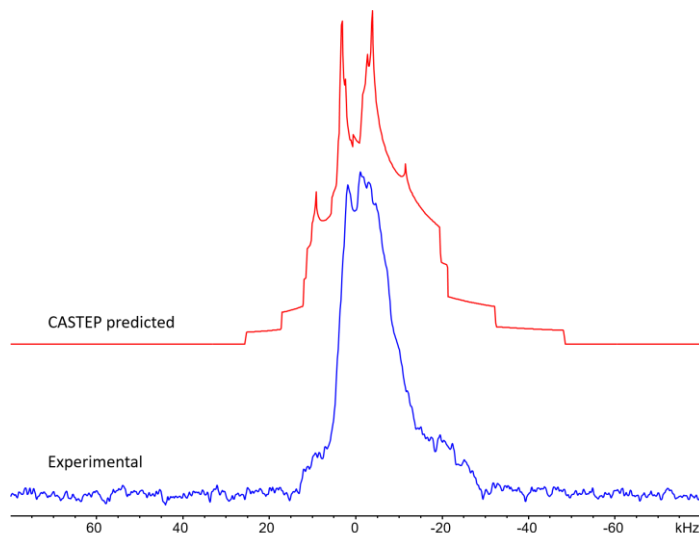
Figure 2-22. The figure compares the 21.1 T static [67]Zn SSNMR spectra of the as-made Zn-formate sample (blue) with that predicted based on CASTEP calculations (red).

Table 2-5 CASTEP calculated QI parameters of the four Zn metal centres in the activated empty α – zinc formate MOF sample.

	Zn_1	Zn_2	Zn_3	Zn_4
C_Q (MHz)	-6.241	-5.220	10.141	-8.440
η_Q	0.959	0.113	0.395	0.950

2.4   Conclusions

Static VT ^{13}C NMR experiments indicate that adsorbed CO_2 and CO guest molecules have reduced mobility and restricted molecular motions when adsorbed within α - zinc formate; while ^{2}H NMR experiments have suggested that adsorbed C_2D_4 guests also have reduced mobility and restricted molecular motions. These experimental SSNMR powder patterns can be motionally simulated to obtain guest dynamic motions. The motional simulation results indicate that all three guest molecules within the studied experimental temperature ranges undergo a C_3 localized rotational wobbling motion upon the adsorption site, as well as a C_2 non-localized hopping motion between adjacent adsorption sites, despite the very different nature of these guests. Adsorbed CO_2 appears to play a role in negative thermal expansion of the α - zinc formate MOF, or some other induced structural change to the α - zinc formate framework. This interesting phenomenon was not observed from the VT experiments on CO loaded α - zinc formate samples. Static ^{1}H-^{13}C CP SSNMR experiments on adsorbed CO_2 and CO confirm that the H-atoms lining the MOF pore interiors act as the adsorption sites for these two guests. SCXRD experiments on CO_2 loaded α - zinc formate at LT revealed the adsorbed CO_2 guest positions are located very close to the inner surface of the channel. The relatively short distances from CO_2 to the three nearest hydrogen atoms indicates they may participate in weak hydrogen bonding or electrostatic interactions with CO_2 guests. Moreover, there are odd trends in the NMR parameters of certain guests adsorbed in this MOF. The span or breadth of ^{13}C SSNMR spectra of CO_2 reaches a minimum at 293 K, which contrasts with the typical negative correlation observed for guests such as CO. The ^{2}H SSNMR spectra of C_2D_4-loaded α - zinc formate reveal the ^{2}H asymmetry parameter η_Q reaches a minimum at 273 K, rather than the linear relationship seen for C_Q in this system. This data hints that some guest-triggered changes to the host Zn-formate MOF structure may occur near room temperature. For a better understanding of the interactions occurring between the α - zinc formate framework and adsorbed guests, static 21.1 T ^{67}Zn

NMR experiments on Zn centres of this MOF were performed. However, the ^{67}Zn NMR experimental results indicate that the activation process and presence of various guests such as CO_2, CO and C_2D_4 do not have an obvious influence on the local electronic environment about the fully saturated Zn atoms. It appears that the guests do not directly interact with the Zn atoms or even perturb their local environment.

For future work, we plan to perform ^{67}Zn static SSNMR on the as-made α - zinc formate samples at a magnetic field of 35.5 T (National High Magnetic Field Laboratory, Florida State University) to shed light on any host-guest interactions with these Zn metal centres. Although we have assumed the Zn metal centres do not play a role in guest adsorption, any changes in the Zn local chemical environments with guest adsorption should be very apparent in ^{67}Zn SSNMR spectra.

The non-porous β - zinc formate and related bulk compound zinc formate dihydrate are thought to be inconvenient for studying guest adsorption behaviour. However, the discoveries made from this work provide us a possible path to trap guests inside these non-porous compounds by taking advantage of the phase transformations via porous α - zinc formate; guests can be loaded in the α - zinc formate phase, a phase transformation with temperature can be triggered, and then the behaviour of trapped CO_2 within the new phase of Zn-formate can be investigated.

88

2.5   Bibliography

1.   Li, J.-R.; Kuppler, R. J.; Zhou, H.-C., Selective gas adsorption and separation in metal–organic frameworks. *Chem. Soc. Rev.* **2009,** *38* (5), 1477-1504.

2.   Lee, J.; Farha, O. K.; Roberts, J.; Scheidt, K. A.; Nguyen, S. T.; Hupp, J. T., Metal–organic framework materials as catalysts. *Chem. Soc. Rev.* **2009,** *38* (5), 1450-1459.

3.   Lowrance, E. G., Ethylene production process. US Patent 3,530,199, Jun 22, 1967

4.   Böhme, U.; Barth, B.; Paula, C.; Kuhnt, A.; Schwieger, W.; Mundstock, A.; Caro, J. r.; Hartmann, M., Ethene/ethane and propene/propane separation via the olefin and paraffin selective metal–organic framework adsorbents CPO-27 and ZIF-8. *Langmuir* **2013,** *29* (27), 8592-8600.

5.   Viertelhaus, M.; Anson, C. E.; Powell, A. K., Solvothermal synthesis and crystal structure of one-dimensional chains of anhydrous zinc and magnesium Formate. *Z. Anorg. Allg. Chem* **2005,** *631* (12), 2365-2370.

6.   Wang, Z.; Zhang, Y.; Kurmoo, M.; Liu, T.; Vilminot, S.; Zhao, B.; Gao, S., $[Zn_3(HCOO)_6]$: a porous diamond framework conformable to guest inclusion. *Aust. J. Chem.* **2006,** *59* (9), 617-628.

7.   Zhang, Y.; Lucier, B. E.; Huang, Y., Deducing CO_2 motion, adsorption locations and binding strengths in a flexible metal–organic framework without open metal sites. *Phys. Chem. Chem. Phys.* **2016,** *18* (12), 8327-8341.

8.   Lucier, B. E.; Chan, H.; Zhang, Y.; Huang, Y., Multiple modes of motion: Realizing the dynamics of CO adsorbed in M-MOF-74 (M= Mg, Zn) by using solid-state NMR spectroscopy. *Eur. J. Inorg. Chem.* **2016,** *2016* (13-14), 2017-2024.

9.   Lucier, B. E.; Zhang, Y.; Lee, K. J.; Lu, Y.; Huang, Y., Grasping hydrogen adsorption and dynamics in metal–organic frameworks using ^{2}H solid-state NMR. *Chem. Commun.* **2016,** *52* (48), 7541-7544.

10.   Khudozhitkov, A. E.; Kolokolov, D. I.; Stepanov, A. G.; Bolotov, V. A.; Dybtsev, D. N., Metal-cation-independent dynamics of phenylene ring in microporous MOFs: a 2H solid-state NMR study. *J. Phys. Chem. C* **2015,** *119* (50), 28038-28045.

11.   Bruker-AXS, SAINT version 2013.8, **2013**, Bruker-AXS, Madison, WI 53711, USA

12.   Bruker-AXS, SADABS version 2012.1, **2012**, Bruker-AXS, Madison, WI 53711, USA

13.   Spek, A., Single-crystal structure validation with the program PLATON. *J. Appl. Crystallogr.* **2003,** *36* (1), 7-13.

14.   Sheldrick, G. M., SHELXT–Integrated space-group and crystal-structure determination. *Acta Crystallogr., A, Found. Crystallogr.* **2015,** *71* (1), 3-8.

15.   Gabe, E.; Le Page, Y.; Charland, J.-P.; Lee, F.; White, P., NRCVAX–an interactive program system for structure analysis. *J. Appl. Crystallogr.* **1989,** *22* (4), 384-387.

16.   Dybowski, C.; Neue, G., Solid state 207 Pb NMR spectroscopy. *Prog. Nucl. Mag. Res. Sp.* **2002,** *41* (3), 153-170.

17.   Fulmer, G. R.; Miller, A. J.; Sherden, N. H.; Gottlieb, H. E.; Nudelman, A.; Stoltz, B. M.; Bercaw, J. E.; Goldberg, K. I., NMR chemical shifts of trace impurities: common laboratory solvents, organics, and gases in deuterated solvents relevant to the organometallic chemist. *Organometallics* **2010,** *29* (9), 2176-2179.

18.   Harris, R. K.; Becker, E. D.; Cabral de Menezes, S. M.; Goodfellow, R.; Granger, P., NMR nomenclature. Nuclear spin properties and conventions for chemical shifts (IUPAC recommendations 2001). *Pure Appl. Chem.* **2001,** *73* (11), 1795-1818.

19.   Eichele, K., WSolids NMR Simulation Package, Version 1.20. 21; 2013.

20.   Vold, R. L.; Hoatson, G. L., Effects of jump dynamics on solid state nuclear magnetic resonance line shapes and spin relaxation times. *J. Magn. Reson.* **2009,** *198* (1), 57-72.

21.   Beeler, A. J.; Orendt, A. M.; Grant, D. M.; Cutts, P. W.; Michl, J.; Zilm, K. W.; Downing, J. W.; Facelli, J. C.; Schindler, M. S.; Kutzelnigg, W., Low-temperature carbon-13 magnetic resonance in solids. 3. Linear and pseudolinear molecules. *J. Am. Chem. Soc.* **1984,** *106* (25), 7672-7676.

22.   Clark, S. J.; Segall, M. D.; Pickard, C. J.; Hasnip, P. J.; Probert, M. I.; Refson, K.; Payne, M. C., First principles methods using CASTEP. *Z. Kristallogr.-Cryst. Mater.* **2005,** *220* (5/6), 567-570.

23.   Wang, W. D.; Lucier, B. E.; Terskikh, V. V.; Wang, W.; Huang, Y., Wobbling and hopping: studying dynamics of CO_2 adsorbed in metal–organic frameworks via ^{17}O solid-state NMR. *J. Phys. Chem. Lett.* **2014,** *5* (19), 3360-3365.

24.   Lu, Y.; Lucier, B. E.; Zhang, Y.; Ren, P.; Zheng, A.; Huang, Y., Sizable dynamics in small pores: CO 2 location and motion in the α-Mg formate metal–organic framework. *Phys. Chem. Chem. Phys.* **2017,** *19* (8), 6130-6141.

25.   Aguilar-Armenta, G.; Hernandez-Ramirez, G.; Flores-Loyola, E.; Ugarte-Castaneda, A.; Silva-Gonzalez, R.; Tabares-Munoz, C.; Jimenez-Lopez, A.; Rodriguez-Castellon, E., Adsorption kinetics of CO_2, O_2, N_2, and CH_4 in cation-exchanged clinoptilolite. *J. Phys. Chem. B* **2001,** *105* (7), 1313-1319.

26.   Hartmann, S.; Hahn, E., Nuclear double resonance in the rotating frame. *Phys. Rev.* **1962,** *128* (5), 2042.

27.   Chen, S.; Lucier, B. E.; Boyle, P. D.; Huang, Y., Understanding the fascinating origins of CO_2 adsorption and dynamics in MOFs. *Chem. Mater.* **2016,** *28* (16), 5829-5846.

28.   Espinosa, E.; Molins, E.; Lecomte, C., Hydrogen bond strengths revealed by topological analyses of experimentally observed electron densities. *Chem. Phys. Lett.* **1998,** *285* (3), 170-173.

29.   Pake, G. E., Nuclear resonance absorption in hydrated crystals: fine structure of the proton line. *J. Chem. Phys.* **1948,** *16* (4), 327-336.

30.	Lide, D. R.; Paul, M. A., *Critical evaluation of chemical and physical structural information: proceedings of a conference*. National Academies: **1974**.

2.6 Appendices
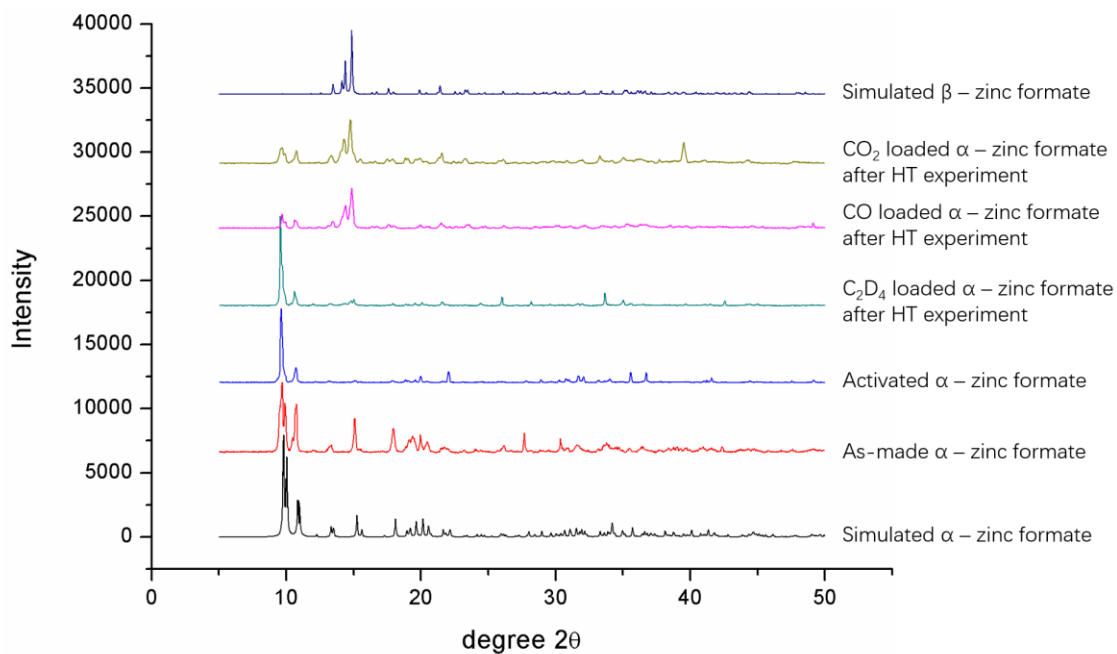
Figure S2-1. The figure shows pXRD powder patterns of corresponding zinc formate samples. After heating up the activated CO and CO_2 loaded α – zinc formate samples respectively at 433 K for about 2 hours in the SSNMR spectrometer, the α phase of zinc formate partially transformed into the non-porous β phase, representing a mixture of α and β phases simultaneously. Because C_2D_4 loaded α – zinc formate sample was only heated up to 363 K, which is lower than the phase transfer temperature at 393 K, no diffraction change was observed compared to activated empty sample.
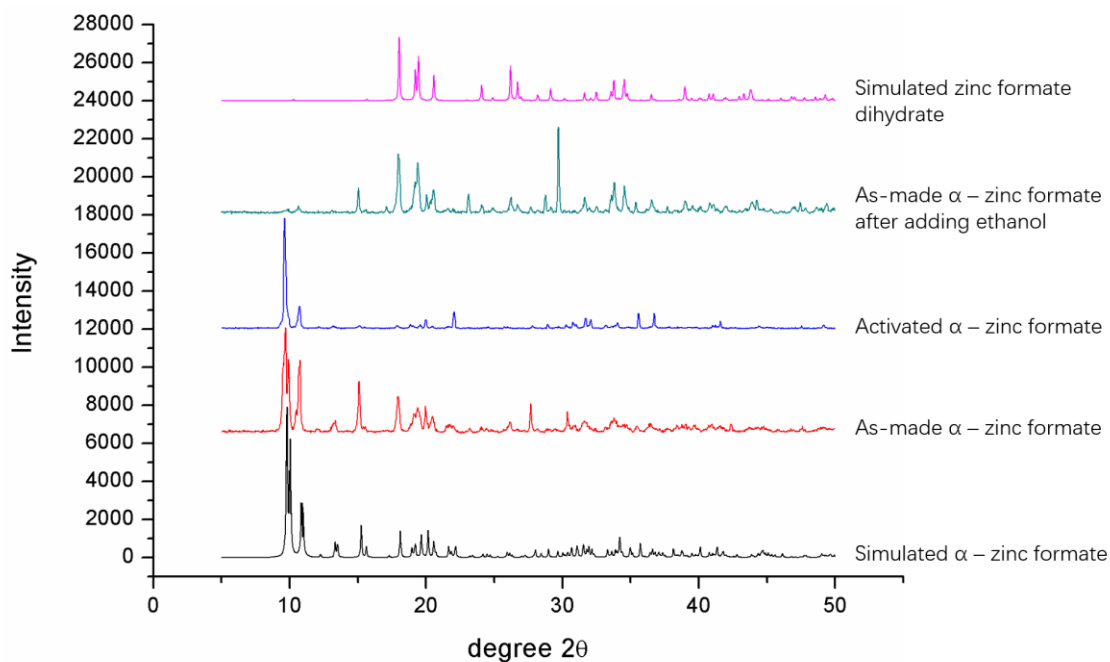
Figure S2-2. The figure shows pXRD powder patterns of corresponding zinc formate samples. Adding ethanol to as-made α – zinc formate MOF yields non-porous zinc formate dihydrate. The diffraction powder pattern of zinc formate dehydrate is in good agreement with the simulated one, except for one preferred orientation reflection at 2θ = 30˚ and one low angle reflection at 2θ = 15˚ that originates from the remaining as-made α – zinc formate.
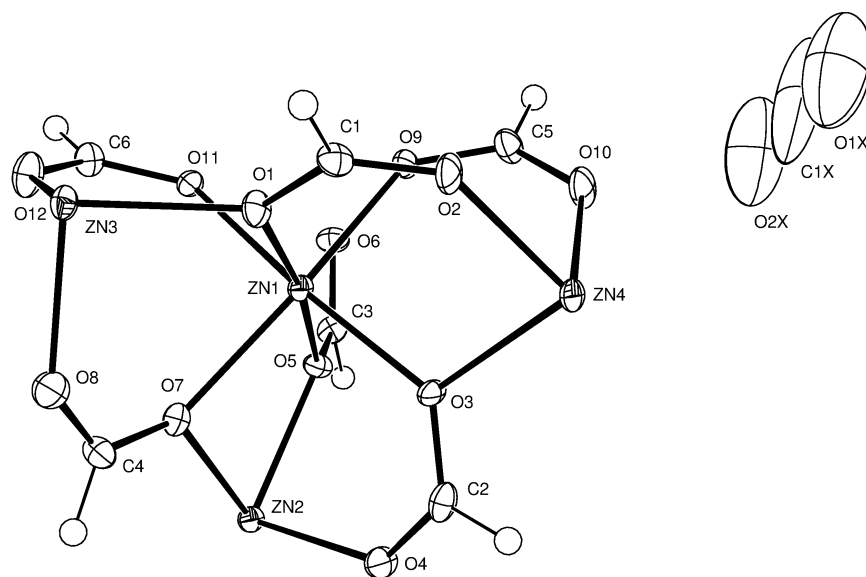
Figure S2-3. ORTEP drawing of ***n17100 asymmetric unit*** showing naming and numbering scheme. Ellipsoids are at the 50% probability level and hydrogen atoms were drawn with arbitrary radii for clarity.
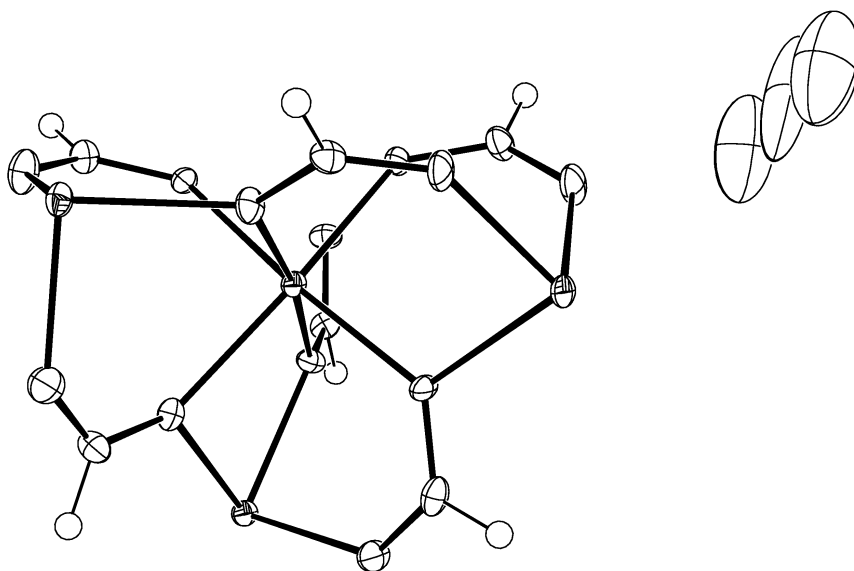
Figure S2-4. ORTEP drawing of *n17100 asymmetric unit*. Ellipsoids are at the 50% probability level and hydrogen atoms were drawn with arbitrary radii for clarity.
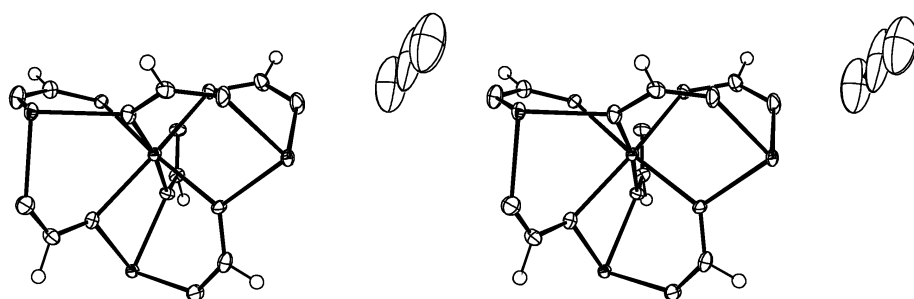
Figure S2-5 Stereoscopic ORTEP drawing of *n17100 asymmetric unit*. Ellipsoids are at the 50% probability level and hydrogen atoms were drawn with arbitrary radii for clarity.

Table S2-1. Summary of crystal data for *n17100*

Formula	$C_{6.25}H_6O_{12.50}Zn_3$
Formula Weight (*g/mol*)	477.22
Crystal Dimensions (*mm*)	$0.657 \times 0.617 \times 0.177$
Crystal Color and Habit	colourless prism
Crystal System	monoclinic
Space Group	P 2_1/n
Temperature, K	120
a, Å	11.3261(15)
b, Å	9.8210(14)
c, Å	14.4412(19)
α,°	90
β,°	91.297(5)
γ,°	90
V, Å^3	1605.9(4)
Number of reflections to determine final unit cell	9044
Min and Max 2θ for cell determination, °	6.12, 135.18
Z	4
F(000)	934
ρ (*g/cm*)	1.974
λ, Å, (CuKα)	1.54178
μ, (*cm^{-1}*)	5.787
Diffractometer Type	Bruker-Nonius KappaCCD Apex2
Scan Type(s)	phi and omega scans
Max 2θ for data collection, °	135.17
Measured fraction of data	0.973
Number of reflections measured	5024
Unique reflections measured	5024
R$_{merge}$	?
Number of reflections included in refinement	5024
Cut off Threshold Expression	I > 2sigma(I)
Structure refined using	full matrix least-squares using F^2

Weighting Scheme	$w=1/[sigma^2(Fo^2)+(0.0507P)^2+2.3833P]$ where $P=(Fo^2+2Fc^2)/3$
Number of parameters in least-squares	245
R_1	0.0303
wR_2	0.0986
R_1 (all data)	0.0306
wR_2 (all data)	0.0992
GOF	1.224
Maximum shift/error	0.000
Min & Max peak heights on final ΔF Map ($e^-/\text{Å}$)	-0.724, 0.559

Where:

$R_1 = \Sigma(|F_o| - |F_c|) / \Sigma F_o$

$wR_2 = [\Sigma(w(F_o^2 - F_c^2)^2) / \Sigma(w F_o^4)]^{1/2}$

$GOF = [\Sigma(w(F_o^2 - F_c^2)^2) / (\text{No. of reflns.} - \text{No. of params.})]^{1/2}$

Table S2-2. Atomic coordinates for *n17100*

Atom	x	y	z	$U_{iso/equiv}$
Zn1	0.24331(4)	0.07756(5)	0.36832(3)	0.00978(16)
Zn2	0.24050(4)	0.39126(5)	0.31300(3)	0.01070(16)
Zn3	0.5000	0.0000	0.5000	0.01207(19)
Zn4	0.0000	0.0000	0.5000	0.01229(19)
O1	0.3157(2)	-0.0274(3)	0.47692(18)	0.0137(6)
C1	0.2572(4)	-0.1057(4)	0.5306(3)	0.0139(8)
O2	0.1496(2)	-0.1141(3)	0.5339(2)	0.0171(6)
O3	0.1025(2)	0.1551(3)	0.43955(18)	0.0124(5)
C2	0.0706(4)	0.2786(4)	0.4488(3)	0.0157(8)
O4	0.1118(2)	0.3792(3)	0.40880(19)	0.0163(6)
O5	0.1919(2)	0.1994(3)	0.25419(18)	0.0120(5)
C3	0.1699(3)	0.1720(4)	0.1697(3)	0.0133(8)
O6	0.1833(2)	0.0606(3)	0.13111(19)	0.0155(6)
O7	0.3472(2)	0.2554(3)	0.39048(19)	0.0123(6)
C4	0.4222(4)	0.2883(4)	0.4533(3)	0.0165(8)
O8	0.4814(2)	0.2092(3)	0.5024(2)	0.0189(6)
O9	0.1494(2)	-0.0832(3)	0.30488(18)	0.0125(5)
C5	0.0458(4)	-0.1294(4)	0.3133(3)	0.0157(8)
O10	-0.0234(2)	-0.1044(3)	0.3761(2)	0.0189(6)
O11	0.3700(2)	-0.0069(3)	0.28039(18)	0.0122(6)
C6	0.4814(3)	-0.0149(4)	0.2878(3)	0.0136(8)
O12	0.5411(2)	0.0035(3)	0.3596(2)	0.0192(6)
C1X	-0.255(3)	-0.251(5)	0.300(2)	0.137(18)
O1X	-0.260(2)	-0.298(4)	0.3736(19)	0.124(12)
O2X	-0.245(2)	-0.173(3)	0.2402(17)	0.109(10)
H1	0.300(4)	-0.158(4)	0.569(3)	0.004(9)
H2	0.003(4)	0.292(5)	0.491(3)	0.006(10)
H3	0.138(4)	0.249(4)	0.136(3)	0.008(11)
H4	0.438(5)	0.392(7)	0.460(4)	0.045(17)
H5	0.017(4)	-0.189(5)	0.269(3)	0.008(10)
H6	0.525(5)	-0.040(6)	0.234(4)	0.031(14)

Table S2-3. Anisotropic displacement parameters for *n17100*

Atom	u^{11}	u^{22}	u^{33}	u^{12}	u^{13}	u^{23}
Zn1	0.0100(3)	0.0097(3)	0.0098(3)	0.00014(18)	0.00347(19)	0.00060(18)
Zn2	0.0115(3)	0.0101(3)	0.0106(3)	-0.00007(18)	0.00315(19)	0.00103(18)
Zn3	0.0090(4)	0.0147(4)	0.0126(4)	-0.0006(3)	0.0019(3)	0.0013(3)
Zn4	0.0104(4)	0.0134(4)	0.0133(4)	-0.0014(3)	0.0058(3)	0.0016(3)
O1	0.0118(13)	0.0168(14)	0.0127(13)	-0.0019(11)	0.0038(10)	0.0029(11)
C1	0.017(2)	0.013(2)	0.0118(19)	-0.0002(15)	0.0012(16)	0.0031(15)
O2	0.0105(14)	0.0189(15)	0.0223(15)	-0.0013(11)	0.0064(11)	0.0063(11)
O3	0.0128(12)	0.0091(14)	0.0158(13)	0.0012(11)	0.0073(10)	0.0015(11)
C2	0.0116(19)	0.023(2)	0.0124(19)	0.0003(16)	0.0034(16)	0.0006(17)
O4	0.0178(14)	0.0133(15)	0.0182(14)	0.0002(11)	0.0076(11)	0.0023(11)
O5	0.0151(13)	0.0092(14)	0.0119(13)	-0.0010(11)	0.0023(10)	-0.0003(10)
C3	0.0149(18)	0.014(2)	0.0105(18)	0.0024(15)	-0.0011(14)	0.0013(15)
O6	0.0194(14)	0.0126(14)	0.0144(13)	0.0014(11)	-0.0010(11)	-0.0031(11)
O7	0.0104(14)	0.0155(15)	0.0112(14)	0.0007(9)	0.0003(11)	0.0013(10)
C4	0.0155(19)	0.014(2)	0.020(2)	-0.0030(16)	0.0012(16)	-0.0013(17)
O8	0.0174(14)	0.0174(15)	0.0216(15)	0.0012(12)	-0.0034(12)	0.0006(12)
O9	0.0116(13)	0.0124(14)	0.0137(13)	-0.0017(10)	0.0042(10)	-0.0014(10)
C5	0.016(2)	0.017(2)	0.015(2)	-0.0056(16)	0.0040(16)	-0.0033(16)
O10	0.0150(14)	0.0242(16)	0.0178(15)	-0.0058(11)	0.0081(12)	-0.0021(12)
O11	0.0112(13)	0.0114(14)	0.0144(13)	0.0002(10)	0.0047(10)	-0.0025(10)
C6	0.0133(19)	0.018(2)	0.0100(19)	-0.0007(15)	0.0031(15)	0.0005(15)
O12	0.0134(14)	0.0303(18)	0.0140(15)	0.0002(11)	0.0016(11)	0.0017(12)
C1X	0.036(18)	0.26(4)	0.12(2)	0.02(2)	0.020(17)	0.08(3)
O1X	0.071(17)	0.20(3)	0.100(18)	0.01(2)	0.024(14)	0.05(2)
O2X	0.056(13)	0.20(3)	0.074(14)	-0.007(16)	0.000(11)	0.025(16)

Table S2-4. Bond lengths for *n17100*

Zn1-O1	2.034(3)		O1-C1	1.286(5)
Zn1-O3	2.063(3)		C1-O2	1.224(5)
Zn1-O9	2.102(3)		C1-H1	0.89(5)
Zn1-O11	2.108(3)		O3-C2	1.273(5)
Zn1-O5	2.108(3)		C2-O4	1.241(5)
Zn1-O7	2.126(3)		C2-H2	1.00(5)
Zn2-O6[1]	2.033(3)		O5-C3	1.269(5)
Zn2-O4	2.036(3)		C3-O6	1.238(5)
Zn2-O11[1]	2.076(3)		C3-H3	0.97(5)
Zn2-O7	2.105(3)		O6-Zn2[4]	2.033(3)
Zn2-O5	2.134(3)		O7-C4	1.271(5)
Zn2-O9[1]	2.147(3)		C4-O8	1.238(5)
Zn3-O8	2.066(3)		C4-H4	1.03(6)
Zn3-O8[2]	2.066(3)		O9-C5	1.267(5)
Zn3-O12[2]	2.090(3)		O9-Zn2[4]	2.147(3)
Zn3-O12	2.090(3)		C5-O10	1.236(5)
Zn3-O1	2.124(3)		C5-H5	0.92(5)
Zn3-O1[2]	2.124(3)		O11-C6	1.266(5)
Zn4-O10[3]	2.074(3)		O11-Zn2[4]	2.076(3)
Zn4-O10	2.074(3)		C6-O12	1.239(5)
Zn4-O2[3]	2.080(3)		C6-H6	0.96(6)
Zn4-O2	2.080(3)		C1X-O1X	1.161(7)
Zn4-O3	2.116(3)		C1X-O2X	1.161(7)
Zn4-O3[3]	2.116(3)			

1. -x+1/2, y+1/2, -z+1/2
2. 1-x, -y,1+ -z
3. -x, -y,1+ -z
4. -x+1/2,-1+ y+1/2, -z+1/2

Table S2-5. Bond angles for *n17100*

O1-Zn1-O3	96.05(10)	O10-Zn4-O3	93.48(10)
O1-Zn1-O9	98.42(11)	O2^3-Zn4-O3	88.08(10)
O3-Zn1-O9	96.05(10)	O2-Zn4-O3	91.92(10)
O1-Zn1-O11	89.84(11)	O10^3-Zn4-O3^3	93.48(10)
O3-Zn1-O11	172.00(11)	O10-Zn4-O3^3	86.52(10)
O9-Zn1-O11	77.68(10)	O2^3-Zn4-O3^3	91.92(10)
O1-Zn1-O5	171.92(10)	O2-Zn4-O3^3	88.08(10)
O3-Zn1-O5	88.68(10)	O3-Zn4-O3^3	180.0
O9-Zn1-O5	87.55(10)	C1-O1-Zn1	124.3(3)
O11-Zn1-O5	86.11(10)	C1-O1-Zn3	119.9(2)
O1-Zn1-O7	95.07(11)	Zn1-O1-Zn3	115.74(12)
O3-Zn1-O7	93.04(11)	O2-C1-O1	126.2(4)
O9-Zn1-O7	162.82(11)	O2-C1-H1	118(3)
O11-Zn1-O7	91.82(10)	O1-C1-H1	116(3)
O5-Zn1-O7	78.10(10)	C1-O2-Zn4	139.6(3)
O6^1-Zn2-O4	94.71(11)	C2-O3-Zn1	128.9(2)
O6^1-Zn2-O11^1	96.19(10)	C2-O3-Zn4	118.9(2)
O4-Zn2-O11^1	92.24(11)	Zn1-O3-Zn4	112.16(12)
O6^1-Zn2-O7	94.26(11)	O4-C2-O3	126.8(4)
O4-Zn2-O7	90.75(11)	O4-C2-H2	119(3)
O11^1-Zn2-O7	168.86(10)	O3-C2-H2	114(3)
O6^1-Zn2-O5	169.75(11)	C2-O4-Zn2	130.2(3)
O4-Zn2-O5	92.10(11)	C3-O5-Zn1	132.5(3)
O11^1-Zn2-O5	91.19(10)	C3-O5-Zn2	127.8(2)
O7-Zn2-O5	77.97(10)	Zn1-O5-Zn2	97.22(11)
O6^1-Zn2-O9^1	88.29(11)	O6-C3-O5	126.6(4)
O4-Zn2-O9^1	169.44(11)	O6-C3-H3	121(3)
O11^1-Zn2-O9^1	77.36(10)	O5-C3-H3	113(3)
O7-Zn2-O9^1	99.14(11)	C3-O6-Zn2^4	126.8(3)
O5-Zn2-O9^1	86.39(10)	C4-O7-Zn2	125.8(3)
O8-Zn3-O8^2	180.0	C4-O7-Zn1	132.5(3)
O8-Zn3-O12^2	88.59(11)	Zn2-O7-Zn1	97.57(12)

$O8^2$-Zn3-$O12^2$	91.42(11)	O8-C4-O7	126.4(4)
O8-Zn3-O12	91.41(11)	O8-C4-H4	118(3)
$O8^2$-Zn3-O12	88.58(11)	O7-C4-H4	115(3)
$O12^2$-Zn3-O12	180.0	C4-O8-Zn3	132.0(3)
O8-Zn3-O1	91.62(11)	C5-O9-Zn1	133.4(3)
$O8^2$-Zn3-O1	88.38(11)	C5-O9-$Zn2^4$	126.2(3)
$O12^2$-Zn3-O1	84.87(10)	Zn1-O9-$Zn2^4$	97.82(10)
O12-Zn3-O1	95.13(10)	O10-C5-O9	127.2(4)
O8-Zn3-$O1^2$	88.38(11)	O10-C5-H5	114(3)
$O8^2$-Zn3-$O1^2$	91.62(11)	O9-C5-H5	119(3)
$O12^2$-Zn3-$O1^2$	95.13(10)	C5-O10-Zn4	131.3(3)
O12-Zn3-$O1^2$	84.87(10)	C6-O11-$Zn2^4$	127.6(2)
O1-Zn3-$O1^2$	180.0	C6-O11-Zn1	131.6(3)
$O10^3$-Zn4-O10	180.0	$Zn2^4$-O11-Zn1	99.92(11)
$O10^3$-Zn4-$O2^3$	91.39(12)	O12-C6-O11	125.9(4)
O10-Zn4-$O2^3$	88.61(12)	O12-C6-H6	116(3)
$O10^3$-Zn4-O2	88.61(12)	O11-C6-H6	118(3)
O10-Zn4-O2	91.39(12)	C6-O12-Zn3	132.9(3)
$O2^3$-Zn4-O2	180.0	O1X-C1X-O2X	163(6)
$O10^3$-Zn4-O3	86.52(10)		

1. -x+1/2, y+1/2, -z+1/2
2. 1-x, -y,1+ -z
3. -x, -y,1+ -z
4. -x+1/2,-1+ y+1/2, -z+1/2

Table S2-6. Torsion angles for *n17100*

Zn1-O1-C1-O2	-11.3(6)	Zn2-O7-C4-O8	176.3(3)
Zn3-O1-C1-O2	168.1(3)	Zn1-O7-C4-O8	24.6(6)
O1-C1-O2-Zn4	-21.9(7)	O7-C4-O8-Zn3	6.4(7)
Zn1-O3-C2-O4	7.7(6)	Zn1-O9-C5-O10	-14.2(7)
Zn4-O3-C2-O4	-170.5(3)	Zn2[1]-O9-C5-O10	-171.9(3)
O3-C2-O4-Zn2	1.2(6)	O9-C5-O10-Zn4	-8.2(7)
Zn1-O5-C3-O6	-6.2(6)	Zn2[1]-O11-C6-O12	-151.9(3)
Zn2-O5-C3-O6	152.1(3)	Zn1-O11-C6-O12	15.1(6)
O5-C3-O6-Zn2[1]	-6.5(6)	O11-C6-O12-Zn3	19.8(6)

1. -x+1/2,-1+ y+1/2, -z+1/2

Table S2-7. Potential hydrogen bonds for *n17100*

Hydrogen Bond	D—H (Å)	H⋯A (Å)	D⋯A (Å)	D—H⋯A (°)
C3-H3⋯O8[1]	0.97(5)	2.62(5)	3.395(5)	137(3)
C4-H4⋯O6[2]	1.03(6)	2.51(6)	3.162(5)	121(4)
C6-H6⋯O4[3]	0.96(6)	2.67(5)	3.181(5)	114(4)

1. x-1/2,1+ -y-1/2, z-1/2
2. -x+1/2, y+1/2, -z+1/2
3. -x+1/2,-1+ y+1/2, -z+1/2

Chapter 3

3   A solid-state NMR study of cation influence on CO_2 adsorption in ion-exchanged FAU and LTA zeolites

Zeolites are a class of porous aluminosilicate materials widely used as adsorbents for ion exchange, gas separations and industrial catalysis. Zeolites are attractive due to their low prices, ease of large-scale production, and environmentally-friendly syntheses. Zeolites are typically used for CO_2 adsorption from gas mixtures, but the dynamic behaviour of adsorbed CO_2 in zeolites has not been extensively studied. By studying the behaviour of guest molecules adsorbed in porous materials, one can obtain information on the specific adsorption mechanisms present and the location of guests, which is helpful for understanding the connection between guest molecule dynamics and adsorption capacity, as well as assisting in the design of more effective zeolites, especially for large-scale industrial purposes. Solid-state NMR (SSNMR) is sensitive to the local electronic, magnetic, and chemical environment about the nucleus of interest, such as types, angles, and rates of guest motion; SSNMR is thus a powerful technique for probing guest molecule location and dynamics that can enhance our understanding of the CO_2 adsorption behaviour and host-guest interaction mechanisms in zeolites. In this study, several ion-exchanged zeolites belonging to the FAU and LTA families have been prepared and used as porous CO_2 adsorbents, and then SSNMR has been used to probe the dynamics and location of adsorbed CO_2 guests. Variable-temperature (VT) static direct-excitation ^{13}C and ^1H -^{13}C cross polarization (CP) SSNMR spectra have been obtained to shed light on the interactions between CO_2 guests and charge-balancing cations within these zeolite materials, as well as to investigate the adsorption behaviour of CO_2 guest within these zeolite frameworks.

3.1   Introduction

3.1.1 General introduction

Zeolites, also known as molecular sieves, are microporous aluminosilicate materials that were originally discovered in nature[1] and are now typically manufactured in large amounts for industrial applications. Most zeolites are thermally stable and their structures do not collapse even if heated at high temperatures (*e.g.*, 600 °C) for dehydration or calcination purposes.[2] The porous structures of zeolites mean that they can adsorb and trap small molecules, and reactions involving guests can also take place inside the zeolite cavities. Zeolites are now used as adsorbents and reaction vessels in industrial productions, especially in the refining and catalysis industries.[3]

Natural aluminosilicate zeolites usually feature three-dimensional structures consisting primarily of $Si(IV)O_4$ tetrahedral building blocks. Some of the $Si(IV)O_4$ tetrahedra are substituted by $Al(III)O_4$ tetrahedra in a specific ratio, known as the Si/Al ratio. The presence of negatively charged $Al(III)O_4$ tetrahedra introduces a negative overall charge to the zeolite frameworks. To balance the net negative charge of the zeolite, various cations are present within the large structural cages, tunnels and cavities.[4] The presence of charge-balancing cations allows the porous zeolites to act as "sieves" for guest molecules of certain dimensions and properties, allowing selected molecules to go deeper into and/or fully penetrate through the pores. The cations can also be involved in various physical sorption processes or chemical reactions, depending on the type of zeolite, its pore structures, and the type of cations present.[5] The cations within zeolites are rather loosely bound and can be exchanged with other cations in aqueous solution.[6] In this manner, synthetic zeolites with specific types of incorporated cations can be manufactured or ion-exchanged in order to carry out specific reactions or adsorb certain types of molecules.

Zeolites have been extensively studied in various fields, ranging from organic catalysis to selective gas adsorption and selective ion capture or exchange.[7] Zeolites have been proven to be excellent organic catalysts,[8] especially in the field of petroleum chemistry. Gasoline and diesel, along with many other liquid fuels, are mostly

manufactured and refined through zeolite-based catalysts.[9] Zeolites are also involved in many other important organic reactions, such as alkyl cracking, hydrogenation, isomerization and conversions of aromatic compounds.[10] Several solid-state NMR (SSNMR) studies have been performed to investigate the mechanisms of organic reactions involving CO_2 where the zeolites act as catalysts.[11] Because zeolites are microporous materials, they are well-suited for applications in gas storage and separation, particularly the separation of air, natural gas, organic isomers, noble gases, and many other gases.[12] Additionally, the exchangeable nature of zeolite cations means that both natural[13] and synthetic[14] zeolites can be used to remove heavy and radio-active metal cations from aqueous solution, thus zeolites can be used for the treatment of polluted[15] or radioactive water.[16]

Many important properties of zeolites originate from the extra-framework cations within the frameworks, which are positively charged and feature electrostatic interactions that can be used to adsorb gases, organic molecules and other adsorbates.[17] The adsorption capabilities of ion-exchanged zeolites are highly dependent on the strength of the electrostatic interactions, which are determined by the specific cation types present, along with the Si/Al ratio and framework configuration of the host zeolite.[18] Although pure silica zeolites have shown interesting features and functions in some cases, the charge-neutral nature of pure silica means that very few or no cations are present to balance the charge of these zeolites. Thus, aluminosilicate zeolites, with their net negative charges, play a major role in various fields such as gas separation and adsorption. Several straightforward characterization techniques such as infrared studies,[19] neutron diffraction techniques,[20] pressure swing adsorption (PAS),[21] and molecular dynamics simulation studies,[22] have been employed to study how CO_2 guests interact with the extra-framework cations in zeolites,[18, 23] but relatively few studies have probed CO_2 guest dynamics at elevated temperatures.[24] Using SSNMR spectroscopy, the dynamic behaviour and motional patterns of adsorbed CO_2 guests can be examined within several ion-exchanged zeolites that have several industrial applications.[25]

In this study, ion-exchanged type X and Y zeolites from the FAU family along with type A zeolites from the LTA family have been prepared and loaded with NMR active $^{13}CO_2$ guest molecules to investigate the effects of different alkali and alkali earth cations

on CO_2 adsorption behaviour using ^{13}C SSNMR, which is a sensitive probe of adsorbed CO_2 guests in porous materials.[26] Understanding the differences in CO_2 guest behaviour within various ion-exchanged zeolites should shed light on the specific CO_2-cation interactions within zeolite structures, and it may also assist in the design of new synthetic zeolites with improved properties for applications in fields such as CO_2 separation and storage, as well as industrial gas purification.

3.1.2 FAU-Type Zeolites
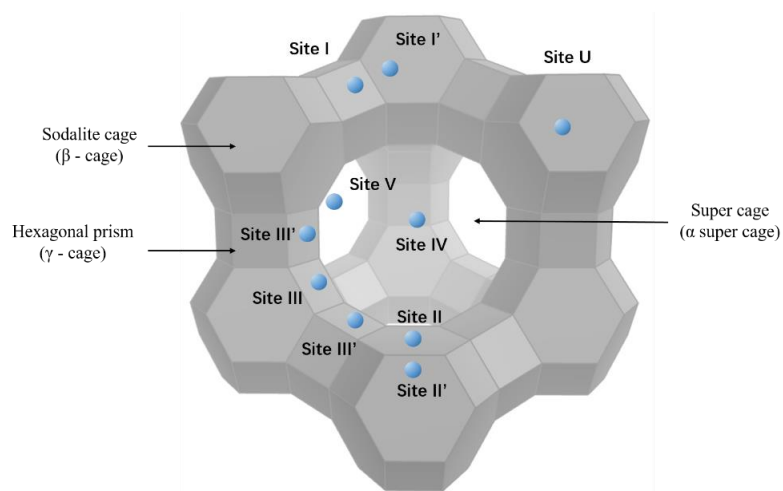
Figure 3-1 The Faujasite (FAU) zeolite framework structure is also shared by type X and Y zeolites, and places charge balancing cations at several available locations. Cation Site I is in the hexagonal prism, while Site I' sits outside the prism but in the sodalite cage. Site II places cations in the 6-member ring structure of a sodalite cage, on the ring plane or pointing towards to the α – super cage depending on the specific cation species. Site II' is found near Site II but is located inside the sodalite cage. Sites III and III' are found on the inner walls of an α – super cage. Site IV is located at the centre of the α – super cage, while Site V is found in the 12-member window connecting two adjacent α – super cages. Site U sits at the centre of the sodalite cages. Cations of the same species cannot occupy Sites I and I', II and II', or I and III simultaneously, due to the strong electrostatic repulsions between each site pair. Sites U, IV and V can only be found in the hydrated forms of these FAU-type zeolites.

Zeolites X, Y and the naturally occurring faujasite (FAU) zeolite share the same framework structure but have different Si/Al ratios. Type X is associated with a Si/Al ratio between 1.0 and 1.5, type Y has a Si/Al ratio between 1.5 and 3.0, and natural faujasite has a Si/Al ratio about 2.3.[27] Four types of cations (Na^+, K^+, Ca^{2+} and Mg^{2+}) are found in the natural faujasite zeolite.[27] Meanwhile, zeolites X and Y are typically synthesized with Na^+ cations, which can then be exchanged by other alkali and alkali earth metal ions, and even some transition metals.[28] Therefore, "zeolite Na-X" is a term referring to zeolite X that is loaded with Na^+ cations. If the sodium cations are replaced by some other ion, the atomic symbol of the newly incorporated ion will be used. For instance, if 70 % of sodium is exchanged by Ca^{2+} ions in Na-X, the name of the zeolite becomes Ca-X, or 10X. The corresponding effective pore diameter in the zeolite may also change as sodium is substituted by other cations.[27]

The space group of the FAU- type zeolite framework is F d $\overline{3}$ m, which describes a typical cubic system. In the FAU zeolite (Figure 3-1), each unit cell contains 192 Si, Al T-sites,[29] which form 8 α – super cages, 8 sodalite cages, 16 hexagonal prisms, 16 12-member rings connecting neighboured α – super cages, and 32 single 6-member rings connecting sodalite cages with α – super cages.[30] The unique structural features of FAU-type zeolites, including α - super cages, sodalite units (β – cages) and hexagonal prisms (γ – cages), are shown in Figure 3-1. The largest cages are α - super cages, which are approximate 12 Å in diameter, which are connected to 4 neighbouring α - super cages by 12-member rings with a diameter of 8 Å.[29] These α - super cages are where many catalytic reactions within zeolites take place, such as those involving gasoline and liquid fuels.[29, 31] There are also sodalite units with an internal diameter of 6.6 Å which are known as β – cages.[32] It has been proven that the Si/Al ratio affects the stability of the sodalite β – cages, and also influences the catalytic preference of zeolites for specific reactions.[33] Each β – cage is linked to four hexagonal prisms, known as γ - cages. Charge-balancing cations such as Li^+,[34] K^+,[35] Mg^{2+},[36] and Ca^{2+},[37] have been located at specific places in the FAU framework, however, the occupancy numbers of exchanged cations may differ and heavily depend on specific Si/Al ratios.[38] Simulations show that some extra-framework cations in zeolite X and Y may migrate throughout the cages at high

temperatures when CO_2 guests are loaded, and the specific movement paths and migration destinations can be affected by different CO_2 loading levels.[22b]

3.1.3 Cation distributions in Faujasite zeolite X, Y and LSX

The cation positions vary in the hydrated and dehydrated forms of zeolites. Several cation sites have been located in the FAU framework (Figure 3-1).[38] Cation Site I is found inside the hexagonal prisms and allows the cation to interact with nearby oxygen atoms. At Site I', cations are located near the side of the sodalite cage and proximate to the hexagonal window structure of the hexagonal prism, and can coordinate to the 3 oxygen atoms found on the hexagonal window. Site I and I' cannot be occupied simultaneously by the same cation species due to strong cation-cation electrostatic repulsion. Cation Site U can only be found in hydrated zeolite FAU, at the centre of sodalite cages. The cation Sites II and II' are very close to each other, near the 6-member-ring window, and Site II cation can penetrate into the α – super cage for a short distance.[38] Cations located at Site II cations are usually positioned in the 6-member ring plane, or outside the ring plane on the α – super cage side, while Site II' cations are found inside the sodalite cage. Site III cations occupy the square windows inside the α – super cage, between the middle of two nearby Site II hexagonal windows, while Site III' cations occupy the other two square windows. Additionally, Site IV cations can be found at the centre of α – super cages. Site V is found at the centre of the 12-member windows connecting two neighboured α – super cages. Among the many cation positions, Sites U, IV and V only exist in hydrated FAU type zeolites. Li and Na cations prefer to occupy sites in the order of Site II > I' > III, while K, Mg and Ca preferentially occupy Site II > I > III. Once these sites are fully occupied, the remaining cations are placed at Site III'.[38]

FAU zeolites X, low-silica X (LSX) and Y have the same framework topology, but the specific cation distribution varies according to their distinct Si/Al ratios.[38] In the dehydrated Na-X zeolite (Figure 3-2a), studies have shown that in each α – super cage, the total number of Site II positions occupied by Na^+ can be up to 4, Site I and I' positions can accommodate 4 – 6 cations, and Site III and III' can host 3 cations.[39]

Available cation sites in FAU zeolite X

Available cation sites in FAU zeolite K,Na-LSX

Available cation sites in FAU zeolite Y

(a)　(b)　(c)
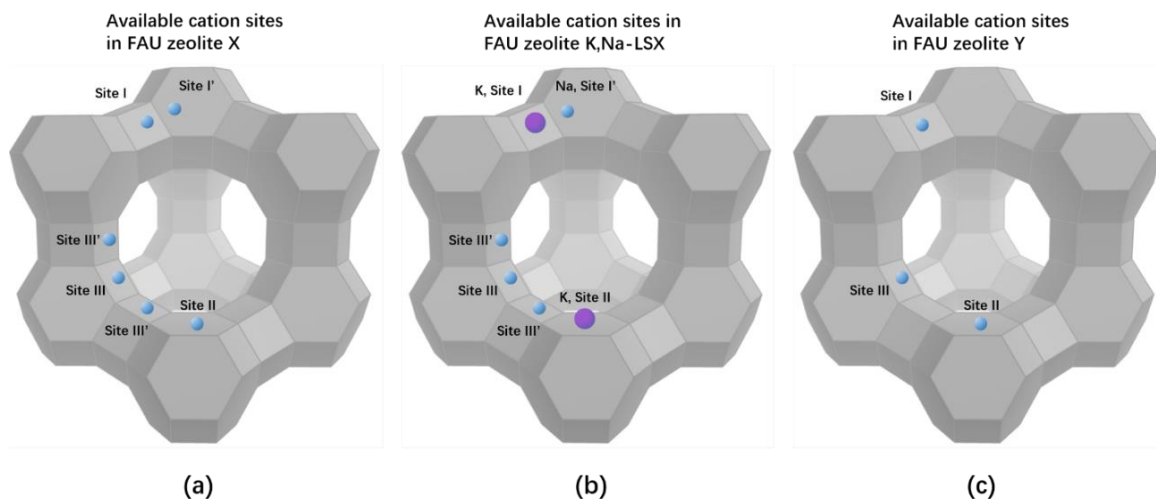
Figure 3-2 The cation distributions in Faujasite type (a) X, (b) LSX and (c) Y zeolites, with charge balancing cations shown on several of the well-defined cation locations. Not all cation positions have to be fully occupied.

In dehydrated LSX (Figure 3-2b), more cations can be found in each α –super cage due to the lower Si/Al ratios compared to type X zeolites. This is because a lower Si/Al ratio means that more aluminium atoms have been introduced into zeolite framework, bringing more net negative charges to be neutralized by charge-balancing cations. In each α – super cage, at Site II in these dehydrated LSX zeolites, 4 cations can be found, while Sites I and I' can be occupied by 3-4 cations in total. Sites III and III' together can host 5-8 cations.[40] Less cations are found in type Y zeolites (Figure 3-2c): the maximum numbers are 4 cations at Site II, 4 cations at Site I' and only 1 cation at Site III per α – super cage.[20b, 41]

3.1.4 LTA-Type Zeolites

Unlike FAU zeolites, LTA (Linde Type A) zeolites can only be obtained through synthesis and cannot be found in nature.[42] The space group of LTA-type zeolites is P m $\overline{3}$ m, a cubic system. Zeolite A is an LTA zeolite that is usually synthesized with sodium counter-ions, which is designated as zeolite 4A with an idealized unit cell composition of $Na_{12} \cdot (AlO_2)_{12} \cdot (SiO_2)_{12} \cdot 27\ H_2O$. When 45% of Na^+ cations are exchanged by

potassium, the zeolite is known as 3A, while 5A represents a calcium form when 80% of Na is replaced by Ca.[27]

In a typical 4A scheme (Figure 3-3), eight sodalite cages, noted as β – cages, are located on each corner of the unit cell, and are connected by eight γ -cages (four bridging oxygen atoms) to form one α - cage at the unit cell centre. The diameter of the α - cage is approximately 11.4 Å, while the sodalite cages have an inner diameter of 6.6 Å. The window structure connecting adjacent α – cages are 8-member rings, with ring apertures of 4.2 Å, but this size may vary slightly according to the specific cation types present.[43]
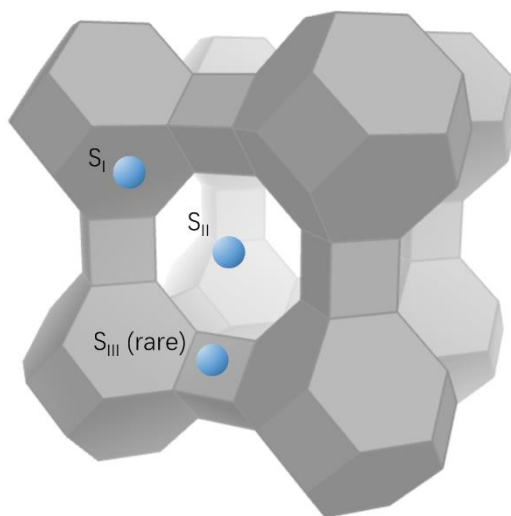
Figure 3-3 In the LTA zeolite framework, there are 12 cations per α –cage. S_I cations sit at eight 6-member ring structures, four S_{II} cations guard the 8-member windows connecting neighboured α –cages, while S_{III} cations at the 4-member squares are seldom reported.[43]

In the fully hydrated 4A framework, 27 water molecules can be found per unit cell. In each unit cell, two sites for charge-balancing cations have been reported. 8 of 12 sodium cations are located at cation site I, denoted as S_I, which is located near the centre of 6-member rings inside the sodalite cages. The remaining 4 sodium cations prefer the S_{II} site, which are positioned inside the eight-member ring windows facing the α – cage. The sodium cations in the S_{II} positions interact with H_2O molecules trapped in the α – cage.[43] In dehydrated zeolite 4A, sodium cations are found in distinct positions from the

hydrated form. In dehydrated 4A, the sodium cations at S_I move 0.4 Å towards the α – cage, and the 3 sodium cations at S_{II} shift about 1.2 Å from their original positions, guarding the 8-member rings which connect adjacent α – cages. Several different extra-framework cation locations in ion-exchanged LTA zeolite frameworks have been reported.[42-43]

3.1.5 Cation distributions in Linde type A zeolites

In dehydrated type A zeolites, only 12 charge-balancing cations are distributed within each α – cage and the cations are usually found on S_I, located above the hexagonal 6-member rings, and on S_{II}, located in the 8-member window connecting neighboured α – cages. S_{III} cations, which are located in the 4-member square structures in α – cages, are rarely found in dehydrated type A zeolites.[42, 44] For the purposes of ion exchange, Li^+, Mg^{2+} and Ca^{2+} prefer to substitute for Na^+ cations at S_I positions while K^+ usually occupies the S_{II} position.

3.1.6 Interactions with adsorbed CO_2 guests via cations in FAU and LTA zeolites

Zeolites are widely used as CO_2 adsorbents for industrial applications, and the interaction mechanisms between adsorbed CO_2 guests and charge balancing cations in zeolites have been studied in detail. Ward and Habgood,[45] Angell et al.,[46] and other groups have examined the CO_2-cation interactions in alkali and alkali earth metal exchanged FAU type zeolites X and Y, [20d, 47] and LTA type zeolite A.[23a, 48] Three types of CO_2 adsorption mechanisms in zeolites have been documented: physical adsorption, chemisorption to form carbonate-like species, and adsorption based on ion-polar interactions. The physical adsorption of CO_2 guests upon zeolite cations (Figure 3-4a) occurs between the positively charged zeolite cation and one negatively-charged oxygen atom of a linear CO_2 guest, while the positively-charged CO_2 carbon atom is attracted to oxygen atoms from nearby 6-member ring structures. There is also a contribution from Van der Waals dispersion forces. The whole CO_2 molecule is not perfectly linear in this case, because each atom from the physically adsorbed CO_2 separately interacts with cations or framework oxygen atoms.[45b] Chemisorption of CO_2 in zeolites is an interesting process (Figure 3-4b): one CO_2 oxygen atom is attracted to the zeolite cation, while the

CO_2 carbon atom forms a chemical bond with a framework oxygen atom near the zeolite cation, bending CO_2 guests away from linearity and into a "carbonate-like" configuration. This chemisorption is quite strong in many cases, for example, experiments have shown that the chemisorbed carbonate-like CO_2 molecule in the Mg-X zeolite will not desorb even after being heated up to 773 K.[46] The ion-dipole interaction (Figure 3-4c) is a common adsorption route found in most cation-neutral molecular interactions.[49] The positively-charged zeolite cation interacts with the partial negative charge localized on a neutral guest molecule, such as the oxygen atom in the CO_2 molecule or the carbon atom in the CO molecule. In this case, the ion-polar interaction between extra-framework cations and CO_2 molecule in zeolites is defined as electrostatic quadrupolar interaction[50] since CO_2 molecule has a quadrupolar moment.

(a)   (b)   (c)
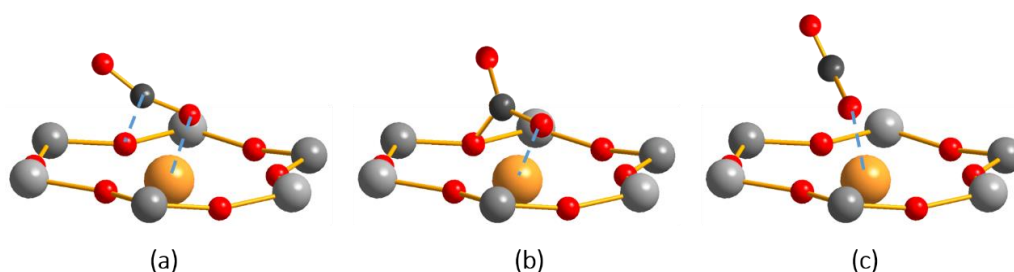
Figure 3-4 The three possible ways that CO_2 guests can interact with cations in FAU and LTA zeolite frameworks: (a) physical adsorption, (b) chemisorption resulting in the formation of a carbonate-like species using an oxygen atom from a nearby ring structure, and (c) ion-dipole interactions.

Guest CO_2 molecules are known to be adsorbed within α – super cage cavities,[23b, 51] and no reports have yet shown that CO_2 guests can enter the sodalite cages in both the FAU and LTA zeolite structures. The adsorption locations of CO_2 guests are also known: CO_2 guests prefers to adsorb upon Site II rather than Site III cations in FAU-type zeolites.[45b] In LTA zeolites, binary cation pairs of the form S_I-S_{II} or S_I-S_I [40] are the favoured adsorption sites for CO_2 molecules. It should be noted that some reports suggest that alkali earth cations in zeolites may form MOH^- ions, such as $MgOH^-$ species,[45b] rather than exposing the bare cation to the cavity interior, even in fully dehydrated zeolites. This cation-hydroxyl species could reduce the adsorption capabilities of guest molecules.

3.2   Experimental Section

3.2.1 Synthesis

In this study, ion-exchanged zeolites are noted in the form of "cation name – zeolite name", for instance, 13X is noted as Na-X and 3A is noted as K-A.

Zeolite 4A (Na-A, Strem Chemicals, Si/Al = 1, 600 mesh powder), Zeolite 3A (K-A, Union Carbide, Si/Al = 1, powder), 13X (Na-X, Strem Chemicals, Si/Al = 1.23, 600 mesh powder), NaY (Strem Chemicals, Si/Al = 2.35, powder), NH_4Y (HSZ-341 NHA, Tosoh Co., Japan, Si/Al = 3.3 – 3.8, powder) commercial products were directly used without any further purification.

The ion-exchanged zeolite samples Li-A, K-A, Ca-A, Li-X, K-X, Mg-X and Ca-X were synthesized following a modified ion-exchange procedure from Shepelev and his co-workers[34-36], which is outlined here 1.00 g of the commercial zeolite sample in sodium form (Na-A or Na-X) was placed in a 25 mL Teflon chamber, mixed with 20 mL of deionized water, and left unagitated for 24 hours at room temperature. The upper layer of solution was then decanted, and 20 mL of aqueous solution containing the chlorine salt of the cation to be introduced to the zeolite was poured into the Teflon chamber, which was then capped, sealed, and secured within a Teflon-lined stainless-steel autoclave. The sealed autoclave was then placed into an oven and heated at 383 K for 20 h. After the autoclave was removed from the oven and cooled down to room temperature, the upper layer of solution was removed and the solid zeolite sample at the bottom was washed with 25 mL deionized water, placed in a 50-mL plastic centrifuge tube, and centrifuged at a rate of 3300 rpm for 5 minutes, followed by a refill of 22 mL cation chloride solution to the zeolite sample. The entire washing, centrifuging and refilling procedure was performed three times between each heating procedure, while the heating procedure was repeated for five times. The 383 K heating duration of the last cycle was chosen to be 46 h in order to ensure the original sodium cations in the zeolite framework were exchanged with the target cations at the maximum ratio. After the final washing and centrifuging cycle, the ion-exchanged zeolite samples were put in an oven and dried at 363 K for 24 hrs. The Mg-A zeolite could not be synthesized due to hydrolysis effects of LTA type zeolites in $MgCl_2$ solutions, which may cause structural decomposition; see Figure S3-4

in the appendix. The cation/chloride salts used and the concentration of solutions in these ion-exchange experiments were: 1.0 M LiCl (Caledon, 99 wt %), saturated KCl (BDH chemicals, 99.0 – 100.5 wt %), 0.6 M MgCl$_2$ (MgCl$_2$·6H$_2$O, Caledon, 99.0 – 102.0 wt %) and 0.6 M CaCl$_2$ (BDH chemicals, 96.0 wt %).

Hydrogen-incorporating H-Y zeolites were synthesized through a calcination process.[52] The commercial NH$_4$Y (HSZ-341 NHA, Tosoh Co., Japan, Si/Al = 3.3 – 3.8) zeolite was put in a glass vial and heated at 413 K for 18 h as the pre-dehydration step. Then in the calcination step, the NH$_4$-Y sample was placed in a crucible and heated in a furnace, with the temperature increased at a rate of 3 K / min from room temperature to 573 K. The calcination temperature of 573 K was then held for 1 h. The zeolite sample was then subjected to a second heating progress, where temperatures were brought up at a rate of 3 K / min to 873 K and then held at this level for another 3 h. After this second heating process, the oven was then gradually cooled down to room temperature and the zeolite H-Y products were collected.

A type of zeolite X with a low Si / Al ratio called low-silicate X or LSX was synthesized using a hydrothermal method.[53] The starting reagents were sodium hydroxide (NaOH, Caledon, pellets, 97.0%), potassium hydroxide (KOH, Fisher Chemical, pellets, 87.0%), sodium aluminate anhydrous (NaAlO$_2$, Riedel-de Haën, 50-56% as Al$_2$O$_3$) and sodium meta-silicate pentahydrate (Na$_2$SiO$_3$·5H$_2$O, Fisher Chemical, 54% as Al$_2$O$_3$). The molar composition of the initial mixed gel was 5.5 Na$_2$O : 1.65 K$_2$O : 1.0 Al$_2$O$_3$: 2.0 SiO$_2$: 122 H$_2$O. In a typical run, 3.64 g KOH and 3.62 g NaOH were dissolved into 18.5 mL of deionized water in a beaker and stirred vigorously for 10 min. In a second beaker, 3.22 g sodium aluminate was dissolved into 10.9 mL of water, followed by stirring for 5 min. The mixture in the second beaker was then added into the mixture within the first beaker while stirring. To the resulting mixture, 9.13 g of sodium meta-silicate and 10 mL water were added. This final mixture was stirred at room temperature for 10 min and then equal parts were decanted into three 25 mL Teflon-lined containers, which were then capped, secured, and sealed within Teflon-lined autoclaves. The autoclaves were placed in an oven pre-heated at 343 K and left for 3 h. The autoclaves were then transferred into another oven preheated at 373 K and left for 18 h. Following this procedure, the

autoclaves were taken out from the ovens and cooled down gradually to room temperature, and then the upper layer of liquid in all autoclaves was decanted off. The remaining solid phase was washed with a 0.01 M NaOH solution to avoid problems associated with excessive washing and hydrolysis in a 50 mL plastic centrifuge tube, and centrifuged at a rate of 3300 rpm for 5 minutes. The entire washing and centrifuging procedure cycle was repeated for three times, and the resulting products were air-dried at room temperature.

The commercial, synthesized and ion-exchanged zeolite samples used in this work are listed in Table S3-1.

3.2.2 Activation process

To load $^{13}CO_2$ guest molecules into the zeolite samples, all absorbed H_2O molecules must first be completely removed from the zeolites through an activation process, or the residual H_2O in zeolites may block preferred cation locations and influence CO_2 adsorption and the corresponding SSNMR spectra. To completely dehydrate the zeolite samples, a Schlenk line was employed. First, ca. 0.60 g of the hydrated zeolite sample was placed at the bottom of a 10 mm L-shaped glass tube. Then a small patch of glass wool was used to secure the zeolite sample within the bottom of the glass tube. The L-shaped glass tube containing the zeolite sample was then attached to the Schlenk line, which was connected to a vacuum pump and a pressure gauge to ensure the pressure under dynamic vacuum was ≤ 1 mbar. The sample zeolite was then first heated to 343 K for 1 h to remove loosely absorbed H_2O molecules. Then the temperature was raised by 110 K and held for 1 h three times in a row until reaching a final temperature of 683 K, and the heat was then maintained at 683 K for 22 h. It should be noted that an exception is NH_4-Y, where ca. 0.20 g of NH_4-Y zeolite was placed in a 5 mm L-shaped glass tube. And the activation temperature for NH_4-Y was conducted at 433 K[54], which is much lower activation temperature than that used for other zeolite samples due to the decomposition of NH_4^+ at higher temperatures.

After this process was complete, the sample was then gradually cooled down to room temperature under vacuum conditions to obtain the empty or "activated" zeolite

sample. Static ^1H SSNMR spectra of each zeolite sample were acquired after the activation procedure to ensure the zeolites were completely dehydrated. The ^1H SSNMR spectra (shown in Figure S3-1) did not contain any resonances corresponding to H_2O, indicating that all water molecules in zeolites had been removed completely in the activation procedure.

3.2.3 Gas adsorption

^{13}C isotopically labeled and enriched $^{13}CO_2$ (Sigma-Aldrich, 99% ^{13}C) was used as the guest molecules due to the low abundance (0.96%) of ^{13}C in nature, and $^{13}CO_2$ is simply denoted as CO_2 in this work. The gas adsorption process was performed after the activation process. A small quantity of isotopically labeled $^{13}CO_2$ molecules were transferred from a gas cylinder to an empty round bottom flask. The flask was then attached to a Schlenk line and a known amount of gas was released to the Schlenk line, which occupies a volume of 82.7 mL in total. The bottom of the L-shaped glass tube was kept in liquid nitrogen to condense all CO_2 guest molecules into zeolite samples until the pressure gauge showed a dynamic pressure of 0 mbar. A flame-sealing procedure was then performed to isolate the L-shaped glass tube from the Schlenk line with guest molecule loaded zeolite samples, which was then used for SSNMR experiments.

The gas loading level in the zeolite was expressed by the amount of CO_2 molecules per α - cage in the zeolite. A loading level of 1.12 guest molecules per α – super cage in type X and LSX zeolites (1.12 CO_2 / α - super cage), 1.30 in NH_4-Y, 1.42 in H-Y and 1.76 molecules in Na-Y per α – super cage in type Y zeolites (1.30 ~ 1.76 CO_2 / α - super cage) were used in this study. A loading level of 1.38 CO_2 per α - cage (1.38 CO_2 / α - cage) was used for the type A zeolites.

3.2.4 Powder X-ray diffraction (pXRD)

Powder X-ray diffraction (pXRD) experiments were conducted to identify the purity and crystallinity of commercial, ion-exchanged and synthesized zeolite samples. The pXRD experiments were carried out using a Rigaku diffractometer with Co K_α radiation ($\lambda = 1.7902$ Å) as the radiation source. The zeolite powder samples were scanned through

2θ values from 5 to 50° with an increment of 0.02° at a scanning rate of 10° / min. The experimental pXRD powder patterns are shown in the appendix, and indicate that the samples of FAU type X, Y and LSX zeolites and LTA type A zeolites are pure and of good crystallinity, as determined by comparing simulated powder patterns based on crystal structures to the experimental pXRD data. The results of pXRD experiments are shown in Figure S3-2, Figure S3-3 and Figure S3-4.

3.2.5 ICP-MS characterization

Inductively coupled plasma - mass spectrometry (ICP-MS) characterization was employed to precisely examine the M/Na ratio in ion-exchanged and as-made LSX zeolite samples. The zeolite samples weighed 0.0010 g each. Samples were first dissolved in 10 mL concentrated HNO_3 (Anachemia, 68.0% - 70.0%), and then diluted to 1 ppm while the final concentration of HNO_3 in the sample solutions was kept at 3%. The characterization was conducted on a Thermo Scientific iCAP Q ICP-MS instrument, and was performed to examine the concentration of Li, Na, K, Mg, Ca, Al and Si elements in zeolite samples. The instrument sample camber was first rinsed with a 2 % HNO_3 solution, and then standard solutions containing K and Si at concentrations of 100 ppb, 500 ppb, 1000 ppb and 2 ppm were used as references to check the instrument accuracy. A control group containing 2 % HNO_3 (Anachemia, 68.0% - 70.0%) which was used to dissolve zeolite samples was also examined by the ICP-MS instrument to obtain and eventually subtract the background ion concentrations.

The ion-exchange ratio was calculated based on ICM-MS characterization results. The calculated ion-exchanged ratios and original mass concentration are listed in Table 3-4 and Table S3-5, respectively.

3.2.6 Direct-excitation VT ^{13}C SSNMR characterization

SSNMR experiments were conducted using a Varian Infinity Plus spectrometer, equipped with a wide-bore 9.4 T Oxford Instruments superconducting magnet and a double channel (HX) 5/10 mm Varian/Chemagnetics static probe. The experimental temperature was adjusted between 123 K and 293 K using a Varian VT temperature control unit and the experimental temperature readings were calibrated by the ^{207}Pb

chemical shift of solid $Pb(NO_3)_2$.[55] Direct-excitation ^{13}C SSNMR experiments were conducted using the DEPTH-echo pulse sequence.[56] The chemical shift of all ^{13}C spectra were referenced to tetramethylsilane (TMS) using the methylene carbon of ethanol at 56.83 ppm as a secondary reference.[57]

For VT ^{13}C SSNMR static experiments of CO_2 loaded zeolite samples, an optimized ^{13}C 90° pulse length between 4.40 – 5.60 μs was used, depending on the 10 mm static probe hardware calibrations. For the NH_4Y sample, which was examined using a 5 mm static probe, the calibrated 90° pulse length was 2.50 μs. A calibrated recycle delay ranging from 1-5 s was used for sample acquisition temperatures between 293 K and 173 K, and calibrated recycle delays of 3 - 7 s were used within the temperature range from 173 K to 123 K. Each ^{13}C SSNMR spectrum was assembled from 402 to 1336 scans, except for the 293 K room temperature spectra, which were assembled from 1046 to 12067 scans.

3.2.7 Direct-excitation ^1H SSNMR characterization

For the static ^1H SSNMR experiments examining the dehydration of zeolite samples, the one-pulse sequence was employed with a calibrated 90° pulse length of 15 μs, using a static 10 mm HX probe. The calibrated recycle delay was 10 s for each zeolite sample at 293 K. The chemical shift of all ^1H spectra were referenced to tetramethylsilane (TMS), using the methyl hydrogen resonance of ethanol at 1.17 ppm as a secondary reference.[57] Two 10 mm L-shaped glass tubes of vacuumed empty, and CO_2 loaded but otherwise empty tubes were tested to measure the background noise generated from the glass tube and CO_2 guests. Each ^1H SSNMR spectrum was assembled from 64 scans.

3.2.8 Cross-Polarization (CP) ^1H-^{13}C SSNMR experiments

Static ^1H-^{13}C cross polarization SSNMR experiments were performed on HY and NH_4Y zeolites at 293 K using the 10 mm HX static probe. These experiments were conducted on both the activated (empty) and CO_2 loaded zeolite samples to investigate guest adsorption locations and behaviour. The CP experiments were performed using contact times of 0.5, 5, and 10 ms. All CP experiments used a recycle delay of 1 s and the

spectra of CO_2 loaded HY and NH_4Y samples were assembled from 19000 scans. The activated empty HY and NH_4Y spectra were acquired using 20573 and 13232 scans, respectively.

3.2.9 Chemical shift (CS) tensor convention and SSNMR simulations

The ^{13}C powder patterns in this study are broadened and dominated by the chemical shift (CS) interaction. The CS interaction can be modeled by a second-rank tensor defined by the three orthogonal components δ_{11}, δ_{22} and δ_{33}, which are ordered such that $\delta_{11} \geq \delta_{22} \geq \delta_{33}$. There are three NMR parameters that are used to describe SSNMR powder pattern lineshapes and the CS tensor: the isotropic chemical shift (δ_{iso}, $\delta_{iso} = (\delta_{11} + \delta_{22} + \delta_{33})/3$), the span ($\Omega$, $\Omega = \delta_{33}-\delta_{11}$), and the skew ($\kappa$, $\kappa = 3(\delta_{22} -\delta_{iso})/\Omega$).

The WSolids[58] simulation package was used to extract the observed or apparent CS parameters of CO_2 guest from experimental static ^{13}C NMR spectra of various zeolite samples. The EXPRESS[59] simulation package was employed to obtain motional information of CO_2 guest from static VT ^{13}C NMR spectra by comparing the apparent CS parameters (from WSolids simulations) to the known parameters for static, stationary CO_2 of $\delta_{iso} = 125$ ppm, $\Omega = 335$ ppm, and $\kappa = 1$.[60] The localized rotation of CO_2 guest molecules is modeled by a three-fold "wobbling" motion,[26a] where the three-fold "wobbling" means a continuous and localized motion upon the single adsorption cation in a cone defined by the motional angle θ (Figure 3-5). The rate of all motions was considered as "intermediate" (i.e. $\geq 10^5$ Hz).
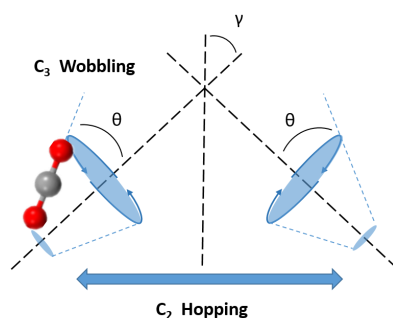
Figure 3-5 The well-defined, localized C_3 wobbling motion through a cone with the angle θ, and inter-site non-localized C_2 hopping motion between two C_3 sites in the angle γ of a CO_2 guest.

3.3   Results and discussions

3.3.1 VT ^{13}C SSNMR experiments of CO_2 loaded FAU type X zeolites

To reveal the changes in CO_2 adsorption behaviour caused by different cations in FAU type X zeolites, SSNMR VT experiments on ion-exchanged and CO_2 loaded zeolite X samples were performed. The type X zeolite samples tested in this work are Li-X, Na-X, K-X, Mg-X and Ca-X. The ^{13}C NMR spectral lineshapes of CO_2 guests within these type X zeolites can be grouped into three separate categories: alkali metal (Li, Na and K) exchanged, alkali earth metal exchanged Mg-X, and the third category of Ca-X. All three categories of ion-exchanged zeolites show very distinct CO_2 lineshapes in VT experiments from 293 K to 123 K.

From 293 K to 193 K, the ^{13}C spectra of alkali metal exchanged zeolite X samples (Na, Li and K) only give rise to a single sharp resonance at 125 ppm (Figure 3-6a-c). The ^{13}C spectral width of the Li, Na, K-X zeolite samples at 293 K are only 2.0, 2.5 and 3.0 ppm respectively, due to the fast tumbling motion of CO_2 guests in the α – super cages of type X zeolites. These α – super cages have a relative large pore size of 12 Å and a symmetric geometry in the FAU zeolite unit cell.[43] The migration of CO_2 guests from one α – super cage to another adjacent one does not contribute any broadening to ^{13}C spectral lineshapes due to the high tetrahedral symmetry of α – super cage distributions in the FAU unit cells. The adsorbed CO_2 guests only very weakly interact with alkali metal cations and are rapidly tumbling through space, corresponding to narrow and sharp resonances from 293 K to 173 K.

The ^{13}C resonances broaden as experimental temperatures decrease, indicating that the mobility of free CO_2 guests is reduced. At each given temperature within the temperature range from 163 K to 123 K, the ^{13}C spectra feature similar, broadened lineshapes, suggesting similar CO_2 adsorption in the Na-X, Li-X, and K-X zeolites. The powder pattern span increases with decreasing temperatures. At 123 K, the lowest experimental temperature, CO_2 guests in all three samples have asymmetric, very broad ^{13}C spectra lineshapes that resemble those of solid CO_2, indicating that CO_2 molecules in the zeolites at 123 K are almost immobilized. The ^{13}C CS spans are around 320 ppm at

123 K (Figure 3-6), which are very close to reported span of 335 ppm for rigid static CO_2 molecules.[60]

Na-X will be discussed first. The asymmetric lineshapes and broad span of this resonance suggest that CO_2 guests adsorbed upon Site II Na^+ cations are almost immobile. Crystallographic reports suggest that in each α – super cage of dehydrated Na-X (Figure 3-8a), 4 Na^+ cations are positioned at Site II and 3.35 Na^+ cations are located at Site I'. The remaining 3.41 Na^+ cations are at Site III, leaving Site I vacant based on the Si/Al ratio and the known sodium site occupancy preferences.[29] In this study, because CO_2 in type X zeolites was loaded at a level of 1.12 guests per α – super cage, CO_2 guests should primarily adsorb at one of the four Site II Na^+ cation positions,[23b] and there should be no strong CO_2- CO_2 interactions. Thus, in Na-X, as the temperature is gradually decreased, the freely tumbling CO_2 guests are gradually adsorbed upon Site II Na^+ cations in the α – super cages, until CO_2 guests are almost immobile at 123 K. Figure 3-7a shows that an additional ^{13}C resonance with a span of 80 ppm centred around 150 ppm can be observed at 123 K, which corresponds to mobile CO_2 guests tumbling at a relatively slow rate in the α – super cages.

The ^{13}C SSNMR spectra of CO_2 guests adsorbed in Li-X started showing broad lineshapes at and below 173 K, and feature a very broad resonance at 123 K. This broad resonance has a span of 310 ppm. Much like in Na-X and K-X, this ^{13}C span is very close to the reported one for solid CO_2 (335 ppm),[60] suggesting that CO_2 guests are almost immobilized in this Li-X system as well. Crystallographic reports have suggested that when the zeolite is fully dehydrated, Li^+ cations first occupy Site II in the 6-member ring plane, and significantly distort the framework structures by generating strong interactions with oxygen atoms from framework.[34] Then, Li^+ cations may replace Na^+ cations at Site I' near the hexagonal prism window. Substitution of Li at Site I inside the oxygen hexagonal prism is unfavorable due to the small cation radius of Li.[34] It has been claimed that Li^+ cations exist at Site III and III' when the exchange ratio is high.[38] But in this study, as shown in Figure 3-8b, Li^+ cations only fully occupy 4 Site II positions and 1.24 Site I' positions, leaving 2.76 Na^+ cations to occupy the rest of the Site I' positions in the sodalite cages and also the 2.76 cation positions at Site III in α – super cages. CO_2 guest adsorption on the Site II Li^+ cations (Figure 3-8b) gives rise to the very broad powder

124
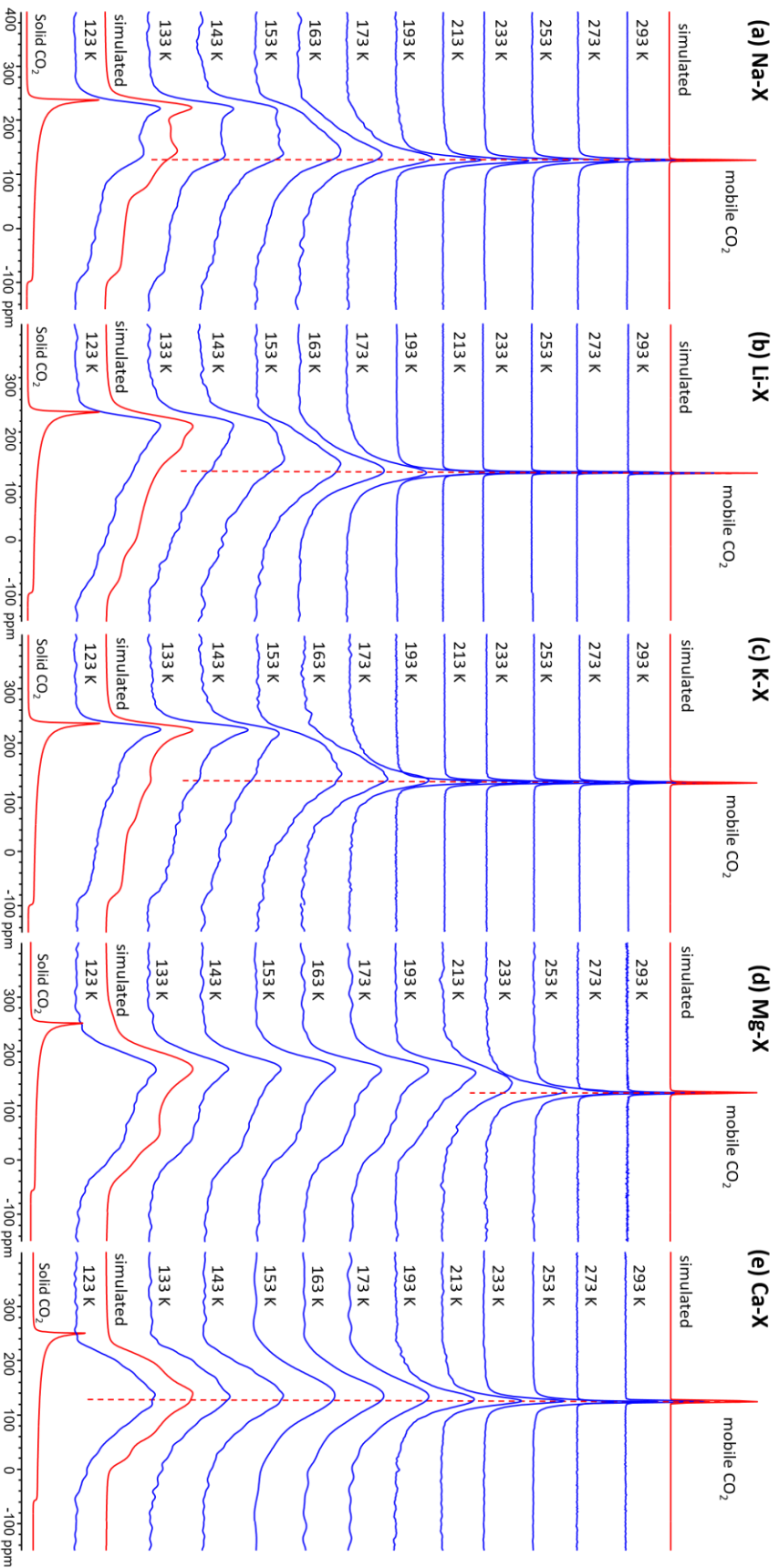
Figure 3-6. The figure shows ^{13}C NMR spectra reflecting similar CO_2 guest behaviour in three groups: (1) when adsorbed in (a) Na, (b) Li, and (c) K, (2) in Mg exchanged type X zeolite, and (3) in Ca-X. The CO_2 guest only yields detailed powder patterns below 173 K in most cases. The ^{13}C NMR spectra clearly indicate that various alkali and alkali earth cations have significantly different influences on CO_2 guests within the experimental temperature range.

pattern, and CO_2 is nearly immobile upon Li. There is again another minor contribution to the ^{13}C powder pattern at 123 K from a small component (Figure3-6b) with a span of 200 ppm. The second resonance suggests that at the lowest experimental temperature of 123 K, there was still some loosely adsorbed or free CO_2 guests undergoing slow tumbling motions, much like mobile CO_2 in Na-X and K-X at 123 K. The second powder pattern is slightly broader here than in Na-X or K-X, suggesting that free CO_2 in Li-X is less mobile.
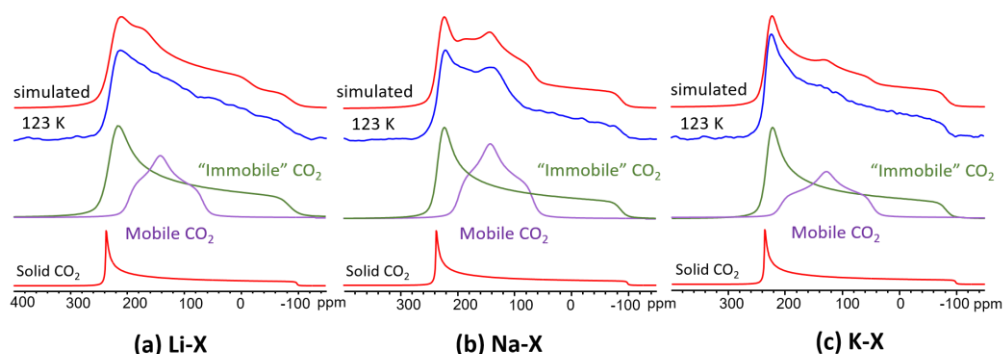
Figure 3-7. Simulated static ^{13}C SSNMR spectra of CO_2 guests at the lowest experimental temperature of 123 K in (a) Na-X, (b) Li -X and (c) K-X zeolites. Resonance contributions from different CO_2 status are labelled. All powder patterns were simulated using two components, see text for details.
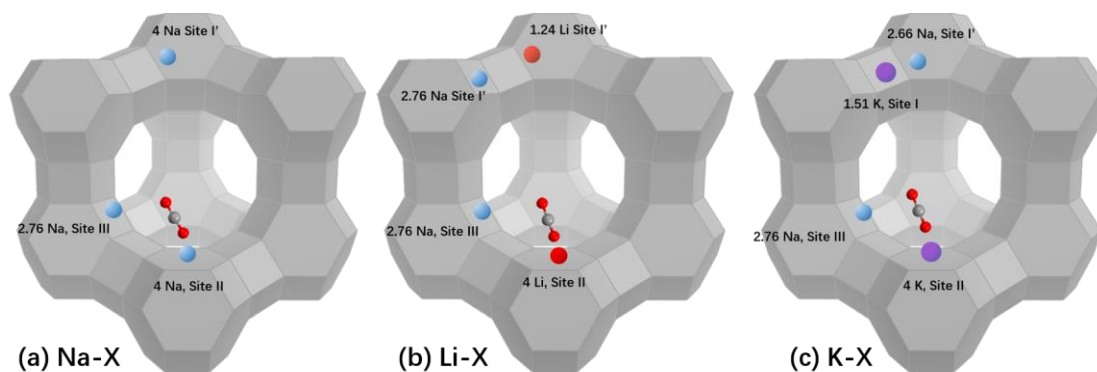
Figure 3-8. The exchanged cation distributions and site numbers for alkali-exchanged type X zeolites.[38] The possible CO_2 guest locations and behaviour in these zeolites is also shown. In (a), it can be seen that Li^+ cations in Li-X prefer to occupy Site I' and Site II. In (b), the Na^+ cations in Na-X are located at Sites I & I', Site II, and Sites III & III'. In (c), the figure shows that ion-exchanged K in K-X is located at Sites I, I', and Site II. The loading level of CO_2 guest in this work is about 1.2 guest per α – super cage.

In K exchanged zeolite X, potassium cations appear to have similar adsorption properties as sodium cations, judging from the similarities in the associated ^{13}C lineshapes of guest CO_2 (Figure 3-6c). The ^{13}C powder patterns of CO_2 guests also begin to feature asymmetric powder patterns at 173 K and lower temperatures. At 123 K, the ^{13}C spectrum is similar to that of CO_2 in Na-X, with a very broad span of 310 ppm. This broad resonance indicates that adsorbed CO_2 guests are nearly immobile. Crystallographic reports of K-X have revealed that K^+ cations prefer to first substitute for Na^+ cations at Site II on the 6-member window position, followed by the exchange of Na^+ cations on Site I, and then finally a substitution at Site III.[35, 38] In this study, as shown in Figure 3-8c, the potassium exchange ratio of 51.16% in type X zeolites means K^+ cations have replaced all four Na^+ cations from Site II and some Na^+ cations at Site I positions, leaving the Site I' positions occupied by Na^+ cations. Meanwhile, the remaining 2.76 Na^+ cations remain at Site III in α – super cage. Thus, all of four Site II positions are occupied by K^+ cations, and CO_2 guests would primarily adsorb upon these K-occupied Site II positions. Thus, the very broad and asymmetric resonances observed from ^{13}C spectra of adsorbed CO_2 guests in the K-X zeolite are due to the adsorption and near-immobilization of CO_2 guests onto K^+ cations at Site II.[23b] Simulation results (Figure 3-7c) also suggest that a second resonance hidden in the centre of the broad powder pattern has a spectral width of 100 ppm with relatively weaker intensity, due to a small amount of mobile CO_2 that remains in the α – super cages undergoing slow tumbling motions. It should be pointed out that this narrow centre resonance is relatively more intense in the ^{13}C SSNMR spectrum of Na-X than it is in K-X, indicating that K^+ cations may adsorb CO_2 more strongly than Na^+ cations.

The ^{13}C SSNMR spectra of CO_2 adsorbed in alkali earth metal (Mg and Ca) exchanged zeolite X are shown in Figure 3-6d and 3-5e. These alkali earth cations influence CO_2 guest adsorption behaviour in a distinct way from alkali metals in type X zeolites, due to the higher positive charge and higher charge densities of Mg^{2+} and Ca^{2+} cations. The different ^{13}C spectral lineshapes of Mg-X and Ca-X may indicate a difference in cation distributions and CO_2 adsorption mechanisms in these zeolites.
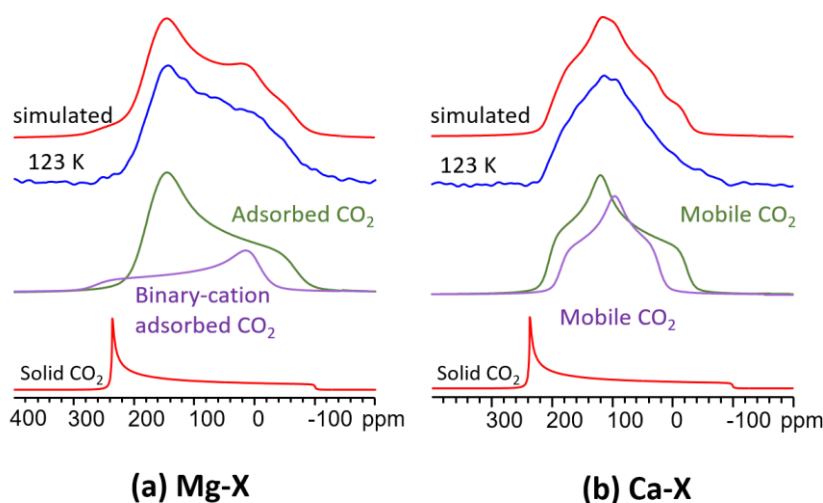
Figure 19-9. Simulated static ^{13}C SSNMR spectra of CO_2 guests at the lowest experimental temperature of 123 K in (a) Mg-X and (b) Ca-X zeolites. The powder patterns of Mg-X were simulated using two components, while one component was used for the simulation of Ca-X, see the text for details.

Within the temperature range from 293 K to 213 K, the ^{13}C SSNMR spectra of CO_2 adsorbed in Mg-X feature a sharp and narrow resonance at 125 ppm, which is associated with mobile CO_2 undergoing fast tumbling motions. At lower temperatures, from 193 K to 123 K, the ^{13}C resonance becomes asymmetric and broader as temperature is reduced, suggesting that adsorbed CO_2 guests have significantly reduced mobility and are interacting with zeolite cations. The powder pattern at 123 K, shown in Figure 3-9a, has a span of 230 ppm, which is less than that of solid CO_2, and also less than that of the immobile CO_2 guests adsorbed within alkali metal exchanged zeolite X samples at the same temperature. The relatively narrower span in Mg-X indicates that adsorbed CO_2 guests are not significantly immobilized in this case, and must undergo some sort of restricted dynamic motions within the α – super cage of Mg exchanged zeolite X.

The unique ^{13}C SSNMR powder pattern and adsorption behaviour of CO_2 guests in Mg-X can be explained by the unique crystallographic structure and Mg^{2+} cation distribution in Mg-X (Figure 3-10a). In partially exchanged Mg-X and under the conditions of this study, the most preferred site for magnesium substitution is Site II, where the Mg^{2+} cation can maximize its interactions with ring oxygen atoms. Only half of the Site II 6-member ring windows can be filled by Mg^{2+} cations for charge-balancing

purposes, leaving the rest of Site II positions vacant. However, the Mg^{2+} cation generates a more significant local electrostatic field and has a higher charge density than that of Na^+. The Mg^{2+} cations can interact with oxygen atoms from the Site II 6-member window, narrowing and distorting the 6-member windows and nearby ring structures. The size of 6-member window in Mg-X is significantly smaller than that in alkali-exchanged zeolite X and Ca-X.[36] The smaller window size and stronger electrostatic field generated by Mg^{2+} cations means that a large portion of the Mg^{2+} cation positive charge is balanced by nearby the negative charges on oxygen atoms on the 6-member ring structure, leaving Mg^{2+} with a relatively weaker electrostatic interaction to adsorb CO_2 and restrict CO_2 guest mobility. The weakened electrostatic interactions with Mg^{2+} allow the adsorbed CO_2 guests to have some mobility upon Mg^{2+} cations, which results in a narrowed ^{13}C powder pattern span. Moreover, the ^{13}C spectra lineshapes of Mg-X are very similar in VT experiments from 193 K to 123 K and no major changes are observed, which indicates that CO_2 molecular motion does not change significantly in this temperature range. According to ^{13}C spectral simulation results (Figure 3-10a), we propose that the more intense powder pattern with a positive skew is due to adsorption of CO_2 guests upon Site II Mg^{2+} cations. There is second, low intensity powder pattern observed from simulation results with a significant span of 240 ppm but a negative skew of -1.0. Additionally, the narrowing effect of Mg^{2+} on the six-member oxygen windows may further displace other cations in nearby ring structures and result in significant differences in CO_2 adsorption. The second preferred Mg^{2+} cation exchange site is Site I, but in this work, only 0.67 Mg^{2+} cations are found at this position per α – super cage. However, the Site I Mg^{2+} cation does not contribute to CO_2 guest adsorption due to being fully blocked by the hexagonal prism.[38] This means that the remaining 2.6 Site III Na^+ cations in each α – super cage may have participated in CO_2 guest adsorptions. The second ^{13}C powder pattern could be due to binary adsorption of CO_2 guests between Site II Mg^{2+} cations and Site III Na^+ cations, which means that these cations adsorb CO_2 guests in between their cation positions. This possible binary-cation adsorption of CO_2 has been observed and confirmed to occur in Na-A[23a] and Ca-A[48d]. The distance from Site II to Site III cations is estimated to be 6.5 Å, which is long enough to adsorb one CO_2 guest in between.

Figure 3-10. The possible CO_2 guest locations and behaviour have been shown, but the mobile CO_2 guest is omitted in the figure. The exchanged cation distributions and occupation numbers of alkali earth metal cations in type X zeolites are also provided. In the Mg-X zeolite shown in (a), Mg^{2+} cations are only found in Site I and Site II,[40b] and CO_2 guests undergoing wobbling motions are adsorbed upon Mg^{2+}, or are adsorbed by Mg-Na binary cation interactions. In the Ca-X zeolite in (b), only 1 Ca^{2+} cation occupies Site I, while the CO_2 guest may have weak interactions with Ca^{2+} cations.

For the other alkali earth metal zeolite in this work, Ca-X, the ^{13}C SSNMR lineshapes of CO_2 guests suggest that CO_2 guests may not interact as strongly with Ca^{2+} cations as was observed for other metal-exchanged zeolites. This is likely linked to the low exchange rate of Ca^{2+} of 18.58%. Within the experimental temperature range from 293 K to 153 K, CO_2 guests produce a featureless and broad single resonance, which becomes even broader as experimental temperatures decrease (Figure 3-6e). From 293 K to 193 K, CO_2 guests are isotropically tumbling, and from 193 K to 123 K, CO_2 guests are only weakly adsorbed and seem to still have a large degree of motional freedom. The width of this resonance increases from 4.5 ppm at 293 K to 180 ppm at 123 K, suggesting that the CO_2 guest mobility was temperature-dependent.

The existence of free CO_2 guests in Ca-X where none were observed in Mg-X can be explained by the greater ionic radii, the weaker electrostatic fields, and the lower degree of exchange of of Ca^{2+} cations (18.58%) versus Mg^{2+} cations (50.49%). Crystallographic studies suggest that calcium prefers Site II of the 6-member ring windows, yielding a relatively larger and less distorted window structure compared to that of Mg-X.[37] Site III

being occupied by Ca^{2+} has seldom been reported.[38] According to the exchange ratio of Ca-X in this work, there is a low occupancy of Ca^{2+} on Site II windows of only 1 cation per α – super cage. Because only one Ca^{2+} cation can be found from the four Site II positions in each α – super cage, and these ^{13}C SSNMR spectra indicate weaker adsorption of CO_2 guests (Figure 3-9b), the acquired ^{13}C spectra are hypothesized to be the result of a distribution of weakly adsorbed CO_2 upon Site II Ca^{2+} cations, which are randomly distributed in α – super cages. No ^{13}C resonance due to CO_2 adsorption upon Site II Na^+ cations was observed.

From 143 K to 123 K, the powder patterns are asymmetric with some lineshape features, corresponding to a span of 180 ppm at 123 K. This is due to stronger adsorption of CO_2 guests on Site II Ca^{2+} cations (Figure 3-10b) at the lowest temperature. This increase in spectral breadth and the appearance of lineshape features means that the mobility of CO_2 guests has further been reduced, and CO_2 may be undergoing restricted motions upon the Site II Ca^{2+} cations. However, these Site II Ca^{2+} cations are randomly distributed and not of crystallographic equivalency in each α – super cage, so the overall lineshape contributions of adsorbed CO_2 guests yields a distribution of CO_2 orientations and motional parameters, giving rise to a ^{13}C SSNMR spectrum that appears similar to a Gaussian distribution.

In summary, adsorbed CO_2 guest behaviour is diverse and varied across the alkali and alkali earth metal cation-exchanged forms of zeolite X, resulting in distinct ^{13}C SSNMR spectral lineshapes at and below temperatures of 193 K. At the lowest experimental temperature of 123 K, the CO_2 guest tends to be condensed and almost immobile when adsorbed upon Site II alkali metal cations (Li^+, Na^+ and K^+) in exchanged-X zeolites; while the presence of alkali earth cations (Mg^{2+} and Ca^{2+}) in exchanged-X zeolites results in increased mobility of the adsorbed CO_2 guests, although CO_2 still undergoes restricted and well-defined motions. The nature of the cations and their distribution within zeolite X are the main reasons why the ^{13}C spectra of CO_2 guests in various ion-exchanged zeolite X are different.

3.3.2 VT ^{13}C NMR experiments of CO_2 loaded FAU zeolite LSX

In aluminosilicate zeolites, the structure consists of partial aluminum substitution of a pure-silica zeolite framework, yielding a zeolite consisting of $Si(IV)O_4$ and $Al(IV)O_4$ tetrahedral sites (T-sites). The aluminum substitution ratio, known as the Si/Al ratio, determines the physical and chemical properties as well as potential applications of corresponding aluminosilicate zeolites. The Si/Al ratio may vary from 1 in LTA type zeolites to $+\infty$ in pure silica zeolites. Zeolites with high Si/Al ratios carry less charge balancing cations in their framework, and show better performance in acid stability, thermal stability and hydrophobicity, meanwhile, zeolites with lower Si/Al ratios show advantages such as hydrophilicity, a higher charge density and higher cation concentrations.[27] The LSX zeolite was first synthesized to have a Si/Al ratio very close to 1. To maintain such a low Si/Al ratio in the FAU type framework, K^+ cations are introduced during the synthesis procedure to stabilize the framework structure against collapse.[53]

Crystallographic reports have revealed that in K, Na-LSX (Figure 3-11), K^+ cations prefer to substitute for Na at Site II 6-member ring windows and at Site I' on both sides of the hexagonal prism windows, leaving Na^+ cations located at Site I inside the hexagonal prism and Site III and III' in the α – super cage.[40b] The placement of K^+ cations in Site I' usually moves the original Na^+ cations to Site I. In this study, the low exchange ratio of K (10.85%) suggests that in each α – super cage, only 1.26 out of 3.5 Site II positions have been exchanged with K^+ cations and the remaining 2.24 Site II positions remain occupied by Na^+.[40] Meanwhile, no Site I' K^+ cations can be found in sodalite cages, based on the predictions shown in Table S3-4. Both Na^+ and K^+ cations in LSX influence CO_2 guest adsorption behaviour in a unique way that is distinct from cations in other type X zeolites. VT ^{13}C SSNMR high-temperature (HT) and low-temperature (LT) experiments (Figure 3-12), as well as WSolids simulations (Figure 3-13), have been carried out to investigate CO_2 guest dynamics, potential adsorption locations and mechanisms in the LSX zeolite (Figure 3-13).
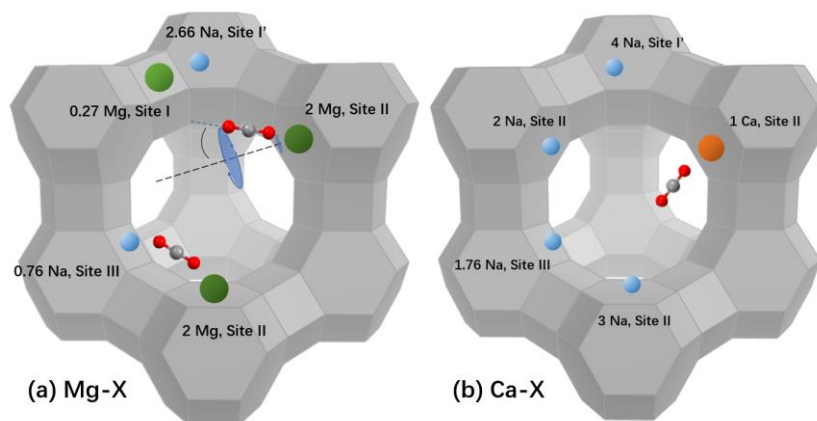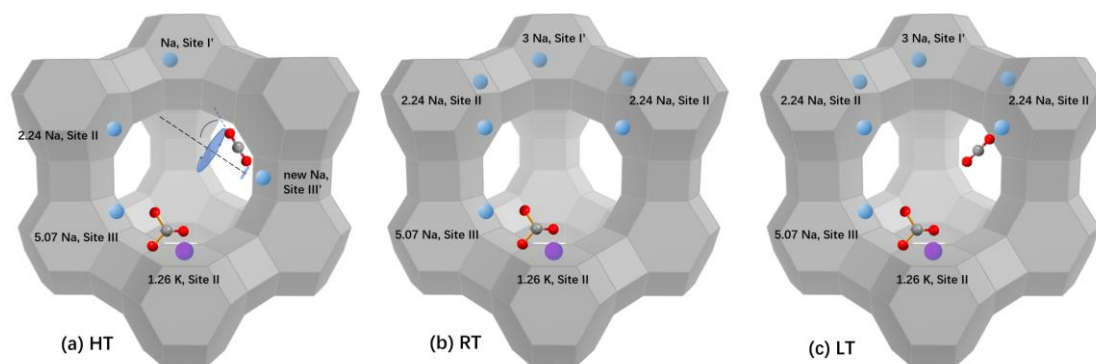
Figure 3-11. The possible CO_2 guest locations and behaviour have also been shown, but the mobile CO_2 guest is omitted. The exchanged cation distributions and occupancies in the Faujasite LSX zeolites examined in this work, shown at (a) high temperature (HT) of carbonate and adsorbed CO_2 undergoing restricted motion; (b) room temperature (RT) 293 K, the majority is carbonate; and (c) low temperature (LT) of carbonate and mostly immobile CO_2.

As opposed to other aluminosilicate zeolites which usually have no obvious interactions with CO_2 guests according to ^{13}C SSNMR spectra at 293 K, SSNMR results show that the LSX zeolite strongly interacts with CO_2 guests, as evidenced by the two obvious ^{13}C resonances (Figure 3-12). One sharp resonance at 125 ppm is associated with free CO_2 guests that are rapidly isotropically tumbling, while the second resonance with a broad and featured lineshape is observed at higher frequency than the mobile CO_2 resonance. These two resonances suggest at 293 K, CO_2 guests exist in two distinct states: (1) non-adsorbed and undergoing fast isotropic tumbling, and (2) adsorbed while undergoing well-defined restricted motion. Spectral simulations (Figures 3-13 and 3-14) reveal three ^{13}C resonances are actually present from 433 K to 123 K: (a) resonance I from a carbonate species, (b) resonance II from mobile CO_2 guests, and (c) resonance III, arising from adsorbed CO_2 guests in zeolite LSX.
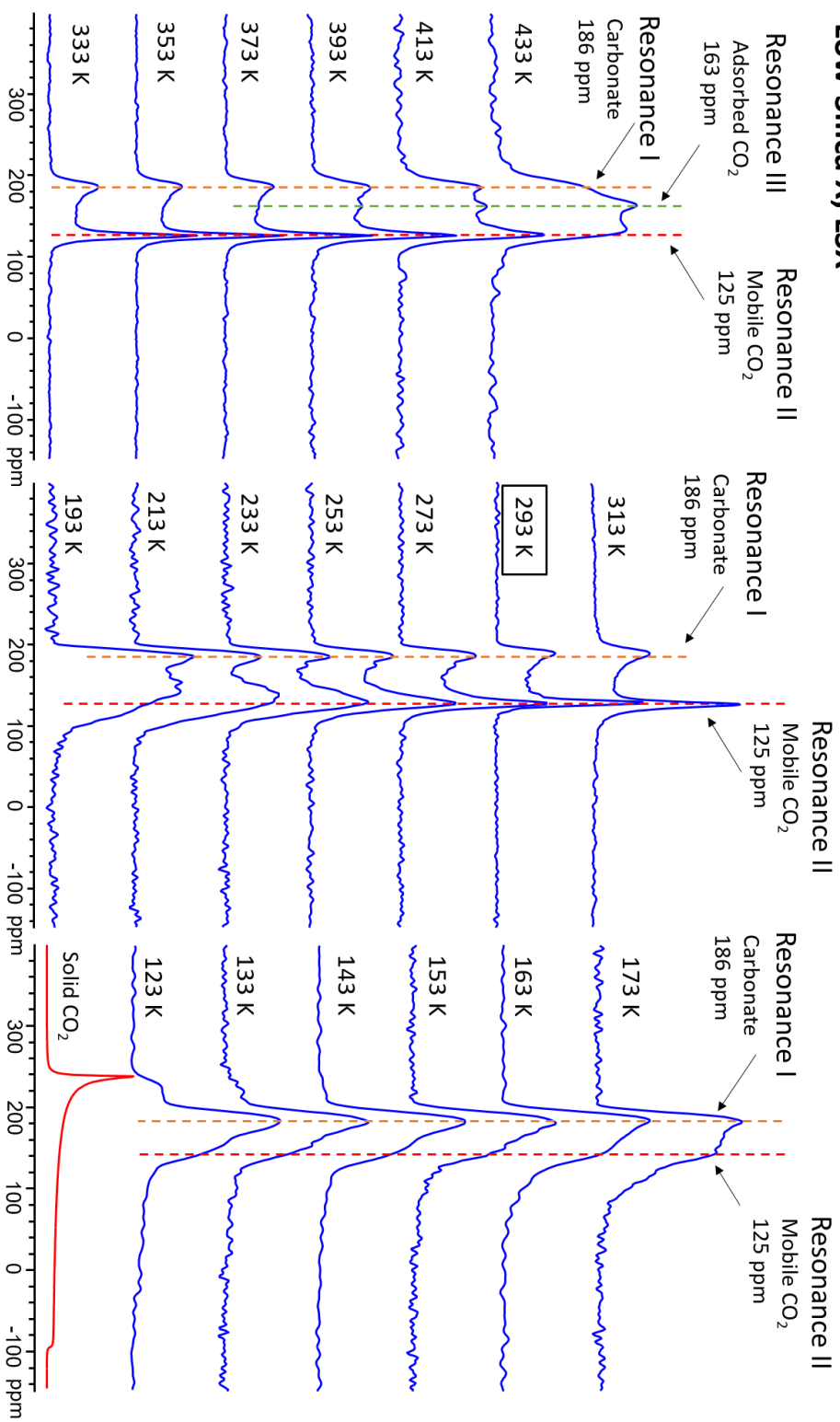
Figure 3-12. Static VT ^{13}C SSNMR spectra of CO_2 guests in low-silica X zeolite containing K and Na charge balancing cations from 433 K to 123 K. Three resonances can be observed in these spectra: Resonance I, assigned to a carbonate species; Resonance II, assigned to mobile CO_2 guests; and Resonance III, assigned to adsorbed CO_2 undergoing well-defined motions.

In the HT experiments, CO_2 guests in LSX exhibit very interesting behaviour. Starting at room temperature, the spectral width or span of the entire ^{13}C lineshape narrows as the temperature increases to 353 K, reaching a minimum value of 103 ppm. However, as temperatures climb above 373 K, the spectral width starts increasing rather than decreasing, due to the emergence of a third resonance centred at 163 ppm in between the two previously observed resonances. This new third resonance draws its intensity from that of the free CO_2 resonance, and becomes the most intense resonance in the entire spectrum at 433 K.

The emergence and growth of the third ^{13}C resonance at 163 ppm from 373 K to 433 K can be explained by a mechanism of the cation migration theory which allows the relocation of cations from sodalite cages to α – super cages. Computational research on the CO_2 loaded FAU type Na-X zeolite at 400 K has pointed out that Site I' cations may hop to Site II positions from the sodalite cage to the α – super cage, while cations that were previously located at Site II can migrate to Site III or III'.[22b] This cation re-distribution from the sodalite cage to α – super cages will increase the CO_2 adsorption capacity at HT. We propose that the appearance of the third ^{13}C resonance in HT experiments is due to CO_2 adsorption on the Site III or III' Na^+ cations in LSX, which is linked to Na^+ cations being transferred from sodalite cages to the α – super cage. The decreasing intensity of the mobile CO_2 resonance (located at 125 ppm) in HT experiments also implies that free CO_2 guests in the α – super cage can be adsorbed by the newly relocated cations at Site III' when the experimental temperature is raised. Eventually, at higher temperatures, the 125-ppm resonance of mobile CO_2 guests vanishes and transfers all its intensity to the third, adsorbed CO_2 resonance at 163 ppm.

Interestingly, the intensity and lineshape of the resonance with its "horn" shown at 186 ppm is relatively unchanged between 293 and 433 K in HT experiments (Figure 3-14a). The resonance emerging at 186 ppm originates from a carbonate species formed from chemisorption of CO_2, with observed chemical shifts ranging 166-169 ppm. Literature reports have confirmed that carbonate generates similar chemical shifts, span and lineshapes as the observed 186 ppm resonance in this study.[61] Thus, the 186-ppm resonance should be due to the formation of carbonates via strong chemisorption of CO_2
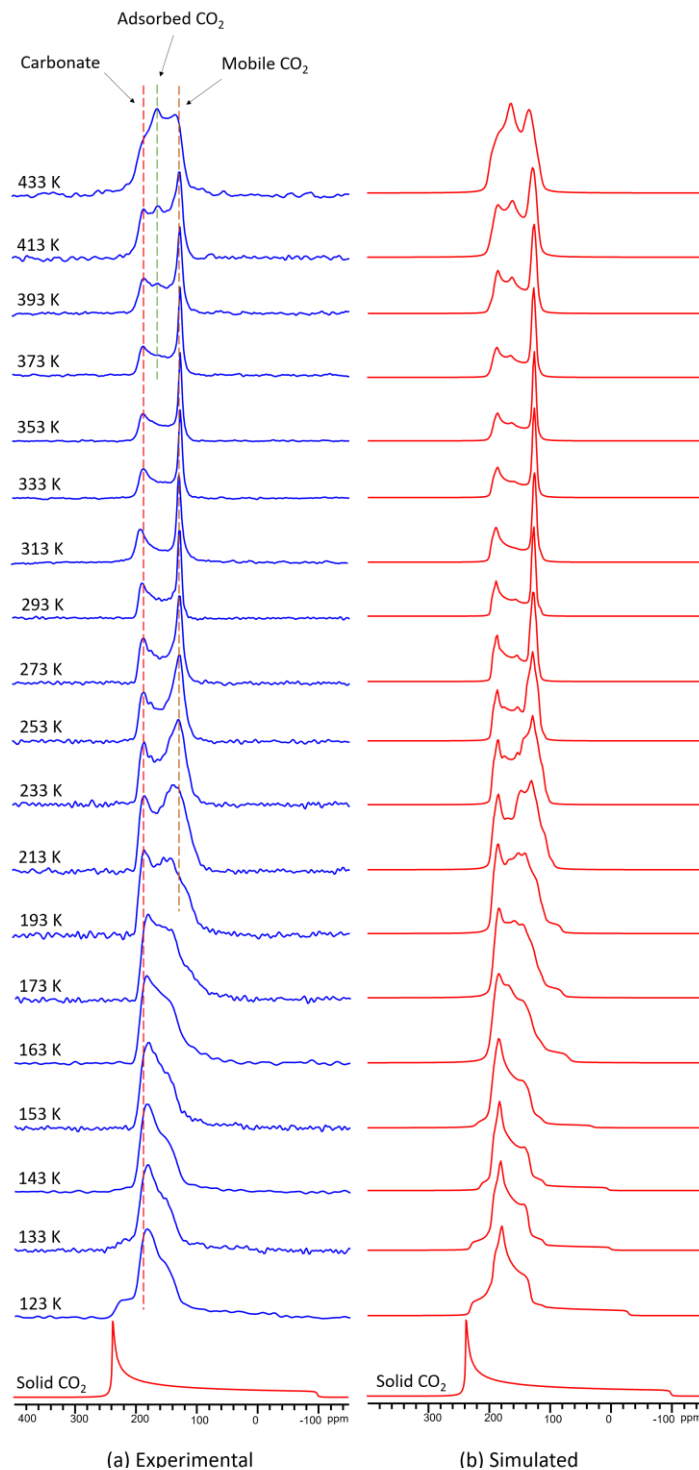
Figure 3-13. The figure shows (a) experimental and (b) simulated ^{13}C VT SSNMR spectra of CO_2 loaded zeolite LSX at temperatures ranging from 433 K to 123 K. Three resonances can be observed, which are attributed to carbonate spices, adsorbed CO_2, and mobile CO_2 guests.

Table 3-1 Observed CS parameters of ^{13}C spectra of three ^{13}C components in LSX zeolite

	Resonance I, Carbonate			Resonance II, Free CO_2			Resonance III, Adsorbed CO_2		
	δ_{iso} (ppm)	span (ppm)	skew	δ_{iso} (ppm)	span (ppm)	skew	δ_{iso} (ppm)	span (ppm)	skew
433 K	166(2)	68(3)	0.80	133.5(5)	18(2)	0	160(2)	85(3)	0.15
413 K	168(2)	68(2)	0.80	127.5(5)	15(1)	0	160(1)	81(2)	0.05
393 K	168(1)	69(2)	0.80	127.0(5)	11(1)	0	160(2)	85(1)	0.10
373 K	169(2)	70(2)	0.78	126.5(5)	8(1)	0	160(1)	85(1)	0.15
353 K	169(1)	70(2)	0.78	126.5(5)	6(1)	0	160(1)	85(1)	0.10
333 K	168(1)	76(2)	0.75	126.5(5)	7(1)	0	158(2)	80(2)	0.05
313 K	167(2)	85(2)	0.78	126.5(5)	8(1)	0	158(1)	80(1)	0.05
293 K	166(1)	83(1)	0.80	126.5(5)	9(1)	0	156(1)	59(2)	0
273 K	166(1)	80(1)	0.79	127.0(5)	14(1)	0	152(1)	60(1)	0.10
253 K	166(1)	79(2)	0.77	128.0(5)	23(2)	0	146(1)	69(1)	0.28
233 K	166(1)	78(1)	0.74	128.0(5)	38(1)	0	144(1)	75(1)	0.35
213 K	166(1)	78(1)	0.72	130.0(5)	52(1)	0	138(1)	79(1)	0.38
193 K	166(2)	78(1)	0.74	140.0(5)	62(2)	0	138(1)	100(1)	0.42
173 K	167(1)	70(2)	0.72	143.0(5)	63(2)	0	142(1)	110(2)	0.43
163 K	169(1)	66(2)	0.68	140.0(5)	63(2)	0	145(1)	130(1)	0.50
153 K	170(1)	65(1)	0.62	143.0(5)	63(3)	0	145(1)	190(1)	0.63
143 K	172(2)	62(2)	0.62	140.0(5)	63(2)	0	145(1)	210(2)	0.68
133 K	172(2)	60(3)	0.59	143.0(5)	63(5)	0	145(2)	230(2)	0.73
123 K	170(3)	61(2)	0.55	143.0(5)	63(5)	0	135(1)	260(3)	0.75
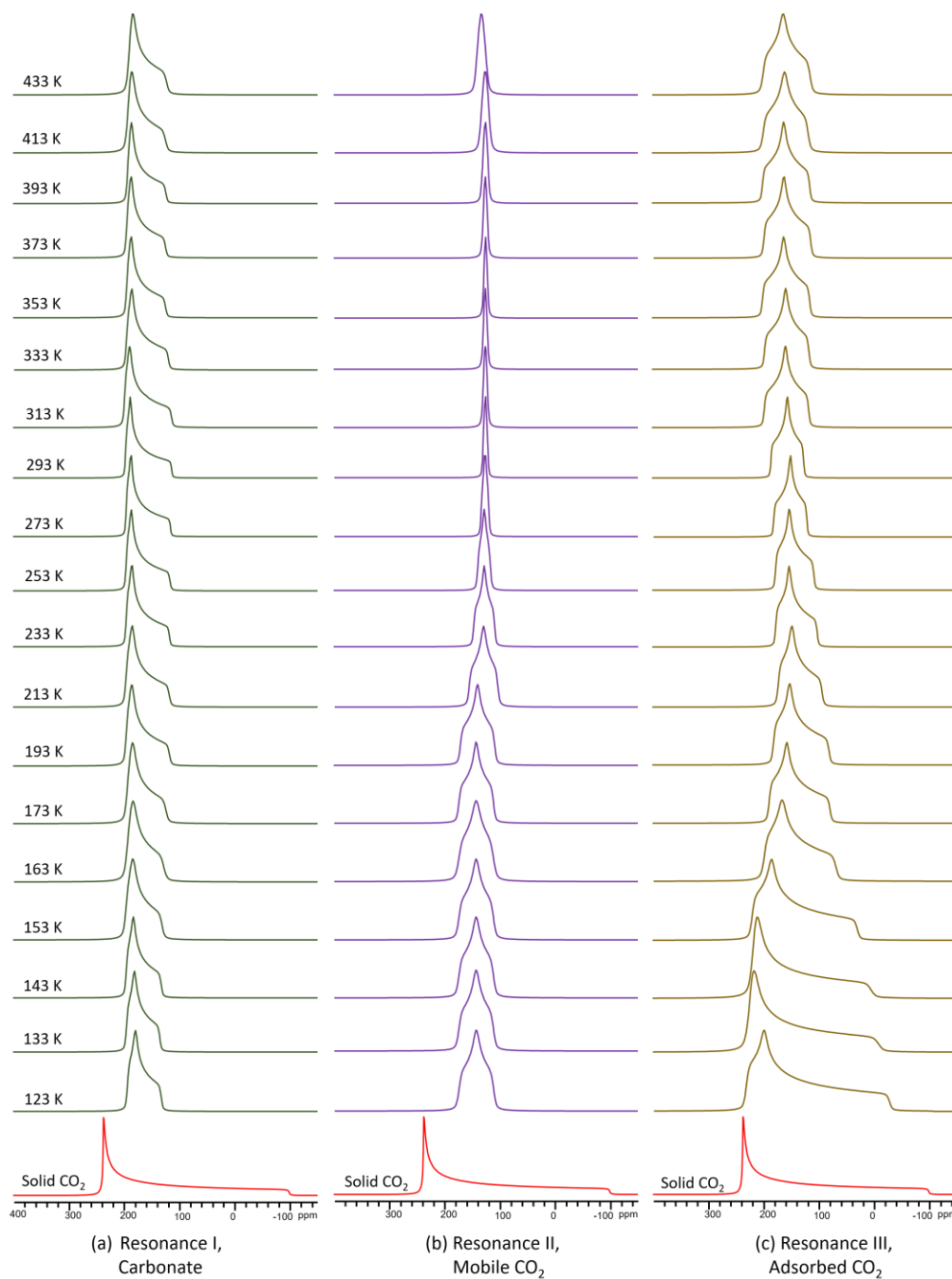
Figure 3-14. Simulated ^{13}C spectral lineshapes of (a) Resonance I, carbonate species, (b) Resonance II, mobile CO_2 guests, and (c) Resonance III, adsorbed CO_2 guests in zeolite LSX from 433 K to 123 K. The lineshapes corresponding to the carbonate species in (a) do not change much with temperature, and reach their maximum span around 293 K; the width of the mobile CO_2 guest powder patterns in (b) generally gets broader at lower temperatures; the span of adsorbed CO_2 guests in (c) becomes broader at very high and very low temperatures.

guest to Site II K or Na^+ cations, along with oxygen atoms from nearby 6-member ring structures,[45] as shown in Figure 3-11b. Research on this carbonate species in zeolites has proven that this chemisorption is irreversible, and CO_2 will not desorb even being heated up to 773 K.[46]

In the LT SSNMR experiments from 293 K to 123 K, the LSX zeolite also exhibits a significant influence on CO_2 guest behaviour. As experimental temperature was decreased, no obvious change was observed in the carbonate resonance in terms of its span and lineshape, proving the carbonate species are indeed stably chemisorbed. As the experimental temperature was lowered, the resonance representing free CO_2 guests at 125 ppm decreases in intensity until it vanishes at 133 K. This is also linked to the emergence of a very broad resonance, which increases in span from 190 ppm at 153 K to 240 ppm at 123 K. In LT experiments, the formation of this broad powder pattern is due to the gradual adsorption of free CO_2 guests, as shown in Figure 3-12. This resonance is less broad than the span of solid CO_2. Thus, the condensed and adsorbed CO_2 guests must be undergoing certain motions to narrow the span, and Site II cations would be the preferred adsorption site for CO_2.[45b]

Three ^{13}C resonances, corresponding to a chemisorbed carbonate species, free CO_2, and adsorbed CO_2 guests, are observed in the temperature range from 433 K to 123 K. A transfer of population between free and adsorbed CO_2 guests is also apparent from HT and LT spectra, according to the respective spectral intensities from ^{13}C NMR experimental spectra and WSolids simulation results. The various unique behaviours of adsorbed CO_2 guests in LSX is mainly due to the low Si/Al ratio in this zeolite, which means that many more cations are present than in common type X zeolites.

3.3.3 VT ^{13}C NMR experiments on CO_2 loaded zeolites type Y

Figure 3-15 shows the VT static ^{13}C SSNMR spectra of CO_2 loaded zeolite (a) NaY, (b) HY and (c) NH4Y**,** at a loading level of 1.76, 1.42 and 1.30 CO_2 guests per α – super cage, respectively. The experimental spectra were acquired at temperatures ranging from 293 K to 123 K. The sharp and narrow ^{13}C resonances suggest that the CO_2 guest in all three types of zeolite Y are very mobile, and undergo fast isotropic tumbling motions

through the zeolite structures within the entire temperature range. These narrow resonances indicate that there are no obvious strong adsorption interactions between CO_2 guests and the cations in zeolite Y. The narrow widths of these ^{13}C NMR spectra of CO_2 loaded samples reveal that type Y zeolites containing Na^+, H^+ and NH_4^+ cations have a poor ability in forming electrostatic-quadrupolar interactions with CO_2 guests. The absence of broad, featured ^{13}C powder patterns are at least partially due to the relatively higher Si/Al ratio in type Y zeolites, which means that less cations can be found at the Site II and Site III positions in type Y zeolites[29] than in type X zeolite (Si/Al = 1.23). At lower temperatures, the resonances are slightly broadened, which suggests that the CO_2 motion is very slightly restricted, although isotropic tumbling is still occurring. At 293 K, the ^{13}C resonance widths of CO_2 in NaY, HY and NH_4Y zeolites were 0.8, 1.0 and 0.8 ppm, respectively. As the temperature was decreased, the spans slowly increased, reaching the maximum values of 11, 17 and 22 ppm, respectively, at the lowest temperature 123 K
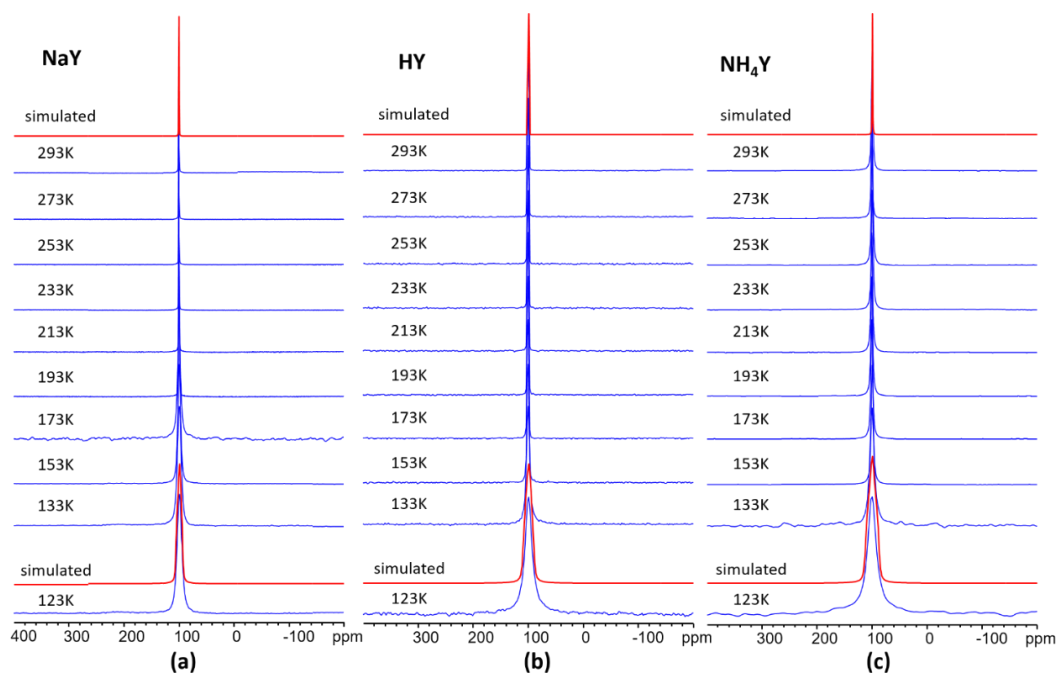
Figure 3-15. VT static ^{13}C SSNMR spectra of CO_2 guests in (a) NaY, (b) HY and (c) NH_4Y. The sharp and featureless resonances suggest that no obvious interactions are taking place between CO_2 guests and the charge balancing cations that serve as adsorption sites.

3.3.4 ^{1}H-^{13}C CP experiments of CO_2 loaded zeolite HY and NH$_4$Y

The ^{1}H-^{13}C CP SSNMR experiment relies on the distance-dependent ^{1}H-^{13}C dipolar interaction. In ^{1}H-^{13}C CP experiments, only ^{13}C nuclei involved in strong ^{1}H-^{13}C dipolar coupling interactions can be observed, which refers to ^{13}C nuclei that are spatially close or directly bound to ^{1}H nuclei. Polarization is transferred from ^{1}H to ^{13}C nuclei in CP experiments using a mixing pulse that lasts for a specific period, called the contact time. The contact time duration in ^{1}H-^{13}C CP experiments determines which ^{13}C resonances will be observed. ^{13}C resonances generated by carbon atoms that are directly bound to H atoms are favoured when short contact times (e.g. 0.5 ms) are used during ^{1}H-^{13}C CP experiments, while longer contact times permit detection of ^{13}C signals that correspond to nuclei which are relatively more distant from ^{1}H. Thus, the contact time can be used to filter specific resonances and understand structural connectivity and ^{1}H-^{13}C distances. In this study, static ^{1}H-^{13}C CP SSNMR experiments were carried out at 293 K using three contact times of 0.5, 5 and 10 ms, and acquiring each spectrum for 5.3 hours. By comparing the differences in experimental ^{1}H-^{13}C CP powder patterns, as well as the CO_2 guest resonances from direct-excitation ^{13}C spectra, the adsorption locations of CO_2 guests within H-Y and NH$_4$-Y zeolites can be examined.

The static CP spectra acquired from activated empty and CO_2 guest-loaded H-Y and NH$_4$-Y zeolite samples are illustrated in Figure 3-16, with the direct-excitation static ^{13}C spectra stacked at the top for comparison. The background ^{13}C lineshapes were acquired from activated empty zeolite samples and are stacked at the bottom of Figure 3-16. In the ^{1}H-^{13}C CP SSNMR spectra of the H-Y zeolite (Figure 3-16a), there are three powder patterns of similar lineshapes, despite the differences in CP contact times. The activated empty H-Y zeolite sample was also acquired at 293 K using CP experiments with a contact time of 5 ms, but no resonance was observed. These results suggest that all resonances in the CO_2 loaded H-Y sample that are detected by ^{1}H-^{13}C CP SSNMR experiments arise from dipolar coupling between ^{1}H from the zeolite framework and ^{13}C from CO_2 guests. The ^{1}H-^{13}C CP spectra are of a poor signal/noise ratio at all contact times, and especially short contact times, suggesting that CO_2 adsorbed guests near H$^+$ in the zeolite framework are in very rapid motion, and also suggesting that there is a very

low amount of adsorbed CO_2 guests. The majority of CO_2 guests are rapidly tumbling in the α – super cage, yielding a sharp and strong resonance that obscures the weak, broad signal of adsorbed CO_2 guests underneath.
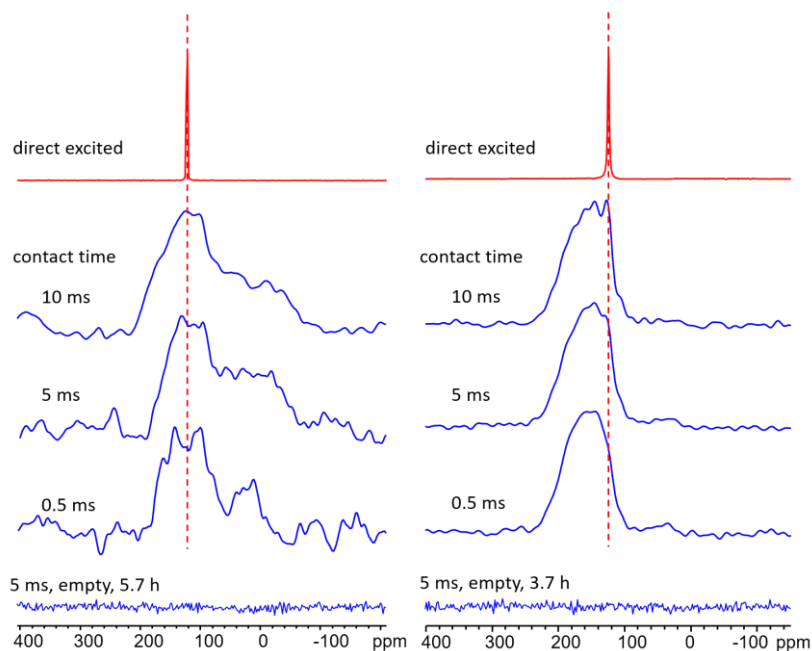
Figure 3-16. Static ^1H - ^{13}C CP SSNMR spectra of CO_2 loaded HY and NH_4Y zeolites at 293 K. The rather noisy lineshape for H-Y reveals that only a small amount of CO_2 guest interacts directly with the zeolite protons in (a), while the more intense signal for the NH_4-Y zeolite suggests some CO_2-H interactions are present in (b).

An asymmetric broad powder pattern which has a span of about 240 ppm can be observed in the CP spectra. The asymmetric lineshape and broad span suggest that there is a small amount of CO_2 guests adsorbed and undergoing restricted motion at or near H^+ atoms. Based on the crystallographic distribution of proton cations in H-Y zeolite, hydrogen can only exist in the form of bridging hydroxyl groups between two Si-O-Al T-sites,[62] acting as the Brønsted acid centres for catalyzing reactions.[63] Some reports have indicated four crystallographically inequivalent distributions of bridging hydroxyl groups exist (Figure 3-17b), where two H1 groups stick to the opposite sites of the hexagonal prism and point into the α – super cage whereas the H2 and H3 sites are oriented into the plane of the Site II 6-member ring structure.[64] All four proton sites are accessible and available for CO_2 guests, with unexchanged Na^+ cations located at Site I'. The current ^1H-

^{13}C CP experiments reveal that in the fully dehydrated H-Y zeolite, trace amounts of CO_2 guests are close to the bridging hydroxyl groups and may engage in weak interactions with the hydrogen atoms. The broad, asymmetric CP spectral lineshapes also imply that CO_2 guests adsorbed upon the bridging hydroxyl groups are undergoing restricted motions. In order to fully analyze this work in the future, additional experiments must be performed to obtain accurate CO_2 adsorption positions.
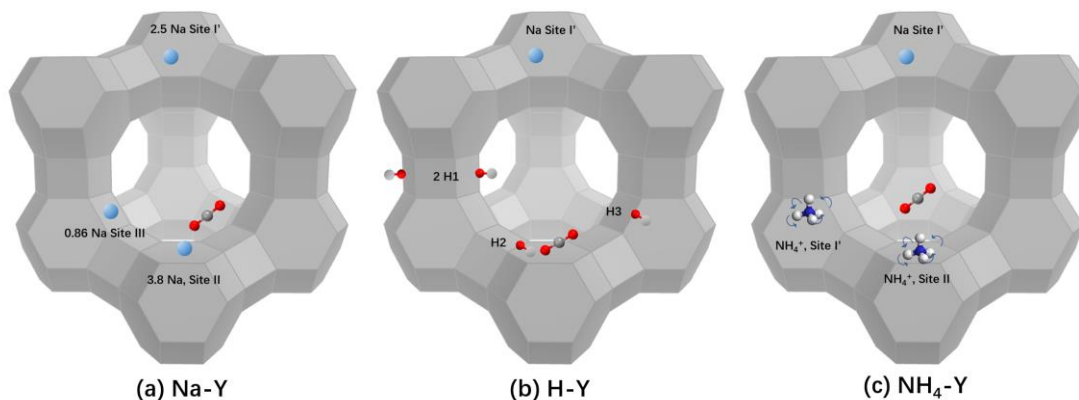
Figure 3-17. The cation distribution of Na^+, H^+, and NH_4^+ in Faujasite type Y zeolites. The possible CO_2 guest locations and behaviour have also been shown. The loading level of CO_2 guests in this work is about 1.76, 1.42 and 1.30 guest per α – super cage, respectively, and CO_2 guests in these figures represent all possible CO_2 locations. The Na^+ cations in Na-Y can only be found in their preferred Site I and Site II positions due to the low Si/Al ratio of zeolite type Y in (a).[38] The protons in (b)H-Y exist in the form of bridging H-O hydroxyl groups where two H1 are at opposite positions of a hexagonal prism, sticking into the α - cage, and H2 and H3 are pointing into the plane of 6-member ring structure of sodalite cage in (b).[64] The ammonium cations prefer the positions at Site I' and II in zeolite Y framework, as shown in (c).[29] Mobile CO_2 guest is not shown.

In the static ^{1}H-^{13}C CP SSNMR spectra of the NH$_4$-Y zeolite in Figure 3-16b, there is a broad, featureless, symmetric powder pattern centred around 160 ppm, along with a sharp narrow second resonance at 125 ppm that increases in intensity as contact times are extended from 0.5 ms to 10 ms. The activated empty NH$_4$-Y zeolite sample was also acquired at 293 K using static ^{1}H-^{13}C CP experiments with a contact time of 5 ms and no resonances were observed. These results confirm that all ^{13}C resonances in the CP

spectrum of CO_2 loaded NH_4-Y zeolite arise due to ^1H-^{13}C dipolar coupling interactions between ^1H from NH_4^+ cations and ^{13}C from CO_2 guests, and CO_2 is thus located near the NH_4^+ cations. The symmetric powder pattern lineshapes of CP spectra are 120 ppm wide and likely due to loose/weak adsorption of CO_2 molecules by NH_4^+ cations at site II in the 6-member rings, a relatively long H-C distance, and dynamics of NH_4^+ cations themselves at Site II in the 6-member rings that reduce the effective ^1H-^{13}C dipolar coupling and also give rise to a small distribution of possible CO_2 orientations and locations.

Most CO_2 guests are rapidly isotropically tumbling fairly distant from NH_4^+, producing a sharp and strong resonance that is more intense at longer contact times. Based on the crystallographic distribution of NH_4^+ cations in the NH_4-Y zeolite, these NH_4^+ cations can only be found at Site II and Site I. Only the Site II NH_4^+ cations are accessible for CO_2 guests, but the fast tumbling of NH_4^+ cations at Site II reduces the effective dipolar interaction strength between ^1H and ^{13}C. It should be mentioned that the signal-to-noise ratio of ^1H-^{13}C CP SSNMR spectra of NH_4-Y zeolites was much better than that of the H-Y zeolite spectra, which could be due to the increased quantity of protons available in the system from NH_4^+ cations. Since these ^1H-^{13}C CP experiments can only reveal the existence of dipolar interactions between H atoms or NH_4^+ cations and adsorbed CO_2 guests, additional work using X-ray/neutron diffraction and computational methods is required to locate the positions of the adsorbed CO_2 guests and rationalize the SSNMR data.

3.3.5 VT ^{13}C NMR experiments of CO_2 loaded LTA zeolites

The effects of different cations on the CO_2 adsorption behaviour in type A zeolites are quite interesting. Static ^{13}C VT SSNMR experiments were performed on CO_2 loaded Li-A, Na-A, K-A and Ca-A zeolites to investigate possible adsorption mechanism.
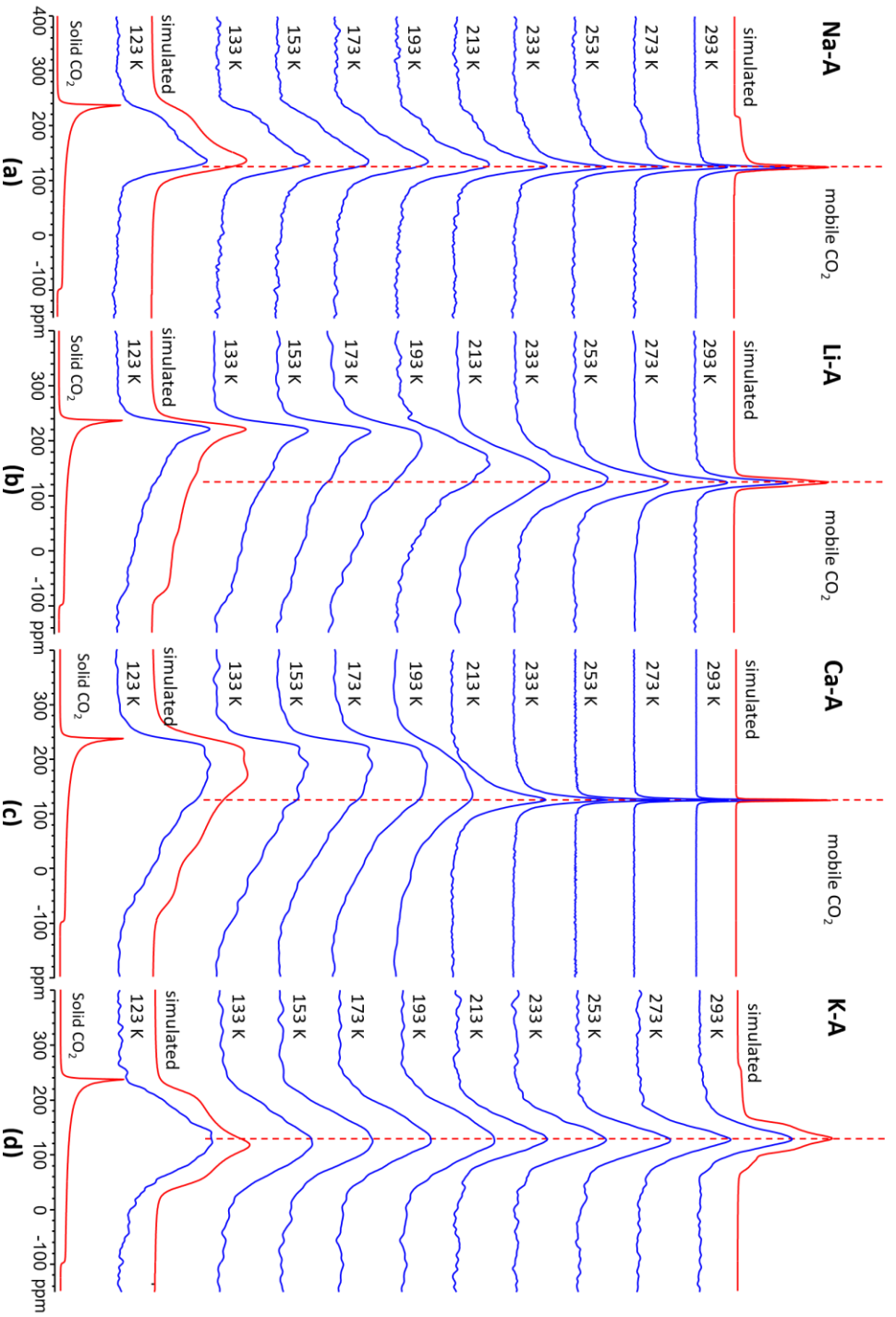
144

Figure 3-18. Static VT ^{13}C SSNMR spectra of CO_2 loaded within the (a) Li, (b) Na, (c) K and (d) Ca-exchanged type A zeolites. Each of the four exchanged cations have a distinct influence on the adsorbed CO_2 guest behaviour, which is due to the various cation properties and distributions within zeolite A framework.

Unfortunately, the Mg-A zeolite could not be synthesized because $MgCl_2$ salt gives acidified solution when dissolved in de-ionized water, which decomposed the zeolite A framework during the ion-exchange process.

The static VT ^{13}C SSNMR spectra of CO_2 loaded (a) Na-A, (b) Li-A, (c) Ca-A and (d) K-A zeolites are shown in Figure 3-18. The sodium cations in the Na- A zeolite may have strong or unique interactions with adsorbed CO_2 guests, due to the relatively unchanged resonance at 162 ppm within the whole experimental temperature range, as shown in Figure 3-19. The spectra of Li-A and Ca-A suggest a similar CO_2 guest behaviour as that observed in alkali metal exchanged zeolite X. In K-A, the observed static VT ^{13}C experimental spectra suggest that CO_2 guest behaviour may not have strong adsorption with K^+ cations, as reflected by the relatively featureless resonance.

The ^{13}C spectra of Na-A (4A) in Figure 3-18a first feature a sharp resonance at 125 ppm at 293 K, indicating the presence of mobile and free CO_2 guests. At the base of this sharp resonance, a second weaker and broader resonance centred at 153 ppm with a detailed lineshape is present, indicating the presence of adsorbed CO_2 guests. As the experimental temperature is reduced, the sharp resonance continually declines in intensity until it is overtaken by the broad resonance of adsorbed CO_2 guests in between the temperatures of 193 K and 173 K. The span of the adsorbed CO_2 guest ^{13}C resonance at 123 K is 180 ppm, which is less than that of solid CO_2, indicating that this resonance originates from adsorbed CO_2 guests undergoing restricted motions. Simulations show that the span of the adsorbed resonance does not change very much across the experimental temperature range, slightly increasing from 100 ppm at 293 K to 118 ppm at 123 K. This resonance may indicate the formation and presence of binary-cation adsorption of CO_2 between two Na^+ cations. Some computational studies on CO_2 loaded type A zeolites have explored this concept.[23a] According to the calculation results, [23a] when CO_2 guests are adsorbed in the α – cage, the Site I and Site II sodium cations strongly interact with two oxygen atoms from a CO_2 guest, and can bind or adsorb the CO_2. As the experimental temperature was reduced, more and more free CO_2 guests become less dynamic and less mobile, eventually being adsorbed by sodium cations at low temperatures. At 173 K and lower temperatures, no resonance representing mobile

CO_2 guest can be observed, indicating that all CO_2 molecules have been adsorbed and trapped by Site I and Site II sodium cations in the zeolite 4A framework (Figure 3-20a).[40]
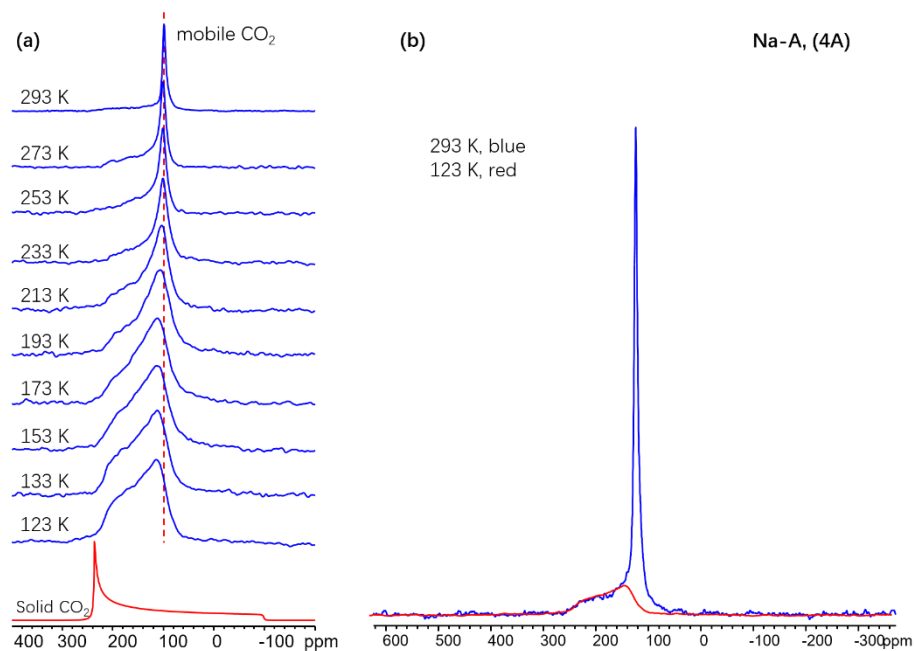
Figure 3-19. ^{13}C SSNMR spectra of the CO_2 loaded Na-A (4A) zeolite. In (a), static VT ^{13}C SSNMR spectra are shown from 293 K to 123 K. In (b), after overlaying the ^{13}C SSNMR spectra acquired at 293 K and 123 K, it can be seen that some CO_2 guests within zeolite A framework undergo restricted motions which are only slightly influenced by experimental temperatures.

The powder pattern lineshapes contained within the static VT ^{13}C SSNMR spectra of CO_2 loaded Li-A (Figure 3-18b) indicate that, from 293 K to 233 K, CO_2 guests within the framework are mobile and free, but the spectral breadth indicates that there are some restrictions preventing the full isotropic tumbling of guest CO_2. As the temperature is decreased from 193 to 123 K, the lineshape transforms into a broad and asymmetric powder pattern that resembles that of solid CO_2 guests,[60] with a span of 310 ppm (Figure 3-18b) at 123 K. Intermediate lineshapes were observed between 213 and 193 K, which are higher temperatures than those in which intermediate powder patterns were observed in alkali-exchanged zeolite X. The differences in CO_2 behaviour between Li-A and alkali-exchanged zeolite X may be due to the smaller unit cell of the LTA type zeolites, which

allows CO_2 guests less available space and forms stronger electrostatic-quadrupolar interactions between cations and CO_2 guests.
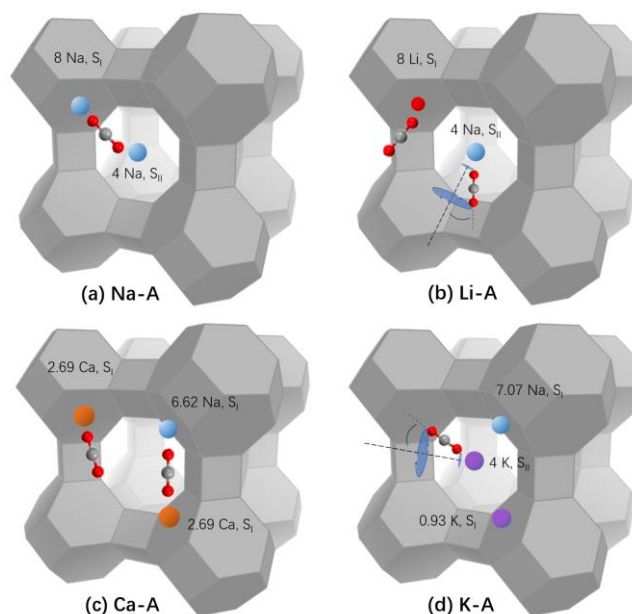
Figure 3-20. The Linde Type A zeolites have two cation sites located in the α – cage: Site I is located in the 6-member ring and Site II is in the 8-member ring structure. The possible CO_2 guest locations and behaviour have also been shown. The loading level of CO_2 guests in this work is about 1.38 guest per α – cage. The Li^+ cations prefer Site I in (a), while Na^+ cations occupy all Site I and Site II locations in (b). K^+ cations are positioned near the 8-member ring structure connecting two adjacent α – cage in (c) and Ca leaves the 8-member window vacant and stays in the 6-member ring structure in (d).[43]

Crystallographic studies of partially exchanged Li-A[42] zeolites have shown that the Li^+ cations are distributed at S_I near the centre of the 6-rings inside the α-cage, where cations can strongly interact with CO_2 guests. In this case, lithium cations have substituted all 8 original sodium cations in S_I, leaving 4 sodium cations in the S_{II} positions (Figure 3-20b).[42] This cation distribution results in most CO_2 guests being adsorbed upon the lithium cations, due to its smaller radius and stronger electrostatic attraction to CO_2 guests than that of the sodium cation. Thus, in Li-A, the very broad resonance with a 310-ppm span at 123 K (Figure 3-21b) arises from nearly immobile CO_2 guests adsorbed upon Li^+ cations at S_I sites. The second, less intense resonance observed in simulated ^{13}C

spectra at 123 K from Li-A is due to adsorbed CO_2 guests undergoing restricted motions upon Na^+ cations. This second resonance is associated with asymmetric lineshapes with a smaller span compared to the resonance arising from nearly immobile CO_2 (Figure 3-21b).

In Figure 3-18c, the ^{13}C powder pattern of Ca-A suggests that similar CO_2 adsorption behaviour is present in this zeolite as was observed in the Li-A zeolite. From 293 K to 233 K, the ^{13}C resonances are sharp and narrow. The width of the resonance is only 4 ppm at 293 K, suggesting fast isotropic tumbling of free CO_2 guests. However, as temperatures are reduced from 233 K to 193 K, a second broad resonance appears at a higher frequency than the free CO_2 resonance, and rapidly gains intensity as the temperature decreases to 173 K at the expense of the free CO_2 resonance. From 173 K to 123 K, the lineshapes do not vary much, and consist of one resonance with a very broad span of 300 ppm that corresponds to adsorbed immobile CO_2. There is a second resonance presence with a similar intensity but a smaller span of 153 ppm (Figure 3-21c). Crystallographic studies show that Ca^{2+} cations only occupy S_I positions in partially exchanged Ca-A, leaving S_{II} vacant, because the α – cage in LTA type A zeolites only needs 12 positive charges to neutralize the net negative charges from its framework. Both Ca^{2+} and Na^+ cation prefer to stay at the S_I position as their primary substitution site. Thus, due to the 2+ charge of Ca and the limited positive charges necessary for neutralization, S_{II} is left vacant in the Ca-A zeolite. (Figure 3-20c).[43] In this study, only 2.69 calcium cations can be found in each α - cage. Some neutron diffraction studies have revealed that adsorbed CO_2 guests can be bound by two nearby cations in Ca-Na, Na-Na or Ca-Ca arrangements.[48d] This unique adsorption behaviour can account for the second resonance observed in static ^{13}C SSNMR spectra of Ca-A at 123 K (Figure 3-21c). Thus, two CO_2 adsorption sites have been located in the Ca-A zeolite: the broader powder pattern originates from relatively immobile CO_2 guests adsorbed upon Ca, while the second narrower resonance arises from binary-cation adsorption upon two nearby cations.

In K-A (Figure 3-20d), potassium cations are positioned in the 8-member window structures and only allow the entrance of small molecules with a diameter of no more than 3 Å.[43] This structure explains why fully dehydrated K-A exhibited a rather poor CO_2 adsorption capability in the gas loading procedure, because CO_2 has a kinetic diameter of

about 3.3 Å, which prevents K-A from achieving a comparable uptake compared to other ion-exchanged type A zeolites. In Figure 3-18d, the static VT ^{13}C SSNMR spectra of CO_2 loaded K-A zeolite indicates that only rather mobile CO_2 guests are present in a wide temperature range from 293 K to 133 K, as indicated by the symmetric and broad single resonances contributed by mobile CO_2 guests. Simulations also prove that only one resonance is present, with a moderate span of 180 ppm at 123 K (Figure 3-21d). The featureless nature of the spectrum also suggests that a distribution of CO_2 environments is present. These results suggest that at this 123 K temperature, CO_2 guests have started to interact with the few S_{II} K^+ cations located on 8-member windows in the K-A zeolite.
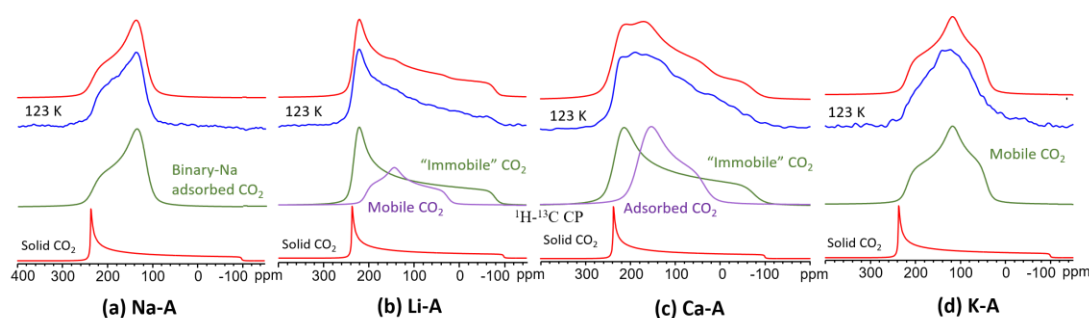
Figure 3-21. Simulated and experimental static ^{13}C SSNMR spectra at 123 K of CO_2 guests in (a) Na-A, (b) Li-A, (c) Ca-A and (d) K-A zeolites. Two resonances are present in the ^{13}C SSNMR spectra of (b) Li-A and (c) Ca-A, while only one component is found in the ^{13}C SSNMR spectra of (a) Na-A and (d) K-A. See the text for details.

Compared to the ^{13}C SSNMR spectra of ion-exchanged K-A (Figure 3-22a), the VT ^{13}C SSNMR experiments on commercial K-A zeolites (Figure 3-22b), which has a higher exchange ratio of about 60% (0.6 K_2O: 0.40 Na_2O : 1 Al_2O_3 : 2.0 ± 0.1SiO_2 : x H_2O),[65] yielded spectra are similar to the spectra of ion-exchanged K-A. Thus, we it appears that the reason that the ^{13}C SSNMR spectra of K-A are relatively featureless is due to the low exchange ratio 41.08% of ion-exchanged K-A.
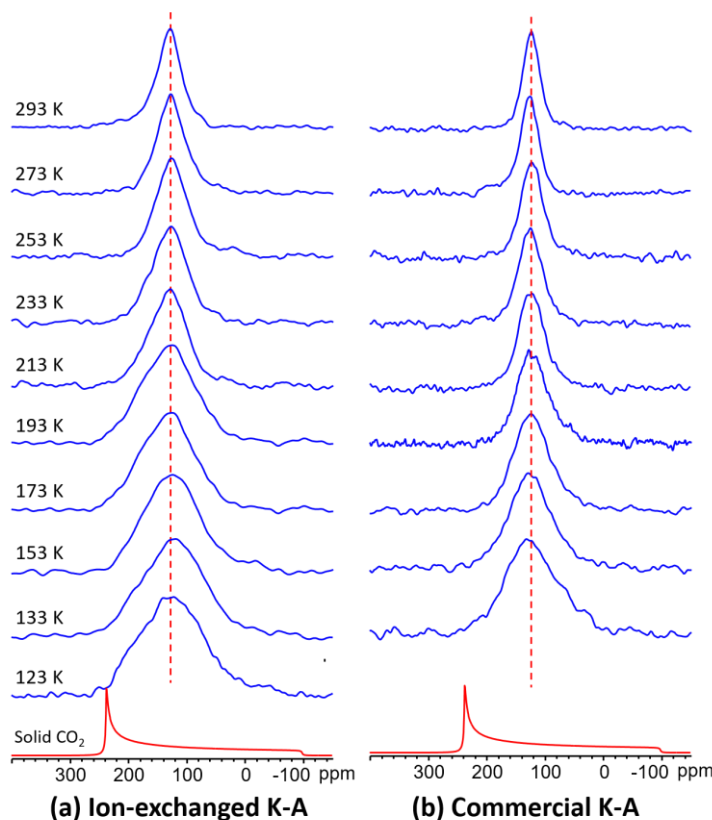
Figure 3-22. ^{13}C SSNMR spectra of (a) ion-exchanged K-A and (b) commercial K-A acquired using static VT experiments. Both K-A zeolites gave the same powder pattern lineshape, which proves that the low exchange ratio in (a) was not the reason for only obtaining one resonance within the whole temperature range.

3.3.6 Dynamic simulations of ^{13}C SSNMR spectra at 123 K

The specific types of motion and the associated motional angles and rates of CO_2 guests adsorbed in five ion-exchanged zeolites at 123 K have been identified by simulating experimental static VT ^{13}C SSNMR spectra using the EXPRESS[59] simulation package. There is a localized C_3 rotational wobbling motion of CO_2 through an angle θ, as well as a non-localized C_2 hopping motion of CO_2 through an angle γ. In type X zeolites containing alkali metal cations (Li$^+$, Na$^+$ and K$^+$ cations, see Figure 3-23a-c), the nearly immobilized CO_2 guests yield very broad resonances similar to those of static solid CO_2,[60] but simulations reveal these guests are actually undergoing localized C_3 wobbling

motions upon the corresponding alkali metal cations that act as CO_2 adsorption sites. In agreement with the evidence from ^{13}C SSNMR that CO_2 guests are nearly immobilized on the cations, the localized wobbling motion of CO_2 in Li-, Na- and K-X zeolites at 123 K occur through very small motional angles, from 8° in Li-X, 10° in Na-X to 11° in K-X. The slight increase in wobbling angles, suggest the cation-CO_2 interactions and CO_2 adsorption capabilities of three zeolite X samples are ordered Li-X > Na-X > K-X, although the differences in this series may not be very large.
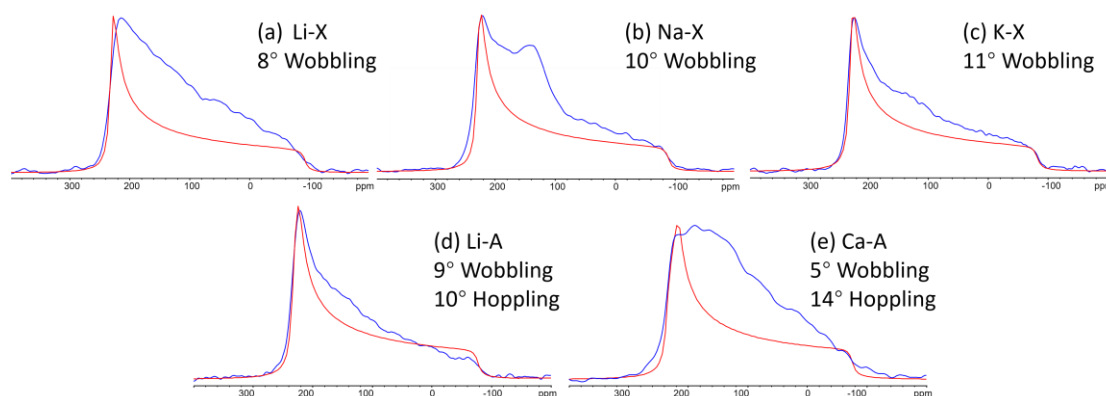
Figure 3-23. EXPRESS simulated ^{13}C spectra of adsorbed CO_2 guest at 123 K in (a) Li-X, (b) Na-X, (c) K-X, (d) Li-A and (e) Ca-A. The extra resonance compared to simulated powder patterns are contributed by mobile CO_2 guest undergoing lower motional rates. Only wobbling motion of adsorbed CO_2 guest upon alkali cations throughout very small angles in type X zeolites are found. While, in Li^+ and Ca^{2+} exchanged type A zeolites, wobbling and hopping combination motional patterns are found.

In Li-A and Ca-A, dynamic simulations reveal the presence of a non-localized C_2 hopping motion of CO_2 in addition to localized C_3 wobbling. In Li-A, the adsorbed CO_2 guests are undergoing a wobbling motion through an angle of 9° and a hopping motion through an angle of 10°, while in zeolite Ca-A, CO_2 participates in wobbling through 5° along with hopping through a 14° angle. This combined "wobbling and hopping" motional dynamic behaviour of CO_2 guest has been observed within many types of porous MOFs.[26a, 26b] The distinct dynamic behaviour of CO_2 in Li-A and Ca-A versus Li-X, Na-X, and K-X zeolites is likely due to the reduced α – cage diameter in type LTA

zeolite (11.4 Å) than in FAU zeolite (12 Å), as well as the different topologies in these zeolites.

3.4   Conclusions

Static ^{13}C VT SSNMR experiments on FAU type X, LSX and Y and LTA type A ion-exchanged zeolite samples reveal that the various extra-framework cations have a significant influence on the adsorption and behaviour of CO_2 guests in fully dehydrated zeolites across a wide range of temperatures. The substituted cation type, cation distribution, framework structure and Si/Al ratio are the four key factors that determine the behaviour of adsorbed CO_2 guests within zeolites. Literature reports of extra-framework cation distributions and reaction mechanisms in various ion-exchanged zeolites provide insight into the CO_2 adsorption trends and differences observed from ^{13}C SSNMR spectra. In particular, the nature of the cation species has a tremendous effect on adsorbed CO_2 guests, even for cations in the same periodic group such as the Li, Na, K alkali metals or the Mg and Ca alkali earth metals.

^{13}C powder patterns feature broader spans when the experimental temperature is decreased, indicating that CO_2 guests have reduced mobility when adsorbed in various ion-exchanged zeolites. A complete set of VT SSNMR data for any given zeolite permits observation of how CO_2 dynamics and adsorption change in various ion-exchanged zeolites from 293 K to 123 K. At the lowest experimental temperature of 123 K, the ^{13}C lineshapes and simulated CS parameters suggest that CO_2 guests may become nearly immobilized, judging from the similarities between the experimental lineshapes and spans versus those reported for solid static CO_2 molecules. The CO_2 guest behaviours are also related to the zeolite framework structures and Si/Al ratios, which determine the cation quantity, positive charge densities and available free space in the zeolite cavities.

The CO_2 guests behave in a distinct manner from each other when adsorbed within the FAU type X, Y and LTA type A zeolites, but are generally free and mobile at 293 K. At 173 K, CO_2 guests begin to experience partially restricted motions at the adsorption sites, and CO_2 is mostly immobilized at 123 K, except for some cases of binary cation-CO_2 adsorption in Mg-X and Na-A , as well as weak cation-CO_2 adsorption in Ca-X and K-A. Another special case of CO_2 guest adsorption was observed in the LSX zeolite, in which CO_2 guests are strongly adsorbed upon K^+ or Na^+ cations to form carbonate species via chemisorption at room temperature. To further investigate CO_2 adsorption and

behaviour in the LSX zeolite, HT and LT ^{13}C SSNMR spectra were collected at temperatures ranging from 433 K to 123 K, which in turn suggest that CO_2 dynamics and cation re-distributions are present throughout the whole temperature range. The HT experiments have suggested that the carbonate species formed via chemisorption of CO_2 are so stable that they do not decompose, even when heated up to 433 K. Moreover, a new resonance was observed when heating up the LSX sample at HT, which may correspond to the reported cation migration effect in the framework, where CO_2 is gradually adsorbed onto these newly emerged or migrated cations in the α – super cages. However, in the three types of Y zeolites incorporating Na^+, H^+ and NH_4^+ cations, CO_2 guests remained extremely mobile within the whole experimental temperature range, and were mobile even at the coldest temperature of 123 K, suggesting that no significant adsorptive interactions were present. Static ^1H - ^{13}C CP experiments in H-Y and NH_4-Y at 293 K have shown that CO_2 guests are proximate to the protons from H^+ and NH_4^+ cations, as evidenced by their distant dipolar coupling interactions which enable the CP process to occur, although the dipolar interactions are rather weak.

In zeolite A, LSX, X and Y with increasing Si/Al ratios from 1 to 2.35, the CO_2 adsorption capabilities are dramatically reduced due to the presence of less charge-balancing cations in the frameworks. The Type A and LSX zeolites have the strongest CO_2 adsorption in this study, while in type X zeolites CO_2 guests have relatively increased mobility, and in type Y zeolites the CO_2 guests are extremely mobile due to very weak interactions with the extra-framework cations.

When adsorbed into the alkali and alkali earth ion-exchanged FAU and LTA zeolites studied in this work, CO_2 generally becomes less mobile and eventually is nearly immobilized upon single or binary cations as the experimental temperatures drop to 123 K. The appearance of ^{13}C resonances with increased chemical shifts may be due to the formation of carbonate-like species with metal cations through chemisorption. This interesting dynamic behaviour of adsorbed CO_2 gas in various ion-exchanged FAU and LTA zeolites has never been observed before via SSNMR spectroscopy, which presents a unique opportunity to further investigate the full picture of CO_2 gas dynamic adsorption mechanisms in zeolites by conducting VT experiments. The influence of various cation

species and distributions in the FAU and LTA zeolites have been revealed and explained using SSNMR, with the assistance of crystallographic literature reports. This work will be helpful for understanding adsorbed CO_2 gas behaviour in other zeolites with similar frameworks and topologies.

In the future, more detailed ^{13}C VT SSNMR studies using a wider range of experimental temperatures will be performed. Additional work focused on discovering the exact CO_2 guest adsorption locations and configurations upon the cations in these zeolites will also be carried out to enhance understanding of the CO_2 adsorption mechanisms present and CO_2 interactions with various cations. This should be possible using methods such as neutron diffraction and powder or single crystal XRD experiments. Additional static VT ^{13}C SSNMR experiments can also be performed to explore CO_2 adsorption behaviour in other industrially-relevant zeolites such as the MOR and MFI families.

3.5   Bibliography

1.   Colella, C.; Gualtieri, A. F., Cronstedt's zeolite. *Microporous Mesoporous Mater.* **2007,** *105* (3), 213-221.

2.   Cruciani, G., Zeolites upon heating: Factors governing their thermal stability and structural changes. *J. Phys. Chem. Solids* **2006,** *67* (9), 1973-1994.

3.   (a) Degnan, T. F., Applications of zeolites in petroleum refining. *Top. Catal.* **2000,** *13* (4), 349-356; (b) Park, D. H.; Kim, S. S.; Wang, H.; Pinnavaia, T. J.; Papapetrou, M. C.; Lappas, A. A.; Triantafyllidis, K. S., Selective petroleum refining over a zeolite catalyst with small intracrystal mesopores. *Angew. Chem.* **2009,** *121* (41), 7781-7784.

4.   Jacobs, P.; Flanigen, E. M.; Jansen, J.; van Bekkum, H., *Introduction to zeolite science and practice*. Elsevier: 2001; Vol. 137.

5.   Rouquerol, J.; Rouquerol, F.; Llewellyn, P.; Maurin, G.; Sing, K. S., *Adsorption by powders and porous solids: principles, methodology and applications*. Academic press: 2013.

6.   Ćurković, L.; Cerjan-Stefanović, Š.; Filipan, T., Metal ion exchange by natural and modified zeolites. *Water Res.* **1997,** *31* (6), 1379-1382.

7.   Dyer, A., An introduction to zeolite molecular sieves. John Wiley and Sons Inc.: 1988.

8.   Yilmaz, B.; Müller, U., Catalytic applications of zeolites in chemical industry. *Top. Catal.* **2009,** *52* (6-7), 888-895.

9.   Rahimi, N.; Karimzadeh, R., Catalytic cracking of hydrocarbons over modified ZSM-5 zeolites to produce light olefins: A review. *Appl. Catal. A* **2011,** *398* (1), 1-17.

10.   Venuto, P. B., Organic catalysis over zeolites: a perspective on reaction paths within micropores. *Microporous Mater.* **1994,** *2* (5), 297-411.

11.   (a) Wang, X.; Qi, G.; Xu, J.; Li, B.; Wang, C.; Deng, F., NMR-spectroscopic evidence of intermediate-dependent pathways for acetic acid formation from methane and carbon monoxide over a ZnZSM-5 zeolite catalyst. Angew. Chem. Int. Ed. **2012,** *51* (16), 3850-3853; (b) Moore, J. K.; Sakwa-Novak, M. A.; Chaikittisilp, W.; Mehta, A. K.; Conradi, M. S.; Jones, C. W.; Hayes, S. E., Characterization of a mixture of CO_2 adsorption products in hyperbranched aminosilica adsorbents by ^{13}C solid-state NMR. *Environ. Sci. Technol* **2015,** *49* (22), 13684-13691.

12.   Ackley, M. W.; Rege, S. U.; Saxena, H., Application of natural zeolites in the purification and separation of gases. *Microporous Mesoporous Mater.* **2003,** *61* (1), 25-42.

13.   Pansini, M., Natural zeolites as cation exchangers for environmental protection. *Miner. Depos.* **1996,** *31* (6), 563-575.

14.   Qiu, W.; Zheng, Y., Removal of lead, copper, nickel, cobalt, and zinc from water by a cancrinite-type zeolite synthesized from fly ash. *Chem. Eng. J.* **2009,** *145* (3), 483-488.

15.	(a) Wang, S.; Peng, Y., Natural zeolites as effective adsorbents in water and wastewater treatment. *Chem. Eng. J.* **2010,** *156* (1), 11-24; (b) Kesraoui-Ouki, S.; Cheeseman, C. R.; Perry, R., Natural zeolite utilisation in pollution control: A review of applications to metals' effluents. *J. Chem. Technol. Biotechnol.* **1994,** *59* (2), 121-126.

16.	(a) Rahman, R.; Ibrahium, H.; Hung, Y.-T., Liquid radioactive wastes treatment: a review. *Water* **2011,** *3* (2), 551-565; (b) Osmanlioglu, A. E., Treatment of radioactive liquid waste by sorption on natural zeolite in Turkey. *J. Hazard. Mater.* **2006,** *137* (1), 332-335; (c) Agarwal, S. K., *Heavy metal pollution*. APH publishing: 2009; Vol. 4; (d) Duruibe, J.; Ogwuegbu, M.; Egwurugwu, J., Heavy metal pollution and human biotoxic effects. *Int. J. Phys. Sci.* **2007,** *2* (5), 112-118; (e) Abdi, M. R.; Kamali, M.; Vaezifar, S., Distribution of radioactive pollution of ^{238}U, ^{232}Th, ^{40}K and ^{137}Cs in northwestern coasts of Persian Gulf, Iran. *Marine Poll. Bull.* **2008,** *56* (4), 751-757; (f) Prants, S.; Uleysky, M. Y.; Budyansky, M. In *Numerical simulation of propagation of radioactive pollution in the ocean from the Fukushima Dai-ichi nuclear power plant*, Doklady Earth Sciences, Springer: 2011; pp 1179-1182; (g) Righi, S.; Lucialli, P.; Bruzzi, L., Health and environmental impacts of a fertilizer plant–Part I: Assessment of radioactive pollution. *J. Environ. Radioact.* **2005,** *82* (2), 167-182.

17.	Dunne, J.; Rao, M.; Sircar, S.; Gorte, R.; Myers, A., Calorimetric heats of adsorption and adsorption isotherms. 2. O_2, N_2, Ar, CO_2, CH_4, C_2H_6, and SF_6 on NaX, H-ZSM-5, and Na-ZSM-5 zeolites. *Langmuir* **1996,** *12* (24), 5896-5904.

18.	Walton, K. S.; Abney, M. B.; LeVan, M. D., CO_2 adsorption in Y and X zeolites modified by alkali metal cation exchange. *Microporous Mesoporous Mater.* **2006,** *91* (1), 78-84.

19.	Flanigen, E. M.; Khatami, H.; SZYMANSKI, H. A., Infrared structural studies of zeolite frameworks. ACS Publications: 1971.

20.	(a) Feuerstein, M.; Lobo, R., Characterization of Li cations in zeolite LiX by solid-state NMR spectroscopy and neutron diffraction. *Chem. Mater.* **1998,** *10* (8), 2197-2204; (b) Fitch, A.; Jobic, H.; Renouprez, A., Localization of benzene in sodium-Y-zeolite by powder neutron diffraction. *J. Phys. Chem.* **1986,** *90* (7), 1311-1318; (c) Plevert, J.; Di Renzo, F.; Fajula, F.; Chiari, G., Structure of dehydrated zeolite Li− LSX by neutron diffraction: evidence for a low-temperature orthorhombic faujasite. *J. Phys. Chem. B* **1997,** *101* (49), 10340-10346; (d) Wong-Ng, W.; Kaduk, J. A.; Huang, Q.; Espinal, L.; Li, L.; Burress, J., Investigation of NaY Zeolite with adsorbed CO_2 by neutron powder diffraction. *Microporous Mesoporous Mater.* **2013,** *172*, 95-104.

21.	(a) Sircar, S., Pressure swing adsorption. *Ind. Eng. Chem. Res.* **2002,** *41* (6), 1389-1392; (b) Ko, D.; Siriwardane, R.; Biegler, L. T., Optimization of a pressure-swing adsorption process using zeolite 13X for CO_2 sequestration. *Ind. Eng. Chem. Res.* **2003,** *42* (2), 339-348.

22.	(a) Pillai, R. S.; Peter, S. A.; Jasra, R. V., CO_2 and N_2 adsorption in alkali metal ion exchanged X-Faujasite: grand canonical Monte Carlo simulation and equilibrium adsorption studies. *Microporous Mesoporous Mater.* **2012,** *162*, 143-151; (b) Plant, D.; Maurin, G.; Jobic, H.; Llewellyn, P., Molecular dynamics simulation of the cation motion upon adsorption of CO_2 in faujasite zeolite systems. *J. Phys. Chem. B* **2006,** *110* (29), 14372-14378; (c) Liu, S.; Yang, X., Gibbs ensemble Monte Carlo simulation of

supercritical CO_2 adsorption on Na A and Na X zeolites. *J. Chem. Phys.* **2006,** *124* (24), 244705.

23.   (a) Zukal, A.; Arean, C.; Delgado, M.; Nachtigall, P.; Pulido, A.; Mayerová, J.; Čejka, J., Combined volumetric, infrared spectroscopic and theoretical investigation of CO 2 adsorption on Na-A zeolite. *Microporous Mesoporous Mater.* **2011,** *146* (1), 97-105; (b) Maurin, G.; Llewellyn, P.; Bell, R., Adsorption mechanism of carbon dioxide in faujasites: grand canonical Monte Carlo simulations and microcalorimetry measurements. *J. Phys. Chem. B* **2005,** *109* (33), 16084-16091.

24.   Masala, A.; Grifasi, F.; Atzori, C.; Vitillo, J. G.; Mino, L.; Bonino, F.; Chierotti, M. R.; Bordiga, S., CO_2 Adsorption Sites in UTSA-16: Multitechnique Approach. *J. Phys. Chem. C* **2016,** *120* (22), 12068-12074.

25.   Kulprathipanja, S., *Zeolites in industrial separation and catalysis*. John Wiley & Sons: 2010.

26.   (a) Wang, W. D.; Lucier, B. E.; Terskikh, V. V.; Wang, W.; Huang, Y., Wobbling and hopping: studying dynamics of CO_2 adsorbed in metal–organic frameworks via ^{17}O solid-state NMR. *J. Phys. Chem. Lett.* **2014,** *5* (19), 3360-3365; (b) Lu, Y.; Lucier, B. E.; Zhang, Y.; Ren, P.; Zheng, A.; Huang, Y., Sizable dynamics in small pores: CO_2 location and motion in the α-Mg formate metal–organic framework. *Phys. Chem. Chem. Phys.* **2017,** *19* (8), 6130-6141; (c) Yang, Q.; Vaesen, S.; Ragon, F.; Wiersum, A. D.; Wu, D.; Lago, A.; Devic, T.; Martineau, C.; Taulelle, F.; Llewellyn, P. L., A water stable metal–organic framework with optimal features for CO_2 capture. *Angew. Chem.* **2013,** *125* (39), 10506-10510; (d) Belmabkhout, Y.; Guillerm, V.; Eddaoudi, M., Low concentration CO_2 capture using physical adsorbents: Are metal–organic frameworks becoming the new benchmark materials? *Chem. Eng. J.* **2016,** *296*, 386-397.

27.   Roelofsen, D. P., Molecular sieve zeolites properties and applications in organic synthesis. Delft: 1972.

28.   (a) Godber, J.; Baker, M. D.; Ozin, G. A., Far-IR spectroscopy of alkali-metal and alkaline-earth cations in faujasite zeolites. *J. Phys. Chem.* **1989,** *93* (4), 1409-1421; (b) Rakić, V. M.; Hercigonja, R. V.; Dondur, V. T., CO interaction with zeolites studied by TPD and FTIR: transition-metal ion-exchanged FAU-type zeolites. *Microporous Mesoporous Mater.* **1999,** *27* (1), 27-39.

29.   Kaduk, J. A.; Faber, J., Crystal structure of zeolite Y as a function of ion exchange. *Rigaku J* **1995,** *12* (2), 14-34.

30.   Seo, S.-M.; Lee, O.-S.; Kim, H.-S.; Bae, D.-H.; Chun, I.-J.; Lim, W.-T., Determination of Si/Al ratio of faujasite-type zeolite by single-crystal X-ray diffraction technique. single-crystal structures of fully Tl^+-and partially K^+-exchanged zeolites Y (FAU),| Tl_{71}|[$Si_{121}Al_{71}O_{384}$]-FAU and| $K_{53}Na_{18}$|[$Si_{121}Al_{71}O_{384}$]-FAU. *Bull. Korean Chem. Soc.* **2007,** *28* (10), 1675-1682.

31.   Jacobs, P.; Flanigen, E.; Jansen, J.; van Bekkum, H., *Introduction to zeolite science and practice*. Elsevier: 2001; Vol. 137.

32. Hernández-Maldonado, A. J.; Yang, R. T., Desulfurization of liquid fuels by adsorption via π complexation with Cu (I)− Y and Ag− Y Zeolites. *Ind. Eng. Chem. Res.* **2003,** *42* (1), 123-129.

33. Mabilia, M.; Pearlstein, R.; Hopfinger, A., Molecular modeling of zeolite structure. 1. Properties of the sodalite cage. *J. Am. Chem. Soc.* **1987,** *109* (26), 7960-7968.

34. Shepelev, Y. F.; Anderson, A.; Smolin, Y. I., Crystal structure of a partially lithium-exchanged X zeolite in hydrated (25° C) and dehydrated (275° C) states. *Zeolites* **1990,** *10* (1), 61-63.

35. Shepelev, Y. F.; Butikova, I.; Smolin, Y. I., Crystal structures of the partially K-, Rb-, and Cs-exchanged forms of NaX zeolite in both the hydrated and the dehydrated (400° C) states. *Zeolites* **1991,** *11* (3), 287-292.

36. Anderson, A. A.; Shepelev, Y. F.; Smolin, Y. I., Structural study of Mg-exchanged NaX and CaX zeolites in hydrated (25° C) and dehydrated (400° C) states. *Zeolites* **1990,** *10* (1), 32-37.

37. Bennett, J.; Smith, J., Positions of cations and molecules in zeolites with the faujasite-type framework I. Dehydrated Ca-exchanged faujasite. *Mate. Res. Bull.* **1968,** *3* (8), 633-642.

38. Frising, T.; Leflaive, P., Extraframework cation distributions in X and Y faujasite zeolites: A review. *Microporous Mesoporous Mater.* **2008,** *114* (1), 27-63.

39. Ciraolo, M. F.; Hanson, J. C.; Toby, B. H.; Grey, C. P., Combined X-ray and neutron powder refinement and NMR study of hydrochlorofluorocarbon HCFC-124a (CF_2HCF_2Cl) binding on NaX. *J. Phys. Chem. B* **2001,** *105* (49), 12330-12337.

40. (a) Caldarelli, S.; Buchholz, A.; Hunger, M., Investigation of sodium cations in dehydrated zeolites LSX, X, and Y by ^{23}Na off-resonance RIACT triple-quantum and high-speed MAS NMR spectroscopy. *J. Am. Chem. Soc.* **2001,** *123* (29), 7118-7123; (b) Lee, Y.; Carr, S. W.; Parise, J. B., Phase transition upon K^+ ion exchange into Na-low silica X: combined NMR and synchrotron X-ray powder diffraction study. *Chem. Mate.* **1998,** *10* (9), 2561-2570.

41. Eulenberger, G.; Shoemaker, D. P.; Keil, J., Crystal structures of hydrated and dehydrated synthetic zeolites with faujasite aluminosilicate frameworks. I. The dehydrated sodium, potassium, and silver forms. *J. Phys. Chem.* **1967,** *71* (6), 1812-1819.

42. Reed, T. B.; Breck, D., Crystalline zeolites. II. Crystal structure of synthetic zeolite, type A. *J. Am. Chem. Soc.* **1956,** *78* (23), 5972-5977.

43. Breck, D. W., *Zeolite molecular sieves*. Krieger: 1984.

44. (a) Yanagida, R. Y.; Amaro, A. A.; Seff, K., Redetermination of the crystal structure of dehydrated zeolite 4A. *J. Phys. Chem.* **1973,** *77* (6), 805-809; (b) Breck, D.; Eversole, W.; Milton, R.; Reed, T.; Thomas, T., Crystalline zeolites. I. The properties of a new synthetic zeolite, type A. *J. Am. Chem. Soc.* **1956,** *78* (23), 5963-5972.

45. (a) Bertsch, L.; Habgood, H., An infrared spectroscopic study of the adsorption of water and carbon dioxide by Linde molecular sieve X1. *J. Phys. Chem.* **1963,** *67* (8),

1621-1628; (b) Ward, J.; Habgood, H., The infrared spectra of carbon dioxide adsorbed on Zeolite X. *J. Phys. Chem.* **1966,** *70* (4), 1178-1182.

46.   Angell, C.; Howell, M., Infrared spectroscopic investigations of zeolites and adsorbed molecules. Part V. Carbon dioxide. *Can. J. Chem.***1969,** *47* (20), 3831-3836.

47.   Pirngruber, G.; Raybaud, P.; Belmabkhout, Y.; Čejka, J.; Zukal, A., The role of the extra-framework cations in the adsorption of CO_2 on faujasite Y. *Phys. Chem. Chem. Phys.* **2010,** *12* (41), 13534-13546.

48.   (a) Montanari, T.; Busca, G., On the mechanism of adsorption and separation of CO_2 on LTA zeolites: An IR investigation. *Vib Spectrosc.* **2008,** *46* (1), 45-51; (b) Chen, C.; Ahn, W.-S., CO_2 adsorption on LTA zeolites: effect of mesoporosity. *Appl. Surf. Sci.* **2014,** *311*, 107-109; (c) Jaramillo, E.; Chandross, M., Adsorption of small molecules in LTA zeolites. 1. NH_3, CO_2, and H_2O in zeolite 4A. *J. Phys. Chem. B* **2004,** *108* (52), 20155-20159; (d) Bae, T.-H.; Hudson, M. R.; Mason, J. A.; Queen, W. L.; Dutton, J. J.; Sumida, K.; Micklash, K. J.; Kaye, S. S.; Brown, C. M.; Long, J. R., Evaluation of cation-exchanged zeolite adsorbents for post-combustion carbon dioxide capture. *Energy Environ. Sci.* **2013,** *6* (1), 128-138.

49.   Kappers, M.; Vaarkamp, M.; Miller, J.; Modica, F.; Barr, M.; Van der Maas, J.; Koningsberger, D., Ion-dipole interactions between adsorbed CO and support cations in Pt/K-LTL. *Catal. Lett.* **1993,** *21* (3-4), 235-244.

50.   Ruthven, D. M., *Principles of adsorption and adsorption processes*. John Wiley & Sons: 1984.

51.   Plant, D.; Jobic, H.; Llewellyn, P.; Maurin, G., Diffusion of CO_2 in NaY and NaX faujasite systems: quasi-elastic neutron scattering experiments and molecular dynamics simulations. *Eur. Phys J. Spec. Top.* **2007,** *141* (1), 127-132.

52.   Sato, K.; Nishimura, Y.; Matsubayashi, N.; Imamura, M.; Shimada, H., Structural changes of Y zeolites during ion exchange treatment: effects of Si/Al ratio of the starting NaY. *Microporous Mesoporous Mater.* **2003,** *59* (2), 133-146.

53.   Zhang, L.; Huang, Y., An investigation into the crystallization of low-silica X zeolite. *J. Porous Mater.* **2015,** *22* (4), 843-850.

54.   Hunger, M.; Horvath, T., Multi-nuclear solid-state NMR study of the local structure of SiOHAl groups and their interaction with probe-molecules in dehydrated faujasite, Mordenite and Zeolite ZSM-5. *Ber. Bunsenges. Physik. Chem.* **1995,** *99* (11), 1316-1320.

55.   Dybowski, C.; Neue, G., Solid state [207]Pb NMR spectroscopy. *Prog Nucl Magn Reson Spectrosc.* **2002,** *41* (3), 153-170.

56.   Zhang, Y.; Lucier, B. E.; Huang, Y., Deducing CO_2 motion, adsorption locations and binding strengths in a flexible metal–organic framework without open metal sites. *Phys. Chem. Chem. Phys.* **2016,** *18* (12), 8327-8341.

57.   Fulmer, G. R.; Miller, A. J.; Sherden, N. H.; Gottlieb, H. E.; Nudelman, A.; Stoltz, B. M.; Bercaw, J. E.; Goldberg, K. I., NMR chemical shifts of trace impurities: common

laboratory solvents, organics, and gases in deuterated solvents relevant to the organometallic chemist. *Organometallics* **2010,** *29* (9), 2176-2179.

58.　　Eichele, K., WSolids NMR Simulation Package, Version 1.20. 21; 2013.

59.　　Vold, R. L.; Hoatson, G. L., Effects of jump dynamics on solid state nuclear magnetic resonance line shapes and spin relaxation times. *J. Magn. Reson.* **2009,** *198* (1), 57-72.

60.　　Beeler, A. J.; Orendt, A. M.; Grant, D. M.; Cutts, P. W.; Michl, J.; Zilm, K. W.; Downing, J. W.; Facelli, J. C.; Schindler, M. S.; Kutzelnigg, W., Low-temperature carbon-13 magnetic resonance in solids. 3. Linear and pseudolinear molecules. *J. Am. Chem. Soc.* **1984,** *106* (25), 7672-7676.

61.　　(a) Vinegar, H.; Tutunjian, P.; Edelstein, W.; Roemer, P. In *Determining carbonate content of cores by ^{13}C NMR*, SCA Conference paper, **1989**; (b) Stueber, D.; Patterson, D.; Mayne, C. L.; Orendt, A. M.; Grant, D. M.; Parry, R. W., Carbonates, Thiocarbonates, and the Corresponding Monoalkyl Derivatives. 1. Their Preparation and Isotropic ^{13}C NMR Chemical Shifts. *Inorg. Chem.* **2001,** *40* (8), 1902-1911.

62.　　Curtiss, L.; Brand, H.; Nicholas, J.; Iton, L., Predicted proton affinities of H_3SiO^-, H_3SiOH, $H_3SiOSiH_3$, and $H_3SiOAlH^-_3$. *Chem. Phys. Lett.* **1991,** *184* (1-3), 215-220.

63.　　Turco, R.; Pischetola, C.; Di Serio, M.; Vitiello, R.; Tesser, R.; Santacesaria, E., Selective epoxidation of soybean oil in the presence of HY zeolite. *Ind. Eng. Chem. Res.* **2017**.

64.　　(a) Czjzek, M.; Jobic, H.; Fitch, A. N.; Vogt, T., Direct determination of proton positions in DY and HY zeolite samples by neutron powder diffraction. *J. Phys. Chem.* **1992,** *96* (4), 1535-1540; (b) Brunner, E., 1H MAS NMR investigations on the proton distribution in H　Y zeolites. *Microporous Mater.* **1993,** *1* (6), 437; (c) Mortier, W.; Pluth, J.; Smith, J., Réévaluation of proton positions in hydrogen faujasite. *J. Catal.* **1976,** *45* (3), 367-369.

65.　　Sigmal-Aldrich, Molecular sieve 3A.

http://www.sigmaaldrich.com/chemistry/chemical-synthesis/learning-center/technical-

bulletins/al-1430/molecular-sieves.html (Accessed August 20 2017)

3.6   Appendices
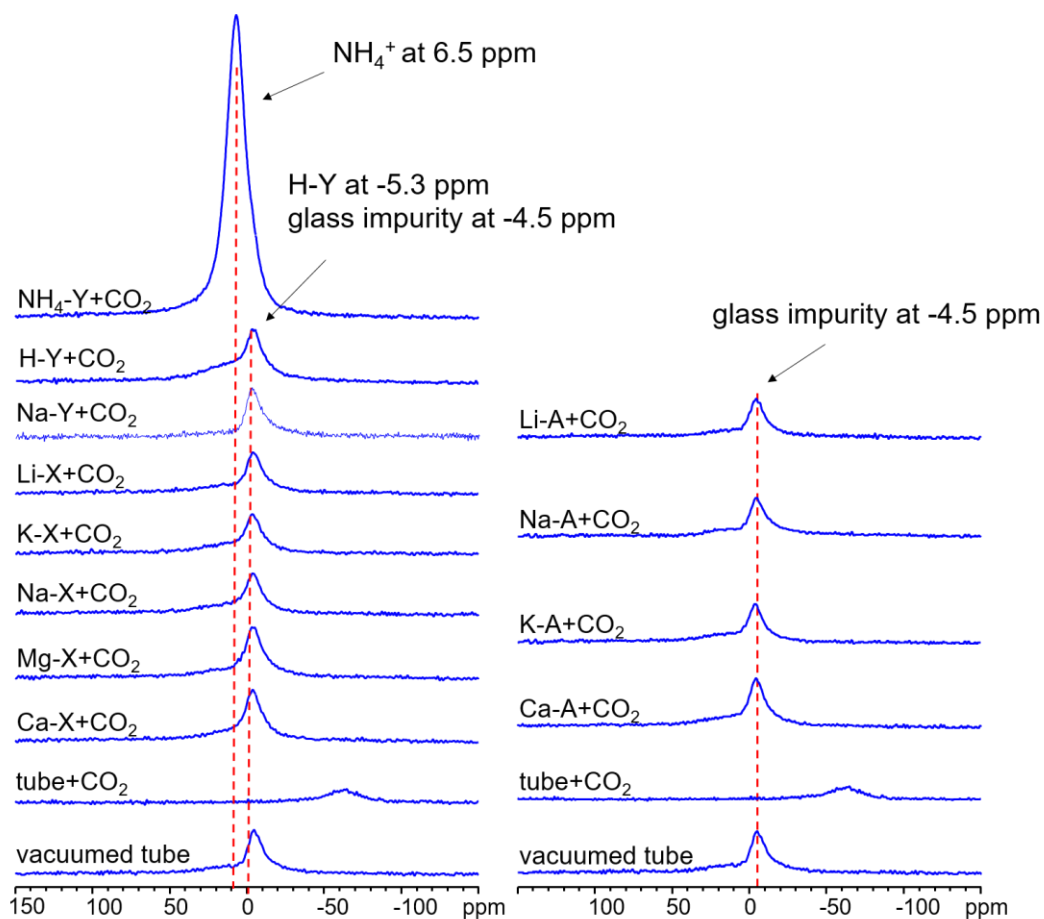
Figure S3-1 - ^{1}H SSNMR static experimental spectra of activated and CO_2 loaded zeolite samples, CO_2 loaded empty tube, and vacuumed tube. The spectra indicate that all ^{1}H resonances come from the impurities of glass tubes, except for the resonance from NH_4-Y zeolite sample, which was contributed by H atoms from ammonium cations.
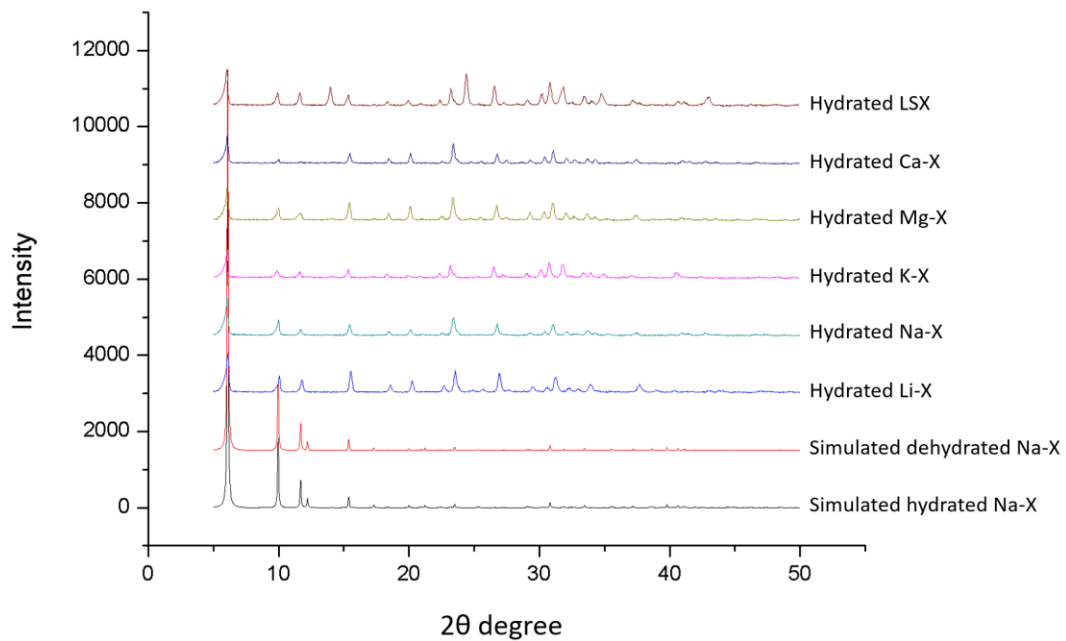
Figure S3-2 - Calculated and experimental PXRD results of ion-exchanged and hydrated Faujasite (FAU) type zeolite X.
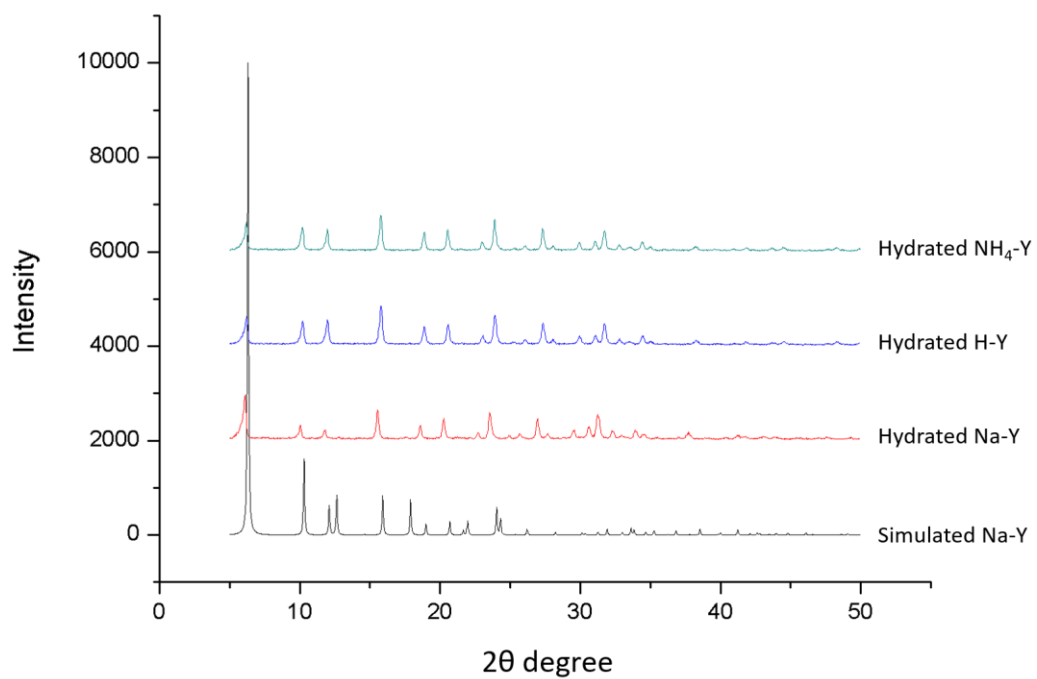
Figure S3-3 - Calculated and experimental PXRD results of commercial and calcined, hydrated Faujasite (FAU) type zeolite Y.
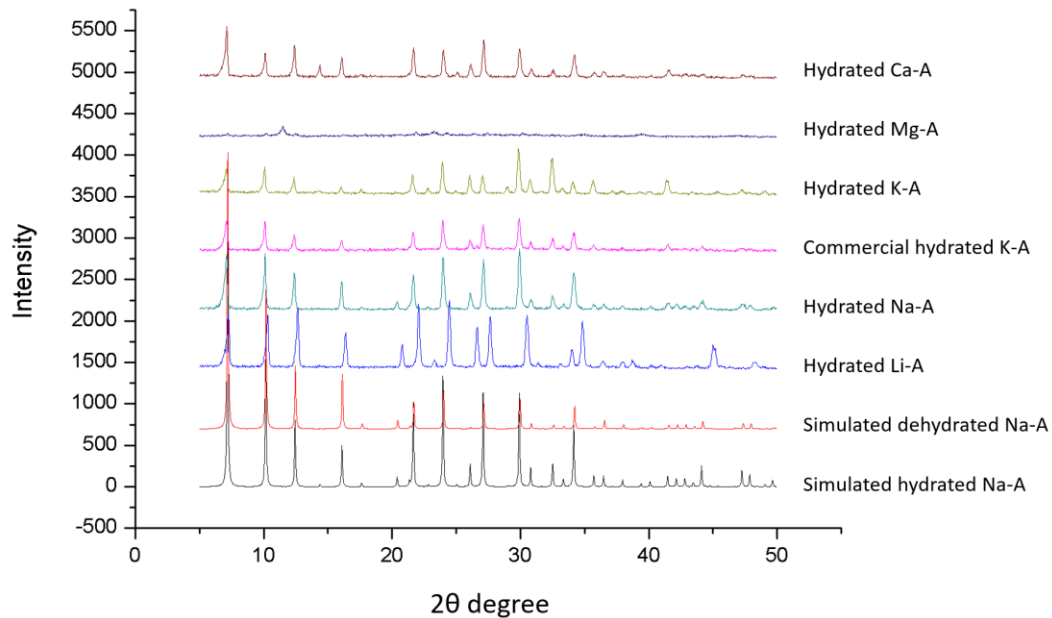
Figure S3-4 - Calculated and experimental PXRD results of ion-exchanged and hydrated Linde Type A (LTA) zeolite.

Table S3-1. Commercial, synthesized and ion-exchanged zeolites used in this work.

Zeolite Type	Charge Balancing Cation Type
LTA, Zeolite A	Li^+, Na^+, K^+, Ca^{2+}
FAU, Zeolite X	Li^+, Na^+, K^+, Mg^{2+}, Ca^{2+}
FAU, Low-Silicate X (LSX)	Na^+ & K^+
FAU, Zeolite Y	Na^+, H^+, NH_4^+

Table S3-2. Exchanged cation occupancy preferences in partially-exchanged and dehydrated FAU type X and Y zeolites. All exchanged cations prefer to occupy Site II firstly as the most favorable site.

Preference	1st	2nd	3rd
Li-X	Site II	Site I'	Site III or III'
Na-X	Site II	Site I'	Site III or III'
K-X	Site II	Site I	-
Mg-X	Site II	Site I	-
Ca-X	Site II	Site I	Site III (rare)
K,Na-LSX	Site II	Site I'	-
Na-Y	Site II	Site I	Site III (rare)
H-Y	H1, H2 and H3 were formed in calcination procedure.		
NH$_4$-Y	Site II	Site I'	-

Table S3-3. Observed ^{13}C CS parameters of ion-exchanged FAU and LTA zeolites

293 K	Site I			Site II		
	Δiso,	Span,	skew	Δiso,	Span,	skew
Li-X				124.5	2.0	0
Na-X				125.5	2.5	0
K-X				125.5	3.0	0
Mg-X				123.5	3.9	0
Ca-X				124.8	4.5	0
Na-Y				125.2	0.8	0
H-Y				124.7	1.0	0
NH$_4$-Y				124.8	0.8	0
Li-A				123.0	18.0	0
Na-A	153.0	100.0	-0.85	125.0	8.0	0
K-A	140.0	190.0	-0.78	130.2	57.0	-0.08
Ca-A				123.1	4.0	0
123 K	Site I			Site II		
	Δiso,	Span,	skew	Δiso,	Span,	skew
Li-X	125.0	200	0.45	122.0	310	1.0
Na-X	140.0	80	0	124.0	320	0.95
K-X	128.0	100	0	125.5	310	1.0
Mg-X	115.0	240	-1.0	115.0	230	0.7
Ca-X				128.0	180	0.12
Na-Y				124.5	11	-0.1
H-Y				124.5	17	-0.05
NH$_4$-Y				125.0	22	0
Li-A	125.0	180	0.3	125.5	310	0.95
Na-A	162.0	118	0.95			
K-A				126.0	180	-0.15
Ca-A	126.0	153	0.53	125.5	300	1.0

Table S3-4. Chemical formula, exchange ratios, site occupancy preferences and possible cation numbers of ion-exchanged zeolites.

FAU zeolite type X, Y and LSX

Zeolite X	Chemical Formula	Exchange ratio	Site II, max 4	Site I', max 4	Site I, max 4	Site III, max 3	M total	Na total
Li-X	$Li_{48.7}Na_{51.3}Al_{100}Si_{123}O_{446}$	48.71%	4 Li	1.24 Li, 2.76 Na	Vacant	2.76 Na	5.24 Li	5.52 Na
Na-X	$Na_{100}Al_{100}Si_{123}O_{446}$	-	4 Na	3.35 Na	Vacant	3.41 Na	-	10.76 Na
K-X	$K_{51.2}Na_{48.8}Al_{100}Si_{123}O_{446}$	51.16%	4 K	2.49 Na	1.51 K	2.76 Na	5.51 K	5.25 Na
Mg-X	$Mg_{24.8}Na_{50.4}Al_{100}Si_{123}O_{446}$	50.49%	2 Mg	0.67 Mg	2.66 Na	2.76 Na	2.67 Mg	5.42 Na
Ca-X	$Ca_{9.3}Na_{81.4}Al_{100}Si_{123}O_{446}$	18.58%	1 Ca, 2 Na	4 Na	Vacant	2.76 Na	1 Ca	8.76 Na

Zeolite LSX	Chemical Formula	Exchange ratio	Site II, max 4	Site I'(Na),	Site I (K),	Site III, max 5-8	M total	Na total
K,Na-LSX	$K_{10.9}Na_{89.1}Al_{100}Si_{107.5}O_{415}$	10.85%	1.26 K, 2.24 Na	3 Na	Vacant	5.07 Na	1.26 K	10.31 Na

Zeolite Y	Chemical Formula	Exchange ratio	Site II, max 4	Site I', max 4	Site II', max 4	Site III, max 1	M total	Na total
Na-Y	$Na_{100}Al_{100}Si_{235}O_{446}$	-	3.8 Na	2.5 Na	-	0.86 Na	-	7.16 Na
NH4-Y	-	-	NH4+	NH4+	Na	-	-	-
H-Y	-	-	H2, H3	H1, outside of hexagonal prism	-	-	-	-

Linde Type A (LTA) zeolite

Zeolite A	Chemical Formula	Exchange ratio	S_I, max 8	S_II, max 4	S_III, max 1	M total	Na total
Li-A	$Li_{65.5}Na_{34.5}Al_{100}Si_{100}O_{400}$	66.52%	8 Li	4 Na	4 Na	8 Li	4 Na
Na-A	$Na_{100}Al_{100}Si_{100}O_{400}$	-	8 Na	4 Na	-	-	12 Na
K-A	$K_{41.1}Na_{58.9}Al_{100}Si_{100}O_{400}$	41.08%	0.93 K, 7.07 Na	4 K	4 K	4.93 K	7.07 Na
Ca-A	$Ca_{22.4}Na_{55.2}Al_{100}Si_{100}O_{400}$	44.89%	2.69 Ca, 6.62 Na	Vacant	Vacant	2.69 Ca	6.62 Na

Table S3-5. Original ICP-MAS elemental analysis data.

	Li	Na	Mg	K	Ca	Al	29Si (KED)
	Y (ppm)	measured previously	Y (ppm)	Y (ppm)	Y (ppm)	Y (ppm)	Y (ppm)
2% HNO₃ rinse	-0.00076604		-0.000359337	-0.017360415	-0.0010682231	-0.000515337	-0.136256722
std 100pb K Si,	0.018930257		0.018954784	0.092114281	0.019350002	0.019182233	0.093899723
std 500ppb K Si,	0.09368993		0.09984089	0.485345092	0.098972028	0.100207217	0.49977084
std 1000ppb K	0.19481445		0.199709308	0.96900261	0.205405762	0.201184486	1.000370395
std 2ppm K Si,	0.400970516		0.400237384	2.019557882	0.397586612	0.399396841	2.000177106
2% wash	1.70576E-05		-4.87407E-06	-0.000230082	0.002203166	-0.000281229	-0.000352301
2%	4.34192E-05		5.362E-05	0.000601363	-0.003397001	3.36578E-05	0.004769304
Li-A	0.061223167	4.608614	0.007140456	0.037060472	0.186836946	0.410295277	0.635136502
Li-X	0.046287859	4.787172	0.006956213	0.036833729	0.286762699	0.412863565	0.837683979
LS-X(K)	0.002406708	4.437961	0.009291729	0.077463817	0.182168296	0.340811033	0.626704333
Mg-X	0.001933735	4.080827	0.055211381	0.028653117	0.178068821	0.275868624	0.647011721
Ca-A	0.002358634	4.493627	0.006042611	0.036658475	0.428646142	0.421183546	0.78089074
Ca-X	0.002019024	3.94203	0.006063743	0.052956824	0.3436561	0.32035218	0.56968855
K-A	0.002729262	5.000552	0.005276184	0.24094048	0.212072896	0.412223681	0.807665862
K-X	0.002540072	4.408683	0.00827336	0.226525822	0.188752409	0.31859797	0.634268494
2% HNO₃	0.000169025		1.65185E-05	0.00210027	0.000988838	-0.000192971	0.02186856
blk acid 2% RG	0.002226822		0.007403279	0.039886882	0.296457052	0.065118453	0.229247327
HNO₃ RG blank	0.001753369	3.540832	0.006504398	0.032932283	0.296457052	0.065118453	0.186912

Chapter 4

4   Summary and future work

4.1   Summary

In this work, the guest dynamic motions and behaviour of CO_2, CO and C_2D_4 adsorbed in the α – zinc formate MOF and in various ion-exchanged FAU- and LTA-type zeolites have been investigated using multinuclear variable-temperature SSNMR spectroscopy. By simulating experimental spectra using the WSolids analytical simulation package and the EXPRESS motional simulation package, both the apparent NMR parameters as well as the dynamic parameters could be obtained. The results in this thesis indicate that static multinuclear ^{13}C, ^{2}H, ^{67}Zn and ^{1}H-^{13}C cross polarization (CP) SSNMR experiments is an effective route for revealing the guest-host interactions within solid adsorbents such as MOFs.

In chapter 2, ^{13}C SSNMR experiments indicate that adsorbed CO_2 and CO guest molecules have reduced mobility within α - zinc formate at lower experimental temperatures. ^{2}H NMR experiments suggest that the mobility of adsorbed C_2D_4 guests is also temperature-dependent, with less mobile C_2D_4 molecules observed at decreased temperatures. Simulation results suggest that CO_2, CO, and C_2D_4 guest molecules all undergo the same well-defined motion patterns in the α - zinc formate MOF within the experimental temperature ranges from 433 K to 123 K in CO_2 and CO loaded samples, and from 363 K to 123 K in C_2D_4 loaded samples: a localized C_3 rotational wobbling motion upon the adsorption site, along with a non-localized C_2 hopping motion between adjacent adsorption sites, despite the very different nature of these guests. Adsorbed CO_2 is particularly interesting, as it seems to induce some structural change that surprisingly restricts CO_2 mobility in the α - zinc formate framework at and above room temperature. ^{1}H-^{13}C CP SSNMR experiments on adsorbed CO_2 and CO confirm that the hydrogen atoms of formate linkers lining the MOF interior act as the guest adsorption sites. Single crystal XRD (SCXRD) experiments on CO_2 loaded α - zinc formate revealed the CO_2 guest positions within the zig-zag shaped one-dimensional channels of this MOF. The results suggest that CO_2 guests are actually adsorbed very close to the inner surface of the

channel. The relatively short distances from CO_2 guests to the five nearest hydrogen atoms indicates the presence of weak hydrogen-bonding or electrostatic interactions between the MOF and CO_2 guests.

There are odd trends in the NMR parameters of certain guests adsorbed in this MOF. The span or breadth of ^{13}C SSNMR spectra of CO_2 reaches a minimum at 293 K and increases as temperature is both increased and decreased from this point, which contrasts with the negative temperature vs. span trend observed for guests such as CO. ^{2}H SSNMR spectra of C_2D_4-loaded α - zinc formate reveal the ^{2}H asymmetry parameter η_Q reaches a minimum at 273 K, rather than the linear negative relationship seen for C_Q (^{2}H) in this system. This data hints that some structural change in the MOF may occur near room temperature. Static ^{67}Zn NMR experiments indicate that the activation process and presence of CO_2, CO or C_2D_4 guests does not have a significant influence on the local electronic environment about the fully saturated Zn atoms. It appears that the guests do not directly interact with the Zn atoms or even perturb their local environment.

In chapter 3, it can be seen that CO_2 guests adsorb upon specific cation sites in fully dehydrated and ion-exchanged zeolites. The nature of the substituted cation, the Si/Al ratio and the framework topology are three main determinants of adsorbed CO_2 guest behaviour within zeolites. The cation exchange ratios in these zeolites have been established by conducting ICP-MS experiments, and are in agreement with predictions of the various cation substitution positions from literature sources. Static ^{13}C SSNMR experiments have provided direct evidence of adsorbed CO_2 dynamics. The ^{13}C SSNMR lineshapes become broader when the temperature is reduced, reflecting reduced mobility of CO_2 guests within these zeolites. At the lowest experimental temperature of 123 K, ^{13}C SSNMR experiments suggest that adsorbed CO_2 guest may become completely immobilized or undergo heavily-restricted motions upon the zeolite cations, based on a comparison between the experimental ^{13}C SSNMR powder patterns and associated NMR parameters versus the known NMR parameters and spectrum of solid CO_2. The low-silica X (LSX) zeolite features the formation of a carbonate species involving CO_2 due to strong chemisorption effects. ^{13}C SSNMR experiments have confirmed that this robust carbonate

compound exists even being heated up to 433 K. ^{1}H-^{13}C CP experiments on H$^+$ and NH$_4^+$ substituted zeolites have provided additional direct evidence of adsorptive interactions between CO_2 guests and the charge-balancing cations in zeolites. These zeolites appear to have moderate CO_2 adsorption capabilities and are candidates for further dynamic studies of CO_2 guest behaviour using VT ^{13}C SSNMR experiments.

4.2   Future work

In chapter 2, it appears that the adsorption of CO_2 in α - zinc formate induces some structural change in this MOF above room temperature, yet this change is only induced by CO_2 guests and is not observed in CO and C_2D_4 loaded α-zinc formate. These SSNMR results alone are not enough to completely investigate the actual chemical environment of CO_2 guests within the α-zinc formate MOF. Thus, single crystal XRD experiments at elevated temperatures should provide key evidence of this phenomenon, and should reveal the CO_2 location and structure, as well as potential interactions between CO_2 guest and α - zinc formate framework.

In this thesis, it has been observed that the α - zinc formate MOF will partially transform into the β – phase if heated up to 433 K. After cooling the MOF down to room temperature, the β – phase remains stable. Attempts to trap CO_2 guests from the α-phase across the phase transition to the transformed non-porous β – phase via various heating strategies and techniques, followed by static VT ^{13}C NMR experiments, should be explored in order to examine the dynamic status and local environment of trapped CO_2 guests in this unique phase.

In chapter 3, various CO_2 guest behaviour has been investigated, as influenced by the alkali and alkali earth cations in the FAU and LTA zeolite families. It appears that the cation types and distributions in these zeolite frameworks are the main factors which directly influence CO_2 guest behaviour. The Si/Al ratio of the zeolite determinates the CO_2 adsorption capabilities, such as the low Si/Al ratio (Si/Al = 1) LSX and LTA zeolites appear the strongest interactions with CO_2 guest, while the type Y zeolites (Si/Al ratio

about 2.3) do not show obvious strong interactions with CO_2 guest, leaving it tumbling fast even at the lowest temperature of 123 K. And various types of CO_2 adsorption behaviour are greatly dependent on the specific type of zeolite. The direct-excitation ^{13}C VT SSNMR results in this thesis can reveal the CO_2 guest behaviour in zeolites, but only provide limited evidence of the type and strength of CO_2-cation interactions. Multinuclear SSNMR studies on the direct interactions of NMR-active Li^+, Na^+, K^+, Mg^{2+} and Ca^{2+} cations with adsorbed CO_2 guests can be performed using other pulse sequences, such as SEDOR, to establish CO_2-cation connectivity, the effects of guest adsorption on the cation local environments, the cation sites preferred for CO_2 adsorption, and to further investigate guest motion Moreover, some other crucial zeolites employed in industrial applications, such as ZSM-5, zeolite-β, ferrierite, mordenite and many other modified zeolites, like aluminophosphate zeolite ALPO-18 and silicoaluminophosphate zeolite SAPO-34, are excellent zeolite adsorbents that are well-suited for VT SSNMR experiments on adsorbed CO_2 guest dynamics and locations, in which the specific zeolite features may directly link to certain types of CO_2 motion/adsorption.

Moreover, exchanging transition metal cations, such as Cu^+. $Cu2^+$, Ni^{2+}, Co^{2+}, into zeolite frameworks usually boosts the catalysis properties of corresponding zeolites. And studies on the transition metal centres, CO_2 motional dynamics and CO_2-cation interactions in these transition-metal-exchanged zeolites may also be helpful to related catalysis applications.

Curriculum Vitae

Name: Bowei Wu

EDUCATION

Sep. 2015– present	• M.Sc. candidate, Department of Chemistry, Faculty of Science, Western University
	Course taken at Western:
	Crystallograpy I (66/100);
	Advanced mineralogy & Crystalograpy (86/100);
	Chemistry 9658: Seminar (76/100)
Sep. 2010–Jun.2014	• B.Sc. in College of Chemistry and Chemical Engineering (Polymer Chemistry), Xiamen University (GPA 3.2/4)

RESEARCH EXPERIENCE

Sep. 2015 – present	Solid-state NMR study on host-guest interactions in metal organic frameworks and zeolites
Sep. 2012– Jun.2014	Comprehensive study on force-response polymer synthesis and related reactions

WORK EXPERIENCE

Sep. 2010– present	Laboratory Teaching Assistant for Chem 1301 and 1302, Department of Chemistry, Faculty of Science, Western University.
Jun.-Jul.2014	Intership in Xiamen Entry-Exit Inspection And Quarantine Bureau
Jun.2014	Group vice-leader of Graduation Society Practice
Sep. 2011–Aug.2013	Vice-Chair of student union central office in College of Chemistry and Chemical Engineering, Xiamen University
Jun.2014	Group leader of Chemistry Society Practice

CONFERENCE AND PUBLICATION

Poster presentation "Investigating CO_2, CO and C_2D_4 Dynamics in the α- Zinc Formate and $M_2(BDC)_2DABCO$ MOFs via Solid-State NMR", 100 th Canadian Chemistry Conference and Exhibition, Toronto, ON, Canada, May 28 - June 1, 2017. Honorable mention.

B. Yang, H. Zhang, H. Peng, Y. Xu, B. Wu, et al. Self-healing metallo-supramolecular polymers from a ligand macromolecule synthesized via copper-catalyzed azide–alkyne cycloaddition and thiol–ene double "click" reactions, *Polym. Chem.*, **2014**, *5*, 1945-1953